Probing Higgs boson production at the high momentum frontier using $H \to b\bar{b}$ decays



Federico Celli

Somerville College

University of Oxford

A thesis submitted for the degree of

Doctor of Philosophy

Michaelmas Term 2022

In loving memory of my dear friend Chiara

Acknowledgements

This DPhil degree has been one of the most educational and enriching experiences of my life. The journey that led to the writing of this thesis has been long and challenging, but one that has allowed me to meet many wonderful people and to live in a completely new and stimulating environment. Here, I would like to thank all those who have contributed to making this experience so special and unforgettable.

First of all, I would like to express my deepest gratitude to my supervisor James Frost, who gave me the opportunity to work on this research degree. This experience would not have been the same without your continued support, your expertise and your patience. Thank you for having guided my work, for your kindness, and for your understanding in times of need.

I am also grateful to all the members of the ATLAS Exotics group at Oxford, for having accompanied and helped me throughout this journey. In particular, I would like to thank Todd Huffman for being, effectively, a second supervisor. Thank you for taking interest in my research work, for encouraging me and giving me valuable advice.

Special thanks to all members of my cohort and, in particular, to Jonas, Dan, Philipp, Kamil, Hayden, James and Maria. Thank you for all the times you helped me, for the laughs and for the many bops. I am also grateful for the short, but fun, time we spent together in Geneva, for the movie nights, the fun conversations at the "CERN Lunch Club", and for the great hikes.

During the final year of my degree, I had the pleasure of sharing my office with some of the most amazing people I have ever met. Alessandro, Maggie, Siyuan and Olivier, I will never be grateful enough for the fantastic time we spent together. Thank you all for the happy memories, the funny stories (especially

Alessandro's) and the adventures we shared during my final year. My only regret is not having met you sooner.

I also would like to thank my lifelong friends and members of the "Second Family" - Tom, Carpo, Matte, John, Nando, Fillo, Fede, Alice, Giada, Mattia, Barbara and Elvis. Thank you for proving that our friendship goes far beyond the physical distance that separates us. I will always be grateful for the great fun we had every time I travelled home, for the countless calls during the pandemic, and for being, sometimes, so adorably obnoxious.

Thanks should also go to my Mum and Dad, to my sister Giulia and my entire family, for supporting me in the decision to undertake this journey and for always being by my side. Thank you for your care, your patience and for giving me shelter whenever I need it.

Lastly, Alice, words cannot express my gratitude for you enough. Thank you for being by my side for all these years and for the love and care you show for me. Thank you for your courage and perseverance, even in times when we were forced apart from each other. I cannot wait to continue this journey with you.

This thesis is dedicated to my dear friend Chiara, who sadly passed away early this year. Chiara was a truly remarkable person, and a constant presence during my academic life. Her kindness, curiosity and determination have always inspired me and, without her, I would not be the person I am today. For this, and all our happy memories, I will eternally be grateful.

It is just the beginning of a new journey.

Abstract

This thesis presents constraints on the Higgs boson production cross-section from high-momentum $H \to b\bar{b}$ decays, using $\sqrt{s} = 13$ TeV proton-proton collision data collected by the ATLAS experiment during the LHC Run 2, corresponding to an integrated luminosity of 136 fb^{-1}. The Higgs boson is reconstructed within a single large-radius calorimeter jet associated with at least two b-tagged variable-radius track jets. At least one additional large-radius jet is required to be present in the events, representing the recoil target of the high-momentum Higgs boson. For the first time in the $b\bar{b}$ decay mode, the Higgs boson is probed inclusively with contributions from its four main production modes: ggF, VBF, VH and $t\bar{t}$H. Higgs boson measurements are performed in a fiducial volume for Higgs boson transverse momentum $p_{\mathrm{T}}^{H} > 450$ GeV and in the four differential p_{T}^{H} ranges 300-450 GeV, 450–650 GeV, 650–1000 GeV, > 1 TeV. From all measurements, 95% confidence level upper limits on the Higgs boson cross-section are extracted. For the first time, a limit is set on the Higgs boson production at $p_{\mathrm{T}}^{H} > 1$ TeV, which results to be $\sigma_H(p_{\mathrm{T}}^{H} > 1 \text{ TeV}) < 9.6$ fb. All cross-section results are found to be consistent with the Standard Model predictions. A differential $Z \to b\bar{b}$ measurement is also performed in equivalent ranges of Z boson transverse momentum.

Author's Contributions

The author Federico Celli has been part of the team producing the *Boosted* $H(\to b\bar{b}) + jet$ analysis presented in this thesis since December 2019. The analysis team consisted of a couple of PhD students, a couple of postdocs and a handful of seniors guiding. The results were published in *Physical Review D* in May 2022, and they can be found in Reference [1].

This thesis has many commonalities with that of a previous analysis team member [2], whose research work was nevertheless decoupled in time with the author's. While the other student contributed in the early stages of the analysis, the author is responsible for considerable improvements in the analysis strategy, as well as the production of the final published results [1].

The author took a central role within the team, as the main PhD student analyser working with a couple of active postdocs. Federico participated in the multiple unblinding stages of the analysis, producing and validating all Higgs and Z boson measurements in collaboration with the analysis contact. A list of the author's most important contributions is given in the following.

- **Fit Results, Model Development and Validation:** The author participated in the multiple unblinding stages of the analysis by producing final fit results in the various analysis regions and by carrying out pull and correlation studies for the fit parameters. The author also used these and Asimov datasets to validate all fit results, as the analysis moved from inclusive, to fiducial, to differential unblinding, for both Z and Higgs boson deliverables. A more detailed list of the author's contributions to the analysis results is given at the end of the introduction to Chapter 9.

- **Systematic Uncertainties Contributions:** The author developed a tool within the fitting framework used for estimating the contribution of systematics on the total uncertainty of the analysis results. These studies, which are summarized in Tables 9.3, 9.5 and 9.8, helped the team gaining a better understanding of the analysis uncertainties and to assess the extent of contributions coming from various sources.

- **Single Top Quark Background Modelling:** The author was deeply involved in the modelling of the single top quark background process (see Section 7.3.2), whose mass distribution partly overlaps to the Higgs signal and has a comparable yield. The author was also responsible for the estimation and implementation in the fitting framework of the uncertainties on this process, in addition to decorrelation studies on Asimov datasets (see Sections 8.1.3 and 8.2.1).

- **Smoothing Optimisation Studies:** The author carried out the optimisation of the smoothing thresholds (see Section 8.2.2) to be used in the differential Higgs measurements. This involved studying the ratios between systematic and nominal distributions in the regions and determining the threshold values giving the smoothest systematic shapes without removing physical features.

- **Pruning Optimisation Studies:** The author devoted much time and effort towards the optimisation of pruning thresholds in all analysis regions. The pruning procedure, presented in Section 8.2.3, removes systematics with negligible impact and makes the fit procedure simpler and faster. This became of particular relevance after the introduction of the QCD model fine sampling into the fit, rendering the whole procedure very computationally intensive. The pruning procedure optimised by the author helps keeping the computation time to a reasonable level, while having a negligible impact on the uncertainties on the fit results.

- **Impact of Gamma Parameters:** Due to the limited statistical precision of the MC samples, some of the templates used in the fit have bins with large uncertainties. This information can be introduced in the fit using bin-specific nuisance parameters called *gamma parameters*. A gamma parameter is introduced on a template bin if the uncertainty on said bin exceeds a certain adjustable threshold. The introduction of gamma parameters in the fit was first studied by the author and was found to have negligible impact on all analysis results (see Section 8.3). For this reason, these parameters are not introduced in the final implementation of the fit strategy.

- **Sensitivity Studies for New *b*-taggers:** After the analysis publication, the author worked on preliminary sensitivity projection studies for upcoming analysis iterations. In the future, the MV2 b-tagging algorithm used in the analysis will be abandoned in favour of more performant neural network-based algorithms, like DL1r. The early results obtained by the author and presented in Section 9.6.1 are promising and showcase very viable avenues for increased analysis sensitivity.

- **Studies of $t\bar{t}$ Generator Systematics:** During the first half of 2020, the Parton Shower and Matrix Element systematic uncertainties on the $t\bar{t}$ background were estimated by reweighting the nominal $t\bar{t}$ template. This procedure was uniquely performed because only partial alternative samples were available. This method, however, did not achieve perfect closure in the SR, and fully-simulated alternative samples were eventually generated and adopted. The author studied the modelling of these new $t\bar{t}$ systematics, understood and documented their impact on the fit results. The new $t\bar{t}$ generator uncertainties are among the largest modelling systematics in the analysis.

- **Migration to 5 GeV Binning:** Up until the second half of 2020, in order to compensate for limitations in the fitting framework, an artificially narrow mass binning of 0.5 GeV was necessary to avoid introducing biases in the fits. Since then, however, the advancements in the fitting framework explained

in Section 6.4.3 made it possible to perform all fits with a 5 GeV mass binning. The author performed a full and thorough validation that the new fit setup produced consistent results, allowing the team to simplify the analysis strategy significantly and reduce the sensitivity to the exact implementation of systematics smoothing.

- **Jet Substructure Variables:** The author performed early studies on signal purification using jet substructure variables. Preliminary results show that a high degree of $t\bar{t}$ rejection can be obtained by introducing a selection on these variables, which might be used in a future iteration of the analysis to achieve greater sensitivity.

- **Other work:** During the first year of his DPhil course, the author participated in the initial stages of the calibration of a double b-tagger targeting high-momentum resonances decaying to a $b\bar{b}$ pair. The early results of the calibration, performed on a high-momentum $g \to b\bar{b}$ dataset collected by the ATLAS experiment, are presented in Section 5.1. Future iterations of the analysis plan to adopt an updated version of this dedicated tagger to improve b-tagging performance and signal sensitivity.

In order to further clarify the extent of the author's involvement in the analyses presented in this thesis, short declarations are added after the introductions to Chapters 5, 6, 7, 8 and 9. Their goal is to specify which sections of the thesis are the result of the author's personal contribution and which describe briefly the work of other members of the analysis team, that are nonetheless conducive to a thorough presentation of the covered topic.

Contents

Introduction **1**

1 Theoretical Background **5**

1.1 The Standard Model of Particle Physics 5

1.1.1 The Standard Model as a Gauge Theory 8

1.1.2 The Higgs Mechanism 9

1.2 Higgs Boson Production and Decay 13

1.3 The Higgs Boson at High Momentum 16

1.4 Beyond the Standard Model Effects 19

1.5 Experimental Analysis Signature 20

2 The ATLAS Experiment at the LHC **23**

2.1 The Large Hadron Collider 24

2.2 The ATLAS Detector 28

2.2.1 Coordinate System and Variables 29

2.2.2 The Inner Detector 31

2.2.3 The Calorimeter System 36

2.2.4 The Muon Spectrometer 40

2.2.5 The Trigger System 42

3 Proton-Proton Collisions and Their Simulation **45**

3.1 The Internal Structure of the Proton 45

3.2 Phenomenology of Proton-Proton Collisions 46

3.3 Monte Carlo Simulations 48

4 Object Reconstruction at ATLAS **51**

4.1 Jets . . . 52

4.1.1 Jet Clustering . . . 52

4.1.2 Calorimeter Jets . . . 54

4.1.3 Calorimeter Jet Calibration . . . 59

4.1.4 Track Jets . . . 63

4.1.5 Jet Association . . . 65

4.1.6 Truth Flavour Labelling . . . 66

4.2 b-tagging of Jets . . . 66

4.2.1 The MV2 Tagger . . . 67

4.2.2 The DL1r Tagger . . . 71

4.3 Muons . . . 72

5 Identification of Boosted $H \to b\bar{b}$ Jets **75**

5.1 Double b-tagger Calibration . . . 77

5.2 Data and Simulated Samples . . . 77

5.3 Event Selection . . . 78

5.4 Flavour Fraction Correction . . . 79

5.4.1 Flavour Fraction Templates . . . 80

5.4.2 Template Merging . . . 81

5.4.3 Template Fit . . . 82

5.5 Systematic Uncertainties . . . 85

5.5.1 Treatment of Uncertainties . . . 86

5.6 Calibration Procedure . . . 86

5.7 Results . . . 88

5.8 Conclusions . . . 89

6 Experimental Setup **91**

6.1 Datasets and Trigger Strategy 93

6.2 Simulated Samples 95

6.3 Event Selection and Classification 96

6.3.1 Signal and Validation Regions 98

6.3.2 $t\bar{t}$ Control Region 100

6.3.3 W Control Region from $t\bar{t}$ Events 102

6.4 Analysis Strategy 103

6.4.1 Measurements 104

6.4.2 Blinding Strategy 107

6.4.3 Fitting Procedure 108

6.4.4 Asimov Datasets 110

7 Signal and Background Modelling **111**

7.1 Higgs Boson Signal 113

7.1.1 Higgs Modelling for the Fiducial Measurement 115

7.1.2 Higgs Modelling for the Differential Measurement 117

7.2 QCD Multijet Processes 118

7.2.1 QCD Polynomial Function 120

7.2.2 Hybrid VR Slices 120

7.3 Top Quark Production 124

7.3.1 $t\bar{t}$ Pair Production 124

7.3.2 Single Top Quark Production 127

7.4 V + jets 131

7.4.1 Higher-order Corrections 132

7.4.2 W Control Region Modelling 133

8 Systematic Uncertainties **135**

8.1 Sources of Systematic Uncertainties 138

8.1.1 Large-R Jet Uncertainties 138

8.1.2 Flavour Tagging Uncertainties 141

8.1.3 Modelling Uncertainties 143

8.1.4 Spurious Signal Uncertainties 147

8.2 Treatment of Systematic Uncertainties 148

8.2.1 Decorrelation of Systematics 150

8.2.2 Smoothing of Systematics 154

8.2.3 Pruning of Systematics 158

8.3 Gamma Parameters 161

8.4 V + jets Mass Resolution External Constraints 162

9 Results **167**

9.1 Cross-section Calculation 169

9.2 Standalone $\mathrm{CR}_{t\bar{t}}$ Measurements 170

9.3 Inclusive Higgs Boson Measurement 172

9.4 Fiducial Higgs Boson Measurement 175

9.5 Differential Measurements 177

9.5.1 Differential V + jets and Z Boson Results 179

9.5.2 Differential Higgs Boson Result 181

9.6 Future Outlook 188

9.6.1 Preliminary Studies 190

10 Conclusions **195**

Appendices

A $g \to b\bar{b}$ Calibration - Recent Developments **199**

A.1 The Boosted $X \to b\bar{b}$ Tagger 199

A.2 Changes to the $g \to b\bar{b}$ Calibration 201

B Muon-in-Jet Correction **203**

C QCD Polynomial Order Optimisation **205**

D Single Top tW Interference with $t\bar{t}$ **211**

E Systematic Decorrelation Tests **213**

F Results - Support Material **217**

F.1 Higgs Boson Acceptance and Efficiency 217

F.2 Yield Tables 217

F.3 Differential V + jets Result 220

F.4 Impact Rankings 221

References **223**

Introduction

Ever since the discovery of the Higgs boson at the Large Hadron Collider (LHC) by the ATLAS and CMS Collaborations [3, 4], great effort was dedicated to the measurement of its properties and couplings [5, 6]. With the second period of data taking at the LHC (Run 2), the great increase in luminosity and mature analysis techniques allowed the ATLAS and CMS experiments to perform differential Higgs boson cross-section measurements and, therefore, to start exploring the momentum evolution of Higgs boson production. Despite, at the time of writing, no significant deviations from the Standard Model (SM) predictions having been observed, the Higgs sector is still largely unexplored. Because of its peculiar property to couple to all massive particles, the Higgs boson represents a potential gateway to new physics discoveries beyond the Standard Model (BSM).

Of particular interest in the search for BSM physics is the gluon-gluon-fusion (ggF) Higgs boson production mode [7, 8]. The virtual fermion loop that characterises this process is sensitive to possible contributions from new physics particles, and to the presence of anomalous couplings that give rise to an effective gluon-gluon-Higgs interaction. These BSM effects would be suppressed at energies lower than an unknown new physics scale, but they might become observable as a large Higgs boson cross-section enhancement at high momentum.

Studying this high-energy regime, however, is a challenging endeavour: the rapidly falling Higgs momentum spectrum makes it such that most analyses, such as $H \to \gamma\gamma$ and $H \to ZZ^* \to 4\ell$ [9, 10], start running out of Higgs boson events at transverse momenta (p_{T}) of around 100 GeV [10]. This effect can be mitigated by measuring the Higgs boson via its most abundant decay mode, a bottom anti-bottom quark pair ($b\bar{b}$), which corresponds to a branching ratio of about 58%. The larger number of Higgs boson events collected at high-p_{T} using

this analysis approach, however, comes at a cost. The hadronic $H \to b\bar{b}$ final state is deeply buried in background activity mainly originating from Quantum Chromodynamic (QCD) processes that characterise proton-proton collisions at the LHC. For this reason, a precise knowledge of all background processes and their modelling is of the utmost importance.

This thesis presents an analysis probing the Higgs boson production at high transverse momentum using $H \to b\bar{b}$ decays recorded by the ATLAS experiment during Run 2. The analysis specifically targets very high-p_{T} events by requiring the Higgs boson to recoil against one or more jets of hadronic particles. Since no restrictions on the nature of the recoil objects are required, the Higgs boson is selected inclusively with contributions from its four main production modes: ggF, VBF, VH and $t\bar{t}$H. Therefore, the analysis will be potentially sensitive to BSM effects in the ggF loop at very high p_{T}.

The results of the analysis have been published in May 2022 [1], marking the first time $H \to b\bar{b}$ events are probed inclusively in the four main Higgs boson production modes. The event selection gives access to some of the most energetic Higgs bosons produced at the LHC, with transverse momenta p_{T}^{H} up to and above 1 TeV. Higgs boson cross-section measurements are determined in a fiducial region for $p_{\mathrm{T}}^{H} > 450$ GeV, and within four differential p_{T}^{H} ranges 300–450 GeV, 450–650 GeV, 650–1000 GeV and $>$ 1 TeV.

The Higgs boson decay to a $b\bar{b}$ pair was first experimentally observed by the ATLAS and CMS experiments in 2018, using Higgs boson events produced in association with a vector boson, i.e. $VH(\to b\bar{b})$ [11, 12]. Since then, analyses have started exploring the high-p_{T} $H \to b\bar{b}$ regime by selecting specific Higgs production modes, in most cases excluding the most abundant ggF channel. Therefore, these analyses exploit only a fraction of the available Higgs boson events produced at high-p_{T} and are not sensitive to potential BSM effects in the virtual ggF loop. For example, recent ATLAS results targeting high-momentum $VH(\to b\bar{b})$ events do not give access to a p_{T} regime much higher than 400 GeV [13, 14].

A remarkable result has been recently obtained by the CMS Collaboration, who searched for high-momentum $H \to b\bar{b}$ decays produced via the ggF mode and measured a Higgs boson signal strength of $\mu_H = 3.7^{+1.6}_{-1.5}$ for $p_{\mathrm{T}}^H > 450$ GeV [15]. The analysis presented in this thesis constitutes the first publication on this experimental signature by the ATLAS Collaboration, and it uses the full LHC Run 2 dataset (136 fb^{-1}). A preliminary result using a partial Run 2 dataset (80 fb^{-1}) and a less advanced analysis methodology was previously released in a conference note in 2018 [16] and showed a 1.6σ excess in Higgs boson signal strength.

This thesis is organised as follows: Chapter 1 briefly presents the theoretical background, Chapter 2 describes the LHC and the ATLAS experiment, Chapter 3 introduces the main concepts on the phenomenology and simulation of proton-proton collisions, Chapter 4 describes the physics object reconstruction procedures utilised in this thesis, Chapter 5 presents the calibration of a double b-tagger aimed at high-p_{T} resonances decaying to $b\bar{b}$, Chapter 6 introduces the experimental setup of the analysis, Chapter 7 describes the modelling of the signal and background processes, Chapter 8 presents the systematic uncertainties and their treatment and, finally, Chapter 9 summarises the analysis results and showcases preliminary studies towards future analysis iterations.

1 Theoretical Background

Contents

1.1 The Standard Model of Particle Physics 5
1.1.1 The Standard Model as a Gauge Theory 8
1.1.2 The Higgs Mechanism 9
1.2 Higgs Boson Production and Decay 13
1.3 The Higgs Boson at High Momentum 16
1.4 Beyond the Standard Model Effects 19
1.5 Experimental Analysis Signature 20

1.1 The Standard Model of Particle Physics

The *Standard Model* (SM) currently constitutes the most accurate and predictive theoretical framework describing particle physics phenomena. This mathematical theory encompasses all discovered particles and describes their mutual interactions.

Three fundamental forces are responsible for particle interactions in the SM: the *strong force*, the *electromagnetic force* and the *weak force*. A particle can undergo a specific interaction only if it possesses a corresponding fundamental property called *charge*: particles with an *electric charge* can interact through the electromagnetic force, those with a *colour charge* through the strong force, and, finally, those with

a *weak isospin* through the weak force. Figure 1.1 classifies the particle content of the SM based on their fundamental properties.

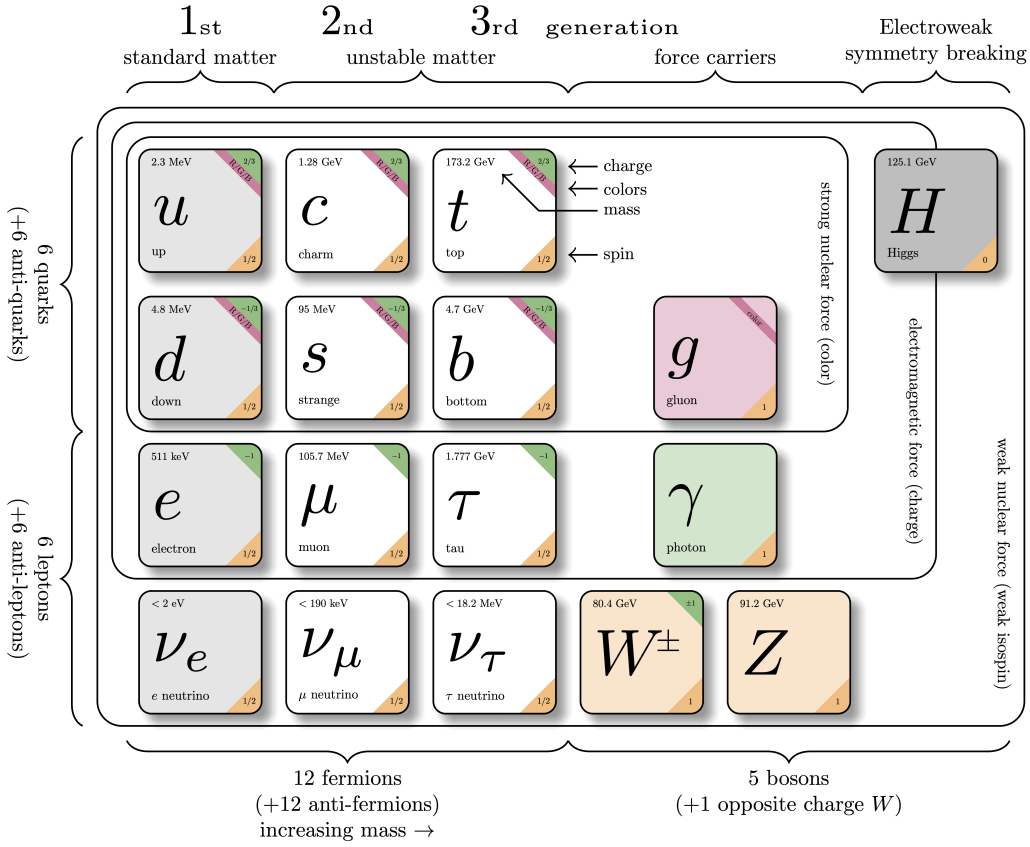

Figure 1.1: Fundamental particles and their properties as described by the Standard Model. Adapted from [17].

Within the SM, particles are divided in two main groups based on their intrinsic angular momentum, i.e. their *spin*: *fermions* are particles with half-integer spin, while *bosons* have integer spin. Fermions are further divided into *quarks* and *leptons*.

Quarks are the only fermions that can interact through the strong force, as they carry a colour charge. They are also the only known particles whose electric charge values are fractions of the elementary charge e: the up (u), charm (c) and top (t) quarks have electric charge $+\frac{2}{3}e$, while the down (d), strange (s) and bottom (b) quarks have $-\frac{1}{3}e$. Quarks are never observed isolated, as they are always confined within colour-neutral bound states of quarks called *hadrons*, which are kept together

by the strong force[1]. This property is called *colour confinement*.

In contrast to quarks, leptons cannot interact through the strong force. The electron (e), muon (μ) and tau (τ) possess an electric charge and can thus undergo the electromagnetic interaction, while the electron neutrino (ν_e), muon neutrino (ν_μ) and tau neutrino (ν_τ) are electrically neutral.

Finally, the weak interaction between fermions is described through an additional property analogous to the spin called *weak isospin* T. Particles with left-handed chirality (L) have weak isospin $T = 1/2$, while right-handed (R) particles have weak isospin $T = 0$. Left-handed particles are arranged into doublets based on the third component of their weak isospin T_3, e.g. $\begin{pmatrix} \nu_e \\ e^- \end{pmatrix}_{\mathrm{L}}$, where ν_e has $T_3 = +1/2$ and e^- has $T_3 = -1/2$. Right-handed particles are instead arranged in weak isospin singlets with $I_3 = 0$, e.g. $(e^-)_{\mathrm{R}}$. All fermionic particles in the SM possess a weak isospin and can thus interact through the weak force. Weak interactions that change the electric charge of a particle (charged-current interactions) only occur between left-handed particles belonging to the same isospin doublet. Conversely, weak interactions that do not result in a change in electric charge (neutral-current interactions) can happen between any particles, but they cannot change their type (flavour).

The fermion content shown in the diagram of Figure 1.1 is doubled, as to every fermionic particle corresponds an anti-particle sharing the same mass, but having opposite intrinsic quantum numbers (i.e. the charges). The anti-matter counterpart of a particle is denoted with a bar on top of the corresponding symbol, i.e. the anti-top quark is labelled as $\bar{t}$.

By looking at the diagram, a pattern emerges among the fermionic particles, which appear to be divided into three generations (arranged in columns in the diagram). Particles arranged on the same row share the same properties, but greatly differ in mass. The fermions belonging to the first generation describe all stable matter in the Universe: the up and down quarks are the building blocks of protons and neutrons, which, together with the electron, generate all existing atomic structures. On the other hand, fermions belonging to the other generations are

[1]The top quark t is an exception as its lifetime is so short ($\approx 10^{-25}$ s) that it decays before the hadronisation process can take place. Therefore, bound states of the top quark are not observed.

unstable, and they tend to decay into the lightest-generation fermions. Despite their instability, such particles can be measured by producing them in high-energy particle interactions.

In contrast to fermions, bosons are particles with integer spin. Within the SM, the interaction between particles is described as being mediated by spin 1 bosons, also known as *gauge bosons*: the electromagnetic force is mediated by the massless photon (γ), the strong force by the massless gluon (g) and the weak force by the charged-current (W^+, W^-) and neutral-current (Z) massive vector bosons. The particle content of the SM is completed by the Higgs boson. As shall be explained later in the chapter, this scalar (spin-0) particle represents a massive excitation of the Higgs field, responsible for giving mass to the particles.

1.1.1 The Standard Model as a Gauge Theory

The SM is a quantum field theory (QFT), which describes particles as quantised excitations of more fundamental entities called *fields*. Such fields are mathematically defined as functions of the space-time coordinate and can be excited (i.e. new particles can be created) by providing energy to the vacuum via particle collisions. In particular, the SM is a *gauge* QFT, namely a theory where particle interactions are derived from symmetries of the theory with respect to specific group transformations.

The dynamical properties of all particles in the SM are described through a particular function of their fields called the *Standard Model Lagrangian* ($\mathcal{L}_{\text{SM}}$). In order to ensure the invariance of $\mathcal{L}_{\text{SM}}$ with respect to a certain local group transformation[2] (gauge invariance), a number of boson fields, also known as *gauge fields*, need to be introduced into the function. Therefore, by requiring a gauge invariant theory, interaction terms between fermions and gauge bosons appear in the Lagrangian, together with charges that are conserved in the interactions (such as the colour charge for the strong force). In the Standard Model, interactions

[2]A local group transformation depends on the space-time coordinate x. For instance, a field $\psi(x)$ transforms under the 1-dimensional local unitary group U(1) as $\psi(x) \to \psi'(x) = e^{i\alpha(x)}\psi(x)$, where $\alpha(x)$ is a space-time dependent phase.

between particles are thus interpreted as the exchange of gauge bosons, which represent the force carriers.

In order to describe experimental observations, the Standard Model Lagrangian is required to be invariant under the gauge group $\mathrm{U(1)_Y} \times \mathrm{SU(2)_L} \times \mathrm{SU(3)_c}$. The electromagnetic and weak interactions are found to be low-energy manifestation of the same unified force called *Electroweak* (EW), which is described by the $\mathrm{U(1)_Y} \times \mathrm{SU(2)_L}$ symmetry group. Transformations belonging to the $\mathrm{SU(2)_L}$ group only act on weak isospin doublets, following the observation that the W boson only couples to left-handed particles. Transformations of the $\mathrm{U(1)_Y}$ conserve a particular kind of charge called *hypercharge* (Y).

Invariance under the EW gauge group requires the introduction of four gauge fields, which can be reinterpreted as the photon field γ mediating the electromagnetic interaction, and the vector bosons W^+, W^- and Z mediating the weak interaction. Additionally, the invariance of the Lagrangian under the gauge group $\mathrm{SU(3)_c}$ requires the existence of gluon fields g, which mediate the strong interaction between particles with colour charge c.

Despite being able to describe all discovered fermions and their mutual interactions, the theory outlined so far only predicts massless particles, thus contradicting experimental observations. As a matter of fact, no explicit mass terms can be introduced into the Lagrangian whilst respecting its gauge invariance. This problem is resolved with the introduction of the *Higgs mechanism*.

1.1.2 The Higgs Mechanism

As previously mentioned, the $\mathrm{U(1)_Y} \times \mathrm{SU(2)_L}$ symmetry requirement results in massless gauge boson mediators for the EW interaction. In contrast to the photon, however, the $W^\pm$ and Z bosons are observed to be massive [18], suggesting that the EW symmetry of the SM Lagrangian must be spontaneously broken. Spontaneous symmetry breaking happens whenever the Lagrangian of a physical system is invariant under transformations of the symmetry group, but the vacuum state, namely the state of minimum energy, is not.

The spontaneous breaking of the EW symmetry can be introduced in the SM through the *Higgs mechanism* [19, 20]. By introducing an additional scalar field in the theory that spontaneously breaks the EW symmetry, the Higgs mechanism is able to elegantly explain how both vector boson mediators and fermions acquire mass.

The simplest version of the Higgs mechanism introduces two complex scalar fields, placed in the weak isospin doublet

$$\phi = \begin{pmatrix} \phi^+ \\ \phi^0 \end{pmatrix} = \frac{1}{\sqrt{2}} \begin{pmatrix} \phi_1 + i\phi_2 \\ \phi_3 + i\phi_4 \end{pmatrix}, \tag{1.1}$$

where ϕ^+ is electrically positive, ϕ^0 is neutral and ϕ_1, ϕ_2, ϕ_3 and ϕ_4 are real fields.

The complex field doublet ϕ enters the SM Lagrangian through the additional terms

$$\mathcal{L}_H = (D_\mu \phi)^\dagger (D^\mu \phi) - V(\phi), \tag{1.2}$$

where the first term is a kinetic term in which the covariant derivative D_μ is implicitly a function of the gauge boson fields in order to conserve the $\mathrm{U(1)_Y \times SU(2)_L}$ symmetry. The $V(\phi)$ is instead known as the *field potential*, and its functional form is chosen such that the ground state breaks the EW symmetry. The simplest allowed formulation is given by

$$V(\phi) = \mu^2 \phi^\dagger \phi + \lambda (\phi^\dagger \phi)^2, \tag{1.3}$$

where λ and μ^2 are real numbers. By choosing $\lambda > 0$ and $\mu^2 < 0$, the potential is characterised by an infinite set of degenerate minima satisfying $\phi^\dagger \phi = -\frac{\mu^2}{2\lambda}$. Figure 1.2 shows the shape of the resulting potential, which is colloquially known as *Mexican hat potential*.

Due to the shape of the potential, the ground state is not symmetric, and it can occupy any of the infinite degenerate minima. Without loss of generality, the vacuum solution can be conveniently set to be equal to

$$\langle 0|\phi|0\rangle = \frac{1}{\sqrt{2}} \begin{pmatrix} 0 \\ v \end{pmatrix}, \tag{1.4}$$

where $v = \sqrt{\frac{\mu^2}{\lambda}}$ is called *vacuum expectation value* (VEV).

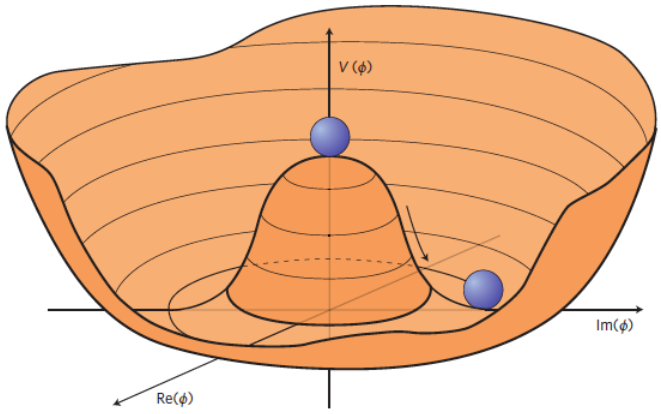

Figure 1.2: Illustration of the field potential $V(\phi)$ as function of the real and imaginary part of the complex scalar field doublet ϕ. The blue spheres represent the transition from a symmetric state to one that spontaneously breaks the EW symmetry of the SM Lagrangian [21].

After the introduction of spontaneous symmetry breaking, the properties of the SM Lagrangian can be studied by expanding the field ϕ for small oscillations around the minimum as

$$\phi = \frac{1}{\sqrt{2}} \begin{pmatrix} 0 \\ v + H \end{pmatrix}, \tag{1.5}$$

where the perturbations around the minimum are described by a new scalar field H called *Higgs field*.

By inserting Equation 1.5 into Equation 1.2 and expanding up to terms that are quadratic in the fields, one gets

$$\mathcal{L}_H = \frac{1}{2}\partial_\mu H \partial^\mu H + \frac{1}{2} m_H^2 H^2 + \frac{1}{2} m_W^2 W_\mu^+ W^{-\mu} + \frac{1}{2} m_Z^2 Z_\mu Z^\mu + ... \tag{1.6}$$

The first two terms represent, respectively, the kinetic and mass terms of the scalar Higgs field. Therefore, the Higgs mechanism predicts the existence of a scalar boson, the Higgs boson, with mass $m_H = \sqrt{2\lambda v^2}$. By inspecting the equation, it is also noted that the Higgs mechanism introduces mass terms[3] for the W^+, W^- and Z mediators in the SM Lagrangian, while no such term is introduced for the photon. The higher order terms that are not shown in Equation 1.6 explain the interactions of the Higgs boson with the vector bosons and with itself (self-interactions).

[3]The Lagrangian mass term of a gauge boson $\mathcal{A}^\mu$ is given by $\frac{1}{2} m^2 \mathcal{A}_\mu \mathcal{A}^\mu$, where m is the boson mass. The values of m_W and m_Z depend the VEV and of the EW couplings g_W and g'.

From measurements of the Higgs boson mass and of the W boson coupling, the VEV of the Higgs field is estimated to be $v \approx 246$ GeV [22]. As a matter of fact, the VEV appears in the Lagrangian terms describing the triple and quartic couplings of the Higgs boson to the W gauge bosons, as in

$$\mathcal{L}_{HWW} = 2\frac{m_W^2}{v} W_\mu^- W^{+\mu} H + \frac{m_W^2}{v^2} W_\mu^- W^{+\mu} HH. \tag{1.7}$$

Fermion Masses

Elegantly, the Higgs mechanism can also be used to describe the method through which fermions acquire mass. Similarly to the vector bosons, the introduction of explicit mass terms for the fermions ($-m\bar{\psi}\psi$) into the SM Lagrangian would break the EW invariance, as they mix left-handed and right-handed components of the fermion fields. Instead, for every fermion, an additional EW-symmetric *Yukawa term* is added to the SM Lagrangian. For instance, in the case of the electron field e, such a term is defined as

$$\mathcal{L}_e^{\text{Yukawa}} = -g_e \begin{pmatrix} \bar{\nu}_e & \bar{e} \end{pmatrix}_{\text{L}} \begin{pmatrix} \phi^+ \\ \phi^0 \end{pmatrix} (e)_{\text{R}} + \text{h.c.} \tag{1.8}$$

where g_e is a real number called a *Yukawa coupling* and h.c. denotes the Hermitian conjugate of the first term in the equation.

After spontaneous breaking of the EW symmetry, the Yukawa Lagrangian can be expanded for small oscillations around the minimum using Equation 1.5. In the case of the electron field, one gets

$$\mathcal{L}_e^{\text{Yukawa}} = -\frac{g_e v}{\sqrt{2}} \bar{e}e - \frac{g_e}{\sqrt{2}} \bar{e}eH, \tag{1.9}$$

where the first term is the electron mass term (with $m_e = \frac{g_e v}{\sqrt{2}}$), while the second describes the interaction between the electron and the Higgs boson, with coupling m_e/v. Following a similar strategy, it is possible to introduce similar terms for all other fermions in the SM[4].

[4]Neutrinos are an exception as the Yukawa mass terms couple left-handed and right-handed particles, but right-handed neutrinos (left-handed anti-neutrinos) are not observed. The mechanism that gives mass to neutrinos is an unanswered question within the SM.

Therefore, by introducing the Higgs field, the original EW symmetry of the Yukawa term in Equation 1.8 is spontaneously broken and mass terms for all fermions appear in the SM Lagrangian. Interestingly, the coupling between fermions and the Higgs bosons is proportional to the fermion mass. Therefore, the Higgs boson will couple preferentially to the heavier fermions, a unique feature that has important consequences on the Higgs production and decay processes.

As a final remark, it is important to note that the Higgs mechanism describes the way SM particles acquire mass, but it does not predict the mass values. These are free parameters in the SM that must be measured experimentally.

The SM is an incredibly predictive theory that has been validated by countless experiments ever since its formulation. However, it cannot be considered as a complete theory: open questions in particle physics such as the nature of dark matter or the mechanism through which neutrinos acquire mass do not find an answer within the SM. Furthermore, all attempts made so far at including the gravitational interaction within the theoretical framework of the SM have failed. Given the incomplete nature of the theory, the Higgs boson could potentially reveal itself a gateway to new physics discoveries beyond the Standard Model (see Section 1.4), one reason why it currently occupies a central role in high-energy physics research.

1.2 Higgs Boson Production and Decay

The Higgs mechanism was first theoretically formulated in 1964 [19, 20]. However, the first direct experimental observation of the Higgs boson only came nearly five decades later. The discovery was made by the ATLAS and CMS experiments at CERN (European Organisation for Nuclear Research) in 2012, using $\sqrt{s} = 8$ TeV proton-proton collisions delivered by the LHC (Large Hadron Collider) [3, 4].

Since its discovery, the Higgs boson has been at the core of the scientific programmes of the ATLAS and CMS Collaborations. Its properties have been measured with progressively increased precision and have proven to be in good agreement with the SM predictions. Currently, the best estimate of the Higgs boson

mass - the average of all measurements - is given by $m_H = 125.25 \pm 0.17$ GeV [22]. The relatively large mass of the Higgs boson was one of the reasons for its late discovery, which required advancements in accelerator technology to achieve particle collisions with high enough centre-of-mass energy.

Another reason why measuring the Higgs boson represents a challenge is its very small production cross-section σ, which, for a centre-of-mass energy of 13 TeV is around 56 pb. For comparison, this value is around 9 orders of magnitude smaller than the cross-section of the inelastic proton-proton collisions delivered by the LHC. This implies that vast datasets need to be collected by the experiments in order to obtain a statistically significant Higgs sample to analyse.

In proton-proton collisions with a centre-of-mass energy of $\sqrt{s} = 13$ TeV, the Higgs boson is predominantly produced via gluon-gluon interactions (87%) through the gluon-gluon-fusion (ggF) process. Since the gluon is massless, it cannot couple directly to the Higgs boson. Instead, ggF goes through the virtual fermion loop shown in Figure 1.3a, which is dominated by the top quark due to its large mass (and consequently large coupling to the Higgs boson). Other subdominant Higgs production processes are the vector boson fusion (VBF), associated production with a vector boson (VH) and associated production with a top anti-top quark pair ($t\bar{t}$H), which contribute, respectively, with around 7%, 4% and 1%. The leading-order (LO) Feynman diagram for these processes are also shown in Figure 1.3, while the pie chart in Figure 1.4a summarises the fractional contributions of the various Higgs production processes.

Once produced, the Higgs boson decays extremely quickly, having a lifetime of around $\tau = 1.6 \times 10^{-22}$ s. Therefore, the only way of detecting it is by measuring its decay products. Figure 1.4b shows the predicted branching ratios (BR) for a Higgs boson with $m_H = 125$ GeV. As previously discussed, a peculiar characteristic of the Higgs boson is that its couplings to fermions are proportional to their mass. Therefore, it is not surprising to note that its BR to a $b\bar{b}$ pair is the largest (58%). The b quark is, in fact, the heaviest fermion that the Higgs boson can decay into, considering that the decay to a $t\bar{t}$ pair is kinematically disallowed ($m_H < 2m_t$).

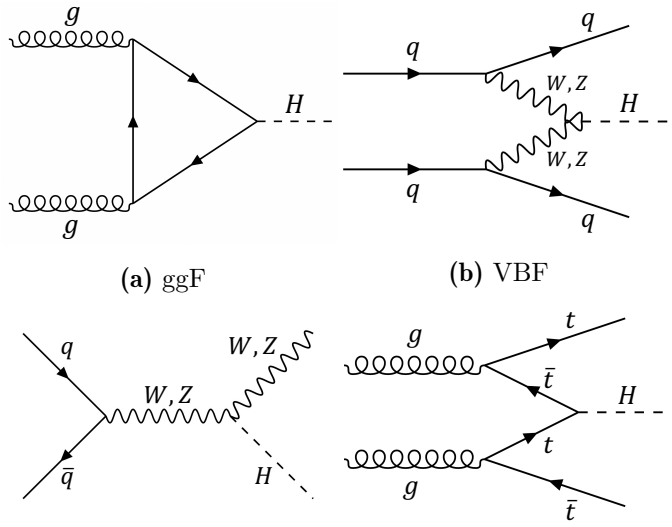

(a) ggF **(b)** VBF

(c) VH **(d)** $t\bar{t}$H

Figure 1.3: Leading order Feynman diagrams for the ggF (a), VBF (b), VH (c) and $t\bar{t}$H (d) Higgs production processes.

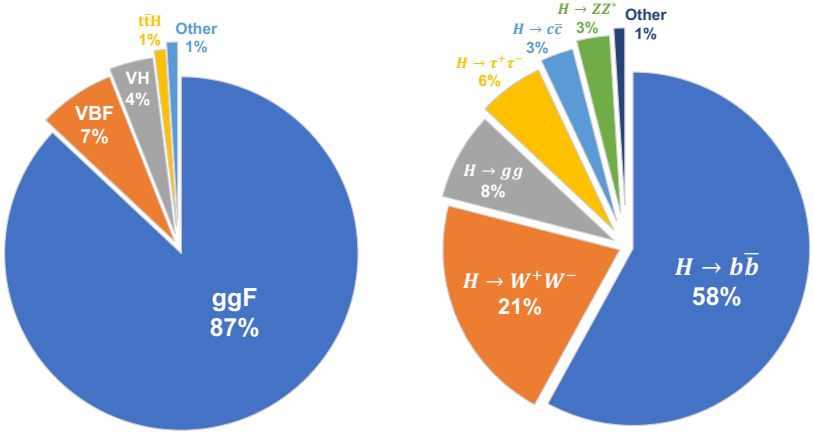

(a) Higgs production modes **(b)** Higgs decay modes

Figure 1.4: Percentage fractions for the Higgs boson production modes (a) and decay modes (b).

Other sub-dominant decay processes are $H \to W^{\pm}W^{\mp}$ and $H \to gg$, which are characterised by predicted BR of around 21% and 8%, respectively.

The Higgs boson discovery was achieved using $H \to \gamma\gamma$ and $H \to ZZ^* \to 4\ell$ decays [3, 4], and the excess was also confirmed in the highly sensitive but low-resolution $H \to W^{\pm}W^{\mp}$ channel. Despite the small branching ratios of the $H \to \gamma\gamma$ and $H \to ZZ^*$ final states, respectively around 0.2% and 2.7%, these decay modes are characterised by very clean experimental signatures. For these final states,

analysis selections can also suppress the already small background contamination very effectively, thus strongly enhancing the Higgs boson sensitivity.

Since its discovery, the exploration of the Higgs boson properties has been at the core of the scientific program of the LHC and cross-section measurements individually targeting specific production modes have been carried out [23]. Figure 1.5a shows a combination of Higgs boson cross-section results obtained by analyses performed by the ATLAS Collaboration. The cross-section measurements of the main Higgs production modes are observed to be in good agreement with the SM predictions.

In addition to $H \to \gamma\gamma$ and $H \to ZZ^*$, measurements of the Higgs boson decaying to W^+W^-, $b\bar{b}$, $\tau^+\tau^-$ and $\mu^+\mu^-$ have been performed [23]. The combined knowledge on the production and decay modes allows for the measurement of the Higgs boson couplings to fermions and vector bosons. Figure 1.5b shows the reduced coupling-strength modifiers $k_F \frac{m_F}{v}$ for fermions ($F = t, b, \tau, \mu$) and $\sqrt{k_V}\frac{m_V}{v}$ for weak gauge bosons ($V = W, Z$) as a function of their masses m_F and m_V, respectively. All results are in very good agreement with the SM, which predicts the Higgs boson coupling to increase linearly with m_F and m_V.

1.3 The Higgs Boson at High Momentum

An important test of the SM is verifying whether or not the Higgs boson cross-section evolves with transverse momentum[5] (p_{T}^H) in the way predicted by the theory. Possible deviations from the theoretical predictions might represent indications of the existence of beyond the Standard Model (BSM) physics (see Section 1.4).

Despite the great scientific interest in the high-p_{T} regime, this kinematic region remains, to this day, largely unexplored. These measurements are, in fact, intrinsically challenging due to the rapidly falling nature of the Higgs momentum spectrum, as noted from Figure 1.6a. Additionally, most analyses targeting the Higgs boson make use of the decay modes with the cleanest signatures (like $H \to \gamma\gamma$ and $H \to ZZ^* \to 4\ell$), which are, however, characterised by comparatively low BR,

[5]The transverse momentum p_{T} of a particle is defined as the projection of its momentum on a plane perpendicular to the collider's beam pipe. The complete definition is given in Equation 2.3.

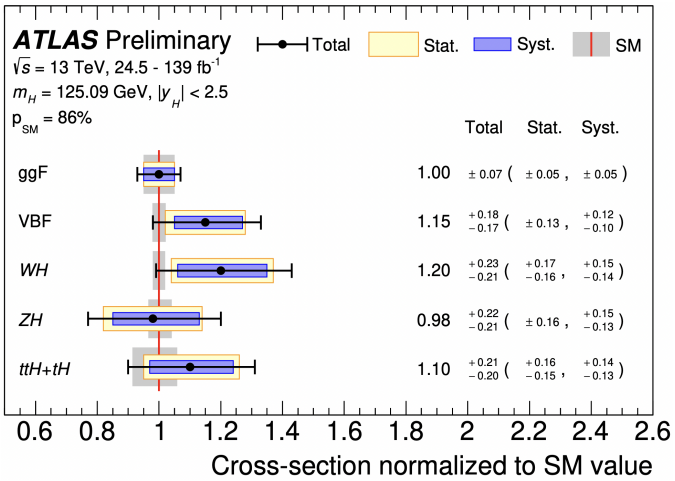

(a) Higgs Production Cross-sections

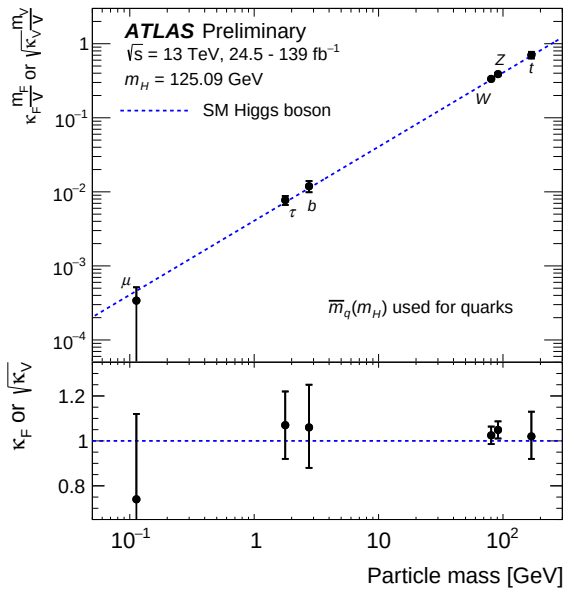

(b) Higgs Couplings

Figure 1.5: Figure (a): cross-sections for ggF, VBF, WH, ZH and $t\bar{t}$H + tH Higgs boson production normalized to their SM predictions, measured assuming SM values for the decay branching fractions. The black error bars, blue boxes and yellow boxes show the total, systematic, and statistical uncertainties in the measurements, respectively. The grey bands indicate the theory uncertainties in the SM cross-section predictions. The level of compatibility between the measurement and the SM prediction corresponds to a p-value of $p_{\mathrm{SM}} = 86\%$ [23]. Figure (b): Reduced coupling-strength modifiers $k_F \frac{m_F}{v}$ for fermions ($F = t, b, \tau, \mu$) and $\sqrt{k_V}\frac{m_V}{v}$ for weak gauge bosons ($V = W, Z$) as a function of their masses m_F and m_V, respectively, and the vacuum expectation value of the Higgs field $v = 246$ GeV. The SM prediction for both cases is also shown (dotted line). The black error bars represent 68% CL intervals for the measured parameters [23].

limiting available statistics. This exacerbates the issue, limiting the Higgs boson p_{T} reach of these analyses to be lower than around 100 GeV [10]. Prior to the analysis presented in this thesis, the highest Higgs p_{T} range probed at ATLAS was around 400 GeV, achieved by the boosted $VH(\rightarrow b\bar{b})$ analysis [14].

The issue of low Higgs yield in the high-p_{T} regime can be partially mitigated by selecting the $b\bar{b}$ decay mode, which corresponds to the largest branching ratio (around 58%). A price, however, is paid in terms of the far larger contamination from background events that characterises hadronic final states.

For the Higgs boson to reach high p_{T} (colloquially, to be *boosted*), at least one additional high-p_{T} recoil object must be present to balance the total transverse momentum of the event. In ggF events this is typically a parton that is radiated by the incoming gluons (initial state radiation - ISR) or by the virtual fermion loop. In VH the recoil object is the associated vector boson, either a W or a Z boson. In VBF the Higgs boson recoils against one or more quarks, while it recoils against the associated $t\bar{t}$ pair in $t\bar{t}$H.

Additional signal yield at high p_{T} can be gained by developing an analysis that is sensitive to all the main Higgs production modes. Figure 1.6 shows the SM prediction of the cumulative Higgs boson production cross-section as a function of p_{T}^{H}, as well as the fractional contributions from the ggF, VBF, VH and $t\bar{t}$H production modes. Despite being dominant throughout most of the p_{T}^{H} spectrum, the ggF contribution decreases significantly with p_{T}^{H}, becoming comparable to other production modes (like VH) at the TeV scale. In other production modes, in fact, the Higgs boson is always produced in association with recoil objects. This increases the chance of high-p_{T} production, which is marked by the flatter behaviour of their fractional contributions with p_{T}^{H}. Therefore, in order to explore the Higgs boson in the TeV range it is highly beneficial to develop an analysis that is inclusive in Higgs production mode.

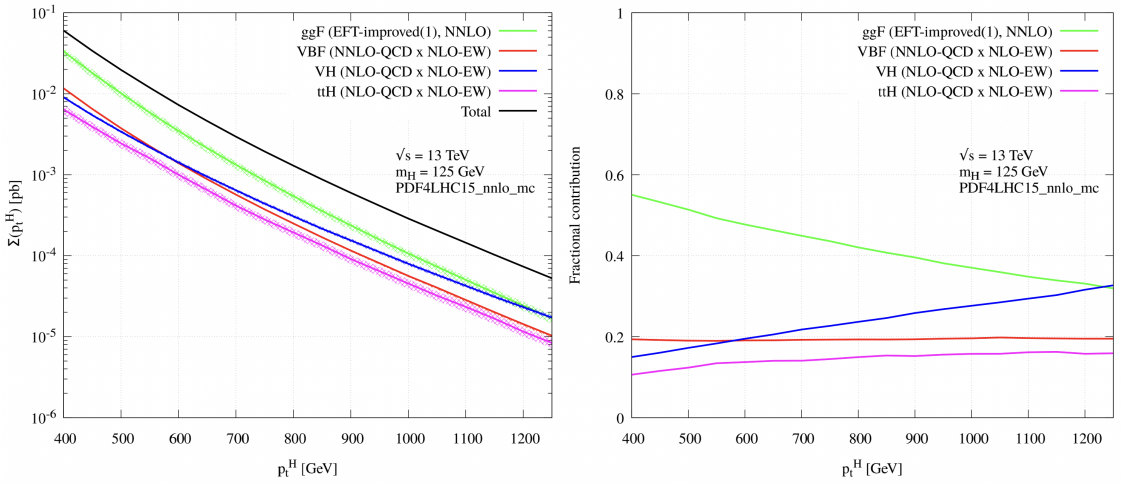

(a) Cumulative Cross-sections **(b)** Fractional Contributions

Figure 1.6: Figure (a): SM prediction of the cumulative Higgs boson production cross-section $\Sigma(p_{\mathrm{T}}^{H}) = \int_{p_{\mathrm{T}}^{H}}^{+\infty}(d\sigma/dp_{\mathrm{T}})dp_{\mathrm{T}}$ as a function of the lowest Higgs boson transverse momentum p_{T}^{H}. The total Higgs boson cross-section (black) is shown together with the individual contributions from the ggF (green), VBF (red), VH (blue) and $t\bar{t}$H (magenta) production processes [24]. Figure (b): fractional contributions of Higgs boson production modes to $\Sigma(p_{\mathrm{T}}^{H})$ as a function of p_{T}^{H} [24].

1.4 Beyond the Standard Model Effects

In addition to having a fundamental role within the SM, the Higgs boson might also represent a gateway to new physics discoveries. Many beyond the Standard Model (BSM) theories predict the existence of new massive particles at the TeV mass scale. So far, no such BSM particles have been observed using direct detection methods, for example, by producing them at particle colliders. However, indirect detection experiments might allow to observe their impact on other well-understood processes.

Massive BSM particles might acquire their mass through the same process that characterises SM particles, namely by interacting with the Higgs field. Therefore, possible deviations in Higgs boson measurements with respect to SM predictions might constitute indirect evidence of the existence of new particles.

In this context, the ggF Higgs production process represents an invaluable probe for BSM effects. As previously mentioned, this process is characterised by an internal fermion loop that is dominated by virtual top quarks. This is due to one of the most peculiar properties of the Higgs boson, namely that it preferentially couples to

high-mass particles. Fermions participating in the virtual loop can be off-mass-shell, namely they can have a much larger mass than kinematically allowed by virtue of the uncertainty principle. Thus, new physics particles with mass in the multi-TeV range can participate in the loop, altering the effective coupling between the incoming gluons and the outgoing Higgs boson. The extent of such effects is expected to become more pronounced at higher Higgs momentum, namely when the new physics particles participating in the loop are closer to being produced on-mass-shell.

Figure 1.7 shows the results of a theoretical work investigating possible variations in the ggF production cross-section induced by BSM particles, as a function of Higgs boson transverse momentum [8]. The coefficients c_g and c_t describe BSM modifications to the effective Higgs boson coupling to gluons and to the Yukawa coupling of the top quark (in the SM: $c_g = 0$, $c_t = 1$). The studied variations are chosen such that the inclusive ggF cross-section would not deviate from the SM by more than 20%, which was roughly the experimental uncertainty at the time the study was performed. It is noted that alterations in the coefficients lead to large variations in the ggF cross-section p_{T} dependence, and that they are particularly pronounced at high-p_{T}.

As already mentioned, the large variations in the p_{T} spectrum correspond to much smaller changes in the total ggF cross-section (20% at most). This means that the accurate cross-section measurements performed so far inclusively in Higgs boson p_{T} do not rule out possible large deviations from the SM predictions at very high p_{T}. Hence the great interest in probing the ggF cross-section as a function of p_{T} and extending the reach to the TeV scale.

1.5 Experimental Analysis Signature

The main goal of this thesis is to describe the first analysis performed by the ATLAS Collaboration targeting $H \to b\bar{b}$ decays at very high momentum. The analysis sets limits on the Higgs production cross-section up to and above 1 TeV, a regime where large deviations from the SM predictions might be observed, in the presence of BSM effects.

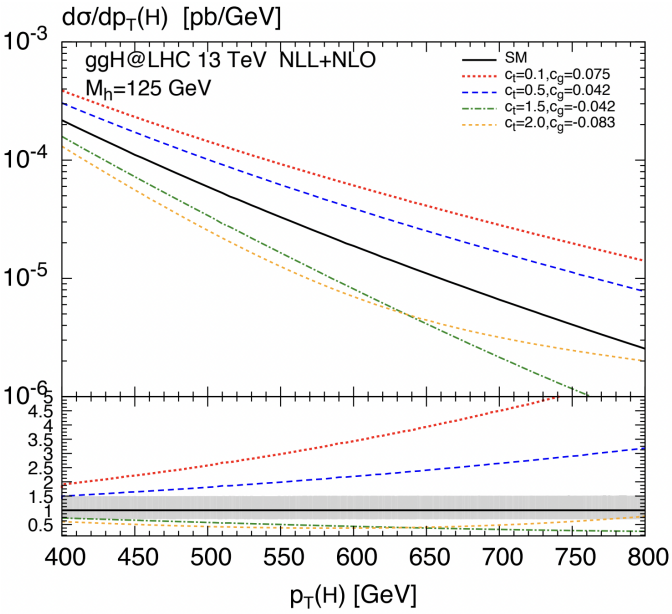

Figure 1.7: The differential cross-section for Higgs boson production via ggF as a function of the Higgs boson p_{T}, both as predicted by the SM (black line) and by applying various BSM modifications (coloured lines). The modifications are introduced by varying the coefficients c_g and c_t, which respectively correspond to the effective coupling between the Higgs boson with gluons, and the Yukawa coupling of the top quark (in the SM: $c_g = 0$, $c_t = 1$). The bottom panel shows the ratio between the modified cross-sections and that predicted by the SM [8].

Due to the colour confinement property of the strong interaction, the b quarks produced in the Higgs decay undergo the fragmentation and hadronisation processes and they are detected as showers of particles named *jets* (see Section 4.1). For Higgs bosons produced at high-p_{T}, the $b\bar{b}$ decay products are highly collimated, and they are thus reconstructed as a single *Higgs jet*. In order to select jets that are compatible with a $b\bar{b}$ sub-structure, the analysis uses b-jet identification techniques based on multivariate methods (see Section 4.2).

The analysis selection, which is thoroughly presented in Section 6.3, specifically targets high-momentum $H \to b\bar{b}$ decays by requiring events to have at least one high-p_{T} recoil object. This is chosen to be an additional hadronic jet, thus giving access to all the main Higgs boson production modes. As a matter of fact, all recoil objects characterising the ggF, VBF, VH and $t\bar{t}$H processes can result in hadronic final states and, therefore, in the production of jets. The strategy developed by this analysis allows to probe the Higgs boson production up to and above 1 TeV.

Due to the requirement of at least one additional jet in the events, the analysis presented in this thesis is named *Boosted* $H(\rightarrow b\bar{b}) + jet$. As shall be discussed in Section 7.1, the Higgs bosons selected by the analysis are in majority produced via the ggF process, thus giving access to possible BSM effects in the high-p_{T} Higgs boson production cross-section.

2

The ATLAS Experiment at the LHC

Contents

2.1 The Large Hadron Collider 24
2.2 The ATLAS Detector 28
2.2.1 Coordinate System and Variables 29
2.2.2 The Inner Detector 31
2.2.3 The Calorimeter System 36
2.2.4 The Muon Spectrometer 40
2.2.5 The Trigger System 42

The first essential requirement for any analysis is data collection and processing. The analysis presented in this thesis makes use of the full dataset collected by the ATLAS experiment between the years 2015 and 2018 (Run 2), corresponding to an integrated luminosity of 136 fb^{-1}[1].

ATLAS (A Toroidal LHC ApparatuS) [25] is one of the four main physics experiments located at the Large Hadron Collider (LHC) [26]. It is a general-purpose detector designed to collect data from the proton-proton (pp) collisions delivered by the LHC and make them available to a broad range of physics analyses.

[1] As explained in Section 6.1, the integrated luminosity used in the analysis is lower than the nominal 139 fb^{-1} because a few large-R jet triggers were not active during the whole Run 2 data taking period.

Section 2.1 provides a brief summary of the LHC structure and operation. Then, in Section 2.2, a description of the ATLAS detector and its components is given.

2.1 The Large Hadron Collider

The Large Hadron Collider (LHC) [26, 27] is a two-ring superconducting hadron accelerator and collider installed in a 26.7 km underground circular tunnel at CERN (European Organisation for Nuclear Research) in Geneva. Nominally, the LHC is designed to accelerate protons up to an energy of 7 TeV per beam, corresponding to a centre-of-mass energy in proton-proton (pp) collisions of $\sqrt{s} = 14$ TeV. The LHC can also deliver heavy ion collisions by accelerating fully ionised lead ions ($^{208}\mathrm{Pb}^{82+}$) up to a design energy of 2.76 TeV/nucleon in both directions. Since ion collisions are not relevant to the analysis presented in this thesis, they will not be considered in the remainder of the chapter. More information on heavy ion collisions is given in Reference [27].

Protons are injected into the LHC ring after being pre-accelerated to 450 GeV by a feed-forward chain of other smaller accelerators housed at the CERN complex (see Figure 2.1): the Linac4, the Proton Synchrotron Booster (PSB), the Proton Synchrotron (PS) and, finally, the Super Proton Synchrotron (SPS). During this pre-acceleration process, protons are also divided into discrete groups of around 10^{11} particles called *bunches*, spaced by 25 ns of each other.

The accelerator ring of the LHC is subdivided into eight arcs and eight straight sections. In the arc sections, superconducting dipole magnets bend the two counter-rotating proton beams, confining them inside of the curving vacuum beam pipes. Being a particle-particle collider, the two counter-rotating beams must circulate inside separate pipes. This is different from particle-antiparticle colliders, where both beams can share the same phase space in a single ring. Building two separate rings, however, was unfeasible, mainly due to space constraints inside the tunnel. For this reason, a two-in-one bending magnet design was adopted, where both beam pipes are integrated inside the same superconducting magnet system.

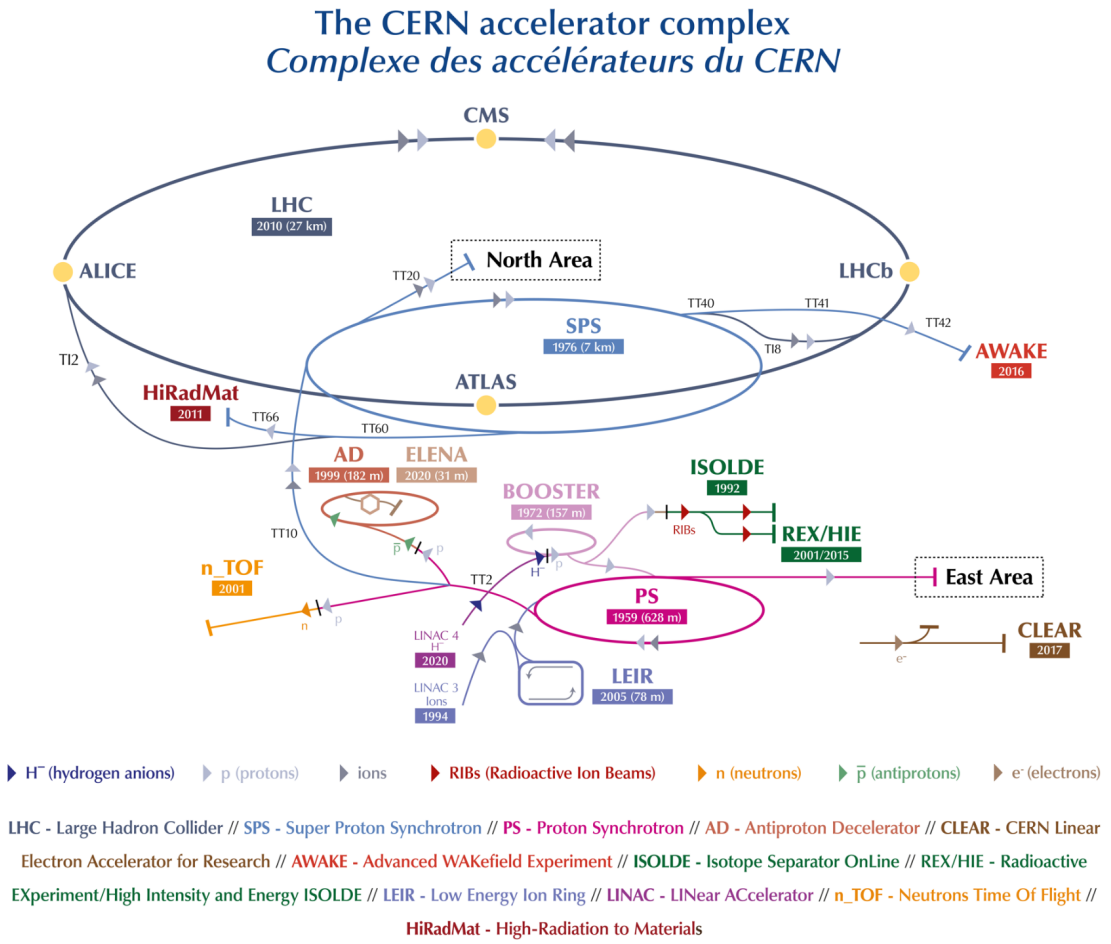

Figure 2.1: Schematic representation of the CERN accelerator complex. Protons are injected into the LHC after being pre-accelerated to 450 GeV by a feed-forward chain of accelerators: the Linac4, the Proton Synchrotron Booster (named BOOSTER in the picture), the Proton Synchrotron (PS) and the Super Proton Synchrotron (SPS) [28].

The eight straight sections distributed along the LHC ring serve a variety of experimental and utility purposes. A total of four sections house the main LHC experiments: ATLAS, CMS, LHCb and ALICE. Here, the counter-rotating beams are focused using quadrupole magnets and collided. Due to the bunch spacing, collision events happen with a frequency of 40 MHz.

The proton bunches are accelerated at one of the straight sections of the LHC using eight superconducting radiofrequency (RF) cavities. These are metallic chambers located along the beam pipe, each supplied with a 2 MV electromagnetic RF field with a frequency of 400 MHz. The cavities are moulded to a specific size and shape so that electromagnetic waves become resonant and build up inside them.

Charged particles passing through the cavities feel the overall force and direction of the resulting electromagnetic field, which transfers energy and pushes them forward along the accelerator. The remaining straight sections are dedicated to other beam utility purposes, like beam dumping and cleaning.

The LHC operates in multiple-year-long periods of activity called *runs*, during which data is taken almost continuously, interspersed with 2-3 month long technical stops at the end of each year for maintenance work. Long periods of inactivity (long shutdowns) are scheduled in between runs for large-scale maintenance and upgrades. The first LHC run (Run 1) began in 2009 and delivered pp collisions with a centre-of-mass energy of 7 and 8 TeV. The second LHC run (Run 2) took place between 2015 and 2018 and delivered pp collisions with a centre-of-mass energy of 13 TeV. The analysis presented in this thesis uses data collected by the ATLAS experiment during the whole of Run 2. At the time of writing, a third run (Run 3) of the LHC has recently started, bringing pp collisions to a record centre-of-mass energy of 13.6 TeV.

As previously stated, proton bunches cross each other at the experiment sites every 25 ns. The number of actual pp collisions at every bunch crossing, however, depends on many factors. The rate at which interaction events with a cross-section σ occur is given by

$$\frac{dN}{dt} = \sigma\mathcal{L}, \tag{2.1}$$

where $\mathcal{L}$ is the *instantaneous luminosity* of the accelerator, a measure of the number of collisions that can be produced in a detector per cm^2 and per second. The instantaneous luminosity is entirely dependent on variables that describe the state of the LHC machine and the particle density in the proton bunches. The higher the instantaneous luminosity, the larger the number of collision events per unit time. The time integral of $\mathcal{L}$ is called *integrated luminosity* L, and it is proportional to the number of collision events N delivered in the timeframe of integration as

$$N = \sigma L. \tag{2.2}$$

At all interaction points, the instantaneous luminosity of the LHC machine is constantly measured using dedicated detectors targeting processes with precisely

known cross-sections [29]. The cumulative integrated luminosity delivered to ATLAS by the LHC during Run 2 is shown in Figure 2.2 as a function of time. Also shown is the luminosity corresponding to events that the ATLAS experiment was able to record, and that satisfying specific quality requirements for scientific analyses [30]. Over Run 2, pp collisions corresponding to an integrated luminosity of 156 fb^{-1} were delivered by the LHC. Of these, 147 fb^{-1} were recorded by the ATLAS experiment and 139 fb^{-1} are usable by analyses.

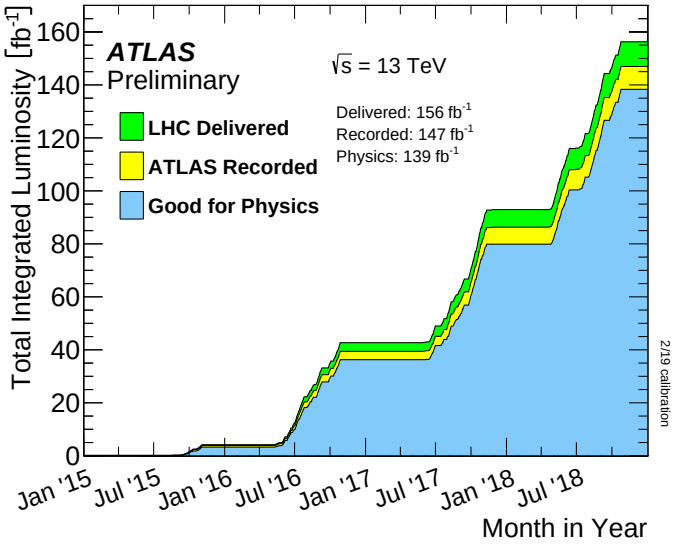

Figure 2.2: Cumulative integrated luminosity delivered by the LHC as a function of time during Run 2. The legend also shows the total luminosity delivered by the LHC during Run 2, that recorded by the ATLAS experiment, and that usable for physics analyses [30].

Processes that are subjects of scientific research at the LHC are usually quite rare, implying that they are characterised by very small cross-sections. Following from Equation 2.2, high luminosity is necessary to increase the chance of producing such rare events. The instantaneous luminosity can be increased - and it has been over the course of the LHC runs - by tuning accelerator parameters or increasing the particle density of the proton bunches. This, however, also increases the chances of multiple pp interactions happening per bunch crossing. This phenomenon is called *pileup* and it greatly increases the complexity of the recorded collision events of interest. Pileup leads to the production of additional, usually low-p_{T}, particles

coming from alternative collision vertices that are independent from the main event. Such particles leave energy deposits in the ATLAS detectors which need to be taken into account during the reconstruction of the main event.

Figure 2.3 shows the luminosity-weighted distributions of the mean number of interactions per bunch crossing μ over Run 2, recorded by the ATLAS experiment. Due to improvements in the performance of the LHC machine, the average μ is seen to increase from 2015 to 2017, to then stabilise in 2018.

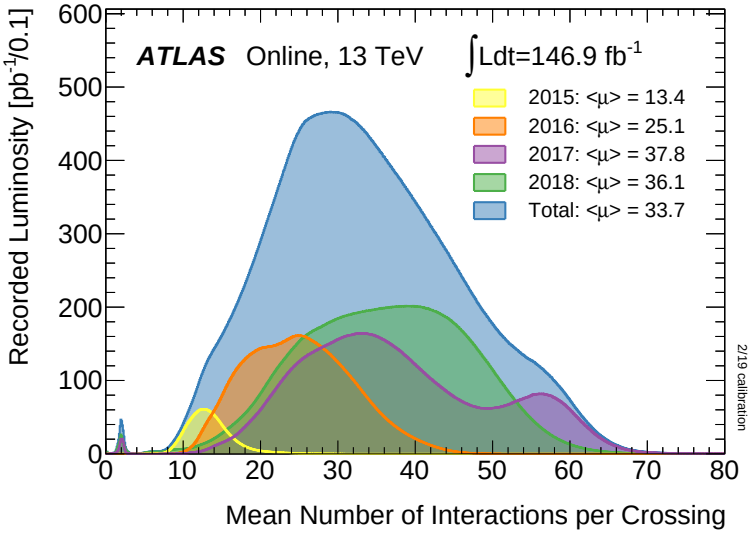

Figure 2.3: Luminosity-weighted distributions of the mean number of interactions per bunch crossing μ over Run 2, recorded by the ATLAS experiment. The legend also shows the average μ value for each of the data-taking years and for the whole of Run 2 [30].

2.2 The ATLAS Detector

ATLAS [25] is one of the main LHC experiments and it is located at one of the four interaction points, inside a large underground cavern. With a total volume of around 22 000 m^3 and a mass of around 7000 tonnes, ATLAS is the largest LHC detector, and it is designed to collect data for a broad range of physical analyses. This is the reason why it is often referred to as a *general-purpose* detector. Figure 2.4 shows the cylindrical structure of the ATLAS detector, featuring a central barrel and two end-caps, which allows for a high degree of geometrical acceptance, especially in the central detector region (i.e. the barrel).

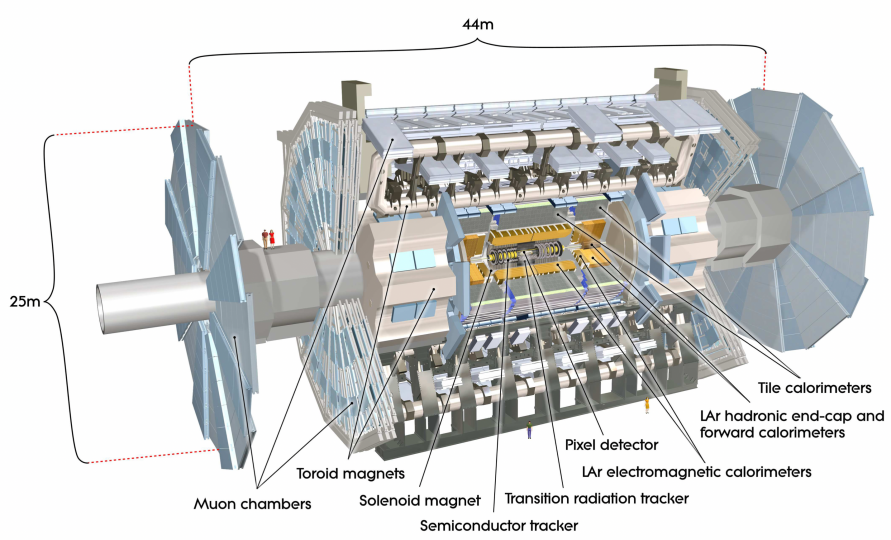

Figure 2.4: Layout of the ATLAS detector [25].

ATLAS is composed of several sub-detectors, each with a specialised role in the measurement and identification of the particles produced in the *pp* collisions. This section describes the structure of the ATLAS detector and provides an overview of the sub-detectors and their scientific goals. Section 2.2.2 describes the *Inner Detector* (ID), the closest sub-detector to the beam pipe, with the task of measuring the trajectory and momentum of charged particles. Section 2.2.3 presents the ATLAS *calorimeter system* which surrounds the ID and allows the measurement of the energy of most particles. The topic of Section 2.2.4 is the *Muon Spectrometer* (MS), a sub-detector designed to identify muons and measure their trajectories and momenta. Finally, Section 2.2.5 briefly describes the ATLAS *Trigger System*, namely the series of procedures, both hardware- and software-based, aimed at exclusively registering events that are interesting for physics analyses.

Before diving into the description of the ATLAS detector, the coordinate system used by the ATLAS experiment is introduced in the next section, together with various useful variables.

2.2.1 Coordinate System and Variables

In any physics experiment, coordinate systems are used for conveniently and unequivocally localising the physical objects reconstructed inside the detector, and

for defining the detector geometry itself.

The ATLAS cartesian coordinate system originates at the centre of the detector, the location inside the beam pipe where the particle collisions nominally take place. The z-axis is aligned to the beam pipe, the x-axis is directed towards the centre of the LHC ring and the y-axis upwards. The x and y axes form the *transverse plane*, namely a plane perpendicular to the direction of the beam pipe. Due to the symmetry of the ATLAS detector, the tranverse plane is often described in terms of r–ϕ coordinates, where r is the radial distance from the z-axis and ϕ is the azimuthal angle around the beam pipe, measured from the x-axis. Finally, the coordinate θ represents the polar angle with respect to the z-axis.

At general-purpose collider experiments, such as ATLAS or CMS, physics events are described using "transverse quantities", namely variables defined in the transverse plane of the detector. The *transverse momentum* p_{T} of a particle is defined as the projection of its momentum vector onto the transverse plane xy, namely

$$p_{\mathrm{T}} = p \sin\theta, \tag{2.3}$$

where p is the magnitude of the particle's momentum vector and θ is the polar angle of the momentum vector with respect to the z-axis.

In any mechanical system, the transverse momentum is a conserved quantity. At the LHC, protons circulate longitudinally in the beam pipe (z-axis), meaning that the transverse momentum of the pp system before a collision event is null. Therefore, after the collision, the transverse momenta of all particles produced in the final state must sum to zero. Typically, whenever a high-p_{T} particle is produced, one or more high-p_{T} particles are produced in the opposite detector hemisphere, so to balance the total transverse momentum of the event.

At the LHC, particle collisions take place in the centre-of-mass of the pp system, which coincides with that of the detector. However, protons have an internal structure composed of partons (quarks and gluons), each carrying a fraction of the proton's momentum. Therefore, the reference frame of the hard scattering between partons will have a longitudinal boost with respect to the centre-of-mass

of the detector. For this reason, angles are usually expressed in terms of the *rapidity* y, defined as

$$y = \frac{1}{2} \ln \left(\frac{E + p_z}{E - p_z} \right), \tag{2.4}$$

where E is the energy of the particle and p_z is its *longitudinal momentum*, namely the projection of its momentum along the z-axis. The use of rapidity has the advantage that rapidity differences are invariant under boosts along the longitudinal axis (z).

The *pseudorapidity* η can be used in place of the rapidity at high energies, in the limit where the mass of the object can be neglected. The pseudorapidity is defined as

$$\eta = -\ln \left(\tan \frac{\theta}{2} \right). \tag{2.5}$$

Differential cross-sections for particle production at colliders are approximately constant with pseudorapidity. This implies that roughly equal numbers of particles are observed in each interval of pseudorapidity, reflecting the forward nature of particle production in pp collisions.

The distance ΔR between two particles in the pseudorapidity-azimuthal angle space is defined as

$$\Delta R = \sqrt{\Delta\eta^2 + \Delta\phi^2}, \tag{2.6}$$

where $\Delta\eta$ and $\Delta\phi$ are, respectively, the pseudorapidity and azimuthal angle difference between the two particles. The ΔR variable commonly finds application in the definition of proximity relations between particles, like in the clustering of jets (see Section 4.1.1).

2.2.2 The Inner Detector

The collision events registered by the ATLAS detector are extremely complicated: every 25 ns an average of a thousand new particles travel through the ATLAS detector. In order to correctly interpret the physics events of interest, it is necessary to reconstruct the trajectories of the largest fraction of particles produced in the pp collisions and match them to their respective interaction vertices. This process is called *tracking*, and it is done at ATLAS mainly by means of the Inner Detector (ID).

The goal of the ID is to measure the trajectory of the electromagnetically charged particles produced in the collisions and to identify primary interaction vertices. Charged particles leave small amounts of energy while travelling through the active detector layers forming the ID, which are converted into position measurements (hits). Robust pattern recognition algorithms are then used to combine hits and reconstruct the particle trajectories (tracks) and the position of the primary interaction vertices.

Additionally, the ID allows for the reconstruction of secondary vertices, which are crucial in the identification of b quarks. Hadrons including the b quark (b-hadrons) have a lifetime of the order of a few ps, allowing them to travel a short distance (typically of the order of a few mm) before decaying. With good enough tracking performance, the decay products of b-hadrons can be observed to originate from a secondary vertex that is displaced from the primary interaction point.

Figure 2.5 shows the geometrical structure and composition of the ATLAS ID. The detector is characterised by cylindrical structure composed of a barrel and two end-caps, and it is designed to provide geometrical acceptance in the pseudorapidity range $|\eta| < 2.5$. The ID is composed of three independent but complementary sub-detectors, located at progressively larger distances from the beam pipe: the *Silicon Pixel Detector*, the *Semiconductor Tracker* and the *Transition Radiation Tracker*. Further details on these different sub-detectors are given later in the section.

A cylindrical superconducting magnet surrounds the ID and generates a solenoidal magnetic field of around 2 T across the whole instrumented volume. Travelling through the strong magnetic field, charged particles follow a helical trajectory whose radius of curvature R is related to the particle's transverse momentum as

$$p_{\mathrm{T}} = 0.3qBR, \tag{2.7}$$

where q is the electric charge of the particle and B is the magnetic flux intensity[2]. Therefore, precise tracking in the presence of a magnetic field allows for the

[2]In the equation, p_{T} is given in [GeV/c], q in units of elementary charge e, B in [T] and R in [m].

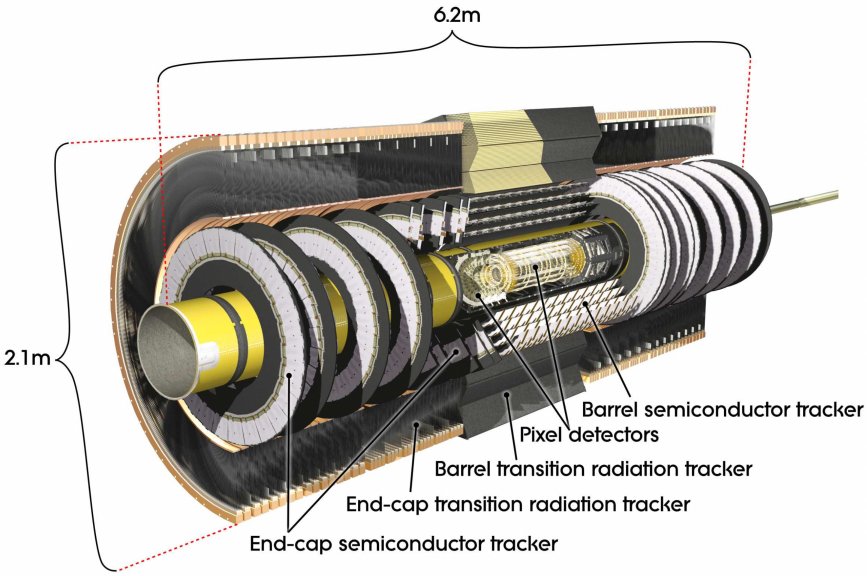

Figure 2.5: Layout of the ATLAS Inner Detector [25].

measurement of a charged particle's momentum. The ID is designed to provide a minimum transverse momentum resolution of

$$\frac{\sigma(p_{\mathrm{T}})}{p_{\mathrm{T}}} \leq 0.05\% \text{ GeV}^{-1} p_{\mathrm{T}} \oplus 1\%. \tag{2.8}$$

Silicon Pixel Detector

The Silicon Pixel Detector is the inner-most sub-detector composing the ID. Its main purpose is to accurately measure the interaction vertices by providing precise tracking close to the interaction point.

In the barrel, the silicon-based sensors (pixels) forming this sub-detector are arranged into three concentric cylindrical layers, respectively located at a distance of 50.5 mm, 88.5 mm and 122.5 mm from the beam axis. Pixels in the end-cap regions are instead arranged in three disks perpendicular to the beam axis. The silicon pixels, which constitute the active area of the detector, are segmented in r–ϕ and z, and they have a minimum area[3] of 50×400 μm^2.

Pixels are inversely polarised silicon pn junctions that can detect the passage of ionising radiation. When a charged particle travels through a pixel, it produces ionisation charge that is then amplified into a detectable electrical signal. Using

[3]Unless otherwise stated, areas in this section are expressed in the r–$\phi \times z$ space.

silicon-based detector technology allows for very fine granularity and, consequently, for precise position measurements. Each of the ~80 million sensors has an intrinsic accuracy of 10 μm in the r–ϕ direction in all regions, and 115 μm both in the z direction in the barrel and in the r direction in the end-cap disks.

In order to improve the performance of vertex reconstruction and tracking for Run 2, an additional inner-most pixel layer, named *Inner B-Layer* (IBL), was added in the barrel region [31]. The IBL is placed at a radius of 33.25 mm from the beam pipe, and it is composed of ~12 million pixels, each with an area of 50×250 μm^2. The pixel sensors in the IBL are smaller than those in the other layers, offering increased resolution (10 μm in r–ϕ, 75 μm in z) for point-in-space measurements very close to the beam pipe.

Semiconductor Tracker

The Semiconductor Tracker (SCT) is composed of 4088 silicon-based micro-strip modules, each equipped with 1536 readout channels. The modules are arranged in four barrel cylinders and 18 end-cap disks, designed so that particles will pass through four SCT layers on their way from the interaction point through the detector. Modules are constructed with back-to-back layers of silicon micro-strips, rotated with a stereo angle of 40 mrad with respect to each other to provide tracking information in the longitudinal direction. In the barrel region, the SCT layers are placed at radial distances of 299 mm, 371 mm, 443 mm, and 514 mm.

Since the SCT is positioned around the pixel detector, it has to cover a larger surface area. The choice of micro-strip sensor technology allows for a high granularity at a lower cost than the more advanced pixel sensors. The intrinsic position measurement resolution of the SCT is 17 μm in the r–ϕ direction in both barrel and end-cap regions, 580 μm in the z direction in the barrel region, and 580 μm in the r direction in the end-caps.

Transition Radiation Tracker

The transition radiation tracker (TRT) is the outer-most sub-detector composing the ID, and it consists of ~300 000 gas filled straw tubes with a diameter of 4 mm each. Each tube is filled with a argon-based gas mixture that, subject to a strong electrical potential, can multiply the ionisation charge left by particles into a detectable signal.

In the barrel region, the TRT extends from a radial distance of 554 mm to 1082 mm from the beam pipe. The straw tubes are 114 cm long and they are arranged into 73 layers parallel to the z-axis. In the end-cap regions, tubes are instead 37 cm long and they are arranged into 160 planes, with each tube pointing radially outward in the r–ϕ direction. In the barrel, the straw tubes do not have a fine segmentation along the z-axis. Therefore, the TRT only provides tracking information in the r–ϕ direction, with an intrinsic accuracy of 130 μm.

Despite offering a lower spatial resolution than the silicon-based sub-detectors, the TRT provides an average of 30 hits per track for particles in the acceptance range $p_{\mathrm{T}} > 0.5$ GeV, $|\eta| < 2$ [32]. The combination of precision position measurements at small radii (pixels and SCT) with the large number of hits in the TRT at a larger radius allows for very robust pattern recognition and high precision in both r–ϕ and z coordinates. The large-radius straw hits contribute significantly to the momentum measurement, since the worse position measurement resolution is compensated by the larger number of hits and longer measured track length.

The TRT can also be used to discriminate electrons from charged pions using the phenomenon of transition radiation, which is emitted by charged relativistic particles passing through a boundary between two media with different dielectric constants. The intensity of the emitted radiation is logarithmically proportional to the Lorentz factor of the particle. Therefore, electrons emit, on average, more transition radiation than pions due to their lower mass.

For this purpose, straw tubes in the TRT are interleaved with polypropylene fibres and foils. These highly inhomogeneous materials favour the emission of transition radiation without significantly affecting the energy of the particles travelling through them. The TRT can aid electron identification by measuring

electric signal enhancements in the straw tubes due to the emission of transition radiation photons. The distinction between transition radiation and tracking signals is obtained on a straw-by-straw basis using separate low and high thresholds in the readout electronics.

2.2.3 The Calorimeter System

The main purpose of the calorimeter system is to measure the energy of the particles produced in the *pp* collisions. Therefore, this detector must be designed in a way that allows most particles to stop and lose all their energy inside it. Additionally, the detector must respond to this energy loss by producing a proportional detectable electrical signal.

When travelling through a material, high-energy particles interact with the medium itself and lose energy via a series of processes resulting in the production of additional particles. Such *particle showers* travel through the material whilst multiplying and losing their energy until, below a certain energy threshold, they primarily interact through ionisation and excitation of the detector material, thus stopping the cascade.

High-energy photons and electrons can only interact with the medium electromagnetically, giving rise to *electromagnetic showers* that primarily progress through the pair production ($\gamma \rightarrow e^+e^-$) and photon bremsstrahlung ($e^\pm \rightarrow e^\pm\gamma$) processes. The propagation of high-energy electrons through a medium is described by means of the *radiation length* X_0, namely the mean distance an electron travels through a medium before losing all but $1/e$ of its energy via bremsstrahlung. This distance is smaller for heavier elements and in lead it is approximately 0.56 cm [33]. Likewise, photons have to travel a distance of $\frac{9}{7}X_0$ to lose the same amount of intensity through pair production [34]. In a medium, an electromagnetic (EM) shower develops until the energy of the particles is low enough that they primarily interact through ionisation and excitation of the detector material.

When travelling through a medium, high-energy hadrons give rise to *hadronic showers*, which are much more complex than electromagnetic ones. Hadrons can,

in fact, interact with matter via many more processes, which are mediated by the strong interaction, i.e. spallation, fission, pion production, etc. Hadronic showers also normally contain an electromagnetic component, initiated by secondary photons produced in neutral pion decays, and by a highly penetrating component, made up of muons and neutrinos produced in secondary charged hadron decays. The longitudinal shower profile of hadronic showers in a material is determined by the mean free path of hadrons, called the *nuclear interaction length* λ. In lead, the nuclear interaction length is approximately 17.59 cm [33]. Since λ is considerably larger than X_0, hadronic showers extend longitudinally more than electromagnetic ones, needing thicker layers of material to be stopped.

Therefore, the thickness and material density of a calorimeter need to be large enough to stop virtually all of the particles produced in the showers (for primary particles in a given energy range). Furthermore, a calorimeter must be composed of an *active material*, namely a medium that responds to the energy deposited by the particle shower by producing a proportional electric signal. This can be achieved via ionisation of the material or by producing scintillation light, which is then converted into an electric signal using photosensitive devices. Since active materials are expensive, they are commonly interleaved with *absorbers*, namely high-density materials that do not provide an energy measurement, but favour a rapid shower development. Calorimeters adopting this solution are called *sampling calorimeters* as, in such cases, the energy is measured discretely only in the active parts of the detector (i.e. it is sampled).

The ATLAS calorimeters consist of a number of sampling detectors with full ϕ-symmetry and coverage around the beam axis, as shown in Figure 2.6. As it is often the case at collider experiments, the calorimeter system is subdivided into two main sub-detectors: the *electromagnetic* (EM) *calorimeter* and the *hadronic calorimeter*. More detail about these two subsystems is given later in the section. An additional *forward calorimeter* is used by the ATLAS experiment to extend the energy measurement to high pseudorapidity. Since the analysis presented in this thesis exclusively studies a pseudorapidity range that is not covered by the

forward calorimeter, this sub-detector is not described in this section. Additional information, however, can be found in Reference [25].

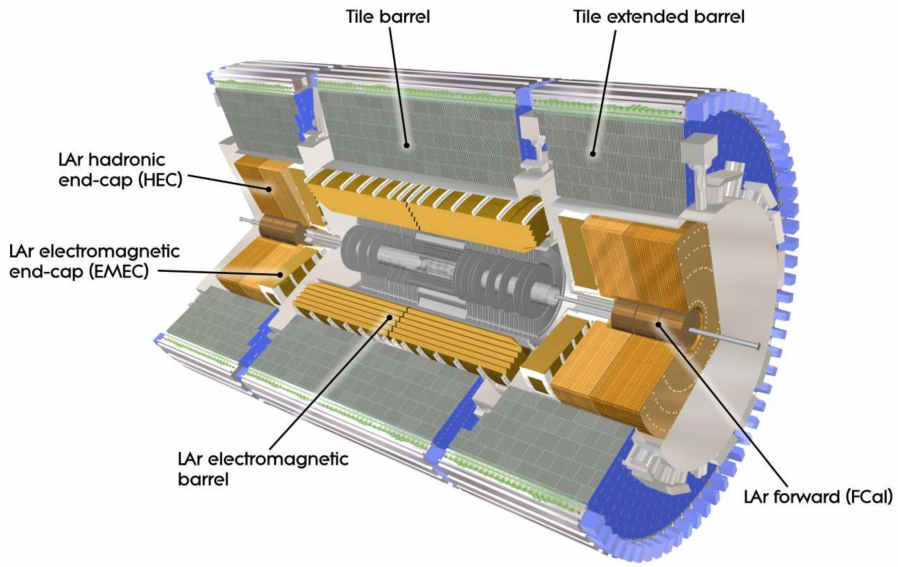

Figure 2.6: Layout of the ATLAS Calorimeter System [25].

Despite being not strictly necessary, designing independent EM and hadronic calorimeters is beneficial in the compromise between cost and performance. Since EM showers develop more rapidly in a medium, the dedicated EM calorimeter is located closer to the beam pipe and it can be smaller in thickness. Therefore, due to the lower volume to be instrumented, more advanced and expensive technologies can be used, granting improved energy resolution and performance in the measurement of EM particles (electrons and photons). Hadronic showers, on the other hand, propagate much deeper in a medium, thus necessitating a much thicker detector. Therefore, the hadronic calorimeter is located around the EM one so to maximise the amount of material along the path of the primary hadrons. Normally, less expensive technologies are used to instrument the larger volume of the hadronic calorimeter, and a more extensive use of absorbers is made.

Energy Resolution

The fractional energy resolution of calorimeters can be parametrised as

$$\frac{\sigma(E)}{E} = \frac{a}{\sqrt{E}} \oplus \frac{b}{E} \oplus c, \tag{2.9}$$

where first term is the *stochastic* term, describing the Poissonian fluctuations in the number of particles in the showers, the second is the *noise* term, describing the contribution coming from the electronic noise of the readout system, while the third is the *constant* term, which includes effects of detector instabilities and mis-calibration.

The calorimeter energy resolution is normally measured before assembling the whole experiment, at dedicated test-beam facilities. There, calorimeter sensors are irradiated with particle beams of various types and energies. From the calorimeter response it is possible to measure the energy resolution as a function of the irradiated particles' energy.

Electromagnetic Calorimeter

The ATLAS electromagnetic calorimeter is a sampling calorimeter consisting of cavities filled with liquid argon separated with accordion-shaped lead absorbers and electrodes. Electrical signals are generated by particles' ionization in the liquid argon cavities that is collected on the electrodes. The choice of liquid argon as an active material is motivated by its linear behaviour, its stability of response over time and its intrinsic radiation-hardness.

The EM calorimeter is subdivided into a barrel and two end-cap regions, housed into three independent cryostats that keep the liquid argon at a temperature of 87 K. The barrel covers the pseudorapidity range $|\eta| < 1.475$, while the end-caps extend the coverage up to $|\eta| = 3.2$. The EM calorimeter features full ϕ coverage around the beam pipe, and it is built externally to the superconducting solenoid magnet. In the barrel, the EM calorimeter extends from a radial distance of 1.4 m from the beam axis to 2 m.

The resolution of the ATLAS EM calorimeter as a function of energy is measured in test-beams [25] and, for the barrel, it is given by

$$\frac{\sigma(E)}{E} = \frac{10\%\ \sqrt{\text{GeV}}}{\sqrt{E}} \oplus \frac{0.2\ \text{GeV}}{E} \oplus 0.2\%. \tag{2.10}$$

Hadronic Calorimeter

The ATLAS hadronic calorimeter is a sampling calorimeter subdivided into a barrel and two end-cap regions. The barrel section of the detector, also named *Tile Calorimeter*, is composed of plastic scintillator tiles interleaved with steel absorbers. The end-cap sections, also known as the *Hadronic End-cap Calorimeter* (HEC), use liquid argon as the active material, interspersed with copper absorber plates arranged in a flat geometry. When charged particles interact with the active material of the detector, a fraction of the energy loss is emitted as scintillation light. Devices called *photomultipliers* (PMTs) are used to convert these photons into a proportional electrical signal.

The Tile Calorimeter covers the pseudorapidity range $|\eta| < 1.7$, while the HEC extends the coverage up to $|\eta| = 3.2$. The ATLAS hadronic calorimeter is positioned around the EM calorimeter, it extends from a radial distance of 2.28 m from the beam axis to 4.25 m, and it features full ϕ coverage.

The energy resolution of the hadronic calorimeter is measured in pion test-beams [35] and, for the tile calorimeter, it results

$$\frac{\sigma(E)}{E} = \frac{52.9\% \sqrt{\text{GeV}}}{\sqrt{E}} \oplus 5.7\%, \tag{2.11}$$

where the electronic noise term is found to be negligible.

2.2.4 The Muon Spectrometer

The muon spectrometer (MS) is the ATLAS sub-detector dedicated to the tracking and identification of muons. These particles are characterised by losing relatively little energy in the interaction with matter (of the order of a few GeV) [22] and can thus penetrate through the calorimeters without stopping. Therefore, the MS is located in the outer-most region of the ATLAS detector system.

The cylindrical structure of the MS, shown in Figure 2.7, is subdivided into a central barrel covering the pseudorapidity range $|\eta| < 1.05$, and two end-cap regions, which extend the coverage up to $|\eta| = 2.7$. In the barrel region, muons are measured using tracking chambers arranged in three cylindrical layers distant

5 m, 7.5 m and 10 m from the beam axis. In the end-cap regions, the chambers are instead installed in three planes perpendicular to the beam axis.

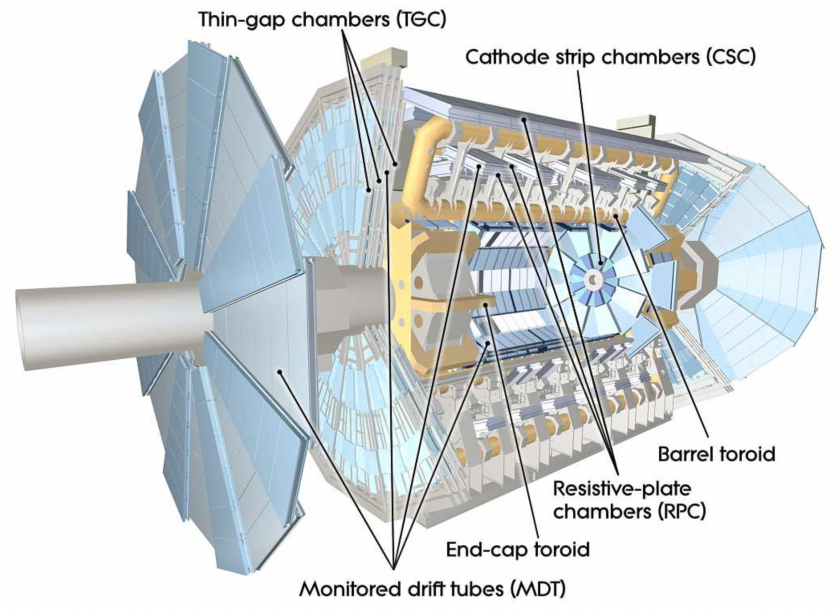

Figure 2.7: Layout of the ATLAS Muon Spectrometer [25].

The MS makes use of four different tracking chamber technologies [25]. *Monitored Drift Tube* (MDT) chambers cover the entire pseudorapidity range of the MS and offer the best tracking resolution. In the forward region ($|\eta| > 2$), where signal rates are higher, multiwire proportional chambers, called *Cathode Strip Chambers* (CSC) are installed, which offer higher granularity. *Resistive Plate Chambers* (RPC) and *Thin Gap Chambers* (TGC) provide muon trigger capabilities (see Section 2.2.5) and additional space point hits in the pseudorapidity ranges $|\eta| < 1.05$ and $1.05 < |\eta| < 2.7$, respectively.

The MS tracking chambers are integrated within three superconducting toroid magnet systems, one in the barrel and two in the end-cap regions. They generate a toroidal magnetic field of around 0.5 T in the barrel and around 1 T in the end-cap regions, perpendicular to the trajectory of the muons.

Details on the reconstruction and identification of muons are given in Section 4.3.

2.2.5 The Trigger System

At ATLAS, proton bunches collide every 25 ns, corresponding to a collision event frequency of 40 MHz. However, due to limitations in data storage, the ATLAS experiment can only record to offline storage around 1 kHz of collision events, implying that most potential data need to be discarded. The ATLAS trigger system [36, 37] is responsible for deciding in real time whether to record data from a given collision or discard them. Events are selected based on interesting physics signatures, such as the presence of energetic leptons, photons, jets or missing transverse energy[4].

In order to achieve a high selection efficiency for rare physics events while strongly suppressing the vast background rate, a two-level trigger system is used. The first level, named *L1 trigger*, is implemented in custom electronics located on the detector and reduces the rate of accepted events to ~100 kHz. The L1 trigger processes reduced granularity information collected by the calorimeters and the muon spectrometer at full rate. This information is combined in the *Central Trigger Processor*, which takes decisions in a fixed time of 2.5 μs. In order to predominantly select the desired rare processes, the L1 trigger searches for exclusive signatures that could identify isolated high-p_{T} muons, electrons, photons, jets, and τ leptons decaying into hadrons. It also selects events with large missing transverse energy and large total transverse energy.

The second trigger level is the software-based *High-Level Trigger* (HLT), which reduces the data acquisition rate from 100 kHz to ~1 kHz. It is executed on a server farm counting about 40 000 processor cores, and it is able to make decisions in about 200 ms. The HLT algorithms use the full granularity and precision of calorimeter and muon spectrometer data, as well as the data from the ID, to refine the trigger selections.

To fulfil the requirements of the rich ATLAS physics programme, events are selected in parallel by about 1500 *trigger chains*, each defined by the selection

[4]Missing transverse energy (E_T^{miss}) serves as an experimental proxy for the transverse momentum carried by undetected particles produced in pp collisions. It is defined as the missing p_{T} in the balance of all particles reconstructed in a given event.

thresholds applied by the L1 trigger and the HLT. In order to satisfy the scientific requirements of the ATLAS analyses, trigger chains are dedicated to selecting events in various kinematic regimes and characterised by specific signatures. The list of trigger chains enabled during data taking is called the *trigger menu*.

Some specific trigger chains are aimed at selecting classes of events that are produced more frequently than the maximum data rate. This is the case, for example, of triggers collecting events with relatively low-p_{T} jets of particles, produced by QCD processes. The problem is dealt with by selecting only a fraction of the events passing the trigger chain. The factor by which the trigger rate is reduced is called a *prescale*, and triggers using prescales are called *prescaled triggers*. After data acquisition, the actual event yield of the process is obtained by multiplying the number of collected events by the prescale.

3

Proton-Proton Collisions and Their Simulation

Contents

3.1 The Internal Structure of the Proton 45
3.2 Phenomenology of Proton-Proton Collisions 46
3.3 Monte Carlo Simulations 48

3.1 The Internal Structure of the Proton

Protons are colour-neutral bound states of colour-charged particles kept together by the strong interaction. The constituent particles are collectively known as *partons* and they are divided into gluons, valence quarks and sea quarks.

A proton is composed of three valence quarks, two up quarks and one down quark (uud), which determine all quantum mechanical properties of the proton (e.g. electric charge, spin, etc.). The valence quarks are bound together by the strong interaction, which is mediated via the exchange of gluons. While propagating within the proton, gluons can produce virtual quark-antiquark pairs, that rapidly annihilate back into gluons. Such quarks, called sea quarks, represent a dynamical component of the proton's quark content.

Quarks and gluons cannot be observed as isolated states, as only colour-neutral bound states of partons are seen to propagate as free particles. This hypothesis, called *colour confinement*, is believed to originate from the gluon-gluon self-interactions. The attractive force between two partons grows with their reciprocal distance, until the energy stored in the gluon field is enough to create new partons, which rearrange the final state particles into colour-neutral objects.

The intensity of the strong interaction between partons is described by the strong coupling constant α_S. The value of α_S depends on the four-momentum transfer Q^2 characterising the interaction as $\alpha_S \propto \frac{1}{ln(Q^2/\Lambda^2)}$, where Λ is an energy scale. This feature determines two different regimes for the strong interaction between partons. Below the GeV range, the value of α_S is large and the outcome of the parton-parton interactions cannot be calculated perturbatively. In this scenario, partons are sensitive to long-distance effects and to the phenomenon of colour confinement. Conversely, for interactions above the GeV range (as in the hard scatterings presented in the next section), the value of α_S is small and the interactions can be calculated perturbatively. For such short-distance effects, the colliding partons behave like free particles, a phenomenon called *asymptotic freedom*.

3.2 Phenomenology of Proton-Proton Collisions

The phenomenology of proton-proton (pp) interactions depends on the four-momentum transfer Q^2 characterising the collisions. *Hard scattering* interactions are the rarest, but also the most scientifically interesting collision events delivered by the LHC. Due to the large momentum transfer, greater than around a few GeV, hard scattering interactions are able to resolve the internal structure of the proton. Therefore, such interactions take place between two constituent partons, rather than between the protons as a whole. At the LHC, the centre-of-mass energy of such collisions can be sufficient to produce heavy resonances such as the Z or Higgs bosons, or to hopefully produce undiscovered ones.

The proton being a composite object, each of its constituent partons carries a fraction x of the longitudinal proton momentum. Therefore, the centre-of-mass

energy s' of a hard scattering interaction is given by

$$s' = x_1 x_2 s, \tag{3.1}$$

where x_1 and x_2 are the momentum fractions of the two interacting partons, and s is the centre-of-mass energy of the pp system. The probability density for finding a parton with a certain fraction x of the proton's momentum for a collision with momentum transfer Q^2 is given by its *parton distribution function* (PDF). Parton distribution functions are an essential component in the simulation of pp collisions. They are estimated by fitting parametric models to data from deep inelastic scattering experiments and precision SM measurements [38].

During a hard scattering, significant momentum transfer occurs, and the protons break up. The final state typically consists of high-energy particles from the hard scattering vertex (including potentially the decay products of heavy resonances accessible at the parton-parton centre-of-mass energy) and typically lower momentum particles from proton remnants, travelling close to the beampipe.

After the hard scattering event, all final state particles propagate away from the interaction point and the unstable ones stochastically decay in-flight over a distance that is determined by their intrinsic lifetime. The propagation of high-energy partons in the final state of a collision is characterised by the *fragmentation* and *hadronisation* processes. Immediately after its production, a high-energy parton starts "fragmenting", namely losing energy by radiating other partons. This cascading process continues until a certain energy threshold is reached ($O(1$ GeV$)$), after which the long-distance effects of colour confinement become dominant. At this stage, new partons are produced from the gluon field, which rearrange all coloured particles into colour-neutral hadrons (hadronisation). Therefore, high-energy partons produced in a hard scattering experimentally manifest as collimated cascades - or *jets* - of hadrons, whose direction is correlated with that of the primary parton.

The phenomenology of pp collisions is further complicated by processes that determine the presence of additional particles in the final state. Within the

strong and electromagnetic fields of the colliding protons, the incoming partons or the outgoing particles can radiate additional high-energy particles, which are called, respectively, *initial state radiation* (ISR) and *final state radiation* (FSR). Furthermore, additional particles can be produced by interactions between the partons not participating in the hard scattering, including the proton remnants. This process is called *underlying event*, and it represent a "soft" component of the collision, adding further low-energy particles (a few GeV) to the overall event activity. The underlying event usually does not produce additional jets but rather a uniformly distributed underlying activity in the form of hadrons. Finally, as already introduced in Section 2.1, the process of pileup results in the production of additional, usually low-p_{T}, particles coming from independent collision vertices during the same bunch crossing.

3.3 Monte Carlo Simulations

Simulations of pp collisions are an invaluable instrument for comparing experimental results to theoretical predictions. Since all particle physics phenomena are stochastic in nature, the *Monte Carlo* (MC) method is particularly suited for simulating the pp collision events delivered by the LHC [39]. The MC method uses pseudo-random sampling to simulate pp collisions on an event-by-event basis. The simulations are performed iteratively, starting with the hard scattering process of interest, following through the evolution of the particle-level state, and lastly, modelling the detector effects. The software used to simulate pp collision events are called *Monte Carlo generators*.

As seen in the previous section, high-energy pp collisions are characterised by a very complex phenomenology, making simulations particularly challenging. The simulation usually starts by estimating the cross-section of a hard scattering process of interest between two partons, e.g. Higgs boson production via the ggF process. Due to the property of asymptotic freedom, the incoming partons can be described as free particles, allowing the cross-section of the hard scattering process to be calculated perturbatively. This is done using *matrix element* (ME) *generators*, which

generally perform cross-section calculations to leading order (LO) or next-to-leading order (NLO) perturbative expansions in terms of α_S. In the MC calculations, the momentum of the incoming partons is sampled considering the corresponding PDFs.

As described in the previous section, final state partons undergo the fragmentation and hadronisation processes. Due to the lower energy scales, these processes are non-perturbative, meaning that the calculation of exact outcomes from first principles would be computationally unfeasible. Hence, the development of the hadronic cascades is sequentially simulated using a simplified probabilistic method carried out by dedicated *parton shower* (PS) *generators*. Within these generators, several parameters can be used to "tune" the fragmentation and hadronisation models to match measured fractions of heavy to light hadrons, mesons to baryons and observed spin states [40]. A correct tuning conserves the universality of the models and their predictions, without making them sensitive to the statistical features of the tuning datasets.

The complete simulation of a *pp* hard scattering interaction must also consider the underlying event and pileup processes, which involve the production of additional high- and low-energy particles. The additional low-energy activity produced by the underlying event is simulated using parton shower generators, with an appropriate tuning. Because pileup are instead *pp* collisions independent from the main hard scattering of the event, they are simulated separately and only included at a later stage.

For any hard scattering process of interest, MC methods provide event-by-event simulations of all final state particles and their properties, as predicted by the underlying theoretical model. Before simulating detector effects, the particles produced by MC generators are called *truth* (or *generator-level*) *particles*, and their corresponding variables *truth variables*.

The interaction of particles with a detector is, again, a stochastic process, meaning that MC methods can be used effectively to simulate it. Based on the geometry of the detector, advanced MC programs are able simulate the detector

response to the passage of particles and model the formation of the electrical signals used for particle detection.

4

Object Reconstruction at ATLAS

Contents

4.1 Jets 52
4.1.1 Jet Clustering 52
4.1.2 Calorimeter Jets 54
4.1.3 Calorimeter Jet Calibration 59
4.1.4 Track Jets 63
4.1.5 Jet Association 65
4.1.6 Truth Flavour Labelling 66
4.2 *b*-tagging of Jets 66
4.2.1 The MV2 Tagger 67
4.2.2 The DL1r Tagger 71
4.3 Muons 72

As described in Chapter 3, the *pp* collisions delivered by the LHC and their simulation are highly complicated processes. Particles streaming out of the collision travel through the ATLAS experiment producing electrical signals in the sub-detectors, which are referred to as *raw data*. In order to be analysed, however, events are reconstructed by turning raw data into more refined physics objects. This is achieved using various reconstruction algorithms, which identify physics objects and determine their properties, e.g. four-momentum, charge.

This chapter describes the most important objects used in the analysis, jets and muons, and the corresponding reconstruction algorithms.

4.1 Jets

Some of the most interesting processes arising from pp collisions at the LHC include the production of high momentum quarks and gluons. As introduced in the previous chapter, these particles, while propagating away from the interaction vertex, undergo fragmentation and hadronisation processes. The hadrons produced in the cascades propagate through the detector and, at the same time, they can decay into lighter hadrons, photons or leptons. The resulting complex experimental signature is that of a *jet*, a collimated stream of particles passing through the ATLAS sub-detectors along the direction of the primary parton.

Despite the complexity, jets constitute an invaluable tool to analyses targeting hadronic final states as they provide a representation of the underlying physical process and allow the reconstruction of the properties of the primary parton that originated the particle shower. Their definition, however, is not unequivocal as it depends on the algorithm used for clustering the detector information into jet objects. Over the course of the LHC scientific programme, a strong interest in hadronic final states has given rise to a wide variety of clustering algorithms, each with their own specific application within the context of particle physics analyses. Section 4.1.1 describes the jet clustering algorithm used in the analysis presented in this work.

Since jets travel through multiple sub-detectors, an additional distinction can be made based on the type of detector information used in the clustering. Section 4.1.2 introduces *calorimeter jets*, which are built by clustering energy deposits in the calorimeters. In Section 4.1.4 *track jets* are described, which are instead built using charged particle tracks reconstructed in the inner detector. Information about calorimeter jet calibration and track-to-calorimeter jet association is also given in Sections 4.1.3 and 4.1.5, respectively.

4.1.1 Jet Clustering

The experimental signature of jets is characterised by quite widespread showers of particles travelling through the ATLAS sub-detectors. The choice of a clustering algorithm is based on the specific needs of an analysis and strongly influences

the jet shape and its sensitivity to non-perturbative effects like hadronisation and underlying event contamination.

All jets in this thesis are clustered using the *anti-k_t* algorithm [41], which is part of the family of *sequential recombination algorithms*. The algorithm iteratively clusters detector signals, which will be generally called *entities*, into jets based on a metric defined in the η-ϕ-p_{T} space.

The algorithm first defines distances d_{ij} between entities i and j and d_{iB} between entity i and the beam direction B as

$$d_{ij} = \min\left(\frac{1}{p_{Ti}^2}, \frac{1}{p_{Tj}^2}\right)\frac{\Delta R_{ij}^2}{R^2}, \tag{4.1}$$

$$d_{iB} = \frac{1}{p_{Ti}^2}, \tag{4.2}$$

where p_{Ti} is the transverse momentum of entity i, R is an adjustable cut-off parameter used to control the width of the jet and ΔR_{ij} is the angular distance (in the η-ϕ space) between entities i and j (see Equation 2.6).

The algorithm then identifies the shortest distance between entities: if it is a d_{ij} entities i and j are combined, if it is the d_{iB} entity i is labelled as a jet and removed from the list of entities. The procedure continues until no entities are left in the list.

This definition preferentially chooses high-p_{T} entities to seed the clustering, and clusters nearby high-p_{T} entities first, resulting in largely conical jet shapes with angular aperture $\Delta R \approx R$. Figure 4.1 shows the shape of jets clustered using the anti-k_t algorithm on simulated particles. In the rapidity-azimuth (y-ϕ) space, clustered areas appear to be centred around high-energy deposits and feature regular circular borders.

The anti-k_t algorithm is *infrared and collinear safe*, meaning that the clustered jets are not affected by the emission of soft radiation or collinear splitting in the particle shower. Since these processes involve non-perturbative effects, they are very hard to predict and it is thus preferable for the jet clustering algorithm, and consequently the jet shape, to be insensitive to them. Since the anti-k_t grows jets around high-p_{T} entities, any additional soft radiation is inconsequentially absorbed

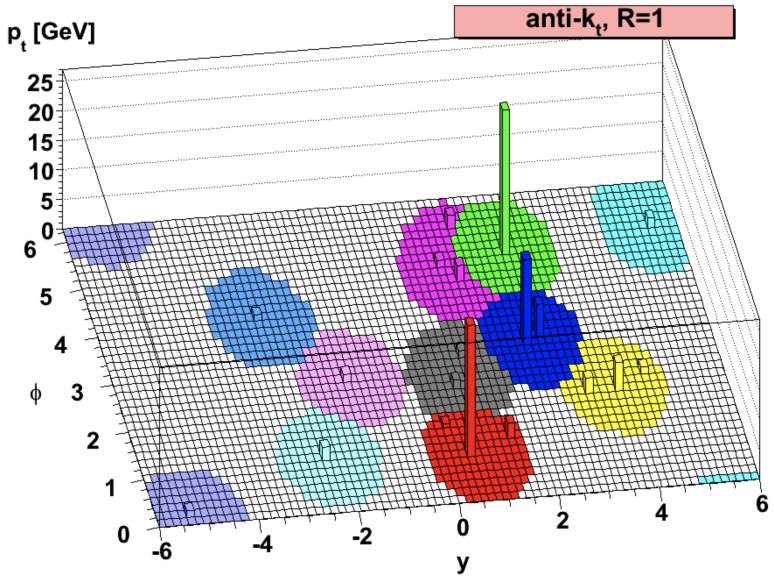

Figure 4.1: Jet shapes in the rapidity-azimuth (y-ϕ) space, obtained by clustering simulated particles with the anti-k_t algorithm [41].

in the clustering. Furthermore, since the algorithm involves angular information in the defined metric, collinear particles are almost immediately clustered as $\Delta R_{ij} \to 0$.

4.1.2 Calorimeter Jets

In the analysis, calorimeter jets are obtained by clustering energy deposits in the calorimeters using the anti-k_t algorithm. As seen in Section 4.1.1, the cut-off parameter R can be used in the algorithm to control the width of the reconstructed jets. In general, jets with different widths find a specific application in the event reconstruction, and the analyses presented in this thesis use two types. *Small radius* (small-R) calorimeter jets are defined by $R = 0.4$ and are used for clustering showers originated from single quarks or gluons. *Large radius* (large-R) calorimeter jets are instead defined by $R = 1.0$ and are used to reconstruct the decay products of entire resonances, such as the Higgs boson decaying to $b\bar{b}$. As a matter of fact, the $b\bar{b}$ final state starts being collimated within $\Delta R < 1.0$ for $p_{\mathrm{T}}^{H} > 250$ GeV[1], and it can thus be clustered inside a single large-R jet representing the kinematic properties of the entire Higgs boson.

[1]The decay products of a resonance of mass m and tranverse momentum p_{T} start being collimated within a jet of radius R approximately when $2m/p_{\mathrm{T}} < R$ [42, 43].

Due to their generally wide area, calorimeter jets (and large-R jets in particular) are susceptible to electronic noise and contamination from soft radiation originating from the underlying event or pile-up. A few strategies are employed in order to reduce these effects, including suppressing them from the input energy deposits and removing them from the jets with a dedicated trimming procedure.

Topological Clusters

Calorimeter cell measurements at ATLAS can be challenging due to fluctuations originating from electronic noise and pile-up. In order to combat this background, calorimeter jets are reconstructed starting from three-dimensional groupings of topologically connected calorimeter cells, also called *topo-clusters* [44]. The clustering is done using an observable called *cell signal significance* ζ, which for any given cell is defined as

$$\zeta = \frac{|E|}{\sigma_{\text{bkg}}}, \tag{4.3}$$

where E is the cell energy measurement and σ_{bkg} is the expected background noise in the cell, accounting for both electronic noise and pile-up.

The procedure that assembles topo-clusters starts by selecting all cells with signal significance $\zeta > 4$, which are then used to seed the clusters. The algorithm starts using the *seed cell* with highest ζ and proceeds through all unclustered seed cells in descending order. For every considered seed cell, a proto-cluster is defined, which contains the seed cell and all neighbouring cells. In case a neighbouring cell has signal significance $\zeta > 2$, its neighbours are collected into the proto-cluster as well. This procedure is iteratively applied to further neighbours until none of the bordering cells have $\zeta > 2$.

The resulting topo-clusters are thus three-dimensional groupings of cells built around a core of highly significant signals. Growing topo-clusters around seed cells in this way intrinsically helps reducing background noise without rejecting significant amounts of signal at the edges. Despite this, however, the energy associated to a topo-cluster is inherently biased. As a matter of fact, ATLAS calorimeters are

non-compensating, meaning that they provide a better response to electromagnetic particles in the jet than hadronic ones. For this reason, topo-clusters are said to be extracted at the *electromagnetic scale* (EM scale) and a correction, described in Section 4.1.3, is thus applied to account for the effect.

Jet Trimming

Jet clustering always presents a trade-off between a large radius, capturing all of the radiation associated with an outgoing parton, and a small radius, which minimises the contamination from other hadrons produced in an event. Despite being a great tool for reconstructing the decay of heavy particles, large-R jets are more subject to contamination from initial state radiation, underlying event and pile-up due to the large area contained in their aperture.

This problem is addressed at ATLAS through a procedure called *jet trimming* [45], which actively identifies and removes contaminating radiation from the large-R jet. This procedure is applied after jet clustering and works under the principles that there is usually only one hard scattering in the event and that sources of contamination are likely much softer.

The main phases of the jet trimming procedure are illustrated in Figure 4.2. Starting from an untrimmed large-R jet, the algorithm declusters it into smaller constituents called *subjets* and removes ones with p_{T} lower than an optimised threshold. The trimmed deposits are finally reclustered into a large-R jet.

Subjets are built using the k_T clustering algorithm [46], with distance parameter $R_{\mathrm{sub}} = 0.2$. The k_T algorithm follows the same procedure outlined in Section 4.1.1 for anti-k_t, but uses a different metric, defined by

$$d_{ij} = \min\left(p_{Ti}^2, p_{Tj}^2\right)\frac{\Delta R_{ij}^2}{R^2}, \tag{4.4}$$

$$d_{iB} = p_{Ti}^2. \tag{4.5}$$

The result is that, differently from anti-k_t, this algorithm clusters soft deposits first and distributes the energy more evenly among subjets. On the contrary, the anti-k_t algorithm would create more unbalanced subjets, leading to a higher

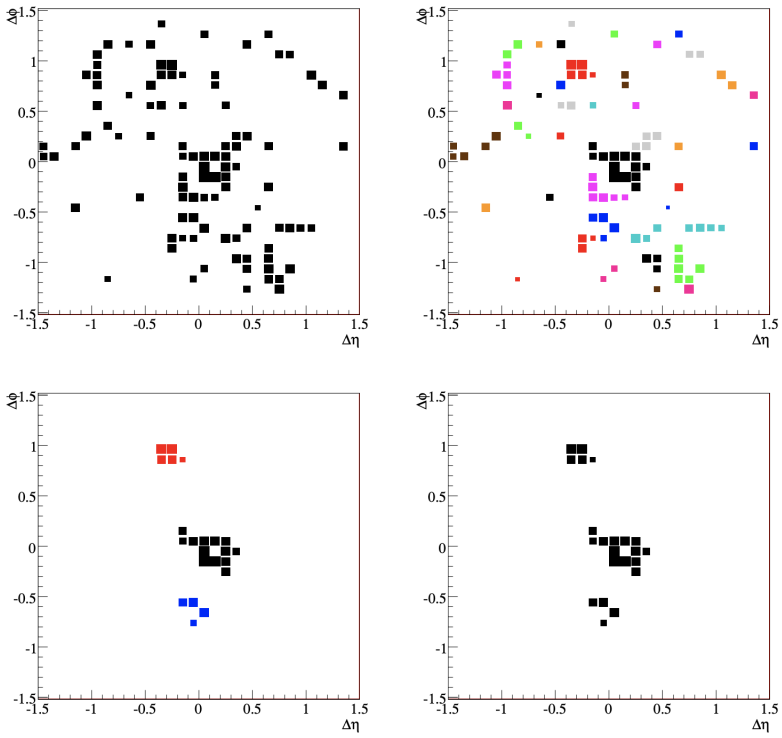

Figure 4.2: Four main phases of the jet trimming procedure. Starting from an untrimmed large-R jet (top-left), the algorithm declusters it into subjets (top-right) and removes ones with p_{T} lower than a threshold (bottom-left). The trimmed deposits are finally reclusted into a large-R jet (bottom-right). Calorimeter deposits are represented as coloured squares in the $\Delta\eta$-$\Delta\phi$ parameter space [45].

risk for part of the hard scattering deposits to be considered as soft radiation and incorrectly removed.

Finally, subjets with p_{T} lower than $f_{\mathrm{cut}} = 5\%$ that of the original jet are removed and the remaining ones are assembled into the final trimmed large-R jet.

Figure 4.3 shows the mean jet mass $\langle M \rangle$ distribution as a function of pileup, extracted from $W \to q\bar{q}'$ and QCD multijet simulated events. Noticeably, the trimming procedure proves to be effective at removing contaminating radiation, strongly mitigating the jet mass dependence on pileup.

Jet Mass

In the analysis presented in this thesis, jets are the most important objects used for event reconstruction. The mass of such jets is thus extensively used to distinguish the Higgs signal from other massive particles and from the continuous background

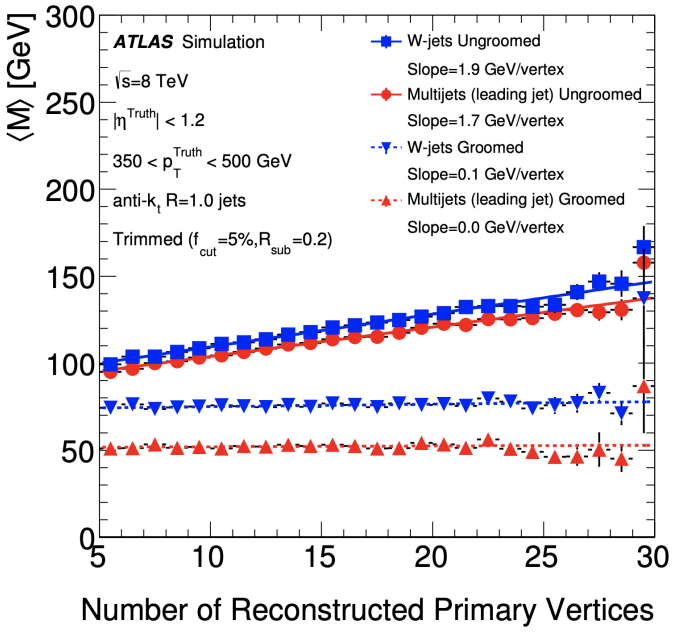

Figure 4.3: Mean jet mass $\langle M \rangle$ distribution as a function of pileup, extracted from $W \to q\bar{q}'$ (blue) and QCD multijet (red) simulated events. Distributions before and after jet trimming are compared [47].

originated from QCD multijet events.

The jet mass can be computed as the invariant mass of all constituent topo-clusters as

$$m^{\text{calo}} = \sqrt{\left(\sum_i E_i\right)^2 - \left(\sum_i \vec{p}_i\right)^2}, \tag{4.6}$$

where the sums are taken over all topo-clusters and $|\vec{p}_i| = E_i$, as topo-clusters are considered to be massless. The jet mass computed following this definition thus depends on the angular separation between topo-clusters. This results in the jet mass resolution degrading at high momentum, when the angular spread of the topo-clusters becomes comparable to the calorimeter's granularity.

In order to increase performance at high momentum, this information can be supplemented by measurements from the tracker, which has better angular resolution. The invariant mass of tracks associated to the calorimeter jet (m^{track}) maintains a high resolution up to very high momentum, but it does not take into account the neutral particle component of the jet. This can be corrected by using

the *track-assisted jet mass* [48], which is defined as

$$m^{\mathrm{TA}} = \frac{p_{\mathrm{T}}^{\mathrm{calo}}}{p_{\mathrm{T}}^{\mathrm{track}}} \cdot m^{\mathrm{track}}, \tag{4.7}$$

where $p_{\mathrm{T}}^{\mathrm{calo}}$ is the transverse momentum of the calorimeter jet and $p_{\mathrm{T}}^{\mathrm{track}}$ is the transverse momentum of the four-vector sum of tracks associated[2] to the calorimeter jet. The $p_{\mathrm{T}}^{\mathrm{calo}}/p_{\mathrm{T}}^{\mathrm{track}}$ ratio is used to correct for fluctuations in the charged-to-neutral component of the jet, improving the resolution of the track-only jet mass definition (m^{track}).

Since the calorimeter jet mass m^{calo} is not explicitly used in the track-assisted jet mass definition, it is possible to further improve the jet mass resolution by combining information from both mass definitions. As the calorimeter jet p_{T} and mass responses are almost independent, the optimal combination is linear

$$m^{\mathrm{comb}} = a \cdot m^{\mathrm{calo}} + b \cdot m^{\mathrm{TA}}, \tag{4.8}$$

where a and b are weights that minimise the jet mass resolution. Figure 4.4 shows the jet mass resolution as a function of jet p_{T} for the calorimeter-based m^{calo}, track-assisted m^{TA} and combined jet mass definitions. Noticeably, while m^{calo} resolution rapidly degrades with jet p_{T}, m^{TA} shows more stable performance across the whole p_{T} range. The combined mass m^{comb} is recommended and used widely across ATLAS analyses, including the one presented in this work.

4.1.3 Calorimeter Jet Calibration

Calorimeter jets must undergo a series of detailed and complex calibrations in order to provide an accurate representation of the underlying physical process. These calibrations correct for effects such as fluctuations and biases in the calorimeter response, mismodelling in jet simulations and contamination from underlying event and pileup.

As shown in Figure 4.5, large-R jets are calibrated in three steps, which are briefly described in this section. Due to their importance in the thesis, only the

[2]The track-to-calorimeter jet association is perfomed using the *ghost association* method, which will be described in Section 4.1.5.

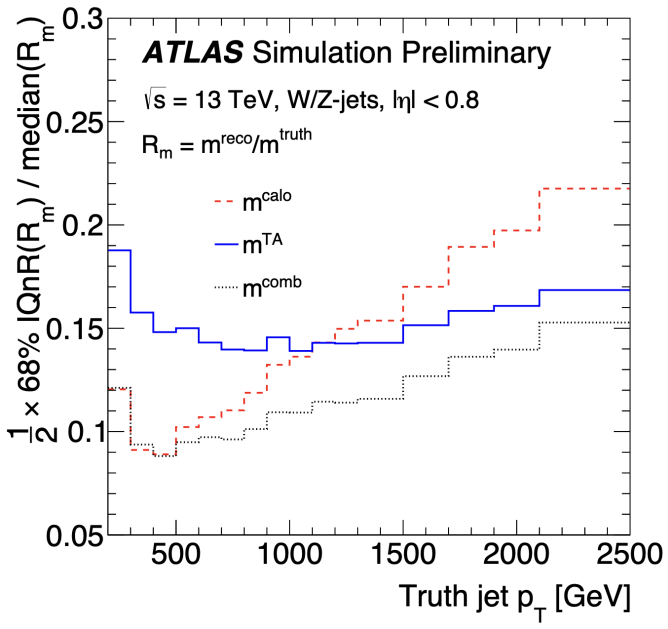

Figure 4.4: Jet mass resolution as a function of jet p_{T} for the calorimeter-based m^{calo} (red dashed line), track-assisted m^{TA} (blue solid line) and combined (grey dotted line) jet mass definitions [48].

calibration of large-R jets is presented in this section. However, an exhaustive overview of small-R jet calibrations can be found in Reference [49].

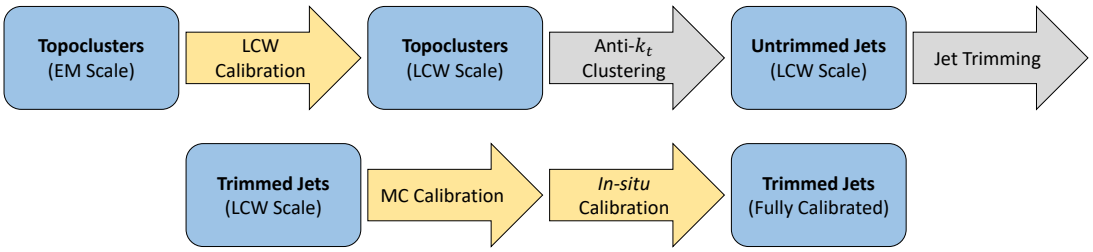

Figure 4.5: Flowchart illustrating the calibration of large-R jets. The yellow arrows represent the three main steps in the calibration procedure: LCW calibration, MC-based calibration and *in-situ* calibration.

Local Hadronic Calibration

The energy of topo-clusters needs to be calibrated to account for several detector effects. First of all, as seen in Section 4.1.2, topo-clusters are extracted at the EM scale due to the non-compensating behaviour of calorimeters. Additionally, the intrinsic noise suppression feature of topo-clusters might lead to true signal losses at

the borders, and thus to a non-linear energy response. Finally, particle interactions in the calorimeters' inactive material might lead to substantial energy losses.

In order to correct these effects, a *local hadronic cell weighting* (LCW) calibration [44] is applied. This method extracts cluster-by-cluster corrections by comparing single charged and neutral pion data registered by the calorimeters to simulations. The comparison is carried out over a wide range of pion energies and in all ATLAS calorimeter regions. More information on this simulation-based approach is given in Reference [44]. The calibration corrects the non-compensating behaviour of calorimeters, bringing topo-clusters from the EM scale to the *LCW scale*.

Reconstructed-to-Truth Scale Calibration

The energy of a jet is not entirely recordable by the detector. The response of calorimeters is not uniform in every direction, and large energy losses occur at boundaries between calorimeter technologies and granularities. Furthermore, a substantial amount of the jet energy goes into overcoming the binding energy in hadron-hadron interactions, which is invisible to the detector.

In order to correct these effects, an additional MC-based calibration [50] is introduced. In simulated dijet events, reconstructed jets are compared to precursor jets of simulated particles, typically referred to as *truth jets*[3]. To large-R jets, this calibration is applied after trimming and brings them to the corresponding truth-level energy scale.

The comparison is carried out by considering the average energy and mass responses $R_X = \langle X_{\text{reco}}/X_{\text{truth}} \rangle$, where $X = \{E, m\}$, while X_{reco} and X_{truth} refer to reconstructed- and truth-level quantities, respectively. R_E and R_m are studied in fine bins of jet η and energy to account for non-uniformities in the detector structure and the energy dependence of hadronic interactions.

The jet energy and mass scale (JES and JMS) calibration scale factors are respectively defined as $c_{\text{JES}} = R_E^{-1}$ and $c_{\text{JMS}} = R_m^{-1}$, and are applied to the reconstructed jet four-momentum as multiplicative factors. In specific regions

[3]Truth jets are created by running the anti-k_t clustering algorithm on the final state particles generated in MC showers.

of the detector, a bias in the η distribution with respect to the truth jets is also found. To resolve this bias, an additional correction on the jet angle is applied. Further details on the calibration procedure can be found in References [50, 51].

Data-to-MC *in-situ* Calibrations

Being MC-based, the jet calibrations introduced in the previous paragraphs heavily rely on the accuracy of simulations. Since jets are highly complex systems, however, they can prove very challenging to simulate. Thus, data-to-MC biases might be present due to mismodelling in the simulation of the shower development or detector response. These residual differences are corrected through *in-situ* calibrations [50], which are extracted using data-driven methods and well-understood processes.

The JES in-situ calibration is performed in two steps. First the η *intercalibration* is performed, which extends the jet calibration beyond the central region of the detector. The calibration is derived from the differences in p_{T} balance between a central reference jet with $|\eta| < 0.8$ and a probe jet with $0.8 < |\eta| < 2.5$ in dijet data and MC. In a second step, the residual JES data-to-MC difference is extracted by comparing the p_{T} balance of a probe jet recoiling against a reference Z boson, photon or multiple small-R jets in data and simulation. Photons and Z bosons are chosen as they are very well known and measured objects at ATLAS, while small-R jets are used to extend the calibrations to the high-p_{T} regime, a kinematic region where other processes do not provide enough events.

The JMS in-situ calibration is performed on dijet events via the R_{trk} method, which uses tracking information to independently measure the jet mass scale and associated uncertainty. The average calorimeter-to-track jet mass response $R^{m}_{\mathrm{trk}} = \langle m^{\mathrm{calo}}/m^{\mathrm{track}} \rangle$ is proportional to the calorimeter-to-truth response. Thus, by comparing R^{m}_{trk} in data and MC it is possible to extract the residual JMS calibration scale factors.

During analysis development, a calibration for the jet energy resolution (JER) and the jet mass resolution (JMR) was not finalised. In the analyis, conservative estimates for JER and JMR systematic uncertainties obtained from Run 1 data [52]

were used. Recently, a full calibration of JER and JMR was finalised [50], which will be exploited in future iterations of the analysis.

4.1.4 Track Jets

Track jets are reconstructed from tracks of charged particles travelling through the ID. Thanks to the high resolution of the ATLAS tracking system, track jets are used for resolving the internal structure of large-R calorimeter jets by means of a robust track-to-calorimeter jet association procedure (see Section 4.1.5). Furthermore, using a method called *b-tagging* (see Section 4.2), it is possible to identify track jets originated from a b quark. For these reasons, the use of track jets is of utmost importance in the identification of large-R jets compatible with a boosted $H \to b\bar{b}$ decay.

Variable Radius Track Jets

In the analysis presented in this thesis, *variable radius* (VR) track jets [53, 54] are used, which are clustered using the anti-k_t algorithm with a cut-off radius defined as

$$R = \frac{\rho}{p_{\mathrm{T}}}, \tag{4.9}$$

where p_{T} is the track jet transverse momentum and $\rho = 30$ GeV. In the VR method, the radius R is thus a function of the track jet p_{T} and it is allowed to vary between $R_{\mathrm{min}} = 0.02$ and $R_{\mathrm{max}} = 0.4$. The minimum value of the radius is determined by the resolution of the inner detector.

Clustering track jets with the VR method is crucial for accurately resolving the internal structure of large-R jets produced by the decay of highly boosted resonances, like $H \to b\bar{b}$. At high-p_{T}, decay products become highly collimated and can prove challenging to resolve using track jets with fixed R parameter, also called *fixed radius* (FR) track jets. In strongly boosted $H \to b\bar{b}$ decays, the FR method might, in fact, cluster both Higgs decay products inside a single jet.

The adaptive radius of VR track jets, on the other hand, reduces the double-clustering chance in dense environments and provides increased reconstruction

performance across a wide p_{T} range. Figure 4.6 shows the efficiency of exclusively associating generator-level b-hadrons to the two leading track jets within a Higgs large-R jet (double b-labelling efficiency). The association is performed using the truth flavour labelling procedure detailed in Section 4.1.6. As a function of the Higgs jet p_{T}, the plot compares the double b-labelling efficiency obtained when reconstructing the Higgs jet substructure using either FR track jets with $R = 0.2$ or VR track jets, for different choices of the ρ parameter. The performance of the fixed radius method is high at low p_{T}, but falls very quickly for $p_{\mathrm{T}} > 1$ TeV. Conversely, the performance of the VR method remains high across the whole p_{T} range, with $\rho = 30$ GeV providing the most uniform distribution.

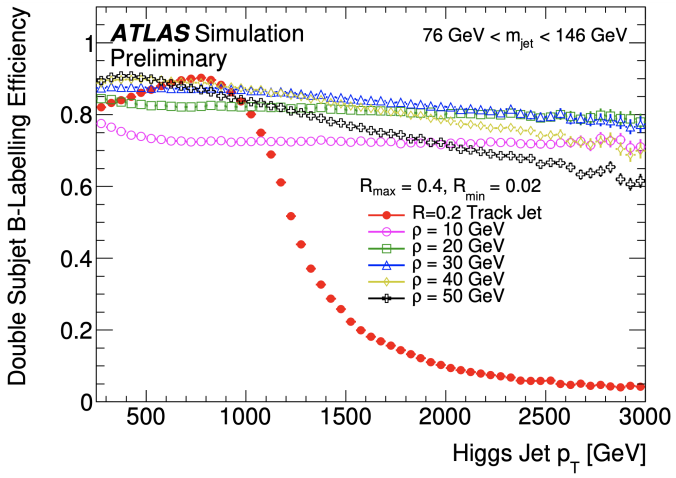

Figure 4.6: Higgs jet double b-labelling efficiency as a function of the Higgs jet p_{T}, with substructure reconstructed using either FR track jets with $R = 0.2$ or VR track jets with $R_{\mathrm{min}} = 0.02$ and $R_{\mathrm{max}} = 0.4$. For VR track jets, results obtained using several values of ρ are shown [54].

In the analysis, VR track jets have to satisfy a set of quality requirements, which are recommended by the ATLAS Collaboration. Tracks within a VR track jet must have $p_{\mathrm{T}} > 0.5$ GeV, $|\eta| < 2.5$, at least 7 hits in the silicon detectors, no more than one hit in the pixel detector shared with other tracks, no more than one missing hit in the pixel detector, no more than two missing hits in the silicon detectors and $|z_0 \sin(\theta)| < 3$ mm.

After jet clustering, tracks passing looser requirements are added to the jet if they fall within a certain distance of its axis. These “loose tracks” are selected in

the same way as the other tracks, but they do not need to pass the longitudinal impact parameter requirement. Their inclusion in the VR jet allows for a more reliable reconstruction of secondary vertices, which are used in the identification of track jets originated from a b quark (see Section 4.2). Finally, only track jets with $p_{\mathrm{T}} > 10$ GeV, $|\eta| < 2.5$, and containing at least two tracks are used in the analysis.

Overlap Cleaning

In sufficiently dense environments, even the VR method might lead to overlapping track jets. In such situations, an ambiguity arises on how to associate the loose tracks, thus rendering the b-tagging assessment of overlapping jets unreliable.

Overlapping VR track jets are removed through a procedure called *overlap cleaning*. This procedure requires the ΔR between any two track jets with $p_{\mathrm{T}} > 5$ GeV in a large-R jet to be larger than either of their respective variable radii. Large-R jets not passing this selection are not considered by the analysis.

4.1.5 Jet Association

In the analysis, track jets are matched to large-R jets in order to resolve and identify their internal substructure. In events with a dense hadronic environment, however, ambiguities might arise in the matching. The association is thus performed using *ghost-association* [55–57], which provides a robust reclustering procedure for matching jets with irregular boundaries.

In this technique, track jets are treated as infinitesimally soft "ghosts" by setting their p_{T} to 1 eV, thus retaining only the directional information. The association is performed by including these ghosts to the list of un-trimmed calorimeter inputs and then running the large-R jet finding algorithm described in Section 4.1.1. Since the ghosts are infinitesimally soft, the resulting large-R jets are unaffected by the procedure, but they retain the matched track jets as associated objects.

4.1.6 Truth Flavour Labelling

In simulated events it is possible to match reconstructed jets to the generator-level particles that initiated them. This procedure, called *truth flavour labelling*, is particularly useful in assessing the performance of b-tagging algorithms (see Section 4.2).

Jets are labelled as b-jets if they are matched to at least one weakly decaying generator-level b-hadron having $p_{\mathrm{T}} > 5$ GeV within $\Delta R < 0.3$ of the jet axis. If no b-hadrons are found, c-hadrons and then τ-leptons are searched for, requiring the same selection criteria. Jets matched to a c-hadron (τ-lepton) are labelled as c-jets (τ-jets). The remaining jets are labelled as light-flavour jets.

4.2 *b*-tagging of Jets

The identification of track jets originating from a b quark (b-jets) is fundamental for selecting large-R jets consistent with a boosted $H \to b\bar{b}$ decay and separating them from the immense hadronic background. The techniques for b-jet identification, in short *b-tagging*, exploit the relatively long lifetime of b-hadrons ($\approx$ 1.5 ps), which decay after travelling a measurable distance, typically of the order of a few mm. The resulting events are thus characterised by the presence of secondary vertices (SV), displaced from the primary interaction point, and tracks with large transverse (d_0) and longitudinal (z_0) impact parameters.[4] In addition, b-hadron decays are characterised, on average, by a larger track multiplicity than light hadrons. At ATLAS, b-tagging is performed through several algorithms, subdivided into *low-level* and *high-level* taggers.

Low-level taggers are relatively simple algorithms that identify b-jets using tracking information and the knowledge about the distinctive features of b-hadron decays. Several such algorithms exist, each providing a complimentary approach to b-jet discrimination. IP2D and IP3D [58] use information on the transverse and longitudinal impact parameter of tracks, SV1 [59] is based on the reconstruction of

[4]The transverse (d_0) and longitudinal (z_0) impact parameters are the minimum distance of a track to the PV in the transverse plane (xy) and on the longitudinal axis (z), respectively.

secondary vertices, while JetFitter [60] aims at reconstructing the full topological decay chain of b-hadrons.

Low-level taggers provide output variables that can be used directly to identify b-jets or fed to more complex high-level algorithms that are often based on multivariate methods. In the following section, the high-level b-tagging algorithm used in the $H(\rightarrow b\bar{b}) +$ jet analysis, MV2, is presented.

4.2.1 The MV2 Tagger

The MV2 [61, 62] high-level b-tagging algorithm is a boosted decision tree (BDT) implemented using the ROOT Toolkit for Multivariate Data Analysis [63]. The goal of the MV2 tagger is to discriminate b-jets from c-, τ- and light-jets by exploiting information about track jet kinematics and the IP2D, IP3D, SV1 and JetFitter low-level tagger outputs.

The BDT classifier is trained on a hybrid sample composed of $t\bar{t}$ and Z' simulated events[5]. $t\bar{t}$ events are required to have at least one prompt lepton, ensuring a sufficiently large fraction of b-, c- and light-jets in the sample. A dedicated Z' sample decaying into hadronic jet pairs is included to improve b-tagging performance at high jet p_{T}.

The analysis presented in this thesis makes use of the MV2c10 tagger, a particular MV2 release for which the charm-to-light jet fraction in the training sample is set to 10%. For each assessed track jet, the MV2c10 algorithm outputs a single discriminant defined between -1 and $+1$. Larger values of the discriminant correspond to a higher probability for a jet to have b flavour rather than being a c-, τ- or light-jet. The performance of the tagger is tested on an independent $t\bar{t}$ sample to determine its b-tagging efficiency versus background rejection. The b-tagging efficiency is defined as

$$\epsilon_b = \frac{N_b^{\mathrm{tag}}}{N_b}, \tag{4.10}$$

where N_b is the number of reconstructed jets in the test sample associated to a truth b-hadron, while N_b^{tag} is the number of them that are also b-tagged. Jet association

[5] Z' is a theorised BSM particle. In MC, its mass is set to 4 TeV and it is decayed with equal probability to either $b\bar{b}$, $c\bar{c}$ or to a pair of light quarks $q\bar{q}$.

to truth b-hadrons is defined in MC using the truth flavour labelling procedure outlined in Section 4.1.6. The c-, τ- and light-jet rejections are instead defined as the inverse of the efficiencies at which these jets are selected (and mistagged as b-jets).

Figure 4.7 shows the MV2 c- and light-jet rejection as a function of the b-tagging efficiency for various taggers. Expectedly, MV2 is seen to outperform all the low-level taggers that were used as inputs. Another high-level tagger, DL1, shows slightly better background rejection compared to MV2. The name DL1 refers to an intermediate algorithm stage during the development of the DL1r tagger, which is described in Section 4.2.2. Despite the improved performance of DL1, the MV2 algorithm was finally chosen due to its maturity at a critical point during analysis development.

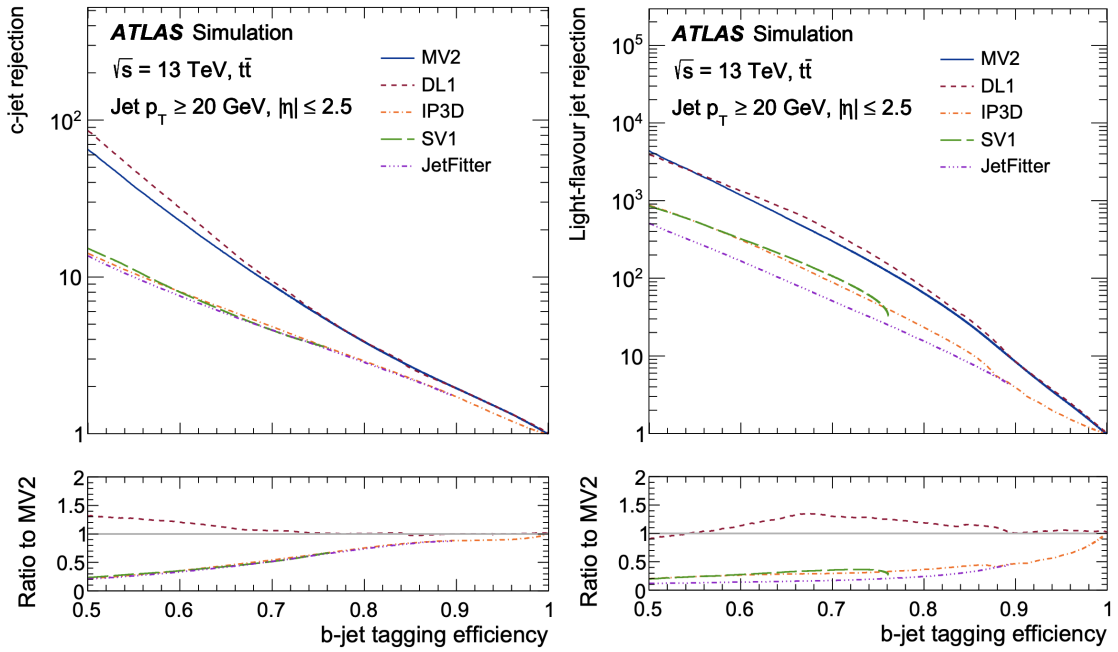

Figure 4.7: The c-jet (left) and light-jet (right) rejections as function of the b-tagging efficiency for the IP3D, SV1, JetFitter, MV2 and DL1 b-tagging algorithms, as measured on a $t\bar{t}$ test sample [64].

A jet is said to be b-tagged if its tagger discriminant value is higher than a certain adjustable threshold called a *working point* (WP). The tagger performance is a compromise between b-tagging efficiency and background rejection, but at a given WP, the b-tagging efficiency is fixed. In the analysis, b-jet identification is

done using MV2c10 with a 77% b-tagging efficiency WP, corresponding to rejection factors of 4.9 for c-jets, 15 for τ-jets and 110 for light-jets.

MV2 Calibration

As seen in the previous section, the MV2 b-tagging algorithm is trained and tested on simulated samples. However, differences in performance between data and MC might arise due to theoretical and detector mismodelling. For this reason, the tagger is calibrated on a pure b-jet sample in Run 2 data that targets dileptonic $t\bar{t}$ decays [64]. Events are selected by requiring the presence of two leptons with opposite charge and two small-R calorimeter jets.

Following the truth flavour labelling procedure described in Section 4.1.6, simulated events are classified according to the generator-level flavour of the leading (j_1) and subleading (j_2) p_{T} small-R jets in the event. Four combinations $j_1 j_2 = bb$, bl, lb, ll are defined, where b denotes a jet associated to a truth b-hadron and l one with no b-hadron association.

Selected events are classified according to the p_{T} of the two jets, allowing the b-jet tagging efficiency to be measured as a function of the jet p_{T}. In each p_{T} bin, the invariant mass of the two associated jet-lepton pairs is used to classify events into a signal region (SR), characterised by high b-jet purity, and three control regions (CR), useful to constrain the bl, lb and ll contributions. Finally, the SR is further subdivided according to the MV2 discriminant of the two jets, using as subdivision the recommended 60%, 70%, 77% and 85% WP values.

In each jet p_{T} and jet MV2 discriminant bin, a maximum likelihood fit is performed, simultaneously on the SR and the three CRs. The fit provides a measurement of the b-tagging efficiency in data (ϵ_{data}), while that in MC (ϵ_{MC}) can be computed from the pre-fit estimates directly from simulation. Thus, multiplicative correction factors called *b-tagging efficiency scale factors* can be defined using $\mathrm{SF} = \epsilon_{\mathrm{data}}/\epsilon_{\mathrm{MC}}$.

Figure 4.8 shows the scale factor values as function of the jet p_{T}, derived at the 77% efficiency WP. Overall, a good agreement between data and MC is

noted, with scale factors lying within 2σ of unity. As the calibration suffers from low data statistics for $p_{\mathrm{T}} > 400$ GeV, a MC-based extrapolation (described in section 10.2 of [64]) was performed to extend the calibration to higher jet p_{T}. The procedure results in an additional extrapolation uncertainty, which is included in the total uncertainty band.

Similarly to the b-tagging efficiency, the c-jet and light-jet mistagging rates are also calibrated. Additional information can be found in References [65] and [66], respectively.

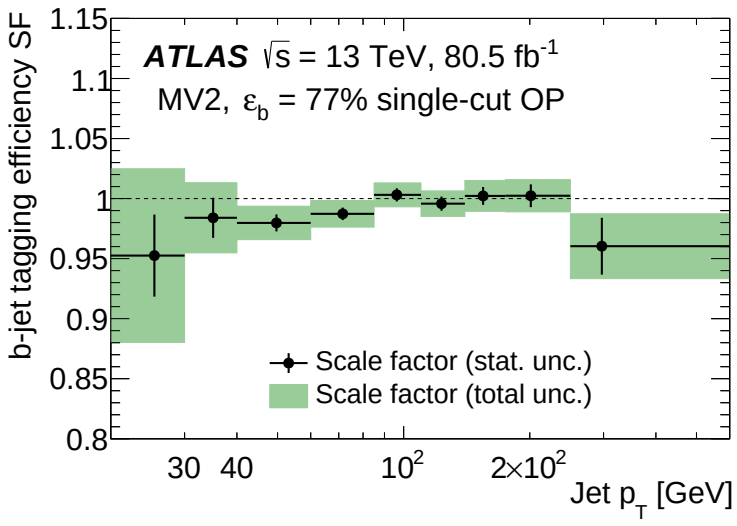

Figure 4.8: Data-to-MC b-tagging efficiency scale factors for the MV2 tagger at the 77% efficiency WP.

The training and calibration of the MV2 tagger presented in this section are performed using small-R ($R = 0.4$) calorimeter jets. This represents the state of the tagger during the early development of the double b-tagging calibration on $g \to b\bar{b}$ events, which is presented in Section 5.1. More recently, the MV2 tagger was re-trained and calibrated on VR track jets using an analogous procedure [67]. This updated version of the tagger and the corresponding scale factors were used in the Boosted $H(\to b\bar{b}) +$ jet analysis, the main focus of this thesis.

4.2.2 The DL1r Tagger

b-tagging is a thriving field of research at ATLAS, subject to continuous and rapid development. Over the course of the analysis time frame, several new b-tagging algorithms were trained and calibrated, some showing better performance than MV2. This section describes DL1r, a recently developed b-tagger based on a deep neural network. Despite the clear improvements that shall be discussed in this section, the DL1r tagger is not used in analysis as it was not yet finalised when the analysis selection was being developed. Section 9.6.1, however, explores avenues for improvement in future analysis iterations making use of this recent tagger.

The DL1r b-tagging algorithm [58] is based on a deep neural network trained using KERAS [68]. The DL1r high-level tagger uses the same input variables as MV2 with the addition of RNNIP [69], a low-level tagger based on a recursive neural network.

For any jet assessed for b-tagging, DL1r provides three outputs, p_b, p_c and p_{light}, corresponding to the probabilities for the jet to be identified as a b-, c- or light-flavour jet respectively. These values are combined into a single score D_{DL1r}, which is defined as

$$D_{\text{DL1r}} = ln\left(\frac{p_b}{f_c \cdot p_c + (1 - f_c) \cdot p_{\text{light}}}\right), \tag{4.11}$$

where f_c is the effective c-jet fraction in the background training sample and can be tuned to enhance the algorithm's discrimination of b- versus c- or b- versus light-jets. After optimisation, $f_c = 0.018$ is chosen. Similarly to MV2, the DL1r tagger is trained over a hybrid $t\bar{t}$ and Z' sample.

Working points corresponding to b-tagging efficiencies of 60%, 70%, 77% and 85% are extracted from a simulated $t\bar{t}$ sample. Figure 4.9 compares the c- and light-jet rejection for the MV2, DL1 and DL1r taggers, as functions of the b-jet efficiency [70]. DL1 refers to an intermediate algorithm stage during DL1r development which does not use the RNNIP input. From the pictures, it is possible to conclude that, at the 77% WP chosen in the analysis, the DL1r tagger offers an improvement in c-jet rejection of around 15% and in light-jet rejection of around 110%.

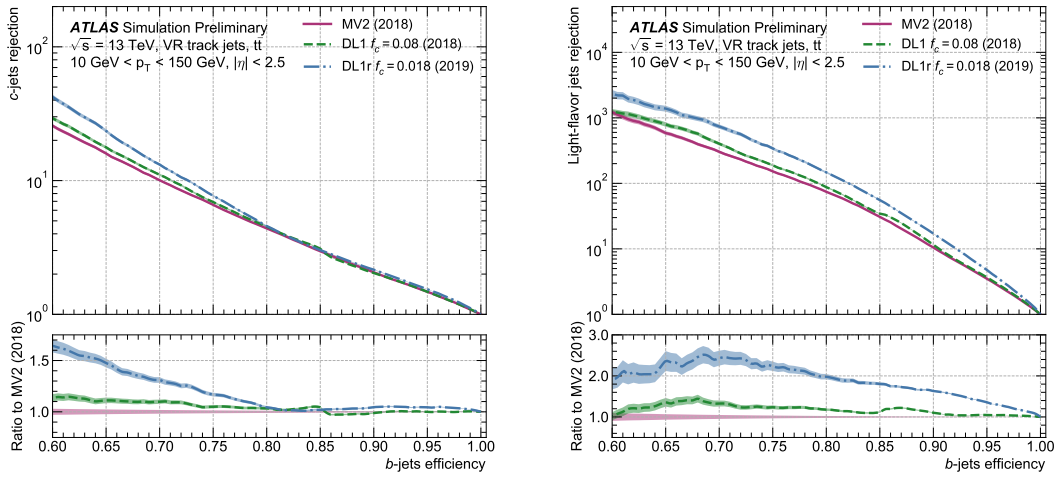

Figure 4.9: *c*- (left) and light-jet (right) rejection curves for the MV2, DL1 and DL1r taggers, as functions of *b*-jet efficiency. In both figures, the lower panels show the background rejection ratio with respect to MV2 and uncertainties [70].

Figure 4.10 compares the performance of the MV2, DL1 and DL1r taggers as function of VR track jet p_{T}, at the 77% *b*-tagging efficiency working point. It is interesting to note that the *b*-tagging efficiency offered by the DL1 and DL1r taggers is around 10% lower than MV2 for track jet $p_{\mathrm{T}} > 40$ GeV. However, this is compensated by strongly reduced mistag rates at high-p_{T}. The DL1r tagger offers *c*- and light-jet rejections that are, respectively, around 1.5 and 2.5 larger than those of MV2 for track jet $p_{\mathrm{T}} > 40$ GeV.

4.3 Muons

Muons and their reconstruction have an important role in the analysis presented in this thesis. As a matter of fact, muons are produced in semi-leptonic *b*-hadron decays and are thus likely found within *b*-tagged jets. Furthermore, as will be explained in Sections 6.3.2 and 6.3.3, the analysis uses control regions whose events are collected using muon triggers.

Muons that are typically produced at the LHC are minimum ionising particles that can travel through all ATLAS sub-detectors only leaving behind relatively small

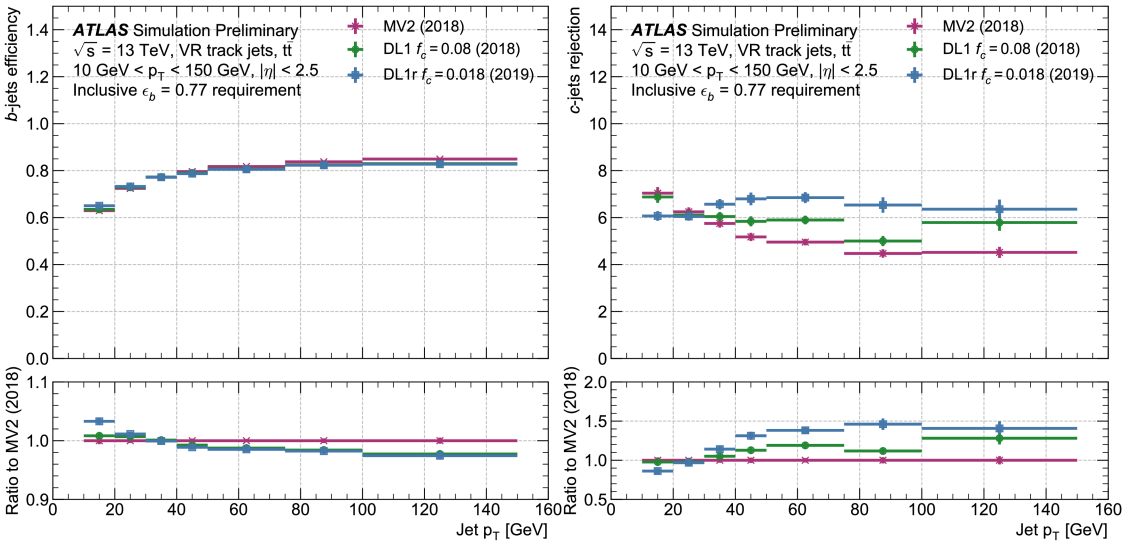

(a) *b*-jet efficiency **(b)** *c*-jet rejection

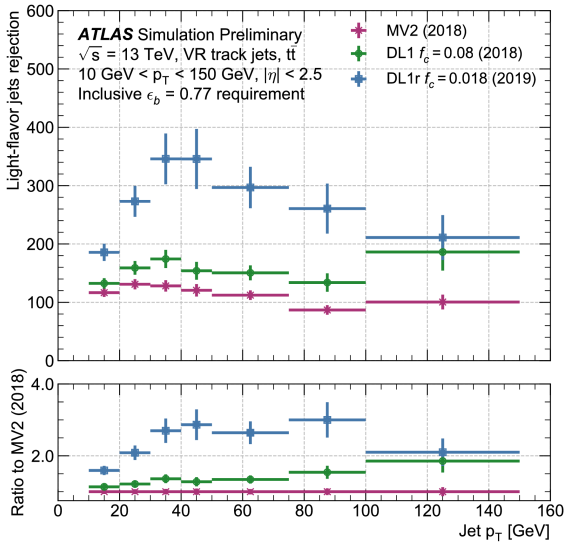

(c) light-jet rejection

Figure 4.10: *b*-tagging efficiency (a), *c*-jet rejection (b) and light-jet rejection (c) of the MV2, DL1 and DL1r taggers as function of VR track jet p_{T}, at the 77% *b*-tagging efficiency working point. In every figure, the lower panel shows the ratio to the MV2 distribution [70].

energy deposits (of the order of a few GeV). Being electrically charged, however, they are detectable as tracks in the inner detector (ID) and muon spectrometer (MS).

Several, often complimentary, muon reconstruction techniques have been developed at ATLAS [71]. The Boosted $H(\rightarrow b\bar{b}) +$ jet analysis uses the *combined muon* reconstruction, which exploits information gathered both from the ID and the MS. The reconstruction starts in the MS, where track candidates are built

from hit patterns in the detector layers. These tracks are then extrapolated and matched to track segments independently reconstructed in the ID. Finally, a combined track is built by performing a global refit to all associated ID and MS hits. During this procedure, MS hits may be added to or removed from the track to improve the fit quality.

A successive procedure called *muon identification* determines whether candidate tracks have likely been originated from a muon or by other background processes. In order to reject background "fake" muons, which mainly originate from π and K decays, a series of selections are recommended by the ATLAS Collaboration [72]. These include hit thresholds, geometrical and kinematic requirements, and use goodness-of-fit information.

The choice of a muon identification selection depends on the specific needs of an analysis in the compromise between muon efficiency and fake muon rejection. The Boosted $H(\to b\bar{b}) + \text{jet}$ analysis identifies muons using the *medium muon* selection, which is default at ATLAS and minimises the systematic uncertainties associated with muon reconstruction and calibration. The double b-tagging calibration described in Section 5.1 instead used the *loose muon* selection, which maximises muon reconstruction efficiency and, in turn, increases the $g \to b\bar{b}$ sample size.

Across the whole thesis, muons are also required to have $p_{\mathrm{T}} > 10$ GeV and $|\eta| < 2.4$. In some analysis regions muons are required to be isolated, namely to be well separated from other activity in the event. The isolation criteria define thresholds on the sums of track momentum ($\sum p_{\mathrm{T}}^{\mathrm{track}}$) and topo-cluster transverse energy ($\sum E_T^{\mathrm{topo}}$) in cones around the direction of the muon p_{T}. In the analysis, the *FixCutLoose* thresholds were used, which are summarised in Table 2 of Reference [72].

5

Identification of Boosted $H \to b\bar{b}$ Jets

Contents

5.1 Double b-tagger Calibration 77
5.2 Data and Simulated Samples 77
5.3 Event Selection 78
5.4 Flavour Fraction Correction 79
5.4.1 Flavour Fraction Templates 80
5.4.2 Template Merging 81
5.4.3 Template Fit 82
5.5 Systematic Uncertainties 85
5.5.1 Treatment of Uncertainties 86
5.6 Calibration Procedure 86
5.7 Results 88
5.8 Conclusions 89

The identification of Higgs bosons decaying to pairs of b quarks constitutes a fundamental part of the physics programme at the LHC. It allows physicists to investigate the properties of the relatively recently discovered Higgs boson, while at the same time searching for potential new resonances decaying to a b quark pair. Ultimately, this also represents the goal of the analysis described in this thesis: separating boosted $H \to b\bar{b}$ decays from the immense hadronic background that is mainly produced by QCD multijet processes and top quark decays.

As will be described in Chapter 6, the Boosted $H(\to b\bar{b}) + \text{jet}$ analysis uses

large-R jets to reconstruct potential high-momentum Higgs candidates, clustering their boosted decay products within their large radius. Their ultimate classification into signal and background categories is done by means of the MV2 b-tagging algorithm (see Section 4.2.1). A Higgs candidate large-R jet is required to be associated with at least two VR track jets, each being individually b-tagged by the MV2 algorithm at the 77% working point.

Due to potential mismodelling in simulated events, a b-tagger might have different performance when applied to data and MC. In the Boosted $H(\to b\bar{b}) + \text{jet}$ analysis, the MV2 data-to-MC corrections in the form of scale factors are individually applied to the two leading b-tagged VR track jets associated to a large-R jet, and their derivation was previously introduced in Section 4.2.1. The validity of this treatment is independently confirmed in high-p_{T} $g \to b\bar{b}$ and $Z(\to b\bar{b})\gamma$ events [73].

An ongoing effort within the ATLAS Collaboration is to provide a dedicated double b-tagging calibration using high-p_{T} $g \to b\bar{b}$ events. This chapter describes a preliminary version of the $g \to b\bar{b}$ calibration, which uses a MV2-based double b-tagger.

Due to rapid development in the flavour tagging group at ATLAS, the calibration has more recently switched its focus to a newly developed neural network-based b-tagging algorithm called the *Boosted $X \to b\bar{b}$ tagger*. By combining the high b-tagging performance for individual subjets offered by the DL1r algorithm and the knowledge of large-R jet kinematics, this new tagger is able to discriminate between large-R jets originating from Higgs bosons, QCD processes or top quarks. Appendix A describes the Boosted $X \to b\bar{b}$ tagger and provides a short summary of the main changes to the $g \to b\bar{b}$ calibration since its introduction.

During the development stage of the Boosted $H(\to b\bar{b}) + \text{jet}$ analysis, the double b-tagger calibration on $g \to b\bar{b}$ events was still far from completion. For this reason, the results presented in this chapter were not used at any point by the Boosted $H(\to b\bar{b}) + \text{jet}$ analysis and should be considered as standalone.

Author's Contributions The purpose of this chapter is to showcase the author's work as a service to the ATLAS Collaboration, i.e. the *Qualification Task* (QT). All results, excluding the treatment of uncertainties presented in Section 5.5, have been entirely produced by the author. The chapter captures the state of the $g \to b\bar{b}$ calibration at an early stage of development, at the time the author was part of the analysis team. More recent results, obtained by other members of the team after the end of the author's QT, are reported in Appendix A.

5.1 Double *b*-tagger Calibration

The MV2-based double b-tagger is calibrated *in-situ* using QCD multijet events collected by the ATLAS detector, where a gluon splits into two b quarks ($g \to b\bar{b}$). The aim of the calibration is to measure the tagger's performance in data and MC, and provide scale factors that can be used by other analyses to correct for deviations from the tagger's modelled response in simulated events.

The $g \to b\bar{b}$ calibration sample represents the largest source of boosted $b\bar{b}$ pairs registered by ATLAS, and allows for the calibration of the tagger up to very high transverse momenta, in a region where other channels (such as $Z(\to b\bar{b})\gamma$) do not provide enough events.

5.2 Data and Simulated Samples

The calibration uses the dataset collected by the ATLAS experiment in 2017 during the LHC Run 2 ($\sqrt{s} = 13$ TeV), corresponding to an integrated luminosity of 44.3 fb^{-1}. It was collected using a single small-R jet ($R = 0.4$) unprescaled trigger with a threshold of $p_{\mathrm{T}} > 380$ GeV. A primary vertex (PV) having at least two tracks with $p_{\mathrm{T}} > 0.5$ GeV is required [74]. In case an event has multiple PVs of this type, the one with the largest $\sum p_{\mathrm{T}}^2$ is considered.

The multi-jet MC samples used in this analysis are simulated using Pythia 8 [75], based on the data-taking conditions characterising the 2017 period (pileup and detector conditions, trigger menus, etc.). Two MC samples are used: an

inclusive sample dominated by light quark (u, d, s) final states, and a muon-filtered sample that requires at least one truth muon in the events, thus enhancing the fraction of heavy quark (c, b) final states. The truth muon is required to have $p_{\mathrm{T}} > 3$ GeV and $|\eta| < 2.8$.

Both data and MC samples are processed using release 21 (R21) of the ATLAS Athena software [76]. Detector effects are simulated using Geant 4 [77].

5.3 Event Selection

The calibration aims at selecting events where a gluon splits into a boosted pair of b quarks. High-p_{T} gluon splitting events are obtained by requiring the presence of at least one additional recoil jet in the event.

The event selection starts by requiring the jet that fired the trigger, or *trigger jet*, to be matched within $\Delta R < 0.4$ to a small-R calorimeter jet. Furthermore, events must have at least one $g \to b\bar{b}$ *candidate*, namely a large-R jet with $p_{\mathrm{T}} > 500$ GeV and $|\eta| < 2.0$, for which the small-R jet trigger is fully efficient and unbiased.

In events with high pileup, additional pp interaction vertices might be misinterpreted as secondary vertices generated by an in-flight decay of a heavy hadron. In order to reduce the extent of this contamination, a selection is applied to every track, requiring their transverse and longitudinal impact parameters to be $|d_0| < 5$ mm and $|z_0 sin(\theta)| < 3$ mm respectively[1].

The $g \to b\bar{b}$ candidate must also be ghost-associated with at least two VR track jets with $p_{\mathrm{T}} > 10$ GeV and $|\eta| < 2.5$. In the following, VR track jets associated to a large-R jet will be generally called *subjets*. In order to enrich the sample with $b\bar{b}$ jets, at least one of the subjets must be matched within $\Delta R < 0.2$ to a reconstructed muon with $p_{\mathrm{T}} > 10$ GeV and passing the loose quality requirements (see Section 4.3). Out of the selected subjets, two are used for the purpose of the calibration:

- **muon jet (j_{μ}^{trk}):** the leading p_{T} track jet associated to a muon,

[1]This selection is applied in addition to the standard ATLAS recommendations, which are described in Section 4.1.4.

- **non-muon jet ($j^{\text{trk}}_{\text{non}-\mu}$):** the leading p_{T} track jet amongst the remaining ones, regardless of muon association.

Finally, the trigger jet is required to be distant at least $\Delta R > 1.5$ from the muon jet to ensure independence between the two objects and a back-to-back topology. A schematic representation of the main characteristics of the events used in the calibration is shown in Figure 5.1.

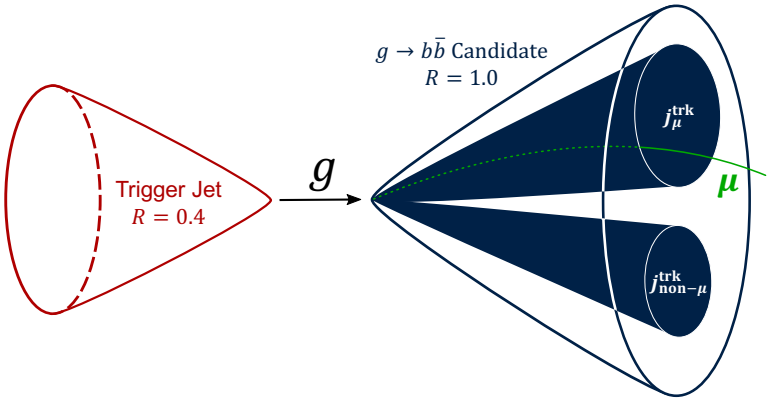

Figure 5.1: Diagram representing the event topology selected for the double b-tagger calibration.

5.4 Flavour Fraction Correction

The event selection described in the previous section aims at isolating events in which a gluon produces a $b\bar{b}$ pair in the final state. However, a number of QCD processes (e.g. gluons splitting to light-flavour quarks) can mimic the desired signature and it is thus important to determine the flavour composition of the selected sample in data. Since QCD multijet events are usually not reliably modelled by simulations, it is necessary to correct the flavour composition of the MC predictions to match the data.

Each candidate large-R jet can be labelled with two flavours, one carried by j^{trk}_{μ} and the other by $j^{\text{trk}}_{\text{non}-\mu}$. Three possible flavours are considered: a subjet could come from a b quark (B), from a c quark (C) or from a lighter quark (L). A $g \to b\bar{b}$

candidate can thus have a total of 9 possible di-flavour combinations, which are shown in Table 5.1. In the di-flavour labels, the j_μ^{trk} flavour is given first.

Table 5.1: The nine possible large-R jet di-flavour combinations. In the labels, the j_μ^{trk} flavour is given first.

		$j^{\text{trk}}_{\text{non}-\mu}$		
		B	**C**	**L**
j_μ^{trk}	**B**	BB	BC	BL
	C	CB	CC	CL
	L	LB	LC	LL

5.4.1 Flavour Fraction Templates

The MC flavour composition can be corrected by fitting the data with templates that are sensitive to the subjet flavour combination (flavour fraction). To this purpose, a particularly sensitive variable is the *signed transverse impact parameter* s_{d_0}, that for each track in a subjet is defined as

$$s_{d_0} = \frac{d_0}{\sigma(d_0)} s_j, \tag{5.1}$$

where d_0 is the transverse impact parameter of the track and $\sigma(d_0)$ is the resolution of the d_0 measurement. Considering a coordinate system originating from the primary vertex (PV), s_j is a sign indicating whether the d_0 vector lies on the same side of a plane perpendicular to the jet axis and passing through the PV, as the jet. In short, s_j is equal to $+1$ if the d_0 vector has a positive projection along the jet direction, and -1 otherwise. A visual representation of the s_{d_0} definition is shown in Figure 5.2.

The s_{d_0} value of a track is sensitive to its flavour for two reasons. Firstly, heavy flavour hadrons containing b quarks have a relatively long lifetime, giving them time to travel along the jet direction, thus leading to larger d_0 and positive s_j values. This results in a broader s_{d_0} spectrum with a larger positive tail. Tracks coming from lighter quarks, on the other hand, will have a narrower distribution, peaked around $s_{d_0} = 0$, and a width mainly dominated by the impact parameter resolution $\sigma(d_0)$. Additionally, it was observed [78] that hadrons with heavy flavour

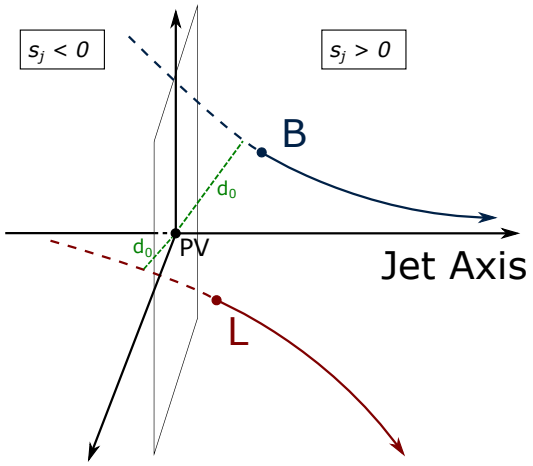

Figure 5.2: Diagram representing tracks coming from a b quark (B) and a light $u/d/s$ quark (L). The s_j sign is $+1$ when the vector representing the transverse impact parameter d_0 of a track has a positive projection along the jet direction, and -1 otherwise.

carry, on average, a larger fraction of the jet's p_{T} than light ones. Consequently, their decay products will be more likely boosted in the jet direction, leading to a larger positive tail in the s_{d_0} spectrum.

In the calibration, the mean s_{d_0} of the three highest-p_T tracks in a subjet ($\langle s_{d_0} \rangle$) is used as a template variable for correcting the MC flavour composition. By using this definition, the template variable is less sensitive to track mis-reconstruction and pileup. In order to increase the heavy flavour statistics, all templates containing B or C are obtained from the muon-filtered sample, while the inclusive sample is only used for producing the LL template.

5.4.2 Template Merging

When evaluated on MC samples, some flavour fractions constitute a very small percentage of the total. Since the BC, CB, LB and LC yields all contribute by less than 1%, they are merged with the flavour categories having the most similar $\langle s_{d_0} \rangle$ template shape: BC is merged into BL, CB into CL, LB and LC into LL. The shape similarity is evaluated using a χ^2 test statistic. This merging procedure produces five effective flavour fraction templates that can be used to fit the data: BB, BL, CC, CL and LL. Reducing the number of templates allows the fit to better constrain the different flavour fractions and to distinguish their shapes.

Figure 5.3 shows a comparison between the five normalised $\langle s_{d_0} \rangle$ templates obtained from simulation, both for j_μ^{trk} and $j_{\text{non}-\mu}^{\text{trk}}$. The previously described s_{d_0} behaviour can be assessed, with the heavy flavour jets showing wider distributions and a skew in the positive direction, and a narrower peak for light jets. Clearly, the different template shapes offer discrimination power between the various flavours. Noticeably, a slight skew in the positive direction is seen for the light jets, most probably due to the production of light long-lived particles, such as K or Λ.

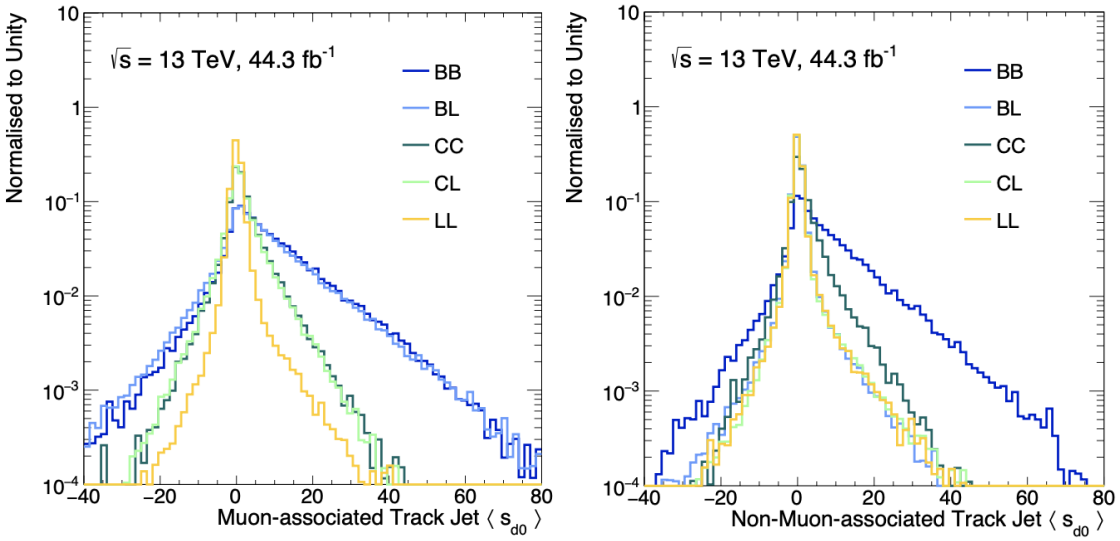

Figure 5.3: Mean impact parameter significance $\langle s_{d_0} \rangle$ distributions for the muon (left) and non-muon track jets (right) inclusive in $p_{\text{T}}(j_\mu^{\text{trk}})$ and $p_{\text{T}}(j_{\text{non}-\mu}^{\text{trk}})$. The double flavour labels denote the flavour of the subjet pair, with the j_μ^{trk} flavour given first.

5.4.3 Template Fit

The flavour composition in data is determined by performing a binned likelihood fit of the $\langle s_{d_0} \rangle$ distribution, simultaneously for j_μ^{trk} and $j_{\text{non}-\mu}^{\text{trk}}$. This is achieved by maximising the likelihood function defined as

$$\mathcal{L} = \prod_{i=1}^{n} p(y_i|\vec{\theta}), \tag{5.2}$$

where n is the number of bins being fitted, y_i is the number of data events populating bin i, and $\vec{\theta} \in \mathbb{R}^5$ is a vector denoting the number of events from every flavour

fraction component. The likelihood function is expressed as the product of individual Poisson probability terms $p(y_i|\vec{\theta})$ that, for each bin i, are defined as

$$p(y_i|\vec{\theta}) = \frac{e^{-\vec{\theta}\cdot\vec{x}_i}(\vec{\theta}\cdot\vec{x}_i)^{y_i}}{y_i!}, \tag{5.3}$$

where $\vec{x}_i \in \mathbb{R}^5$ is a vector whose components x_{ij} denote the ith bin value in the normalised $\langle s_{d_0} \rangle$ template for the jth flavour fraction. The goal of the fit is to find the $\vec{\theta}$ that maximises the likelihood function $\mathcal{L}$.

Since the flavour composition varies with momentum, all selected events are divided into three ranges of j_μ^{trk} p_{T} and four ranges of $j_{\text{non}-\mu}^{\text{trk}}$ p_{T}, within which the flavour fractions are not expected to vary drastically. This results in 12 j_μ^{trk}-$j_{\text{non}-\mu}^{\text{trk}}$ p_{T} bins, which are shown in Table 5.2. In each bin, the variable-size binning of the $\langle s_{d_0} \rangle$ templates is defined such that the relative statistical uncertainty in each bin is lower than 25%.

$\boldsymbol{j_\mu^{\text{trk}}}$	< 100 GeV	$100 < p_{\text{T}} < 200$ GeV	> 200 GeV	
$\boldsymbol{j_{\text{non}-\mu}^{\text{trk}}}$	< 100 GeV	$100 < p_{\text{T}} < 200$ GeV	$200 < p_{\text{T}} < 300$ GeV	> 300 GeV

Table 5.2: j_μ^{trk} and $j_{\text{non}-\mu}^{\text{trk}}$ p_{T} bins where the fit is independently performed.

The fit is performed independently in each bin using the MINUIT software [79], leading to an improvement in the data-to-MC agreement in all regions. Figure 5.4 shows the post-fit j_μ^{trk} and $j_{\text{non}-\mu}^{\text{trk}}$ $\langle s_{d_0} \rangle$ distributions in a representative p_{T} bin.

The validity of the procedure can further be assessed by observing the post-fit agreement for large-R jet variables of interest that are not explicitly used in the fit. Figure 5.5 shows the $g \to b\bar{b}$ candidate p_{T} distribution after the fit, inclusively in subjet p_{T}. The hatched band represents the total post-fit uncertainty on the model, inclusive of the fit and systematic uncertainties (see Section 5.5).

Outputs of the fit procedure are the *correction factors* c_f^r, one for each flavour fraction f and p_{T} bin r. These best estimates are used to renormalise the initial flavour fractions extracted from MC, in preparation for the calibration procedure described in Section 5.6. For variables of interest that are inclusive in j_μ^{trk}-$j_{\text{non}-\mu}^{\text{trk}}$ p_{T}, their distributions are obtained by adding up the contributions of each p_{T} bin, with flavour fractions appropriately renormalised by the corresponding c_f^r.

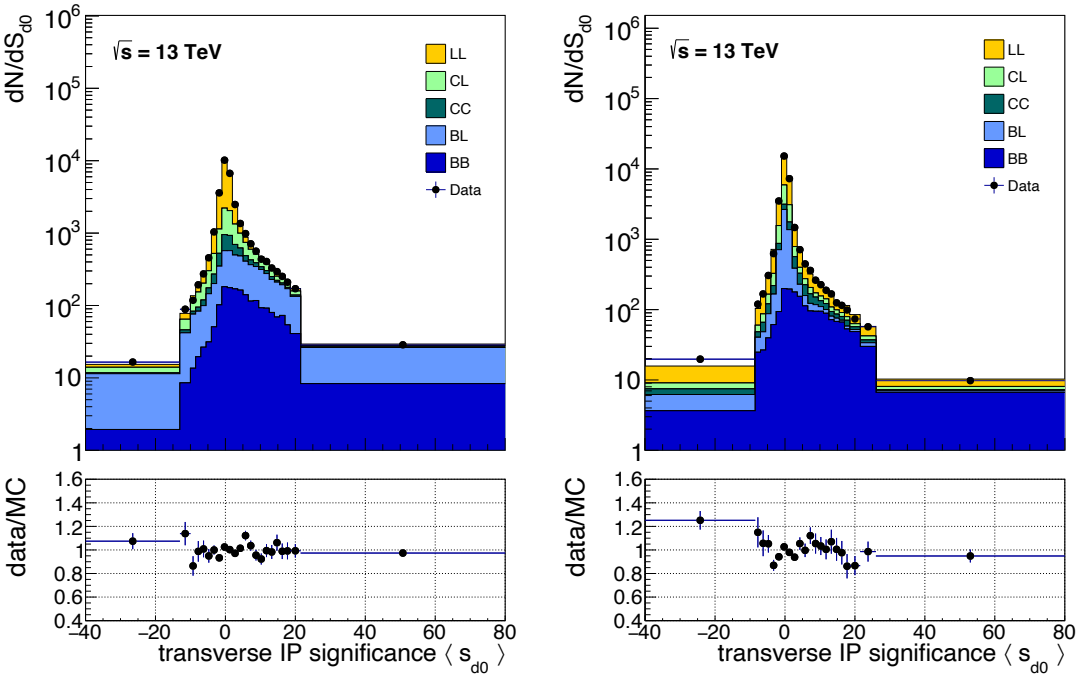

Figure 5.4: Post-fit j_{μ}^{trk} (left) and $j_{\mathrm{non}-\mu}^{\mathrm{trk}}$ (right) $\langle s_{d_0} \rangle$ distributions in the p_{T} bin $p_{\mathrm{T}}(j_{\mu}^{\mathrm{trk}}) > 200$ GeV, $100 < p_{\mathrm{T}}(j_{\mathrm{non}-\mu}^{\mathrm{trk}}) < 200$ GeV.

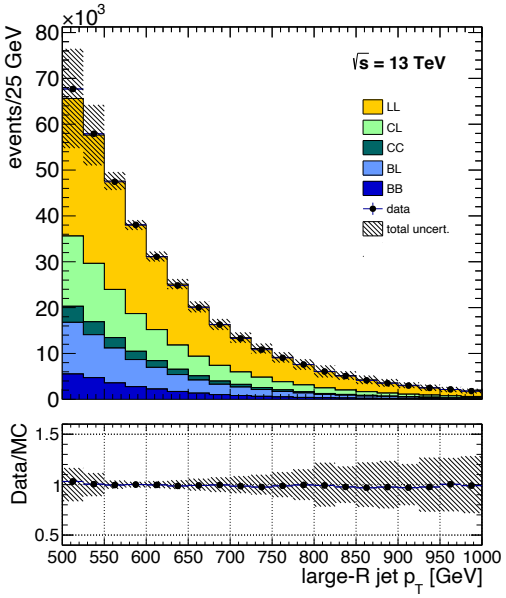

Figure 5.5: $g \to b\bar{b}$ candidate post-fit p_{T} distribution. The hatched band represents the total post-fit uncertainty on the model.

5.5 Systematic Uncertainties

In this section, the main sources of systematic uncertainty affecting the calibration are summarised. They are divided into three main categories: *large-R jet uncertainties*, *flavour tagging uncertainties* and *modelling uncertainties*. Large-R jet uncertainties are provided by the calibrations introduced in Section 4.1.3. These most notably include jet energy scale and resolution and jet mass scale and resolution systematics. Flavour tagging uncertainties, including those on the b-tagging efficiency, c-jet and light-jet rejection, are obtained from the calibrations described in Section 4.2.1. Modelling uncertainties quantify the incomplete knowledge of complex processes that are particularly challenging to model using MC simulations. In the remainder of this section, the main modelling uncertainties affecting the calibration are summarised.

Some processes, like photon conversions, hadronic material interactions, and light long-lived particles such as K or Λ, can produce displaced vertices and tracks with non-trivial transverse impact parameters, that are particularly difficult to model. Following the results of the light-jet mistagging calibration [66], uncertainties are estimated by weighting events containing tracks from photon conversions and hadronic material interactions by an additional $\pm 10\%$, and tracks from light long lived particle decays by an additional $\pm 30\%$.

The resolution of the track transverse impact parameter d_0, denoted $\sigma(d_0)$, is difficult to model and depends on the track momentum. At high-p_{T}, it is largely determined by the intrinsic position resolution and alignment of the ID sensors. At sufficiently low p_{T}, it is instead dominated by the effects of multiple scattering and it is thus sensitive to the amount of material in the ID. Accurate measurements of $\sigma(d_0)$ are performed from minimum-bias, di-jet and Z + jets events in bins of track p_{T} and η [80]. A systematic uncertainty is introduced to account for discrepancies between data and simulations.

The modelling of the parton shower development is known to be strongly dependent on the MC program used to simulate it. The systematic uncertainty related to the choice of the PS generator is derived comparing the nominal Pythia 8

sample to one simulated using the alternative HERWIG++ [81] generator. The parton shower uncertainty is not included in the results presented in this chapter as the alternative sample was not yet available at the time the studies were performed.

5.5.1 Treatment of Uncertainties

Fit uncertainties account for intercorrelations between the different flavour fractions, and they are estimated by means of a pseudo-experiment method. In each of these experiments, a new set of correction factors c_f^r is obtained by varying their best fit values by a Gaussian-distributed random variable which is bound by the eigenvalues and eigenvectors of the fit covariance matrix. This process is repeated 2000 times and, for every variable of interest, as many varied distributions are obtained, each corresponding to a different set of correction factors. For each variable of interest, a bin-by-bin distribution of pulls can be obtained by taking the difference between each experiment and the nominal distribution. The extent of the fit uncertainty in each bin can finally be estimated by the standard deviation of a Gaussian fit to the corresponding pull distribution.

Systematic uncertainties are estimated by repeating the fit on alternative samples, thus obtaining a new set of correction factors. For any variable of interest, the bin-by-bin difference between the nominal distribution and the one obtained with the alternative c_f^r set represents the extent of the corresponding systematic uncertainty. For any variable of interest, the total systematic uncertainty is obtained by summing in quadrature the individual contributions coming from the various systematic sources. This approach is clearly limited, as it does not correctly account for correlations between the systematic sources. For this reason, the systematic uncertainty on the fit results presented in this chapter should be treated as an indication, more than a definitive estimate.

5.6 Calibration Procedure

After the fit procedure is performed and the MC distributions are renormalised by the correction factors c_f^r, the calibration of the b-tagger can finally be carried out.

Prerequisite to the calculation of the scale factors is the double b-tagging efficiency $\epsilon_{b\bar{b}}$, defined both in data and simulations. For MC this is quite straightforward, since the truth information allows for the computation of both terms in the ratio

$$\epsilon_{b\bar{b}}^{\mathrm{MC}} = \frac{N_{\mathrm{BB,\,tag}}^{\mathrm{MC}}}{N_{\mathrm{BB}}^{\mathrm{MC}}}, \tag{5.4}$$

where N_{BB}^{MC} is the number of selected $g \to b\bar{b}$ candidates with BB truth flavour, while $N_{\mathrm{BB,\,tag}}^{MC}$ is the number of these that also pass the double b-tagging requirement.

A problem arises in data, where the true flavour of the selected candidates cannot be known a priori. Thus, the BB fraction used in the definition of $\epsilon_{b\bar{b}}^{\mathrm{data}}$ is estimated by making two assumptions:

1. That the BB component in data is accurately predicted by the fit of the flavour fractions.

2. That the effect of mismodelling of the mistag rate is negligible.

The second assumption simply implies that, after b-tagging, the non-BB components in data and MC are the same, and thus the difference in tagging is only in the BB fraction. This is a safe assumption if the non-BB component makes up such a small fraction after double b-tagging that its mismodelling cannot have a significant impact.

Using these assumptions, the double b-tagging efficiency in data can be measured as

$$\epsilon_{b\bar{b}}^{\mathrm{data}} = \frac{N_{\mathrm{BB,\,tag}}^{\mathrm{data}}}{N_{\mathrm{BB}}^{\mathrm{data}}} \approx \frac{N_{\mathrm{tag}}^{\mathrm{data}} - N_{\mathrm{bkg,\,tag}}^{\mathrm{MC(corr.)}}}{N_{\mathrm{BB}}^{\mathrm{MC(corr.)}}}, \tag{5.5}$$

where $N_{\mathrm{tag}}^{\mathrm{data}}$ is the number of double b-tagged candidate large-R jets in data, $N_{\mathrm{bkg,\,tag}}^{\mathrm{MC(corr.)}}$ is the number of double b-tagged non-BB jets in MC after the flavour correction and $N_{\mathrm{BB}}^{\mathrm{MC(corr.)}}$ is the number of large-R jet candidates with truth BB labelling in MC after flavour correction.

In every p_{T} bin, the double b-tagging efficiencies in data and MC can finally be combined into the scale factors $k_{b\bar{b}}$ by using

$$k_{b\bar{b}} = \frac{\epsilon_{b\bar{b}}^{\mathrm{data}}}{\epsilon_{b\bar{b}}^{\mathrm{MC}}}. \tag{5.6}$$

5.7 Results

Figure 5.6 shows the muon jet and non-muon jet p_{T} distributions after double b-tagging. As the pre-tag distributions were flavour corrected, the post-tag discrepancy between data and MC is assumed to be caused by a different double b-tagging response. It is also noted that post-tag events are dominated by $b\bar{b}$ events, with much smaller contributions coming from lighter flavours. Both plots indicate a slight deterioration in the data-to-MC agreement at high subjet p_{T}.

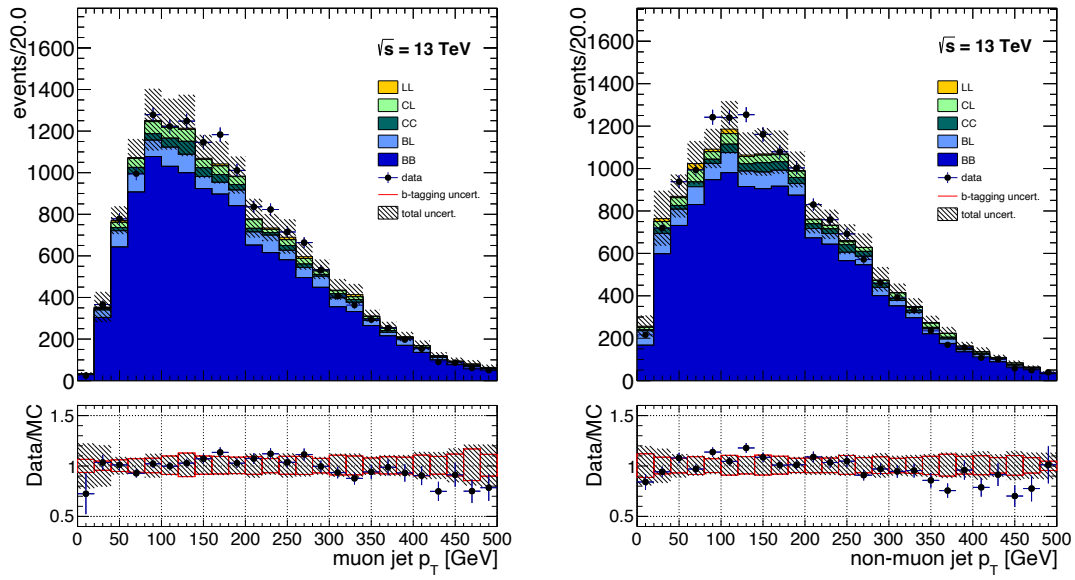

Figure 5.6: Muon jet (left) and non-muon jet (right) p_{T} distributions after double b-tagging. The hatched bands represent the total post-fit uncertainty on the models.

One possible reason for this effect is that, at the time these studies were performed, the double b-tagging calibration on $g \to b\bar{b}$ events used a version of the MV2 tagger that was trained and calibrated on small-R ($R = 0.4$) jets. Therefore, when applied to the narrower VR track jets used in the calibration, the MV2 algorithm's performance might degrade. Furthermore, the MV2 tagger was calibrated on isolated small-R jets, which is a different topology from the high-density final states probed by the $g \to b\bar{b}$ calibration.

It must be stressed, however, that the uncertainty estimation at this early stage of the calibration was quite rudimentary and it lacked the dominant parton shower

contribution. Previous studies performed on a smaller dataset and using an older ATLAS software release showed that the contribution of modelling systematics can be quite large at high-p_{T}, covering the discrepancy observed in post-tag results [73].

Figure 5.7 shows the preliminary scale factors and their corresponding uncertainty, in each j_{μ}^{trk}-$j_{\mathrm{non}-\mu}^{\mathrm{trk}}$ p_{T} bin. All values are seen to lie within 2σ from 1. As previously mentioned, the uncertainty estimation lacks the dominant parton shower contribution, and it should only be taken as an indication.

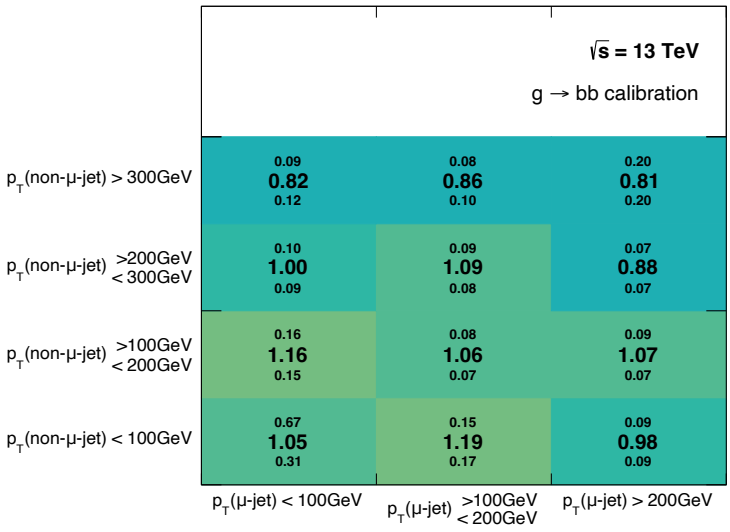

Figure 5.7: Preliminary $g \to b\bar{b}$ calibration scale factors for the MV2-based double b-tagger, calculated in j_{μ}^{trk}-$j_{\mathrm{non}-\mu}^{\mathrm{trk}}$ p_{T} bins.

5.8 Conclusions

The studies and results presented in this chapter describe the MV2-based double b-tagger calibration using $g \to b\bar{b}$ events at a rather early development stage. In all j_{μ}^{trk}-$j_{\mathrm{non}-\mu}^{\mathrm{trk}}$ p_{T} bins, the post-tag $\langle s_{d_0} \rangle$ distributions are seen to be quite well modelled and the extracted scale factor values lie within 2σ from 1. Despite this, further work is needed in order to correctly integrate systematic uncertainties in the fit procedure and to potentially improve the post-tag modelling of the $\langle s_{d_0} \rangle$ distributions.

More recently, the analysis team updated the double b-tagging algorithm to the more sophisticated Boosted $X \to b\bar{b}$ tagger, and the calibration procedure has

been considerably updated. A summary of the latest developments is presented in Appendix A.

Due to the preliminary nature of the $g \to b\bar{b}$ calibration at the time the Boosted $H(\to b\bar{b}) + \text{jet}$ analysis was developed, the results obtained in this chapter are not used in the rest of this thesis. Future iterations of the analysis will take advantage of a fully calibrated double b-tagger, improving the identification of Higgs boson decays to $b\bar{b}$.

6
Experimental Setup

Contents

6.1 Datasets and Trigger Strategy 93
6.2 Simulated Samples 95
6.3 Event Selection and Classification 96
6.3.1 Signal and Validation Regions 98
6.3.2 $t\bar{t}$ Control Region 100
6.3.3 W Control Region from $t\bar{t}$ Events 102
6.4 Analysis Strategy 103
6.4.1 Measurements 104
6.4.2 Blinding Strategy 107
6.4.3 Fitting Procedure 108
6.4.4 Asimov Datasets 110

The end goal of the analysis presented in this thesis is measuring the production rate of the Higgs boson decaying to a $b\bar{b}$ pair, inclusively in production mode. Despite the large BR of the targeted final state, recording such events and separating them from the background is a very challenging endevour. Being all-hadronic in nature, the $b\bar{b}$ final state is vastly dominated by background processes (mainly QCD multijet ones) with several orders of magnitude larger cross-sections.

The general strategy of the ATLAS trigger system for limiting the acquisition of hadronic background bandwidth is to set high p_{T} thresholds on jet triggers. This effectively determines a minimum mass limit on dijet resonances that is much

higher than the 125 GeV Higgs mass [82], rendering the measurement impossible in this resolved channel.

For this reason, the analysis presented in this work addresses the issue by measuring the Higgs boson at high p_{T} (i.e. in the boosted channel). The large momentum boost is obtained by requiring the Higgs to recoil against an additional jet in the event ($H(\rightarrow b\bar{b}) + \text{jet}$). As a result, the Higgs decay products are highly collimated and can be reconstructed inside a single large-R jet. This results in di-jet events that can be triggered either on the Higgs jet or on the recoil jet, giving the analysis sensitivity to the Higgs mass region.

In order to correctly interpret the collected data and perform the Higgs measurement, a theoretical model of the signal and background processes is needed, as predicted in the SM. In particle physics this is done using Monte Carlo generators (see Section 3.3), which are used to estimate the expected kinematic distributions for the Higgs and for many of the backgrounds inhabiting the analysis phase space.

Once data are collected and simulated samples are produced, a series of kinematic cuts are applied to all events in order to select the target topology and phase space. Further selections are used to classify events into different regions, each having a specific purpose in the extraction of the final analysis result.

This section describes the experimental setup of the analysis. Sections 6.1 and 6.2 explain how data are collected and simulated samples are produced. Section 6.3 continues by showcasing the event selections and classification into analysis regions. Finally, Section 6.4 describes the analysis strategy, namely the measurements' setup, the blinding strategy and the fitting procedure.

Author's Contributions In this chapter, Sections 6.1 and 6.2 detail the analysis and simulation requirements that follow from ATLAS triggering and MC strategies. The event selection described in Section 6.3 was largely inherited from a preliminary version of the analysis. The author contributed to the definition of the fiducial and differential measurements (Section 6.4.1) and was responsible for extending the analysis and fit software to implement these more complex measurements, which was

a significant undertaking and amount of software development. Additionally, the validation of these fits and evaluation of the expected performance was performed by the author. This included a full re-validation of the entire analysis fit setup following an underlying fix to the RooFit software that motivated a change in binning strategy.

6.1 Datasets and Trigger Strategy

The analysis showcased in this work uses the full pp collision dataset collected by the ATLAS experiment during Run 2, which spans the years from 2015 to 2018. During this period, the LHC delivered pp collisions with centre-of-mass energy $\sqrt{s} = 13$ TeV.

Since the ATLAS detector does not always operate at full performance, a few per cent of recorded data is not usable for physics analyses and must be rejected. This is done using Good Run Lists (GRLs), a database collecting collision events that satisfy certain detector performance criteria [30].

Data is collected using the logical OR of several unprescaled single large-R jet triggers. They are passed if at least one large-R jet reconstructed in the event satisfies certain kinematic requirements. The p_{T} and mass thresholds are different for each trigger in order to adapt to the changing LHC machine conditions over the years, such as different instantaneous luminosity profiles and the inclusion of pileup suppression techniques within the data acquisition system [83].

Table 6.1 summarises the triggers used in the analysis for each data taking year, their thresholds and the integrated luminosity of the collected samples. Whenever multiple triggers are listed for a given year, all of them were required to be active and at least one had to be passed. It is interesting to note that the p_{T} thresholds had to rise over the years to maintain trigger rates and account for the changing conditions of the LHC machine. Due to the steeply falling nature of the jet p_{T} spectrum, however, such an increase would strongly reduce the number of collected events, negatively impacting the analysis sensitivity. For this reason, since 2017, a mass requirement has been introduced, allowing for a relaxation of the jet p_{T} requirement, while keeping the rates within the allocated trigger bandwidth.

For simplicity, a common offline selection requiring $p_{\mathrm{T}} > 450$ GeV and m > 60 GeV is applied to the trigger jet for any large-R jet trigger. After removing collisions with bad detector performance, the main dataset used in the analysis corresponds to a total luminosity of 136 fb^{-1}. This value is lower than the nominal 139 fb^{-1} of data collected by ATLAS and usable for physics during Run 2. The reason is that the large-R jet triggers used by the analysis to collect data in 2017 were not active for the whole data-taking period, thus resulting in an integrated luminosity loss of around 3 fb^{-1}.

Additionally, muon triggers are used to collect two full Run 2 datasets, orthogonal to the one introduced above. Events collected in this way are used to populate two control regions, $\mathrm{CR}_{t\bar{t}}$ and $\mathrm{WCR}_{t\bar{t}}$, whose definition and purpose are detailed in Sections 6.3.2 and 6.3.3, respectively. Table 6.2 summarises the muon triggers used in the analysis for each data taking year, the muon trigger thresholds and integrated luminosity of the collected samples. Whenever multiple triggers are listed for a given year, at least one of them had to be passed.

Table 6.1: List of single large-R jet triggers used in the analysis. For each trigger the data taking year, the kinematic thresholds and the integrated luminosity of the collected samples are shown. Whenever multiple triggers are listed for a given year, all are required to be active at the same time and at least one must be passed. The last two 2018 triggers (*) have the same thresholds, but different L1 signatures. They are not required to be active at the same time.

Year	Threshold	Luminosity
2015	$p_{\mathrm{T}} > 360$ GeV	3.2 fb^{-1}
2016	$p_{\mathrm{T}} > 420$ GeV	33.0 fb^{-1}
2017	$p_{\mathrm{T}} > 440$ GeV	41.2 fb^{-1}
	$p_{\mathrm{T}} > 390$ GeV, $m > 30$ GeV	41.0 fb^{-1}
2018	$p_{\mathrm{T}} > 460$ GeV	58.5 fb^{-1}
	$p_{\mathrm{T}} > 420$ GeV, $m > 35$ GeV	58.5 fb^{-1*}
	$p_{\mathrm{T}} > 420$ GeV, $m > 35$ GeV	55.4 fb^{-1*}

Table 6.2: List of muon triggers used to collect data populating the $CR_{t\bar{t}}$ and $WCR_{t\bar{t}}$ regions. For each trigger the data taking year, the kinematic thresholds and the integrated luminosity of the collected samples are shown. Whenever multiple triggers are listed for a given year, at least one of them must be passed.

Region	Year	Threshold	Luminosity
$CR_{t\bar{t}}$	All Years	$p_{\mathrm{T}}^{\mu} > 50$ GeV	136.0 fb^{-1}
$WCR_{t\bar{t}}$	All Years	$p_{\mathrm{T}}^{\mu} > 50$ GeV	139.0 fb^{-1}
	2015	$p_{\mathrm{T}}^{\mu} > 20$ GeV	
	2016–2018	$p_{\mathrm{T}}^{\mu} > 26$ GeV	

6.2 Simulated Samples

This section summarises the MC generators used to simulate events in the analysis.

Higgs events are simulated considering the four main production processes: gluon-gluon-fusion (ggF), vector boson fusion (VBF), associated production with a vector boson (VH) and associated production with a $t\bar{t}$ pair ($t\bar{t}$H). Higgs boson ggF production events are generated at next-to-leading-order (NLO) accuracy in QCD using Powheg-Box v2 [84–86] and the Hj+MiNLO [87–89] prescription. NLO accuracy in QCD for VBF and $t\bar{t}$H production and LO accuracy for $gg \to VH$ production is achieved using the Powheg-Box v2 [84–86, 90, 91] program. The $qq \to VH$ process is simulated at NLO accuracy in QCD using Powheg-Box v2, the MiNLO calculation [92] and the GoSam program [93]. All Higgs events are generated using the NNPDF3.0 [94] set of parton distribution functions (PDFs). Corrections for NLO electroweak (EW) effects are applied as a function of the generated Higgs boson transverse momentum for VBF, VH, and $t\bar{t}$H production. The Higgs boson production cross-sections are taken from Reference [95][1]. The parton shower development of all Higgs events is simulated using Pythia 8.2 [75] with the AZNLO tune [96].

Production of V+jets events with hadronic boson decays and subsequent parton shower development are simulated with Sherpa 2.2.8 [97] to NLO QCD accuracy

[1] A scale factor is applied to $t\bar{t}$H events to match the cross-section value reported in the reference.

for one additional parton and LO QCD accuracy for up to four additional partons. As shall be discussed in Section 7.4.1, V + jets events are corrected by NLO EW and NNLO QCD corrections. The former are applied as internal weights in the MC samples, while the latter are provided externally and are applied as multiplicative factors to the final results. Production of $W(\ell\nu)$ + jets events is simulated with Sherpa 2.2.1. All V + jets events are generated using the NNPDF3.0 PDF set.

The production of top anti-top quark pairs ($t\bar{t}$), associated production of a top quark and a W boson (tW), and single top quark t- and s-channel production are modelled using Powheg-Box v2 at NLO accuracy in QCD. In order to account for interference and overlap with $t\bar{t}$ production, the tW sample is produced using the diagram subtraction scheme [98]. In order to model the parton shower development, top quark events are interfaced to Pythia 8.2 with the A14 tune [99] and the NNPDF2.3 [100] PDF set.

Although the QCD multijet background modelling is performed on data (see Section 7.2), simulated QCD dijet events are used to develop the background estimation method. They are generated using Pythia 8.2 with the A14 tune and the NNPDF2.3 PDF set.

All simulated events are run through the full ATLAS detector simulation and reconstruction chain using Geant4 [77, 101]. Pileup is modelled by overlaying the hard-scatter event with inelastic pp collision events generated with Pythia 8.2 using the NNPDF2.3 set of PDFs and the A3 tune [102].

6.3 Event Selection and Classification

At parton level, most signal signatures considered in the analysis are characterised by the production of two primary particles with similar momentum. In the ggF case, for example, a Higgs boson and a QCD recoil object, like a quark or a gluon, are produced back-to-back. During decay and hadronisation, however, several processes such as final state radiation, jet measurement resolution, out of jet-cone activity and semi-leptonic b- and c-hadron decays might alter the p_{T} ordering of the resulting jets.

Table 6.3: The generators used for the simulation of the signal and background processes. Matrix element, parton shower and underlying event are abbreviated as ME, PS, and UE respectively.

Process	ME generator	ME PDF	PS and hadronization	UE model tune	Cross-section order
Higgs Boson					
$gg \to H \to b\bar{b}$	Powheg-Box v2 + MiNLO	NNPDF3.0nnlo	Pythia 8.212	AZNLO	NLO(QCD) + LO(EW)
$qq \to H \to q'q'b\bar{b}$	Powheg-Box v2	NNPDF3.0nlo	Pythia 8.230	AZNLO	NLO(QCD) + NLO(EW)
$qq \to WH$ $\to qq'b\bar{b}$ $\to \ell\nu b\bar{b}$	Powheg-Box v2 + GoSam + MiNLO	NNPDF3.0nlo	Pythia 8.240 Pythia 8.212	AZNLO	NNLO(QCD) + NLO(EW)
$qq \to ZH$ $\to q\bar{q}b\bar{b}$ $\to \nu\nu b\bar{b}$ $\to \ell\ell b\bar{b}$	Powheg-Box v2 + GoSam + MiNLO	NNPDF3.0nlo	Pythia 8.240 Pythia 8.212	AZNLO	NNLO(QCD) + NLO(EW)
$gg \to ZH$ $\to q\bar{q}b\bar{b}$ $\to \nu\nu b\bar{b}$ $\to \ell\ell b\bar{b}$	Powheg-Box v2	NNPDF3.0nlo	Pythia 8.240 Pythia 8.212	AZNLO	LO + NLL(QCD)
$gg \to ttH$ $tt \to$ all $H \to$ all	Powheg-Box v2	NNPDF3.0nlo	Pythia 8.230	AZNLO	NLO(QCD) + NLO(EW)
Vector boson + jets					
$W \to qq$ $Z \to qq$	Sherpa 2.2.8	NNPDF3.0nnlo	Sherpa 2.2.8	Default	NNLO(QCD) approx NLO(EW)
Top quark, mass set to 172.5 GeV					
$t\bar{t} \to$ all	Powheg-Box v2	NNPDF3.0nlo	Pythia 8.230	A14	NNLO+NNLL
tW	Powheg-Box v2	NNPDF3.0nlo	Pythia 8.230	A14	NLO
t t-channel	Powheg-Box v2	NNPDF3.0nlo	Pythia 8.230	A14	NLO
t s-channel	Powheg-Box v2	NNPDF3.0nlo	Pythia 8.230	A14	NLO
Multijet					
Dijets	Pythia 8.230	NNPDF2.3lo	Pythia 8.230	A14	LO

Because of the targeted $b\bar{b}$ decay, the Higgs jet is generally more likely than the recoil object to contain semi-leptonic b-hadron decays, which could bias its kinematic properties due to escaping leptons or neutrinos. Furthermore, because of its three-body nature, the $t\bar{t}$H signal process is more likely to give raise to sub-leading Higgs jets.

Studies performed on a simulated ggF sample show that in nearly 50% of the events the sub-leading large-R jet is originated by the Higgs. Hence the need in the analysis to consider either the leading or subleading jet as a potential signal candidate.

This section describes the event selection and classification used to define the analysis regions. These are a set of signal regions (SR), where the Higgs measurements are performed, validation regions (VR), where the QCD and V + jets

models are trained and tested, and two control regions ($CR_{t\bar{t}}$ and $WCR_{t\bar{t}}$), where an accurate determination of the $t\bar{t}$ background and of the $W+$jets mass resolution are performed.

6.3.1 Signal and Validation Regions

In order to enter the SR or VR, a common selection is initially applied both to data and MC events. Firstly, events are required to pass any of the large-R triggers described in Section 6.1. In order to ensure full trigger efficiency across the whole phase space, an offline selection is applied, requiring at least one large-R jet to have $p_{\mathrm{T}} > 450$ GeV and $m > 60$ GeV. The presence of at least two large-R jets with $p_{\mathrm{T}} > 200$ GeV is required in each event. Finally, either the leading or sub-leading jet must pass a *candidate jet* selection, which applies some kinematic and quality requirements that characterise a Higgs jet. A candidate jet must have $p_{\mathrm{T}} > 250$ GeV, $m > 60$ GeV, $|\eta| < 2$, it must be boosted ($2m/p_{\mathrm{T}} < 1$) and it must be ghost-associated (see Section 4.1.5) to at least two VR track jets with $p_{\mathrm{T}} > 10$ GeV passing the overlap cleaning requirement (see Section 4.1.4).

Events satisfying this initial selection are then divided into signal (SRL, SRS) and validation (VRL, VRS) regions based on the following criteria:

- **SRL:** the leading p_{T} jet is a candidate jet with two b-tagged subjets,
- **SRS:** the sub-leading p_{T} jet is a candidate jet with two b-tagged subjets (and the leading jet is not),
- **VRL:** the leading p_{T} jet is a candidate jet with zero b-tagged subjets (and the sub-leading jet either has the same distinction or it is not a candidate jet),
- **VRS:** the sub-leading p_{T} jet is a candidate jet with zero b-tagged subjets (and the leading jet either has the same distinction or it is not a candidate jet).

The double b-tagging requirement is carried out using the MV2c10 algorithm at the 77% efficiency WP. Here and in the following, MV2c10 b-tagging scale factors

obtained from a calibration on VR track jets are applied individually to the two leading b-tagged subjets associated to the candidate jet.

Double b-tagging is the main discriminant between signal and validation regions in the event classification. In the first, candidate jets are required to pass double b-tagging in order to target $H \to b\bar{b}$ events specifically. Conversely, since validation regions are intended for testing the QCD[2] and V + jets models, they are rendered independent from the SR by means of an anti-b-tagging requirement. In the VR, events where both the leading and sub-leading jets are candidate jets represent kinematically appropriate probes of the SR backgrounds. For this reason, they are used to populate both the VRL and VRS.

The diagram in Figure 6.1 depicts the SR and VR categorisation criteria described in this section.

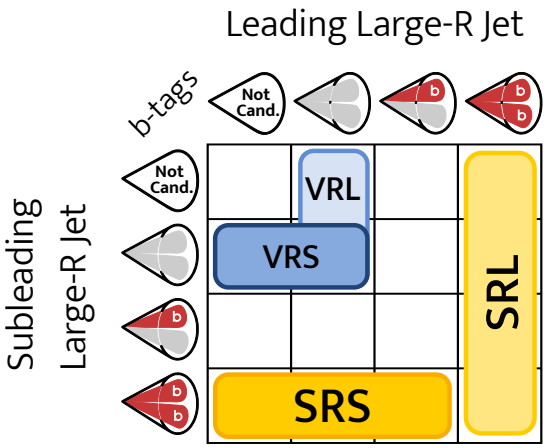

Figure 6.1: Schematic representation of the event categorisation criteria [1].

As shall be explained later in the chapter, the analysis performs Higgs measurements both inclusively and differentially in candidate jet p_{T}. For this reason, the signal regions are split into several reconstructed jet p_{T} ranges: $250 < p_{\mathrm{T}} < 450$ GeV (SRx0), $450 < p_{\mathrm{T}} < 650$ GeV (SRx1), $650 < p_{\mathrm{T}} < 1000$ GeV (SRx2), $p_{\mathrm{T}} > 1000$ GeV (SRx3), with $x = \mathrm{L}, \mathrm{S}$. For the leading jet, no region below 450 GeV (SRL0) is defined, being below the kinematic requirements of the event selection. On the

[2]The QCD multijet mass distribution is modelled using a polynomial function. The polynomial order is optimised on subsets of VR data that are corrected to be kinematically and statistically equivalent to the SR (see Section 7.2.2).

other hand, the sub-leading region above 1 TeV (SRS3) is not considered as it is found to yield insufficient Higgs sensitivity due to low statistics.

As the VR is used to validate the analysis strategy and background models in every configuration, an equivalent classification is applied to the VR. Correspondingly, an analogous naming scheme is used: VRLi for $i = (1, 2, 3)$ and VRLj for $j = (0, 1, 2)$.

6.3.2 $t\bar{t}$ Control Region

The top anti-top pair production process ($t\bar{t}$) represents the second most important background source in the SR, after QCD multijet events. In the high-p_{T} regime studied by the analysis, however, the $t\bar{t}$ process is subject to various modelling uncertainties [103, 104]. In order to obtain a more precise estimate, the $t\bar{t}$ background is thus determined directly on data, in a dedicated control region ($\mathrm{CR}_{t\bar{t}}$), orthogonal to the SR and VR.

The $\mathrm{CR}_{t\bar{t}}$ event selection aims at selecting $t\bar{t}$ events where one top quark decays hadronically and the other leptonically (semi-leptonic decay). Since the top quark decays almost exclusively to a Wb pair, both top quarks in the event result in large-R jets containing at least one b-hadron. While one jet is completely hadronic, however, the other is characterised by the presence of an isolated lepton and missing transverse energy from the leptonic decay of the W boson. This clear experimental signature is used to select a high-purity $t\bar{t}$ sample, orthogonal to the SR and VR, where the top quark background can be measured accurately.

Data are collected using the muon trigger introduced in Section 6.1, and full trigger efficiency is ensured by requiring the trigger muon to have a $p_{\mathrm{T}} > 52.5$ GeV. Selected events must have at least two large-R jets with $p_{\mathrm{T}} > 250$ GeV and $|\eta| < 2$. The *tag-jet*, a large-R jet built around the b quark from the leptonic top quark decay, is identified by requiring the following selection:

- it must be one of the two leading jets in the event,
- it must be ΔR-associated to the trigger muon: $\Delta R(\mu, \text{tag-jet}) < 1.5$,

- it must be ghost-associated to at least 1 VR track jet with $p_{\mathrm{T}} > 10$ GeV passing overlap cleaning,
- exactly one among up to two leading associated VR track jets is required to be b-tagged (MV2c10, 77% WP).

The large-R jet from the top quark hadronic decay, or *probe-jet*, is instead identified using the following selection:

- it must be one of the two leading jets in the event,
- it must be ghost-associated to at least 3 VR track jets with $p_{\mathrm{T}} > 10$ GeV passing overlap cleaning,
- exactly 1 VR track jet (among the leading three) must be b-tagged,
- it must be distant from the tag-jet by at least $\Delta\phi(\text{probe-jet}, \text{tag-jet}) > \frac{2\pi}{3}$.

The reason for requiring 3 VR track jets is to ensure a fully-contained top quark decay within the probe-jet radius. Furthermore, the $\Delta\phi$ cut helps reducing background contamination from QCD multijet and $V+$jets processes. A schematic representation of the $\mathrm{CR}_{t\bar{t}}$ event selection criteria is given in Figure 6.2.

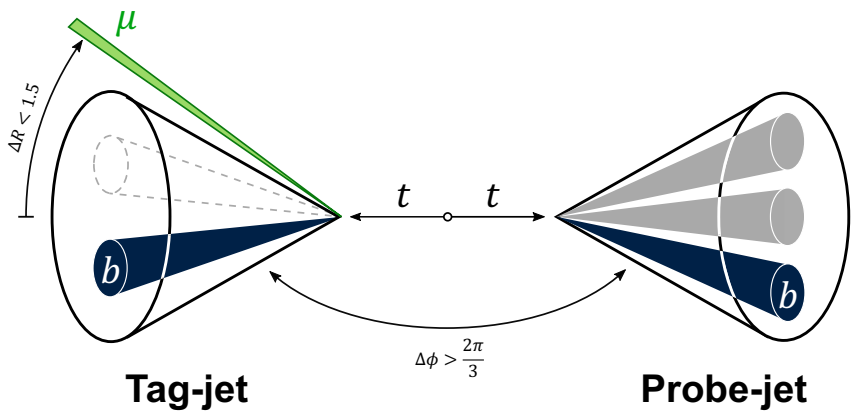

Figure 6.2: Schematic representation of the $\mathrm{CR}_{t\bar{t}}$ event selection criteria.

Because it reconstructs the hadronic decay of a top quark, the probe-jet is the object of interest used in the analysis. Similarly to the SR and VR, the $\mathrm{CR}_{t\bar{t}}$

region is subdivided into the same p_{T} ranges used for differential measurements: $250 < p_{\mathrm{T}}^{\text{probe-jet}} < 450$ GeV ($\mathrm{CR}_{t\bar{t}}0$), $450 < p_{\mathrm{T}}^{\text{probe-jet}} < 650$ GeV ($\mathrm{CR}_{t\bar{t}}1$), $650 < p_{\mathrm{T}}^{\text{probe-jet}} < 1000$ GeV ($\mathrm{CR}_{t\bar{t}}2$), $p_{\mathrm{T}}^{\text{probe-jet}} > 1000$ GeV ($\mathrm{CR}_{t\bar{t}}3$).

The kinematic properties of the $\mathrm{CR}_{t\bar{t}}$ have to resemble those of the signal regions, so that any adjustment to the $t\bar{t}$ process determined in the control region can be directly applied to the SR. For this reason, only events with probe-jet mass in range $140 < m^{\text{probe-jet}} < 200$ GeV are used in the statistical model, thus removing events where the top quark decay products are not fully contained within the probe-jet[3].

The $t\bar{t}$ purity of the $\mathrm{CR}_{t\bar{t}}$ sample is estimated in MC, and it reaches 97% inclusively in probe-jet p_{T}, while remaining above 95% in each of the four p_{T} ranges. The remaining fraction is mainly composed of single-top and $W(\ell\nu)+\text{jets}$, with a negligible contribution from QCD multijet events.

6.3.3 W Control Region from $t\bar{t}$ Events

An additional control region ($\mathrm{WCR}_{t\bar{t}}$) is designed to perform an independent measurement of the mass resolution of large-R jets reconstructing vector boson decays, constraining the corresponding systematic uncertainty (see Section 8.4). Similarly to the $\mathrm{CR}_{t\bar{t}}$ region described in the previous section, the $\mathrm{WCR}_{t\bar{t}}$ region aims at semi-leptonic $t\bar{t}$ events. In this case, however, the goal is to select events where only the W boson from the top quark decay is contained within a large-R jet. These partially-contained top quark decays provide a well-defined W boson sample whose mass distribution can be used to externally constrain the jet mass resolution uncertainty.

Events are collected using the logical OR of two muon triggers, both reaching full efficiency with the offline cut $p_{\mathrm{T}} > 27$ GeV on the trigger muon. Simulated $t\bar{t}$ events populating this region are obtained using the Sherpa 2.2.1 MC generator. In each event, the leptonic top quark is selected by requiring a b-tagged VR track jet (MV2c10, 77% WP), with $p_{\mathrm{T}} > 25$ GeV, within $\Delta R < 1.5$ of the muon. The W boson candidate ($W_{\text{cand.}}$) is instead identified as the leading large-R jet with

[3]Additionally, a kinematic correction is applied to the $\mathrm{CR}_{t\bar{t}}$ to compensate for the effects of using different triggers from those employed in the SR.

distance $\Delta R > 2.0$ from the b-tagged VR track jet from the leptonic top quark decay, thus ensuring the back-to-back $t\bar{t}$ topology. The W candidate jet is required to have $p_{\mathrm{T}}^{W_{\mathrm{cand.}}} > 200$ GeV and to be ghost-associated with at least 2 VR track jets with $p_{\mathrm{T}} > 10$ GeV, passing overlap cleaning. In order to select the topology where only the W boson is clustered within the large-R jet, a b-tagged VR track jet, with $p_{\mathrm{T}} > 10$ GeV, is required to be within $1.0 < \Delta R < 1.5$ of the W candidate. For the jet mass resolution measurements, only the W candidate mass range $60 < m^{W_{\mathrm{cand.}}} < 100$ GeV is considered in order to reduce background contributions from other processes and isolate the desired jet topology. A schematic representation of the WCR$_{t\bar{t}}$ event selection criteria is given in Figure 6.3.

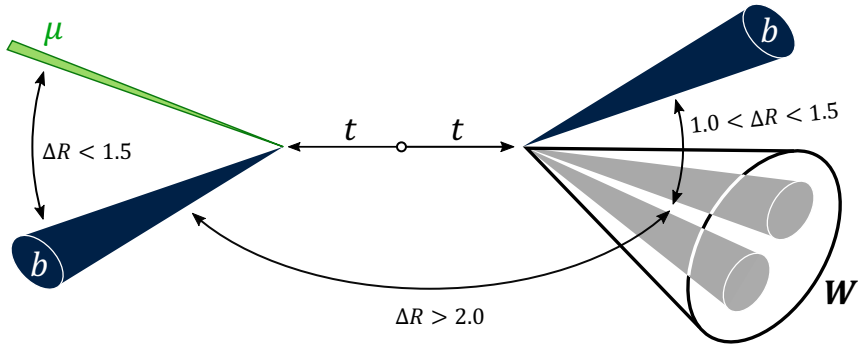

Figure 6.3: Schematic representation of the WCR$_{t\bar{t}}$ event selection criteria.

The region is analysed both inclusively and in the W candidate p_{T} regions $200 < p_{\mathrm{T}}^{W_{\mathrm{cand.}}} < 275$ GeV, $275 < p_{\mathrm{T}}^{W_{\mathrm{cand.}}} < 375$ GeV, and $375 < p_{\mathrm{T}}^{W_{\mathrm{cand.}}} < 1500$ GeV. At high $p_{\mathrm{T}}^{W_{\mathrm{cand.}}}$, statistics are limited by the partial containment requirement of the top quark decay products. The modelling of the processes populating the WCR$_{t\bar{t}}$ region is given in Section 7.4.2.

6.4 Analysis Strategy

So far, this chapter has described how the data are collected, the simulated samples are generated and how all these events are grouped into several analysis regions. This final section summarises the analysis strategy, namely the series of procedures used to extract the analysis deliverables from the defined experimental setup.

The section starts by describing the main analysis deliverables, i.e. three Higgs boson measurements performed in different SR configurations. It then continues by describing the blinding strategy used for ensuring not to bias the measurements while the analysis is set up. Subsequently, the fitting procedure is presented, which is the technique used to extract the results from the data. The section ends by introducing the Asimov datasets, idealised pseudo-datasets used to assess the Higgs sensitivity and to validate and optimise the analysis strategy before unblinding the data.

6.4.1 Measurements

In this section, a brief summary of the main analysis deliverables is given. The main goal of the analysis is to extract the number of events in the SR data where a Higgs boson is produced. This is achieved by performing *binned likelihood fits*, procedures able to find the combination of the signal and background models that best describes the candidate jet mass[4] distribution observed in data. The fit procedure used in the analysis is introduced in Section 6.4.3.

The amount of signal extracted in every measurement is parametrised using the Higgs boson *signal strength* μ_H, which represents the ratio between the number of measured Higgs events and that predicted from SM calculations and MC simulation. The Higgs signal strength is the main parameter of interest (PoI) in the analysis, and it is equivalent to a Higgs boson cross-section estimate.

In all measurements, the SRL, SRS and $\mathrm{CR}_{t\bar{t}}$ are simultaneously fit, meaning that all three regions contribute to the determination of the fit results. The Higgs signal strength, for instance, is "fully correlated" across the SRL and SRS (i.e. it is described by the same parameter in the two regions). The simultaneous fit will thus find a common solution for μ_H that best describes the Higgs signals in the two regions collectively.

Three Higgs boson measurements are performed within the analysis: the *inclusive* measurement, the *fiducial* measurement and the *differential* measurement.

[4]In the signal regions, the candidate jet mass and p_{T} are corrected to account for energy losses due to the presence of muons within the jet. More information about this correction is given in Appendix B.

Inclusive Measurement

The inclusive measurement extracts the Higgs boson signal strength by fitting the SRL, SRS and $CR_{t\bar{t}}$ over their entire available large-R jet p_T range (inclusively in p_T). The SRL is populated by events with candidate jet $p_T > 450$ GeV, while the SRS and $CR_{t\bar{t}}$ by events with $p_T > 250$ GeV. The fit is performed over the candidate jet mass distribution with a 5 GeV binning, spanning the range 70–210 GeV in the SRL, 75–210 GeV in the SRS and 140–200 GeV in the $CR_{t\bar{t}}$.

Fiducial Measurement

The fiducial Higgs boson measurement is performed in a *fiducial volume*, namely a region of the phase space where the ATLAS detector has high efficiency. Extracting measurements in fiducial volumes helps comparing results with other analyses and theoretical predictions. For this measurement, the fiducial volume is defined in terms of truth (or generator-level) Higgs boson quantities as $p_T^H > 450$ GeV, $|y_H| < 2$, where p_T^H and y_H are, respectively, the generated Higgs boson transverse momentum and rapidity.

The fiducial measurement is carried out simultaneously on the SRL, SRS and $CR_{t\bar{t}}$, but their candidate jet p_T range is restricted to $p_T > 450$ GeV. The binning and range of the candidate jet mass distributions considered in the fit are the same as in the inclusive measurement.

In the fit, the Higgs boson mass distribution is divided into two templates: one for Higgs bosons belonging to the fiducial volume ($p_T^H > 450$ GeV, $|y_H| < 2$), and the other for those falling outside the fiducial volume ($p_T^H < 450$ GeV). The Higgs signal strength outside of the fiducial volume is not determined by the fit, but fixed to SM expectation. The signal strength within the fiducial volume is instead measured (free floating in the fit), and finally reinterpreted as an estimate of the Higgs cross-section. The modelling of the Higgs templates is given in Section 7.1.1, while Section 9.4 provides a more in-depth description of the fiducial measurement and its results.

Differential Measurement

A differential measurement is used to probe the Higgs production cross-section as a function of the generated Higgs boson p_{T} (p_{T}^{H}). The SRL, SRS and $\mathrm{CR}_{t\bar{t}}$ are first split into independent reconstructed jet p_{T} bins as explained in Section 6.3.1. Then, within each p_{T} bin i, the Higgs boson mass distribution is divided into five templates $(p_{Tj}^{H})_i$ ($j = \{0, 1, 2, 3, 4\}$) defined by $|y_H| < 2$ and

- $\boldsymbol{p_{T0}^{H}}$**:** $p_{\mathrm{T}}^{H} < 300$ GeV,
- $\boldsymbol{p_{T1}^{H}}$**:** $300 < p_{\mathrm{T}}^{H} < 450$ GeV,
- $\boldsymbol{p_{T2}^{H}}$**:** $450 < p_{\mathrm{T}}^{H} < 650$ GeV,
- $\boldsymbol{p_{T3}^{H}}$**:** $650 < p_{\mathrm{T}}^{H} < 1000$ GeV,
- $\boldsymbol{p_{T4}^{H}}$**:** $p_{\mathrm{T}}^{H} > 1000$ GeV.

The yield of each template is controlled, within the fit, by a dedicated signal strength μ_H^j ($j = \{0, 1, 2, 3, 4\}$), which is fully correlated across analysis regions and p_{T} bins. The fiducial volume for the differential measurement is defined by $p_{\mathrm{T}}^{H} > 300$ GeV, $|y_H| < 2$. Being outside of the fiducial volume, μ_H^0 is fixed to the SM expectation.

The Higgs signal strengths are obtained from a simultaneous fit to all reconstructed jet p_{T} bins in the SRL, SRS and $\mathrm{CR}_{t\bar{t}}$. The fit is performed over the candidate jet mass distribution, with a 5 GeV binning, and spanning the range 70–210 GeV in the SRL1, SRL3 and SRS1, 75–210 GeV in the SRL2, SRS0 and SRS2, and 140–200 GeV for all $\mathrm{CR}_{t\bar{t}}$ p_{T} bins. At the end of the analysis, the signal strength results are finally reinterpreted into a differential Higgs cross-section measurement.

Table 6.4 summarises the Higgs measurements and the candidate jet p_{T} selections defining the analysis regions where they are performed. Also shown are the signal strengths and the fiducial selections used to obtain the corresponding Higgs templates.

Table 6.4: Left: summary of the candidate jet p_{T} requirements for the three SR configurations used in the analysis measurements. Right: the Higgs boson signal strength extracted in the measurements and the fiducial selections (p_{T}^{H}, $|y_H|$) defining the signal templates they control. In the case of the inclusive measurement, no fiducial selection is applied, and the templates are defined inclusively in p_{T}^{H} and $|y_H|$.

Region		SRL Candidate jet p_{T} [GeV]	SRS Candidate jet p_{T} [GeV]	PoI	Measurement p_{T}^{H}[GeV]	$\lvert y_H\rvert$
Inclusive		>450	>250	μ_H	inclusive	inclusive
Fiducial		>450	>450	μ_H	> 450	< 2
Diff.	bin 0	–	250 – 450,	μ_H^1	300 – 450	< 2
	bin 1	450 – 650,	450 – 650,	μ_H^2	450 – 650	
	bin 2	650 – 1000,	650 – 1000	μ_H^3	650 – 1000	
	bin 3	> 1000	–	μ_H^4	> 1000	

6.4.2 Blinding Strategy

In statistical analysis, *blinding* is a common strategy aimed at minimising biases in the results that might arise from the analysers' awareness about specific features in the dataset. In order to avoid possible biases, the Boosted $H(\to b\bar{b}) + \text{jet}$ analysis strategy is developed and validated without directly using the SR data. Only once the analysis is finalised, can the SR data be accessed, and the measurements performed. This process is known as *unblinding*.

The unblinding of the SR data, however, did not happen all at once, but in multiple stages (staged unblinding). First, the signal regions were unblinded except for a ± 20 GeV window around the Higgs mass, which was never shown in validation plots. The aim of this first unblinding stage was to validate the fit strategy on the Z boson mass peak in the SR and study the interplay between the flexible QCD model (see Section 7.2) and an overlaying resonance structure, along the candidate jet mass spectrum. To this purpose, an *inclusive* Z fit was performed, following the same strategy designed for the corresponding Higgs measurement, but fixing the Higgs signal strength to SM expectation ($\mu_H = 1$). Results indicated that a lack of constraint in the jet mass resolution uncertainty led to the possibility for an unnatural fit solution. This fit was thus used for testing a remedy to

this issue, which was successful and thus included in the analysis strategy (more information is given in Section 8.4).

In a second stage of the unblinding, a *differential Z* fit was performed in order to validate the differential fit setup of the analysis. In this fit, the Z boson was treated exactly like the Higgs in the differential setup, while the Higgs signal strength was fixed to SM expectation. The results, which are presented in Section 9.5.1, validated the fit strategy and were eventually considered as additional analysis deliverables.

Finally, the Higgs boson mass window was unblinded and all the remaining analysis measurements were performed.

6.4.3 Fitting Procedure

As already mentioned, the analysis measurements are obtained from binned likelihood fits to data. This corresponds to finding the values of the free parameters in the analysis that best describe the (binned) candidate jet mass distribution observed in data. The free parameters are the yields of the signal and background models, and the parameters controlling the shape of the QCD model.

The best estimates of the parameters are obtained by maximising a likelihood function $\mathcal{L}$, which is defined as

$$\mathcal{L} = \prod_{i=1}^{n} p(y_i | x_i(\boldsymbol{\mu}, \boldsymbol{k}, \boldsymbol{\theta})), \tag{6.1}$$

where n is the number of bins in the mass spectrum and p is the probability of measuring y_i data events in bin i, when x_i are expected. In case of a simultaneous fit across multiple regions, the product is performed over the jet mass spectra of all regions.

The expected number of events in bin i, x_i, depends on three sets of parameters: the yields $\boldsymbol{\mu}$ of all the signals considered in the fit, the yields $\boldsymbol{k}$ of all the backgrounds (equivalent to $\boldsymbol{\mu}$ for the signals), and the set $\boldsymbol{\theta}$ of nuisance parameters (NPs) accounting for the presence of systematic uncertainties (see Chapter 8). It follows that x_i can be expressed as

$$x_i(\boldsymbol{\mu}, \boldsymbol{k}, \boldsymbol{\theta}) = \sum_{s=1}^{n_s} \mu_s x_{i,s}(\boldsymbol{\theta}) + \sum_{b=1}^{n_b} k_b x_{i,b}(\boldsymbol{\theta}), \tag{6.2}$$

where n_s and n_b are, respectively, the numbers of signal and background processes considered in the fit. Since the QCD background is modelled with a polynomial function, the corresponding values of x_i also depend on a set $\boldsymbol{c}_{\mathrm{QCD}}$ of coefficients controlling its shape. It is noted that the signal and background terms have the same role within the equation. Thus, the distinction between $\boldsymbol{\mu}$ and $\boldsymbol{k}$ is dropped, and they are collectively grouped in the same set $\boldsymbol{\mu}$. Furthermore, when presenting the analysis results, the $\boldsymbol{\mu}$ values of the PoIs are normalised to their SM expectations, and in this case, they are generically called *signal strengths*.

Since the number of data events in each bin follows a Poisson distribution, the probability terms $p(y_i|x_i)$ appearing in the likelihood are given by

$$p(y_i|x_i(\boldsymbol{\mu},\boldsymbol{\theta})) = \frac{e^{-x_i(\boldsymbol{\mu},\boldsymbol{\theta})}(x_i(\boldsymbol{\mu},\boldsymbol{\theta}))^{y_i}}{y_i!}. \tag{6.3}$$

Systematic uncertainties enter the likelihood function as nuisance parameters $\boldsymbol{\theta}$, whose prior knowledge is reflected by Gaussian penalty terms that are multiplied to the likelihood. For a nuisance parameter θ, whose prior knowledge is expressed as $\theta_0 \pm \sigma_\theta$, the corresponding Gaussian penalty term is given by

$$G(\theta_0|\theta,\sigma_\theta) = \frac{1}{\sqrt{2\pi\sigma_\theta^2}}\exp\left[-\frac{(\theta-\theta_0)^2}{2\sigma_\theta^2}\right]. \tag{6.4}$$

The fitting strategy of the analysis is developed within the RooFit framework [105], which provides a series of tools for conveniently defining the complex likelihood functions of the analysis measurements. Due to computational advantage, the best values of the free parameters are obtained by minimizing the negative logarithm of the likelihood function (NLL), which is done using the Minuit program [79]. All Gaussian terms representing systematic uncertainties are centred at $\theta_0 = 0$ and have width $\sigma_\theta = 1$, corresponding to the pre-fit $\pm 1\sigma$ systematic variations.

Since the QCD multijet process is modelled using a highly non-linear function, particular care is needed during the NLL minimisation. The contribution of the QCD background to any bin cannot, in fact, be simply estimated as the value of the QCD function at the bin centre. Instead, it is obtained by numerically integrating the QCD function over the mass range of the bin. The integration

is done by finely sampling each bin 1000 times, which significantly increases the fit computation time. This motivates the introduction of a *pruning* procedure (see Section 8.2.3), which removes negligible systematic uncertainties from the fit, reducing its complexity and computation time.

6.4.4 Asimov Datasets

Before unblinding the SR datasets, it is important to validate the fit procedure. Likewise, it is useful to know in advance the expected precision of the various Higgs measurements, given the experimental setup of choice.

These validations are performed on Asimov datasets, idealised pseudo-datasets created by summing together the candidate jet mass models of all signal and background processes. An Asimov dataset is created for each region defined in the analysis.

From their definition, it follows that performing a measurement on an Asimov dataset corresponds, effectively, to fitting a model to a dataset that was created using that same model. Despite seeming trivial, the results of Asimov fits are very useful tools for validating the fit strategy and understanding the expected analysis sensitivity.

Since the Asimov datasets are constructed by injecting signal and background models at their SM rates, the fit results for any PoI μ will be $\mu = 1 \pm \hat{\sigma}(\mu)$, meaning that the fit should be able to recover the injected PoI value. These are called *expected results* and are particularly useful for determining the expected precision of a measurement. The value of $\hat{\sigma}(\mu)$ is, in fact, determined by the fit and takes into account the propagation of all uncertainties and their correlations. For a parameter μ, its *expected significance* $Z_{\mu}^{\text{exp.}} = \mu/\hat{\sigma}(\mu) = 1/\hat{\sigma}(\mu)$ obtained from an Asimov fit represents the level of precision that would be expected if the data were in perfect agreement with the analysis signal and background models.

Performing Asimov measurements is also used for validating the systematic uncertainty model by studying their correlations and constraints in an idealised environment, before proceeding with the unblinding.

7

Signal and Background Modelling

Contents

7.1 Higgs Boson Signal 113
7.1.1 Higgs Modelling for the Fiducial Measurement 115
7.1.2 Higgs Modelling for the Differential Measurement 117
7.2 QCD Multijet Processes 118
7.2.1 QCD Polynomial Function 120
7.2.2 Hybrid VR Slices 120
7.3 Top Quark Production 124
7.3.1 $t\bar{t}$ Pair Production 124
7.3.2 Single Top Quark Production 127
7.4 V + jets 131
7.4.1 Higher-order Corrections 132
7.4.2 W Control Region Modelling 133

Despite being designed to maximise sensitivity to the Higgs boson, the signal regions are also populated by several large background processes. The all-hadronic $H \to b\bar{b}$ final state of choice inevitably leads to an immense background from QCD multijet events, which can mimic the signal topology while having a far larger cross-section. In addition, background events might enter the SR if large-R jets are wrongly double b-tagged, which might happen due to limitations of the b-tagging algorithm.

Figure 7.1 shows the jet mass distributions of the expected signal and background processes in the SRL and SRS. Both figures span the mass range used for the

Higgs measurement: $[70, 210]$ GeV for the SRL and $[75, 210]$ GeV for the SRS. QCD multijet events represent the largest background, characterised by a monotonically decreasing mass spectrum. Events with one or two top quarks in the final state, collectively referred to as "Top", have a broad distribution peaking at the top quark mass ($m_t \approx 175$ GeV) and spreading across the whole spectrum. As shall be explained in Section 7.3.1, this large spread is mainly due to the fact that a sizable fraction of top quark decays are not fully reconstructed inside a large-R jet. W and Z bosons produced in association with jets, collectively named $V+$jets, occupy the low-mass end of the spectrum and show a narrower peak with a long high-mass tail.

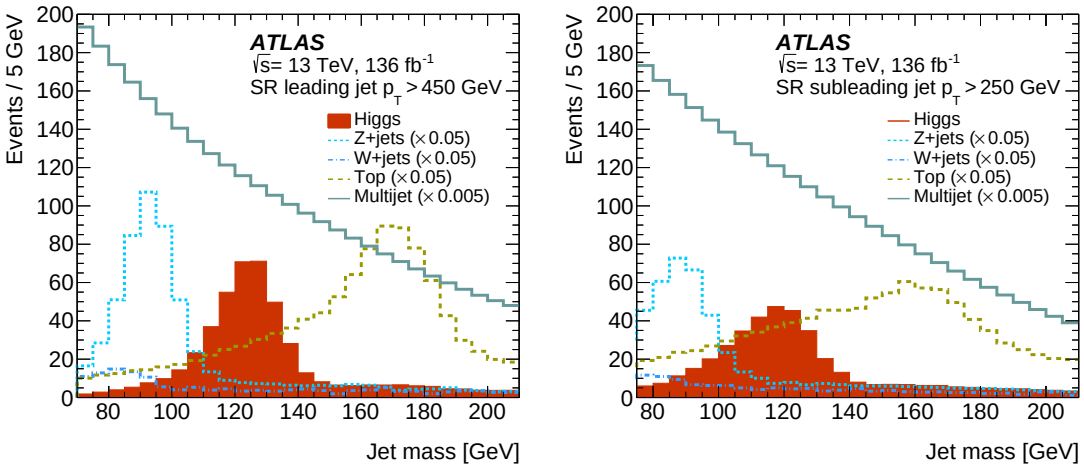

Figure 7.1: Candidate jet mass distributions for the Higgs boson, $Z+$jets, $W+$jets, top quark and QCD multijet processes in the inclusive SRL (left) and SRS (right). The QCD multijet distribution is extracted from data, while the others are simulated with MC. In order to be comparable with the Higgs distribution, the normalisations of the background process distributions are scaled down by the factors shown in the legend [1].

Therefore, the small Higgs mass resonance is found to be dominated by a huge QCD multijet background and surrounded by large resonances with tails extending into its mass range. For this reason, the extraction of the Higgs signal is challenging and requires a precise modelling of all processes.

The resolution of the jet mass measurement also plays a fundamental role in separating the various resonances. From the figures, it is noted that all resonances in the SRS have worse resolutions than in the SRL. This is due to a series of effects that might result in energy losses during the reconstruction of large-R jets.

Examples are final state radiation not being clustered into the jet or energy losses due to semi-leptonic b quark decays (which include escaping neutrinos). Due to the energy reduction, jets affected by these processes will preferentially populate the SRS, which in turn will be characterised by a worse mass resolution.

In this chapter, a description of the signal and background modelling in the SR is given. Where relevant, the modelling of processes populating the $\mathrm{CR}_{t\bar{t}}$ and $\mathrm{WCR}_{t\bar{t}}$ is also described.

Author's Contributions The modelling of the Higgs boson signal was a collective effort within the analysis team. The author led the studies and validations in the fiducial and differential regions of the analysis, and produced the results shown in Section 7.1.

The modelling of the $t\bar{t}$ process in the analysis regions, presented in Section 7.3.1, was largely understood from a preliminary version of the analysis using 0.5 GeV jet mass binning. The studies presented in the section, however, were carried out by the author for the finalised version of the analysis, which features a 5 GeV jet mass binning. The author also studied the $t\bar{t}$ modelling for the first time in the fiducial and differential regions.

The modelling of the single top quark process, described in Section 7.3.2, and its validation in all analysis regions was performed entirely by the author, who also developed code for incorporating this process within the fitting framework.

The author's contributions to the modelling of the QCD and V + jets backgrounds (respectively Sections 7.2 and 7.4) were more limited, to the validation and verification of the suitability of the 5 GeV binning, and to understanding their impact on the overall analysis fits.

7.1 Higgs Boson Signal

An important feature of the event selection is the absence of specific requirements on the nature of the recoil jet, or on the presence of other activity in the event.

Therefore, various Higgs production processes can contribute to the signal model, making the analysis *inclusive* in Higgs production process.

The requirement of at least two energetic jets in the event has a strong impact in determining which Higgs production processes can contribute to the SR. Figure 7.2 shows the simulated Higgs mass distribution in the SRL and SRS, together with the contributions from the various Higgs production processes. In the Higgs mass region $[105, 140]$ GeV, production via ggF is dominant both in the SRL and SRS. Production via VBF, VH and $t\bar{t}$H contribute in a smaller but non-negligible way. The resulting distribution is characterised by a peak around the Higgs mass and by a long high-mass tail, which is mainly composed of $t\bar{t}$H events. This is due to top quark jets in $t\bar{t}$H events being incorrectly identified as Higgs candidates. Possible avenues for reducing this effect in future iterations are explored in Section 9.6.

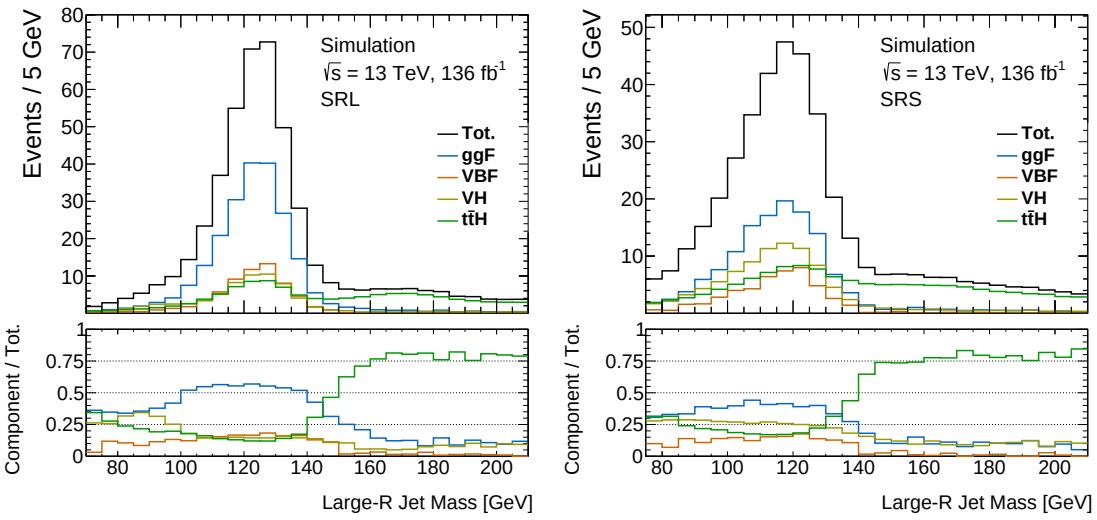

Figure 7.2: Large-R jet mass distributions from simulated Higgs events in the inclusive SRL (left) and SRS (right). Total distributions (black lines) are split into contributions from the ggF, VBF, VH and $t\bar{t}$H Higgs production modes (coloured lines). The lower panel shows the fractional contribution of each production mode, as a function of large-R jet mass.

Table 7.1 summarises the fractional contributions of the various Higgs production processes in the signal regions, restricting the mass range to a window ($[105, 140]$ GeV) around the Higgs mass. The fractions are shown both inclusively in candidate jet p_{T} and in every analysis p_{T} bin. Furthermore, Figure 7.3 shows

the evolution of the same fractional contributions as a function of the candidate jet p_{T}. Inclusively in p_{T}, the ggF production mode is the largest contribution both in SRL and SRS. A trend, however, is observed moving towards higher p_{T}, where contributions from the various production processes become more similar. In contrast to the high-p_{T} behaviour, the $250 < p_{\mathrm{T}} < 450$ GeV region of the SRS is dominated by $t\bar{t}$H events, representing around 40% of the total. Because $t\bar{t}$H is a three-body system, a hadronically decaying top quark can satisfy the jet trigger requirements without a high Higgs p_{T} value. In the Higgs boson mass window, almost 90% of $t\bar{t}$H events arise from $H \to b\bar{b}$ decays, with the remainder being mainly composed of $H \to W^{\pm}W^{\mp}$ events.

Table 7.1: Fractional contributions of each Higgs production process to all analysis signal regions around the Higgs boson peak, defined by $105 < m < 140$ GeV.

Process	Jet p_T range [GeV]				
	Incl.	250–450	450–650	650–1000	> 1000
			SRL		
ggF	0.552 ± 0.004	–	0.562 ± 0.004	0.504 ± 0.010	0.39 ± 0.04
VBF	0.166 ± 0.004	–	0.167 ± 0.004	0.161 ± 0.009	0.17 ± 0.04
VH	0.147 ± 0.002	–	0.141 ± 0.002	0.175 ± 0.004	0.25 ± 0.02
$t\bar{t}$H	0.134 ± 0.001	–	0.129 ± 0.001	0.160 ± 0.004	0.19 ± 0.02
			SRS		
ggF	0.396 ± 0.005	0.280 ± 0.007	0.462 ± 0.006	0.430 ± 0.015	–
VBF	0.147 ± 0.004	0.066 ± 0.005	0.185 ± 0.006	0.210 ± 0.015	–
VH	0.249 ± 0.003	0.261 ± 0.004	0.238 ± 0.004	0.257 ± 0.009	–
$t\bar{t}$H	0.209 ± 0.002	0.394 ± 0.005	0.114 ± 0.002	0.103 ± 0.004	–

7.1.1 Higgs Modelling for the Fiducial Measurement

As already introduced in Section 6.4.1, the fiducial measurement is performed through a simultaneous fit to the SRL, SRS and $\mathrm{CR}_{t\bar{t}}$, restricting their jet p_{T} range to $p_{\mathrm{T}} > 450$ GeV. This requirement excludes events belonging to the SRS0 region (as well as $\mathrm{CR}_{t\bar{t}}0$), which provides very little Higgs sensitivity. In the signal regions, the Higgs mass template is divided into two components, one belonging to the fiducial region defined by $p_{\mathrm{T}}^{H} > 450$ GeV, $|y_H| < 2$, and the other failing this requirement ($p_{\mathrm{T}}^{H} < 450$ GeV).

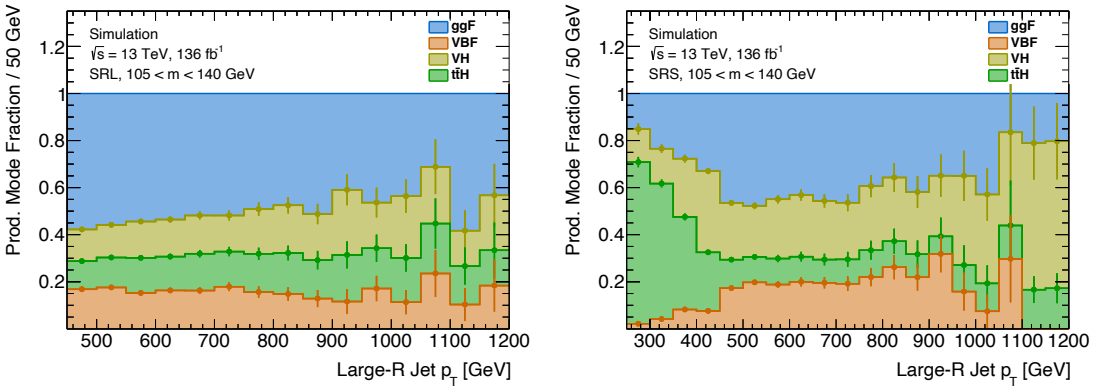

Figure 7.3: Fractional contribution of each production mode as a function of the signal candidate jet p_{T} to the inclusive SRL (left) and SRS (right). Only events contributing to the Higgs boson mass peak, defined by $105 < m < 140$ GeV, are considered.

The two Higgs mass templates are compared in Figure 7.4, both in the SRL and SRS. Clearly, the component outside of the fiducial region has a worse mass resolution and it is characterised by a large tail around the top quark mass. This is due to top quark contamination in the $t\bar{t}$H process, which is the dominant Higgs boson production mode in the 250–450 GeV p_{T} range. Furthermore, Higgs boson candidate jets outside of the fiducial volume tend to be more massive, thus slightly shifting the peak position of the fiducial template towards lower masses.

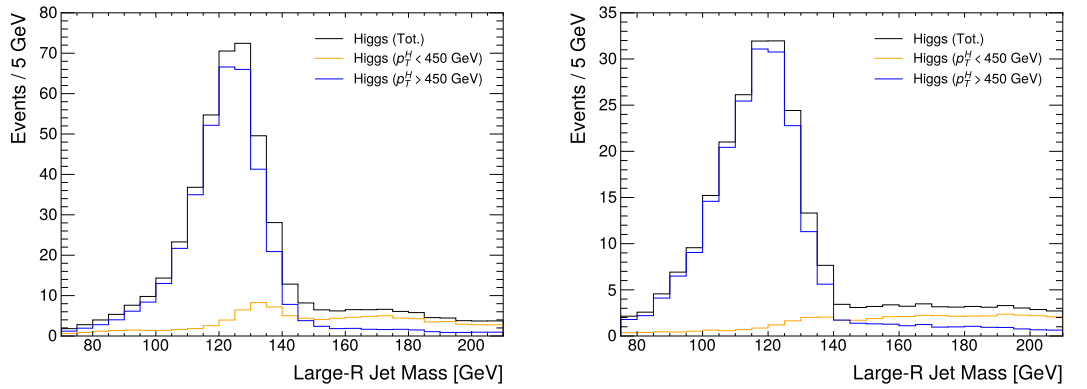

Figure 7.4: Simulated Higgs boson mass distributions in the SRL (left) and SRS (right) with candidate jet $p_{\mathrm{T}} > 450$ GeV. The Higgs mass template within the fiducial volume (blue) is defined by $p_{\mathrm{T}}^{H} > 450$ GeV, $|y_H| < 2$, while the one outside of the fiducial volume (orange) has $p_{\mathrm{T}}^{H} < 450$ GeV.

7.1.2 Higgs Modelling for the Differential Measurement

The Higgs boson differential measurement is performed by splitting the SRL and SRS in bins of reconstructed jet p_{T} as:

$$450 \text{ GeV} < \textbf{SRL1} < 650 \text{ GeV} < \textbf{SRL2} < \quad 1 \text{ TeV} < \textbf{SRL3}, \tag{7.1}$$

$$250 \text{ GeV} < \textbf{SRS0} < 450 \text{ GeV} < \textbf{SRS1} < 650 \text{ GeV} < \textbf{SRS2}. \tag{7.2}$$

Within each reconstructed p_{T} bin, the Higgs boson mass templates are extracted in five truth-level p_{T}^{H} regions defined as

$$\boldsymbol{p_{T0}^{H}} < 300 \text{ GeV} < \boldsymbol{p_{T1}^{H}} < 450 \text{ GeV} < \boldsymbol{p_{T2}^{H}} < 650 \text{ GeV} < \boldsymbol{p_{T3}^{H}} < 1 \text{ TeV} < \boldsymbol{p_{T4}^{H}}. \tag{7.3}$$

Because of mass resolution effects and mis-reconstruction, events populating truth p_{T}^{H} regions might be reconstructed into non-corresponding differential p_{T} ranges. The extent of such migrations is illustrated in Figure 7.5, which shows the fractional Higgs template yield contributions within each SRL and SRS differential region. Although corresponding p_{T} ranges show the largest fractions, contributions are observed in the "off-diagonal" bins, usually in the order of a few per cent. Due to the worse mass resolution, the SRS0 is characterised by the strongest migration effects, the largest being approximately 25% of the yield in that region.

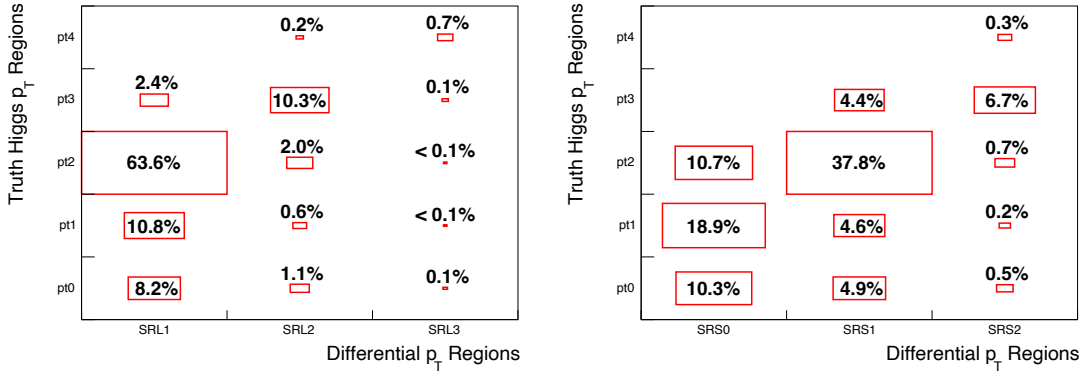

(a) SRL **(b)** SRS

Figure 7.5: Fractional Higgs template yield contributions within each SRL (left) and SRS (right) differential region. Contributions are normalised to the total inclusive yield in the SRL or SRS.

Figure 7.6 shows the Higgs mass distributions in each reconstructed p_{T} bin and their composition in terms of truth-level templates. Apart from SRS0, each differential bin is characterised by the presence of a dominant "diagonal" template. All other templates have much smaller relative contributions, especially in the Higgs mass region. As will be discussed in Section 9.5, a simplification to the statistical analysis strategy is applied by neglecting all systematic uncertainties on the subdominant templates in each region, as they are unlikely to provide significant constraints in the signal extraction. The only exception is the SRS0, which is characterised by larger off-diagonal contributions. In this case, systematics uncertainties on both the p_{T1}^{H} and p_{T2}^{H} templates are considered.

7.2 QCD Multijet Processes

As it is often the case at hadron colliders, in particular when looking at all-hadronic signatures, QCD multijet processes are the largest and most challenging background to model. These events have multiple jets that can mimic the signal topology. For example, gluons splitting into a $b\bar{b}$ pair can be reconstructed as large-R jets associated to two b-tagged track jets.

Unfortunately, the inherent complexity of such processes makes simulations imprecise, and data-driven modelling is often preferred. Since QCD multijet events are characterised by a continuously falling mass spectrum, it can be modelled by a parametric function. This approach has the advantage of being independent of any MC model, but needs to be optimised in order to find the parameters that best describe the QCD background in the SR. For this reason, the QCD model is validated and optimised on the anti-b-tagged VR data, which are, with appropriate corrections, the best proxy for the QCD contribution in the SR.

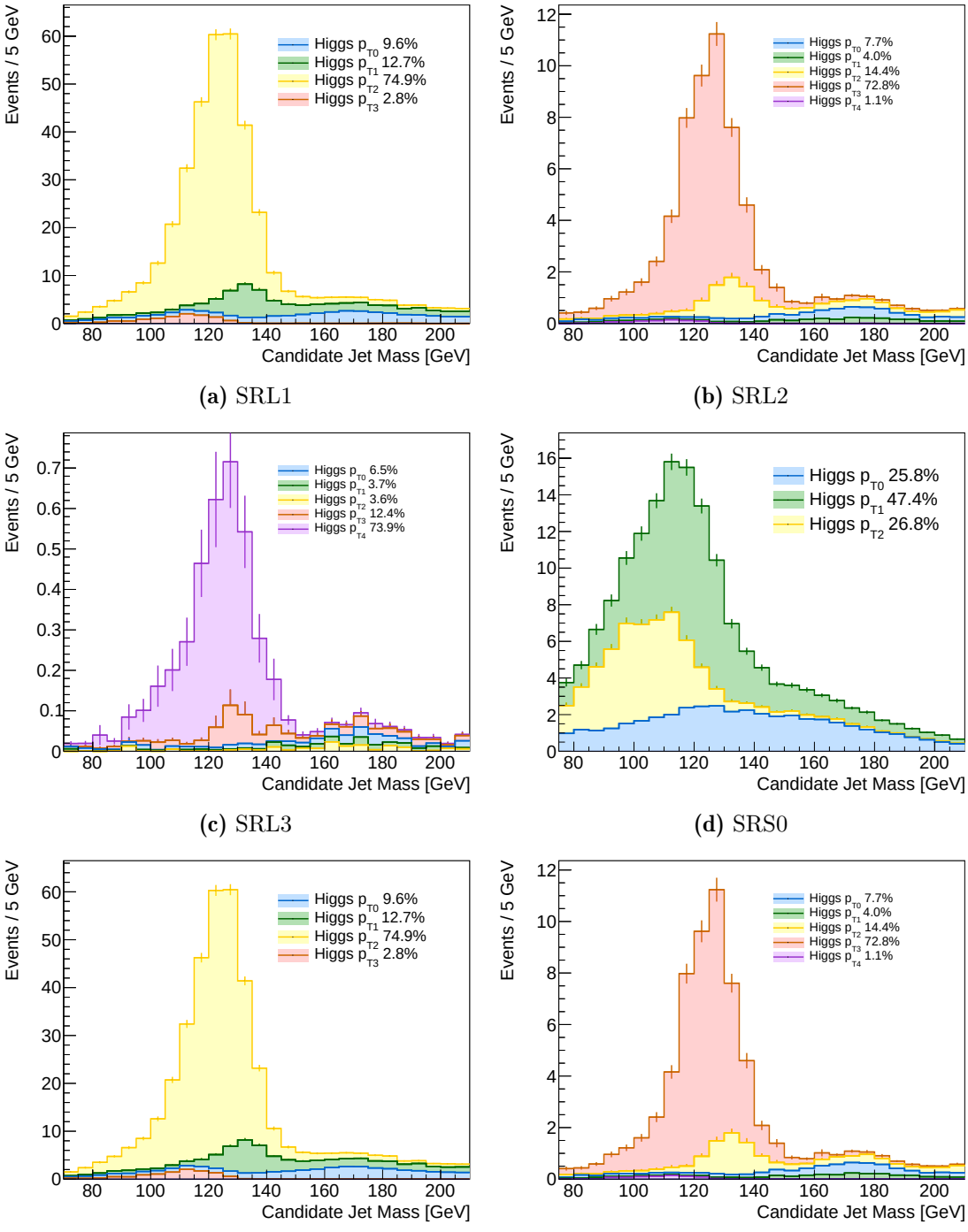

(a) SRL1 **(b)** SRL2

(c) SRL3 **(d)** SRS0

(e) SRS1 **(f)** SRS2

Figure 7.6: Higgs mass distributions in each differential p_{T} bin and their composition in terms of truth-level templates. Fractional yield contributions are given in the legend.

7.2.1 QCD Polynomial Function

In the analysis, the QCD multijet mass spectrum is modelled using the polynomial function

$$f_N\left(x|\vec{\theta}\right) = \theta_0 \exp\left(\sum_{i=1}^{N} \theta_i x^i\right), \tag{7.4}$$

where $x = (m - 150\ \text{GeV})/80\ \text{GeV}$ redefines the large-R jet mass m to be constrained between -1 and 1 in the measurement region, N is the polynomial order and θ_i are fit parameters which are determined independently for each region during signal extraction.

The optimal value of the polynomial order N in each analysis region depends on the number of analysed events and shape of the QCD mass spectrum. With an increased data sample, the greater precision will require a larger N to appropriately model the mass distribution. If N is too large, correlations increase between the multijet and resonant process models, decreasing their statistical significance. If N is too small, on the other hand, the model might not be able discern the subtle features of the mass distribution and provide an accurate fit, or a fit that converges. The optimal polynomial order is obtained by carrying out statistical tests on opportunely corrected subsets of VR data.

7.2.2 Hybrid VR Slices

Due to the different b-tagging requirements in the event selection, the VR data sample is much larger than the SR, with VRL (VRS) containing approximately 58 (51) times the number of events in the SRL (SRS). Since the optimal value of the polynomial order in each region depends on its number of events, it is first of all important to split the VR into subsets with similar numbers of events to the SR.

In addition, the QCD function must be validated and optimised on VR subsets that are kinematically equivalent to the SR. Figure 7.7 compares the SR and VR QCD mass distributions, as obtained from simulation. In the low mass region, a turn-on effect is observed in both the SRL and SRS distributions, which is not present in the VR. This effect is due to the different b-tagging requirements in

the SR and VR event selections. At low mass, decay products become highly collimated and b-tagging more challenging, leading to an efficiency loss in the SR. In the measurement mass ranges ($[70, 210]$ GeV for the SRL and $[75, 210]$ GeV for the SRS) the SR to VR shapes, however, appear to be quite consistent, despite a slight downward trend in the SRS ratio plot.

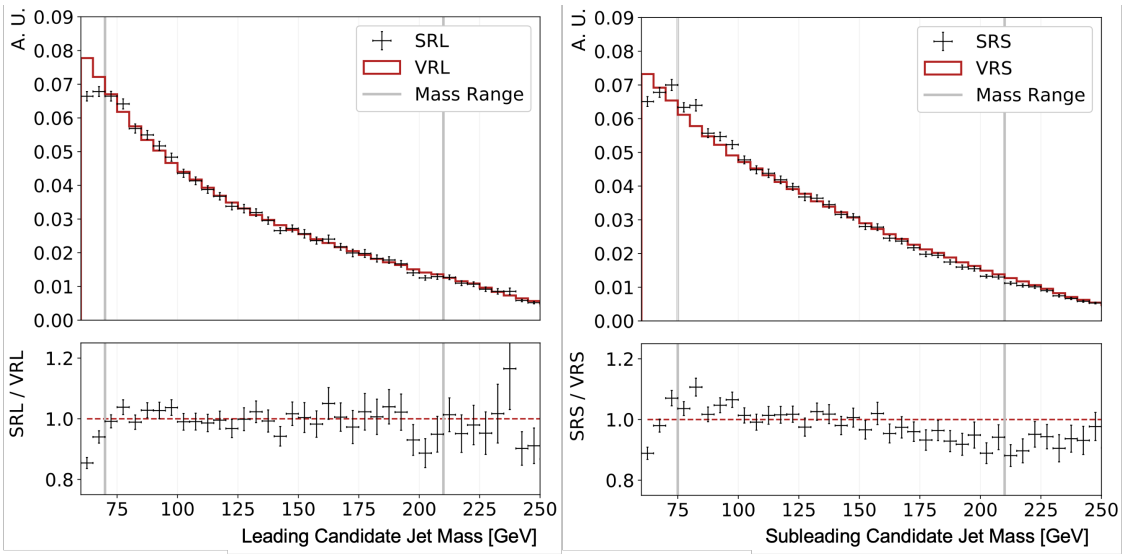

Figure 7.7: Comparison of the SR and VR simulated QCD mass distributions both in the leading (left) and subleading (right) regions. The distributions are normalised within the measurement mass ranges indicated by the vertical lines.

While encouraging, the agreement observed in MC does not necessarily translate to data. For this reason, the QCD function is validated and optimised on *hybrid VR slices* ($\mathrm{VR_{hyb}}$), which represent the best available proxy for the SR data. The hybrid VR slices are generated from the VR subsets by replacing the VR resonance peaks with the corresponding SM prediction in the SR and correcting the underlying QCD multijet mass spectrum shape to match that of the SR.

The shape of the multijet mass spectrum in the SR ($\mathrm{MJ_{SR}}$) is obtained from a blind data fit[1] to the SRL, SRS and $\mathrm{CR}_{t\bar{t}}$, considering all the processes and systematic uncertainties (see Section 8). Since this fit is performed to the SR, the Higgs boson signal normalization parameter is kept blinded.

[1]In all fits described in this paragraph, a polynomial order of $N = 5$ is chosen for the QCD function. No significant differences are observed when choosing $N = 4$ or $N = 6$.

The QCD model in the VR (MJ_{VR}) is created from likelihood fits to VR data divided in ten orthogonal slices[2], considering all processes and systematic uncertainties. The QCD model in VR is built from the average of the QCD parameters obtained from the ten fits.

Figure 7.8 shows the resulting MJ_{SR} and MJ_{VR} QCD models in a representative differential analysis region (SRL1). A sizable difference between the shapes of the QCD models is observed, justifying the need for the hybrid VR approach. Similar results are obtained in the inclusive and other differential regions.

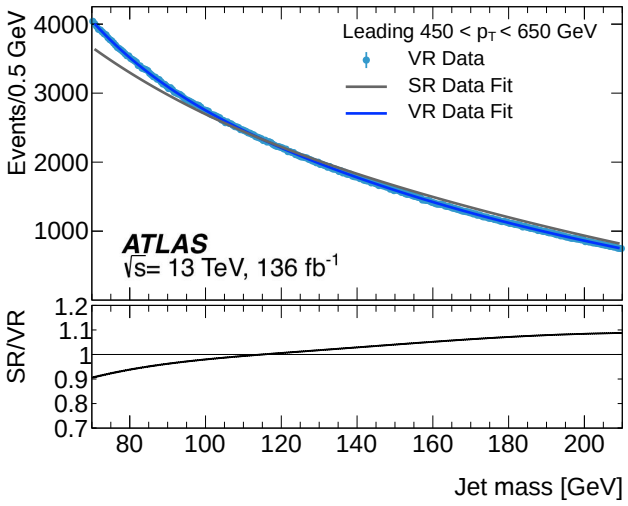

Figure 7.8: Comparison of the QCD multijet mass distribution shapes in the differential SRL1 region. The solid lines show the multijet function shape after a fit with full systematics to the blind SR data (grey) and VR data (blue). The solid points are the data from VR subsets with same statistics as the SR after the SM resonances are subtracted. The bottom panel shows the ratio of the blind SR data fit to the VR data fit (MJ_{SR}/MJ_{VR}) [1].

The $t\bar{t}$ and $V+$jets resonances in VR, V_{VR} and $t\bar{t}_{VR}$ respectively, are obtained from simulations and their normalisation is determined from the average post-fit contributions from the same ten fits to the VR. The SR resonances for the Higgs (H_{SR}), $V+$jets (V_{SR}) and $t\bar{t}$ ($t\bar{t}_{SR}$) processes are obtained from simulations.

For any VR subset VR^i, a hybrid slice VR^i_{hyb} is built following the procedure outlined below.

[2]The VR is divided into ten slices to maximize statistical precision without the need to increase the QCD polynomial order for an accurate description.

1. A proxy of the QCD mass distribution in VR^i is first obtained by subtracting the $V+\text{jets}$ (V_{VR}) and $t\bar{t}$ ($t\bar{t}_{\mathrm{VR}}$) resonances, as expected in VR.

2. The resulting mass distribution is corrected by the factor $\mathrm{MJ}_{\mathrm{SR}}/\mathrm{MJ}_{\mathrm{VR}}$, representing the ratio between the QCD multijet shape in SR and VR data. After applying this correction, the slice represents the best proxy of the QCD multijet mass distribution in the SR.

3. Finally, the Higgs (H_{SR}), $V+\text{jets}$ (V_{SR}) and $t\bar{t}$ ($t\bar{t}_{\mathrm{SR}}$) mass resonances are added, as expected from MC in the SR. The resulting hybrid VR slice represents the best proxy of data in the SR.

The correction procedure can be summarised using the following equation:

$$\mathrm{VR}^i_{\mathrm{hyb}} = (\mathrm{VR}^i - V_{\mathrm{VR}} - t\bar{t}_{\mathrm{VR}}) \times \left(\frac{\mathrm{MJ}_{\mathrm{SR}}}{\mathrm{MJ}_{\mathrm{VR}}}\right) + V_{\mathrm{SR}} + t\bar{t}_{\mathrm{SR}} + H_{\mathrm{SR}}. \tag{7.5}$$

Individually in each signal region (inclusive and differential), the polynomial order of the QCD function is optimised by carrying out likelihood ratio (LLR), linearity and spurious signal tests in the corresponding $\mathrm{VR}_{\mathrm{hyb}}$ proxies. Details on such tests are provided in Appendix C.

Table 7.2 shows the optimal polynomial order N chosen to model the QCD contribution in every region. It is important to note that the $\mathrm{VR}_{\mathrm{hyb}}$ slices are uniquely used to perform optimisation tests. The actual values of the QCD parameters are determined while performing the final measurements, by fitting the optimised model to the SR data.

Table 7.2: Optimal polynomial order N for the QCD function in each analysis region, as determined from the LLR, linearity and spurious signal tests (see Appendix C).

Region	Inclusive	250–450 GeV	450–650 GeV	650–1000 GeV	>1 TeV
SRL	5	–	5	4	4
SRS	5	5	4	5	–

7.3 Top Quark Production

Events with one or two top quarks in the final state represent the second largest background in the SR, corresponding to about 3% of the dominant QCD multijet background. Jets originating from a top quark decay usually contain the remnants of a b quark and the two hadronic decay products of a W boson. Since the W boson decays very rarely to final states including a b quark, most of the top jets populating the SR usually contain at least one mistagged subjet, namely a subjet that is b-tagged despite not being originated by a b quark.

In the analysis, the top quark background is generated by the $t\bar{t}$ pair production and single top quark production processes, which are discussed in this section. Of the two, $t\bar{t}$ is by far the larger contribution, accounting for around 91% of the top quark background in the SR, inclusively in p_{T}.

7.3.1 $t\bar{t}$ Pair Production

As described in Section 6.2, the shape of the $t\bar{t}$ pair production background is modelled using the nominal Powheg-Box v2 and Pythia 8 MC programs. Figure 7.9 shows the simulated $t\bar{t}$ distribution in the SRL and SRS, both inclusively and split into candidate jet p_{T} ranges. As expected, the inclusive distributions peak at the top quark mass ($m_t \approx 175$ GeV) in both regions and have a broad distribution with a long low-mass tail. In the SRS, this tail is mainly populated by events in the lowest p_{T} range, i.e. 250–450 GeV. This effect can be explained considering that, in this p_{T} range, a top quark is not boosted enough for its decay products to be clustered within a single large-R jet. For a top quark, containment within $R = 1.0$ is only expected when $p_{\mathrm{T}} \gtrsim 2m_t \approx 350$ GeV, meaning that a fraction of jets in the lowest p_{T} region will not fully reconstruct the top quark and will consequently have a lower mass.

Due to modelling uncertainties at high p_{T}, a data-driven determination of the $t\bar{t}$ normalisation is performed in the $\mathrm{CR}_{t\bar{t}}$, which targets events with semi-leptonic $t\bar{t}$ decays (see Section 6.3.2). The purpose of the $\mathrm{CR}_{t\bar{t}}$ is to provide a highly pure

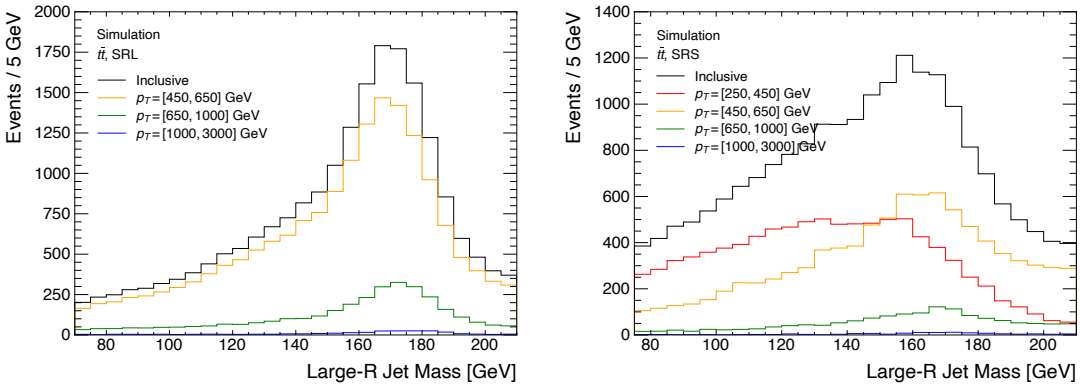

Figure 7.9: The inclusive and p_{T} binned components of simulated $t\bar{t}$ template shapes in the SRL (left) and SRS (right).

$t\bar{t}$ dataset where a precise determination of the $t\bar{t}$ yield can be performed, and the relative systematics can be constrained.

Figure 7.10 shows the probe-jet mass distribution in the inclusive $\mathrm{CR}_{t\bar{t}}$, both in data and simulations. The simulated distribution, which is split into stacked contributions from various processes, is seen to be dominated by $t\bar{t}$. Other minor contributions come from single top quark production and $W(\ell\nu)$ + jets events. Further details on the single top background are given later in this section. The $[140, 200]$ GeV probe-jet mass range used in all $\mathrm{CR}_{t\bar{t}}$ fits is chosen to fully contain the top quark peak, whilst excluding W boson contamination at lower mass.

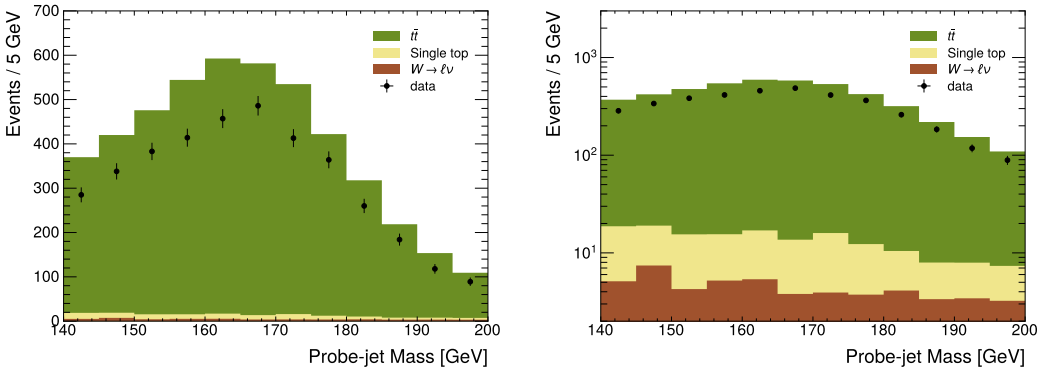

Figure 7.10: Probe-jet mass distribution in the inclusive $\mathrm{CR}_{t\bar{t}}$, both in data and simulation, represented using either a linear (left) or logarithmic (right) scale on the vertical axis of the plot. The simulated distribution is split into stacked contributions from the $t\bar{t}$, single top quark production and $W(\ell\nu)$ + jets processes.

As explained in Section 6.3.2, the $CR_{t\bar{t}}$ is designed and corrected to be kinematically equivalent to the SR. Since the two regions probe a comparable top quark momentum range, the shapes of the simulated $t\bar{t}$ mass distributions are similar and peak around the top quark mass. Therefore, any adjustment of the simulated $t\bar{t}$ events made to improve their agreement with data in the $CR_{t\bar{t}}$ can be directly applied to the SR, and no uncertainty on the extrapolation of the $t\bar{t}$ normalisation is needed. The $CR_{t\bar{t}}$ is used to constrain the $t\bar{t}$ yield in every measurement performed in the analysis. This is done by simultaneously fitting the signal regions and the $CR_{t\bar{t}}$, while keeping the $t\bar{t}$ signal strengths correlated. The high precision achievable in the $CR_{t\bar{t}}$ strongly constrains the $t\bar{t}$ yield in the SR.

Figure 7.11 shows the probe-jet mass distribution in each analysis p_{T} bin in the $CR_{t\bar{t}}$ after the binned likelihood fit described in Section 6.4.3, in the differential configuration. The simulation, shown with a 68% confidence level (CL) uncertainty band, is in good agreement with the data in every region.

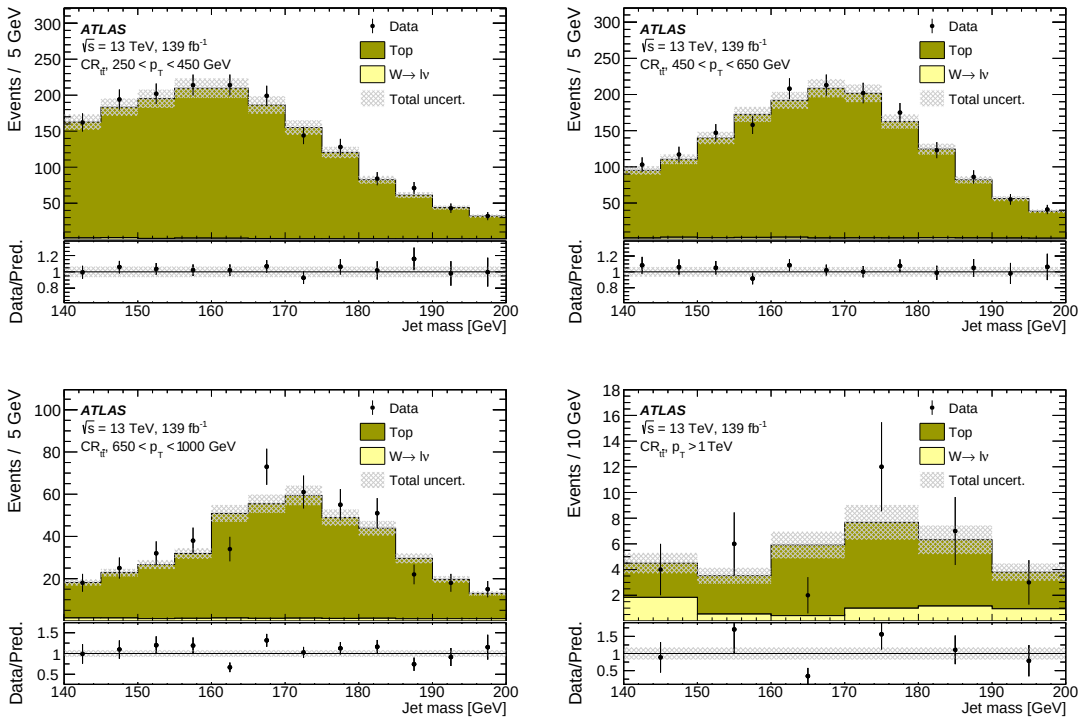

Figure 7.11: Post-fit $CR_{t\bar{t}}$ probe-jet mass distribution in the four p_{T} regions used in the differential fit. The $p_{\mathrm{T}} > 1$ TeV region is shown in larger 10 GeV mass bins. The shaded areas indicate the 68% CL for all background processes [1].

7.3.2 Single Top Quark Production

Events with a single top quark in the final state represent a small yet non-negligible background. For comparison, simulations indicate that the expected single top yield in the SR is 9% that of $t\bar{t}$, while this figure falls to around 2% in the $\text{CR}_{t\bar{t}}$.

Figure 7.12 shows the LO Feynman diagrams for the three main single top quark production modes: tW, t-channel and s-channel. Simulated samples of the single top quark background are produced using the POWHEG-BOX v2 and PYTHIA 8 MC programs. Figure 7.13 shows the simulated large-R jet mass distributions for the various single top quark production modes in the SR and $\text{CR}_{t\bar{t}}$. Single top quark production via tW and t-channel represent the dominant contributions, while production via s-channel is negligible in all analysis regions. As will be explained later in this section, the modelling of the single top quark process in the SR is done by means of $t\bar{t}$ templates, scaled to the single top quark yield expected from MC.

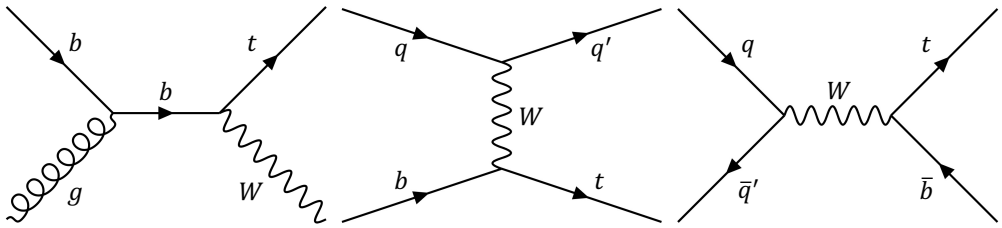

(a) Single top tW **(b)** Single top t-channel **(c)** Single top s-channel

Figure 7.12: Leading order Feynman diagrams for single top quark production in the tW channel (a), t-channel (b) and s-channel (c).

In MC calculations, NLO diagrams for the single top tW process interfere with LO $t\bar{t}$ diagrams. For example, the $gg \to \bar{t}t^* \to \bar{t}bW^+$ reaction[3] contributes at LO to $t\bar{t}$ and at NLO to single top tW. The interference term between the two processes is particularly sizable when the invariant mass of the bW^+ system is comparable to the mass of the top quark, which is realised in the kinematic regime of the analysis. The calculation of the interference term is particularly complicated, and two methods for estimating the tW process have been devised: the *diagram subtraction* (DS) and *diagram removal* (DR) schemes. Appendix D provides a brief description of how

[3]The t^* symbol refers to the fact that the top quark can be virtual in the reaction.

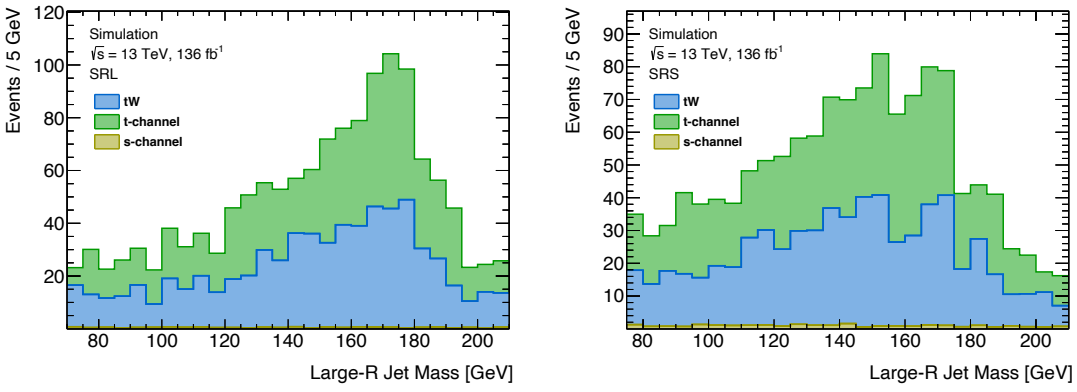

(a) Single top, SRL **(b)** Single top, SRS

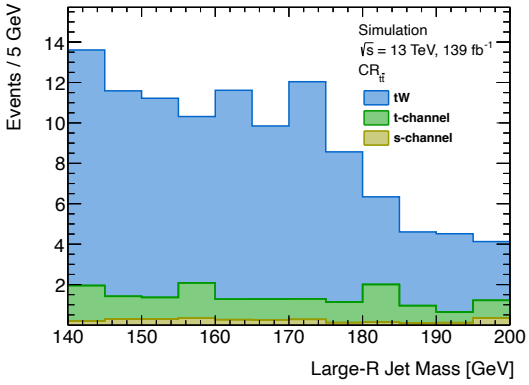

(c) Single top, $\mathrm{CR}_{t\bar{t}}$

Figure 7.13: Simulated single top mass distribution in the inclusive SRL (a), SRS (b) and $\mathrm{CR}_{t\bar{t}}$ (c). Stacked contributions from the tW, t-channel and s-channel production processes are also shown in different colours.

the two calculations are performed. By construction, the difference between the DS and DR predictions is proportional to the interference term with $t\bar{t}$.

Studies performed by the $VH(\rightarrow b\bar{b})$ analyses show that the single top tW process calculated using the DS scheme offers a better description of the data [106]. In the analysis presented in this thesis, the single top tW process is calculated using the DS scheme, which offers a mass distribution similar in shape to that calculated using DR, but with a ~50% lower yield. As shall be explained in Section 8.1.3, the difference between the DS and DR schemes is used as a systematic uncertainty on the modelling of the single top yield in the SRL, SRS and $\mathrm{CR}_{t\bar{t}}$.

A further challenge to the modelling of the single top background in the analysis is posed by the limited size of the corresponding MC samples. Since

the Higgs boson resonance overlaps with the single top mass distribution and the two processes have comparable yields, large bin-to-bin fluctuations in the mass models might induce biases in the signal extraction. Therefore, alternative modelling strategies are explored.

Figure 7.14 shows a comparison between the $t\bar{t}$ and single top candidate jet mass and p_{T} distributions in the SR, normalised to the same integral. For the single top tW process, only the top-matched component is shown, which is made up of events where the candidate jet is associated with a truth top quark (see Section 4.1.6). It is noted that the single top mass and p_{T} distributions are compatible with $t\bar{t}$ in shape.

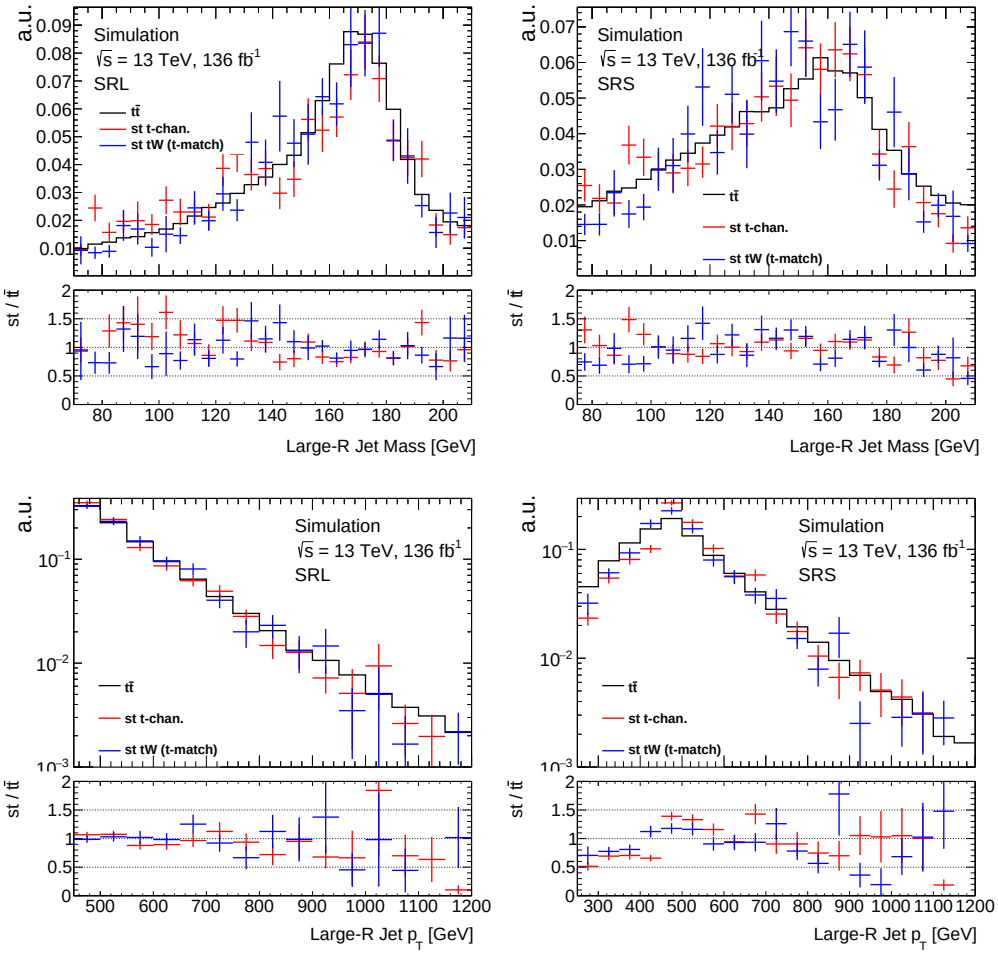

Figure 7.14: Simulated candidate jet mass (top) and p_{T} (bottom) distributions for the $t\bar{t}$ (black), single top t-channel (red) and single top top-matched tW (blue) processes, both in SRL (left) and SRS (right). All distributions are normalised to the same integral.

Given the kinematical equivalence, $t\bar{t}$ templates are used to describe the single top

t-channel process and the top-matched component of the tW process, respectively scaled to match the number of t-channel and top-matched tW events predicted by MC. This way, these processes are modelled using kinematically equivalent templates with much larger statistical accuracy. The fraction of tW events where the candidate jet is not associated with a truth top quark (non-top-matched) accounts for around 30% (20%) of the tW process in the SRL (SRS) and it follows a rather flat mass distribution. An ad hoc template modelling this contribution is not included and it is instead absorbed into the QCD description. These events indeed represent a negligible contribution (at most 0.04%) compared to the QCD multijet process and its statistical uncertainty, meaning that they can be incorporated within the flexible polynomial description of the QCD background.

In the signal regions, the single top process is thus modelled using the corresponding $t\bar{t}$ template, scaled to the single top-to-$t\bar{t}$ fraction estimated from simulations. In this calculation, only the single top t-channel and top-matched tW components are considered. Table 7.3 shows the single top-to-$t\bar{t}$ fractions obtained in each analysis signal region.

Table 7.3: Single top-to-$t\bar{t}$ fractions in the inclusive and differential signal regions for both the single top t-channel and top-matched tW processes.

Region	t-channel	tW (top-matched)
SRL	0.034 ± 0.001	0.023 ± 0.001
SRL1	0.035 ± 0.001	0.022 ± 0.001
SRL2	0.032 ± 0.003	0.024 ± 0.003
SRL3	0.046 ± 0.014	0.018 ± 0.009
SRS	0.034 ± 0.001	0.024 ± 0.001
SRS0	0.020 ± 0.001	0.021 ± 0.002
SRS1	0.046 ± 0.002	0.027 ± 0.002
SRS2	0.052 ± 0.006	0.031 ± 0.005

In the $\mathrm{CR}_{t\bar{t}}$, single top production is a much smaller contribution than in the SR, accounting for around 2% of the $t\bar{t}$ background. Furthermore, reducing template fluctuations is less crucial in this region since it is not directly used

for extracting the Higgs boson signal. The single top background in the $\mathrm{CR}_{t\bar{t}}$ is thus modelled using MC samples.

7.4 V + jets

A precise knowledge of the vector boson production in association with jets (V + jets) is of great importance as this background spans a vast portion of the mass measurement region. Despite peaking around the W and Z boson masses ($\approx [80, 90]$ GeV), the V + jets candidate jet mass spectrum in the SR is characterised by a long tail that extends deeply into the Higgs boson mass range (see Figure 7.1). A precise modelling of this process is thus crucial in preventing biases during signal extraction. In the SR and VR, the hadronic V + jets process is simulated using the Sherpa 2.2.8 generator, which also introduces NLO EW corrections as internal weights. NNLO QCD corrections are provided externally, and their use is described in Section 7.4.1. In the $\mathrm{CR}_{t\bar{t}}$, the minor $W(\ell\nu)$ + jets contribution is simulated using Sherpa 2.2.1.

Figure 7.15 shows the overlaid W + jets and Z + jets mass distributions contributing to the V + jets background process in the inclusive SR and VR. The composition of the V + jets background is seen to strongly depend on the analysis region. In the SR, the flavour tagging requirement favours $Z \to b\bar{b}$ events, which end up surpassing W events by more than a factor of three. Here, candidate jets from the W + jets process either reconstruct the W boson and have two mistagged subjets, or they reconstruct one of the associated jets. Consequently, the W + jets mass distribution shows a poor resolution and a long high-mass tail. In the VR, W + jets events outnumber Z + jets nearly three to one due to the larger cross-section and different acceptance.

Since the vector and Higgs bosons share a similar decay topology, the V + jets peak can be exploited to test the robustness of the background estimation and fitting procedure, before performing the Higgs measurement. The strategies used to extract the Higgs signal in each analysis region are first tested on the vector

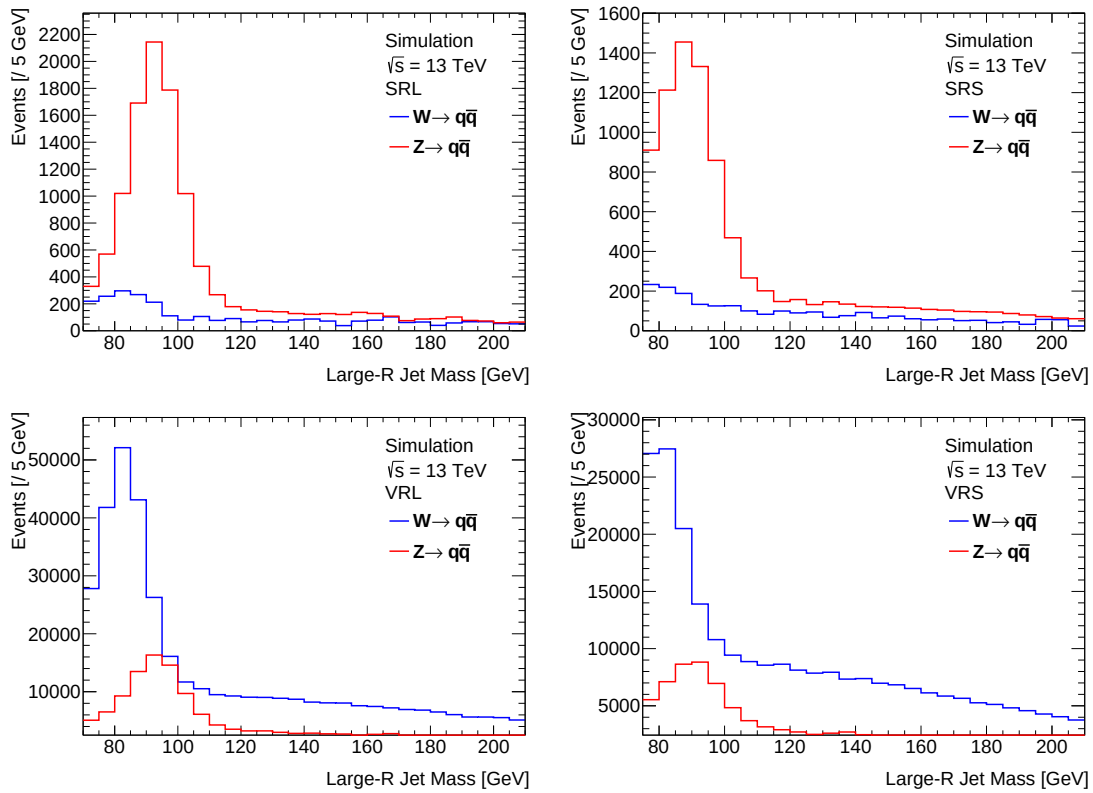

Figure 7.15: Breakdown of the V + jets candidate jet mass into W + jets and Z + jets in the inclusive leading (left) and subleading (right) signal (top) and validation (bottom) regions.

boson resonances in the VR and then in the SR, prior to unblinding the Higgs mass region. Further details on these validations will be given in Sections 8.4 and 9.5.1.

7.4.1 Higher-order Corrections

As previously discussed, the V + jets process is modelled in the analysis using the Sherpa 2.2.8 MC generator which provides LO EW accuracy, NLO QCD accuracy for up one extra parton and LO QCD accuracy for up to four extra partons. However, higher order EW and QCD corrections are available, and they can be introduced in the analysis in order to obtain a more precise estimate of the V + jets background.

Approximate NLO EW corrections are provided as internal weights by the Sherpa 2.2.8 generator, and they are seamlessly included in the V + jets models. These corrections have a sizable impact on the differential production cross-section as a function of the generated vector-boson momentum p_{T}^{V}. After the correction,

the V + jets yield is reduced by 10% to 20% going from 500 GeV to 1 TeV in p_{T}^{V}.

NNLO QCD corrections are also available [107], and they are provided externally to the SHERPA 2.2.8 generator. Their calculation for Z + jets events was performed at $\sqrt{s} = 8$ TeV by the NNLOJET group [108, 109], which also provided custom corrections for $\sqrt{s} = 13$ TeV. Within the Z boson p_{T} (p_{T}^{Z}) range probed by the analysis (from 300 GeV to over 1 TeV), the NNLO QCD corrections are seen to vary between 1% to 9%.

These corrections can be used to correct the Z signal strengths in the differential Z measurement (see Section 9.5.1), as they are calculated in bins of generated p_{T}^{Z}. In the case of Z boson measurements performed in bins of reconstructed jet p_{T}, the NNLO QCD corrections are averaged - or *folded* - considering the reconstructed p_{T} spectrum of the corresponding analysis region. The external QCD NNLO corrections are applied as multiplicative factors to the final Z boson results.

7.4.2 W Control Region Modelling

The W control region ($\mathrm{WCR}_{t\bar{t}}$) is aimed at performing an external measurement of the jet mass resolution of the V + jets process. Its event selection, which is defined in Section 6.3.3, targets semi-leptonic $t\bar{t}$ events where the W from the hadronic top quark decay is reconstructed into a single large-R jet called the "W candidate" ($W_{\mathrm{cand.}}$).

Figure 7.16a shows the pre-fit $W_{\mathrm{cand.}}$ mass distributions both for the data and simulated events populating the inclusive $\mathrm{WCR}_{t\bar{t}}$. The region constitutes a highly pure $t\bar{t}$ sample, with the largest background - single top quark production processes - accounting for only a few per cent. As expected, the single top tW background is found to be negligible, illustrating that the requirement for a near-by b-tagged jet to the W candidate is effective in reducing this background. Both in data and MC, the mass distributions peak at the W boson mass (≈ 80 GeV), with the data having a lower yield and a slightly better mass resolution.

The jet mass resolution measurements, described in Section 8.4, are carried out by fitting the MC model to the mass distribution in data, both inclusively and

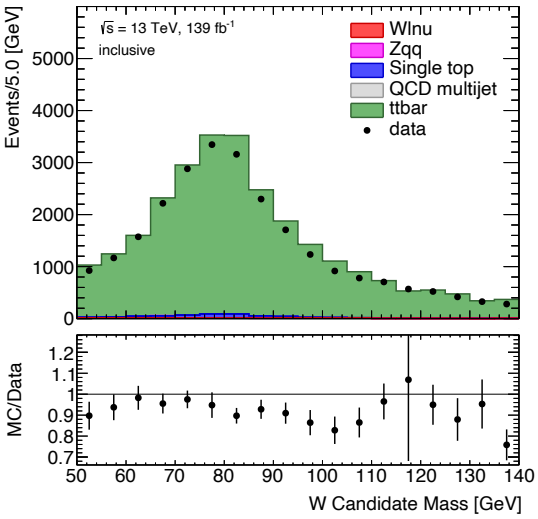

(a) Pre-fit $W_{\text{cand.}}$ mass distribution

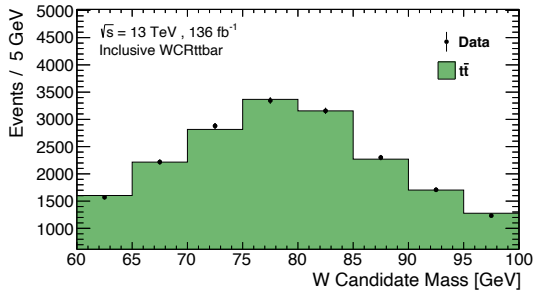

(b) Post-fit $W_{\text{cand.}}$ mass distribution

Figure 7.16: Pre-fit (a) and post-fit (b) W candidate mass distributions in the inclusive $\text{WCR}_{t\bar{t}}$, both in data (black dots) and simulation (coloured stacked histograms). The bottom panel of Figure (a) shows the ratio between the simulated and data mass distributions, as well as the extent of the uncertainties. In Figure (b), the mass window $60 < m^{W_{\text{cand.}}} < 100$ GeV is applied to the W candidate jet mass. The post-fit agreement between data and MC has a χ^2 probability of 0.76.

in various W candidate p_{T} ranges. For these fits, a W candidate mass window $60 < m^{W_{\text{cand.}}} < 100$ GeV is applied to further reduce the background contributions and isolate the desired jet topology. Extracted from the fits are the W boson signal strength μ_W, as well as the pulls and widths of the JMR and JMS nuisance parameters (see Section 8.1.1). The result of the fit to the inclusive $\text{WCR}_{t\bar{t}}$ is shown in Figure 7.16b. Very good agreement is observed between data and MC after the fit, having a χ^2 probability of 0.76.

8

Systematic Uncertainties

Contents

8.1 Sources of Systematic Uncertainties 138
8.1.1 Large-R Jet Uncertainties 138
8.1.2 Flavour Tagging Uncertainties 141
8.1.3 Modelling Uncertainties 143
8.1.4 Spurious Signal Uncertainties 147
8.2 Treatment of Systematic Uncertainties 148
8.2.1 Decorrelation of Systematics 150
8.2.2 Smoothing of Systematics 154
8.2.3 Pruning of Systematics 158
8.3 Gamma Parameters 161
8.4 V + jets Mass Resolution External Constraints 162

The measurements presented in this thesis can be regarded as counting experiments. The number of events in every bin of the candidate jet mass spectrum is Poisson distributed, such that the probability of counting N events in a bin, when μ are expected, is given by

$$P(N|\mu) = \frac{\mu^N e^{-\mu}}{N!}. \tag{8.1}$$

It follows that the statistical uncertainty on each bin is $\sqrt{N}$, namely the variance of a Poisson distributed random variable. As more data N are collected, the statistical uncertainty in any bin decreases as $1/\sqrt{N}$.

Not all uncertainties, however, depend on the collected sample size. Systematic uncertainties are introduced to describe the lack of knowledge about various experimental effects and theoretical shortcomings that might impact the measurement. For example, they can represent the lack of knowledge on how detector effects determine the reconstructed jet mass resolution, or account for approximations made during the MC calculations. In most situations, systematic uncertainties cannot be reduced simply by accumulating more data, but by a more precise understanding of the experimental setup of the analysis, i.e. by improving calibrations, upgrading the detector, performing more precise MC calculations, etc. In all measurement results, the statistical and systematic uncertainties are provided separately. Since the two components are independent, the total uncertainty can be obtained by summing them in quadrature.

As shall be discussed in Chapter 9, the relative importance of systematic uncertainties changes across analysis measurements. By dividing the number of available events in p_{T} bins, the uncertainties on most Higgs boson differential results are dominated by the statistical component (they are *statistically limited*)[1]. As such, the smaller systematic component plays a less crucial, yet non negligible, role.

On the other hand, systematic uncertainties have a stronger impact on the inclusive and fiducial Higgs and Z results, due to the larger number of events in the corresponding analysis regions. Furthermore, in all analysis measurements, the fitted $Z+\text{jets}$ and $t\bar{t}$ signal strengths are dominated by systematic uncertainties, due to their relatively large event yields in the signal regions (and $\mathrm{CR}_{t\bar{t}}$, in the case of $t\bar{t}$). This fact is important when considering that the precise modelling of these resonant processes is used to constrain the much larger QCD background, which, in turn, is strongly correlated with the Higgs boson signal strength. Therefore, developing a robust treatment of the systematic uncertainties that characterise the analysis is precursor to a trustworthy Higgs measurement.

[1]The SRL1 region ($450 < p_{\mathrm{T}} < 650$ GeV) is an exception due to the quite large number of events in this p_{T} range. In this case, the sizes of the statistical and systematic uncertainties are comparable.

This chapter describes the systematic uncertainties characterising the analysis and their treatment. Section 8.1 provides an overview of the sources of systematic uncertainties characterising the signal and background processes. Section 8.2 describes a series of procedures necessary before introducing the systematic uncertainties into the likelihood description. Section 8.3 explores the introduction in the fit of bin-specific nuisance parameters to take into account statistical noise in the templates. Finally, Section 8.4 describes the introduction of externally measured constraints on the vector boson jet mass resolution uncertainty, one of the most impactful systematics in the analysis.

Author's Contributions Section 8.1 largely provides factual information on the sources of systematic uncertainties characterising the analysis. Whilst extending the analysis to include the fiducial and differential regions, understanding and validating the corresponding fits, the author made extensive use of the uncertainty templates and their different sources. Some examples of this are given in Figures 8.1, 8.2 and 8.3. The author also provided an appropriate normalisation uncertainty for the single top quark process by studying its modelling under the *diagram subtraction* and *diagram removal* schemes. Decorrelation studies for this uncertainty, whose results are showcased in Section 8.2.1, constitute another individual contribution of the author.

The author carried out the optimisation of all smoothing thresholds as the analysis moved from a preliminary version using 0.5 GeV jet mass binning to its final version using 5 GeV binning. Such thresholds were also optimised by the author for the first time in the SRL3 and $\mathrm{CR}_{t\bar{t}}3$ regions, which were late additions to the analysis. Section 8.2.2 describes the smoothing procedure and the optimisation process performed by the author, using the $\mathrm{CR}_{t\bar{t}}3$ region as an illustrative example.

All results presented in Section 8.2.3 are direct contributions of the author, who took care of optimising the pruning thresholds in every region of the analysis.

Studies of the impact of gamma parameters on the fit results were carried out exclusively by the author, and the results are described in Section 8.3.

The determination of the $V+$jets mass resolution external constraints, presented in Section 8.4, was performed by other members of the analysis team. The main results are reported for completeness, given their importance in the convergence of the fit procedure.

8.1 Sources of Systematic Uncertainties

This section provides an overview of the systematic uncertainties that characterise the analysis measurements. The sources of uncertainty are grouped and divided into four categories: large-R jet uncertainties, flavour tagging uncertainties, modelling uncertainties and spurious signal uncertainties. Each group contains multiple sources, some of which are much more important than others.

Each uncertainty characterising a process can be split into two components: the *normalisation* component describes the uncertainty on the yield of the process, while the *shape* component quantifies the uncertainty on the shape of its mass distribution. This distinction is important as, in some cases, one of the two components can be neglected, thus simplifying the fit strategy (see Section 8.2.3).

8.1.1 Large-R Jet Uncertainties

Large-R jet uncertainties encompass some of the largest and most impactful systematics in the analysis. They can be subdivided into jet energy scale (JES), jet mass scale (JMS), jet energy resolution (JER) and jet mass resolution (JMR). Among these, the JMR and JMS uncertainties are dominant.

The JMS and JES uncertainties are derived from the calibration procedures described in Section 4.1.3. The JMS systematic is estimated with the R_{trk} method and it is described through the following 6 nuisance parameters:

- **Baseline:** difference between data and the nominal MC sample in the calibration (1 NP).
- **Modelling:** difference between nominal and alternative MC samples in the calibration (1 NP).

- **Tracking [1-3]:** uncertainties on the tracks used as a reference in the calibration (3 NPs).
- **TotalStat:** the statistical uncertainty on the calibration (1 NP).

Figure 8.1a shows the nominal Higgs boson mass template in the inclusive SRL, together with the $\pm 1\sigma$ variations from the JMS Modelling systematic. As expected, this JMS uncertainty acts on the position of the Higgs peak, with the upward (downward) variation moving it towards higher (lower) mass values.

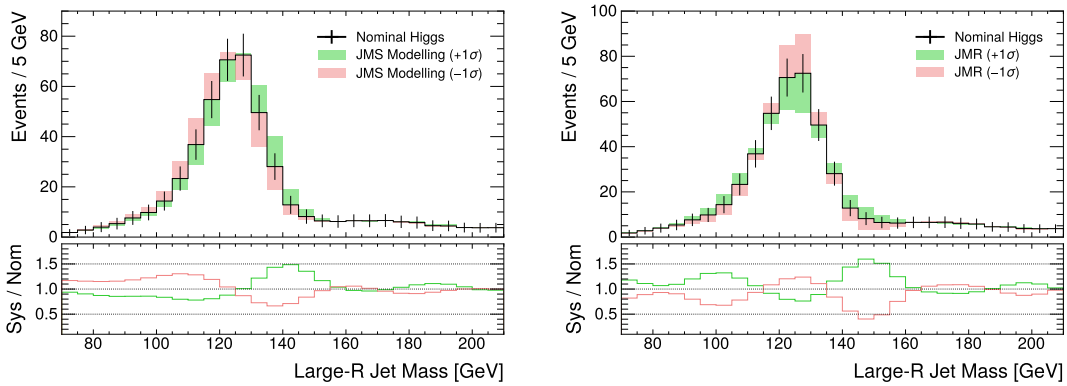

(a) Higgs JMS Modelling **(b)** Higgs JMR

Figure 8.1: Nominal Higgs boson mass template in the inclusive SRL, together with the $\pm 1\sigma$ variations from the JMS Modelling (a) and JMR (b) systematics. The black error bars represent the statistical uncertainty on the nominal distribution. The smoothing procedure described in Section 8.2.2 is applied to the systematic variations.

The JES uncertainty is estimated from two in-situ calibrations: the η inter-calibration and the jet p_{T} balance with respect to known reference objects (see Section 4.1.3). The uncertainty is described through the following 23 NPs:

- **JET Effective NP:** p_{T} balance calibrations (16 NPs).
- **Eta Intercalibration:** modelling, non-closure and statistical uncertainties related to the η intercalibration (3 NPs).
- **JET Flavour:** related to the jet quark-gluon fraction and to the calorimeter response for quarks vs. gluons (2 NPs). They only apply to jets that are truth-labelled as QCD-like.

- **JET Topology Uncertainty:** associated with the topology of top quark and vector boson jets (2 NPs). They are only applied to jets truth-associated to either a top quark or a vector boson.

Conservative estimates from Run 1 data [52] are used for modelling the JER and JMR uncertainties, as during analysis development the corresponding calibrations were not yet finalised. The JER and JMR uncertainties are, respectively, an absolute 2% on the large-R jet energy resolution and a relative 20% on the large-R jet mass resolution.

The JER uncertainty is computed by smearing the MC jet energy distribution using a gaussian with a width of 0.02 and taking the difference with respect to the unsmeared distribution. Since this uncertainty is found to be negligible in all analysis measurements, it is not included in the fit strategy. The JMR uncertainty is instead obtained by smearing the MC jet mass distribution such that the resolution is increased by 20%. This is achieved by smearing the MC using a gaussian with a width of $0.66\sigma_{\text{nominal}}$, where σ_{nominal} is the jet mass resolution of the nominal MC sample.

By definition, the JMR uncertainty is *one-sided*, meaning that the smearing procedure described above only provides the $+1\sigma$ variation. The way such systematics should be treated is subject of debate in the scientific community. Nevertheless, in agreement with ATLAS recommendations, the -1σ variation is created by symmetrising the smeared distribution with respect to the nominal one. The extent of the Higgs JMR uncertainty variations in the inclusive SRL is shown in Figure 8.1b. As expected, the upward variation produces a mass distribution with a wider Higgs mass peak and thus a worse mass resolution.

At the time of writing, the JER and JMR calibrations have been finalised and recommendations for the corresponding uncertainties are available. The new estimates are found to be approximately 50% smaller than those used in the analysis [110].

8.1.2 Flavour Tagging Uncertainties

The flavour tagging uncertainties are obtained from the MV2c10 b-tagging calibration described in Section 4.2.1. The calibration provides systematic uncertainties for three variables of interest: the b-tagging efficiency scale factors, and the c-jet and light-jet mistagging rates. The eigenvector decomposition method described in Section 8.3 of Reference [111] is used to reduce the number of individual sources of systematic uncertainty characterising the calibration, while preserving the correct dependence on track jet p_{T}.

For each of the variables of interest introduced above, the method starts by summing together the covariance matrices related to each source of systematic uncertainty, as functions of the track jet p_{T}. The dimension of the matrices is equal to the track jet p_{T} binning used the calibration. Therefore, the covariance matrices of the b-tagging efficiency scale factors and light-jet mistagging rate have dimension 5, while that of the c-jet mistagging rate has dimension 4. The covariance matrix summation is performed to preserve the correlations amongst p_{T} bins of each systematic uncertainty. As the total covariance matrix is symmetric and positive-definite, an eigenvector decomposition can be performed.

Therefore, the method provides 5 systematic *eigen-variations* both for the b-tagging efficiency scale factors (Eigen B[0-4]) and light-jet mistagging rate (Eigen L[0-4]), and 4 for the c-jet mistagging rate (Eigen C[0-3]). These Eigen B, C and L variations are applied, respectively, to track jets that are truth labelled as either b-, c- or light-jets.

In order to extend the MV2 calibrations to high track jet p_{T}, a MC-based extrapolation is performed. A nuisance parameter is introduced in the analysis to take into account the uncertainty on the extrapolation procedure, which starts having a sizable impact for large-R jet $p_{\mathrm{T}} > 400$ GeV.

One final NP is associated with the uncertainty on the extrapolation of the τ-jet mistagging rate from the c-jet mistagging rate. This systematic, which is exclusively applied to track jets that are truth-associated to a τ lepton, is found to be negligible in the analysis, and it is not included in the likelihood description (see Section 8.2.3).

In summary, the flavour tagging uncertainties are described by the following 15 NPs:

- **Eigen B[0-4]:** uncertainties on the b-tagging efficiency scale factors (5 NPs).
- **Eigen C[0-3]:** uncertainties on the c-jet mistagging rate (4 NPs).
- **Eigen L[0-4]:** uncertainties on the light-jet mistagging rate (5 NPs).
- **Extrapolation:** uncertainty on the extrapolation of the flavour tagging calibrations to high track jet p_{T} (1 NP).

In the inclusive SRL, Figure 8.2 shows the extent of the Eigen B0 uncertainty for the Higgs boson, and of the Eigen L0 uncertainty for the W + jets process. These are amongst the largest flavour tagging variations observed in the analysis, and they correspond to average absolute variations of around 5% and 14%, respectively. The effect of each flavour tagging uncertainty variation is stored as an additional weight for each MC event, and thus their impact on any distribution is given by the sum of the events so weighted.

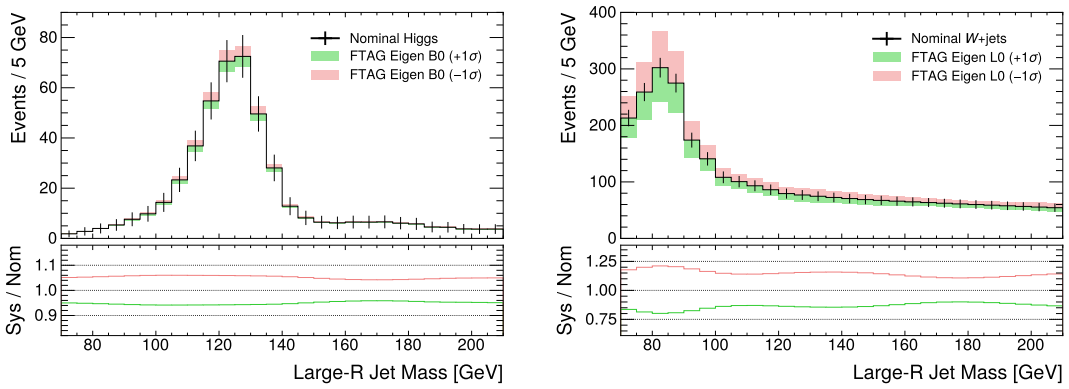

(a) Higgs FTAG Eigen B0 **(b)** W + jets FTAG Eigen L0

Figure 8.2: Examples of some of the largest flavour tagging uncertainties in the inclusive SRL. Figure (a) shows the extent of the 0th component of the b-tagging efficiency scale factor uncertainty (Eigen B0) on the Higgs boson mass template. Figure (b) instead shows the extent of the 0th component of the light-jet mistagging rate (Eigen L0) on the W + jets mass template. The black error bars represent the statistical uncertainty on the nominal distribution. The smoothing procedure described in Section 8.2.2 is applied to the systematic variations.

8.1.3 Modelling Uncertainties

Modelling uncertainties are introduced by the MC models used to simulate the signal and background processes. Uncertainties are associated with the theoretical predictions and to the approximations made during the MC computations. These include uncertainties on the cross-section and acceptance of a process, on the choice of the renormalisation and factorisation scales[2], on the amount of initial- and final-state radiation, on the extent of the NLO electroweak corrections, and on the choice of generators.

In the following, a brief description of the most important modelling uncertainties characterising the signal and background processes is given.

Higgs Boson Modelling Uncertainties

Modelling uncertainties on the Higgs boson are estimated independently for each production mode. They include uncertainties on the choice of the renormalisation and factorisation scales (μ_R and μ_F), PDF, parton shower model, and on the extent of the EW corrections.

The uncertainty associated with the choice of μ_R and μ_F is estimated using the 7-point scale variation method [112]. This is performed by considering seven independent pairs of μ_R and μ_F variations by factors of 0.5 and 2, and comparing the resulting mass distributions to the nominal ones.

For the ggF process, the μ_R and μ_F scale variations are flat both in Higgs jet mass and p_{T}, and can be described with a 2% normalisation uncertainty. The uncertainty associated with the choice of PDF is estimated by comparing the nominal mass distribution to the one obtained using the alternative PDF4LHC15 [113] PDF set. The comparison shows a flat 10% difference both in Higgs boson mass and p_{T}. When estimating the parton shower systematic, no substantial difference is observed when comparing the nominal ggF Higgs mass distribution with the one

[2]In MC simulations, the factorisation scale μ_F and renormalisation scale μ_R are two cut-off scales on the virtuality of intermediate particles and they separate short-distance from long-distance QCD effects. Substructures of loops and real emissions below these scales are only approximated. Calculations performed to higher orders of α_S are less sensitive to the choice of μ_F and μ_R.

obtained using the alternative HERWIG 7 [114] parton shower model. In conclusion, a conservative 20% normalisation uncertainty is considered on the ggF process, accounting for all the effects listed above.

For the VBF, VH, and $t\bar{t}$H production processes, the μ_R and μ_F scale variations can be described with flat 0.5%, 5%, and 13% normalisation uncertainties, respectively. Systematic uncertainties on the EW corrections (expressed as $1 + \delta_{\text{EW}}$) are taken as δ^2_{EW}, following the recommendations in Reference [115]. They range between 2%-6% in normalisation and they are correlated among all three production modes.

All modelling uncertainties are found to be flat in Higgs jet p_{T} and mass, and, therefore, they are treated as normalisation-only (acceptance) uncertainties. Since these uncertainties are not expected to be constrained by the fit, they are not introduced in the likelihood definition, but they are directly summed in quadrature to the systematic uncertainty of the final Higgs signal strength results.

$t\bar{t}$ Modelling Uncertainties

For the $t\bar{t}$ process, comparisons between nominal and alternative simulated samples provide systematic uncertainty estimates for the parton shower (PS) model (HERWIG 7 replaces PYTHIA 8) and the matrix element (ME) calculation (MadGraph5 [116] replaces POWHEG-BOX v2). Similarly to the JMR uncertainty, the PS and ME variations are one-sided. Therefore, the corresponding -1σ variation is obtained by symmetrisation with respect to the nominal distribution.

In the inclusive SRL, Figure 8.3 shows the nominal $t\bar{t}$ mass template together with the PS and ME $\pm 1\sigma$ variations. These systematics are the largest in the analysis, showing average absolute variations of around 18% and 13%, respectively for PS and ME. In the $\text{CR}_{t\bar{t}}$, the impact of modelling uncertainties is expected to be reduced by virtue of its high purity in terms of well-reconstructed top quark jets. This is particularly evident for the PS and ME systematics, whose variations respectively fall to around 7% and 3% in the inclusive $\text{CR}_{t\bar{t}}$. Thanks to the high precision $t\bar{t}$ measurements achievable in the region, the PS and ME systematics

are expected to be constrained quite strongly in the analysis measurements, where the SR regions are always simultaneously fitted with the $CR_{t\bar{t}}$.

Uncertainties associated with the amount of initial- and final-state radiation (ISR and FSR) are estimated by varying internal weights provided in the nominal sample. Across signal regions, the average absolute variations for these systematics are found to range between 1% and 7%.

Similarly to ISR and FSR, internal weight variations are used to estimate uncertainties on the choice of μ_R and μ_F, but they are found to be negligible in all analysis regions.

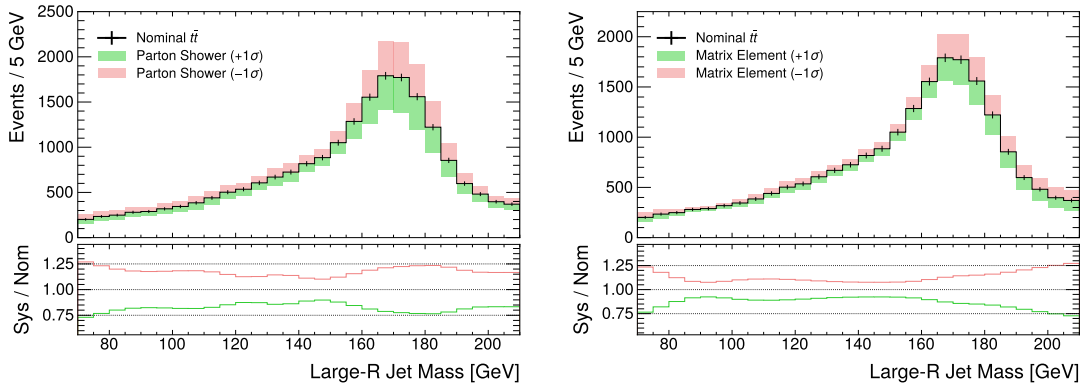

(a) $t\bar{t}$ Parton Shower Variation **(b)** $t\bar{t}$ Matrix Element Variation

Figure 8.3: Nominal $t\bar{t}$ mass template in the inclusive SRL, together with the $\pm 1\sigma$ variations from the Parton Shower (a) and Matrix Element (b) systematics. The black error bars represent the statistical uncertainty on the nominal distribution. The smoothing procedure described in Section 8.2.2 is applied to the systematic variations.

V + jets Modelling Uncertainties

The largest modelling uncertainties characterising the V + jets process are those associated with the renormalisation and factorisation scales. Similarly to the Higgs boson, these are estimated using the 7-point method, and are found to range between 3%-20% across analysis regions.

Following the studies shown in Figure 6 of Reference [117], a 10% uncertainty on the W + jets normalisation is introduced in the SR to account for cross-section uncertainties.

Uncertainties associated with a different choice of PDF set (MMHT2014 [118] replaces NNPDF3.0), α_S variations within the nominal PDF set, and different choice of fragmentation model (Lund string model [119] replaces SHERPA) are found to be negligible.

In the $\mathrm{CR}_{t\bar{t}}$, the minor $W+$jets background contribution, referred to as $W(\ell\nu)+$ jets, is composed of events where a leptonically-decaying W boson is produced in association with one or more jets. Due to the selection requirements of the $\mathrm{CR}_{t\bar{t}}$, however, the probe-jet does not reconstruct the W, but one of the associated hadronic jets. Given the large modelling uncertainties characterising QCD processes, the 10% normalisation uncertainty introduced on the $W+$jets process in the SR is inflated to a conservative 30% in the $\mathrm{CR}_{t\bar{t}}$. Studies performed on Asimov samples show that this change has negligible impact on the expected results. In addition, due to the different reconstructed topologies, the normalisation uncertainty on $W+$jets is described using independent nuisance parameters in the SR and $\mathrm{CR}_{t\bar{t}}$.

Single Top Modelling Uncertainties

As previously discussed in Section 7.3.2, studies performed by analyses probing a similar phase space indicate that the DS scheme provides a more accurate description of the data. For this reason, the DS description is chosen as the baseline model of the single top tW process. However, a systematic uncertainty must be introduced to account for the lack of knowledge on the impact of the interference term between tW at NLO and $t\bar{t}$. This systematic is estimated by considering the difference between the DS and DR descriptions of the tW process. By construction, this difference is, in fact, proportional to the interference term in the phase space probed by the analysis.

Both in the SRL and SRS, Figure 8.4 shows the candidate jet mass distributions of the single top tW component obtained using the DS and DR schemes. Candidate jets are also required to be truth-associated to a top quark. It is noted that the DS/DR ratio is roughly flat around 0.4-0.6. Values in this range are obtained in all analysis signal regions.

Following this observation, a conservative, flat 50% uncertainty is applied to the estimated number of single top events in all analysis regions. Following the decorrelation studies presented in Section 8.2.1, these normalisation uncertainties are kept fully correlated across regions (i.e. they are described by a single NP in the fit).

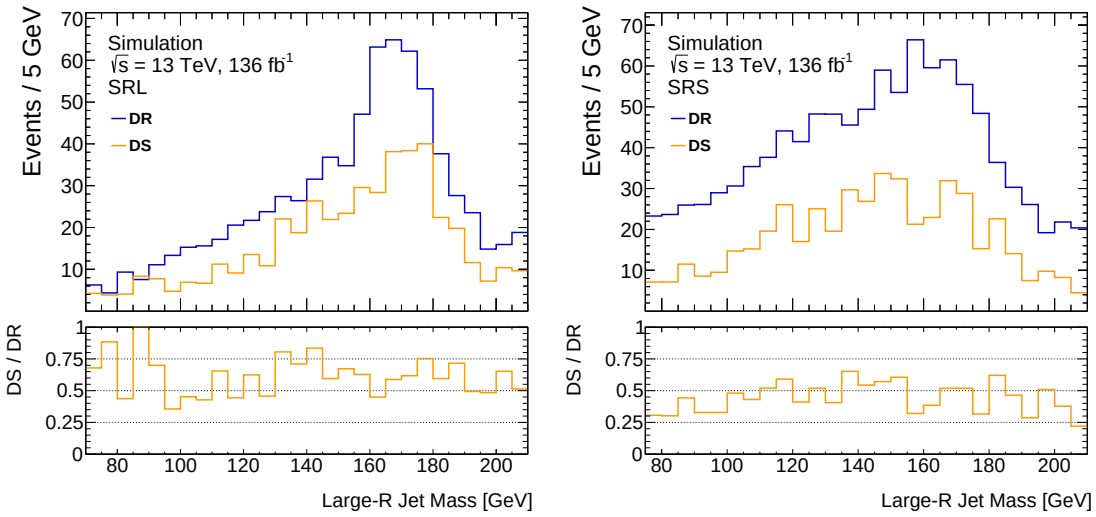

Figure 8.4: Candidate jet mass distributions of single top tW component obtained using the DS and DR schemes, both in the inclusive SRL (left) and SRS (right). Candidate jets are required to be truth-associated to a top quark.

8.1.4 Spurious Signal Uncertainties

The choice of the QCD functional form and polynomial order has an impact on the extraction of the Higgs and Z boson signals. The corresponding systematic uncertainty is estimated by performing a spurious signal test (see Appendix C) using the optimal QCD model. This spurious signal uncertainty, σ_{SS}, is defined as

$$\sigma_{\mathrm{SS}} = \left\langle \frac{\mu^{\mathrm{VR_{hyb}}}}{\sigma_{\mathrm{stat}}^{\mathrm{VR_{hyb}}}} \right\rangle \cdot \sigma_{\mathrm{stat}}^{\mathrm{A,\,SR}}, \tag{8.2}$$

where $\left\langle \frac{\mu^{\mathrm{VR_{hyb}}}}{\sigma_{\mathrm{stat}}^{\mathrm{VR_{hyb}}}} \right\rangle$ is the average spurious signal significance from tests on $\mathrm{VR_{hyb}}$ slices, and $\sigma_{\mathrm{stat}}^{\mathrm{A,\,SR}}$ is the expected statistical uncertainty on the signal strength μ derived from fits to SR Asimov data.

The spurious signal uncertainty is not included in the fit procedure, but added in quadrature to the systematic uncertainty of the signal strength results. This

is done as the fit is not expected to strongly constrain this flat systematic, which would only add noise to the statistical procedure. As σ_{SS} is at most $0.01\sigma_{\mathrm{stat}}^{\mathrm{A,\,SR}}$ and $0.65\sigma_{\mathrm{stat}}^{\mathrm{A,\,SR}}$ for the Higgs and Z boson measurements respectively, the spurious signal systematic has a minor impact on the total sensitivity. This uncertainty is independently estimated for the Higgs and Z boson signal strengths in each analysis region (both in the SRL and SRS, and in each p_{T} bin).

8.2 Treatment of Systematic Uncertainties

This section describes a series of procedures that are applied to systematics before their introduction into the likelihood description. These have the purpose of creating a set of robust, trustworthy systematic uncertainties, that nonetheless maintain the computing time of the fit to a reasonable level.

The procedures and studies presented in the remainder of this thesis make use of a few important tools: *correlation matrices*, nuisance parameters *pulls widths*, and nuisance parameters *impact rankings*.

Correlation Matrices The best estimates of the free parameters in the analysis fits are determined by minimising the NLL, as described in Section 6.4.3. Changes in the value of one parameter generally influences the others. Correlations quantify how big this effect is for any pair of free parameters in the fit.

The MINUIT program used to perform the NLL minimisation provides the covariance $cov(x, y)$ of any pair of parameters x and y that are free floating in the fit. Correspondingly, the correlation $corr(x, y)$ between the two parameters is defined as

$$corr(x, y) = \frac{cov(x, y)}{\sigma_x \sigma_y}, \tag{8.3}$$

where σ_x and σ_y respectively are the post-fit uncertainties on parameters x and y.

By construction, correlations are defined between -1 and $+1$. A positive correlation signifies that to a change of a parameter in one direction would correspond to a variation of the other in the same direction. If the correlation is negative, variations are instead in opposite directions.

The correlations between the free parameters of a fit can be arranged into a *correlation matrix*. This matrix is symmetric ($corr(x, y) = corr(y, x)$) and has diagonal values equal to 1 ($corr(x, x) = cov(x, x)/\sigma_x^2 = 1$). The correlation matrix can be used to conveniently visualise the most important parameters in the determination of a given POI, or to identify undesired effects or unnatural fit solutions (an example of this is given in Section 8.4).

Nuisance Parameters Pulls and Widths In a fit, the pull of a nuisance parameter (NP) is defined as

$$\text{pull} = \frac{\hat{\theta} - \theta_0}{\sigma_\theta}, \tag{8.4}$$

where $\hat{\theta}$ and θ_0 are, respectively, the post-fit and pre-fit values of the NP, and σ_θ is the pre-fit uncertainty on the NP in the direction of the pull.

A NP pull quantifies how significantly the data prefers the systematic uncertainty description compared to the nominal description. For example, a $+1\sigma$ pull in JMR indicates that the data prefers the description offered by the $+1\sigma$ variation of the jet mass resolution uncertainty.

A *width* is always associated to a pull, describing the extent of the uncertainty after the fit. By using the data and the correlations between the parameters, a fit is often times able to change (usually constrain) the uncertainties on the NPs. This is called *profiling*.

In the thesis, nuisance parameter pulls and widths are arranged as in Figure 8.5. For each NP listed on the y-axis, the corresponding pull is represented as a dot on the x-axis. In the figure, Nuisance Parameter A has a positive pull, while B a negative one. Widths are instead represented by the error bar associated with each dot. Constrained NPs have a post-fit width that is smaller than the pre-fit $\pm1\sigma$ uncertainty, represented by the green band. In the figure, Nuisance Parameter A is constrained, while B is under-constrained.

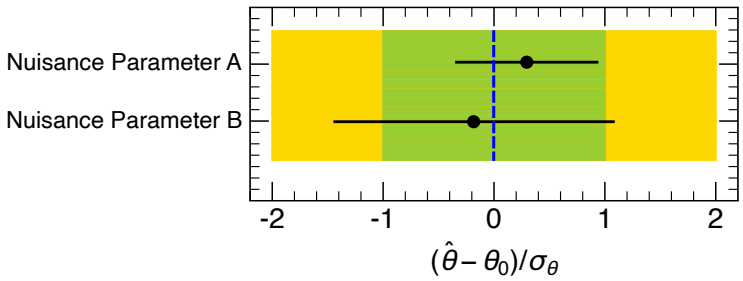

Figure 8.5: Example of a pull plot. For each NP listed on the y-axis, the corresponding pull is represented as a dot along the x-axis, while the associated error bar indicates the post-fit width. The green and yellow bands represent, respectively, the pre-fit $\pm 1\sigma$ and $\pm 2\sigma$ uncertainties.

Nuisance Parameters Impact Rankings Given a parameter of interest μ, it is sometimes instructive to know which fit parameters affect its determination the most. The impact of any given NP θ_i on a parameter of interest μ is defined as

$$\text{impact}_\mu = \frac{\mu(\theta_i^{\text{fixed}}) - \hat{\mu}}{\hat{\mu}}, \tag{8.5}$$

where $\hat{\mu}$ is the best-fit value of μ obtained from minimising the NLL, and $\mu(\theta_i^{\text{fixed}})$ is the best-fit value of μ obtained when the NP in question is fixed to its $+1\sigma$ or -1σ value. For any POI, a nuisance parameter impact ranking can be created by sorting the NPs according to their impact values.

8.2.1 Decorrelation of Systematics

In the analysis measurements, most systematic uncertainties are fully correlated across regions, processes and p_{T} bins, meaning that they are described by a single NP in the fit. This full uncertainty correlation significantly reduces the fit complexity, and it is often times a safe assumption, especially considering that systematic uncertainties are usually provided as functions of large-R jet p_{T}.

This assumption, however, has limitations, and biases in the fit results might be introduced if the data is able to strongly constrain systematics in some p_{T} regions, or for some processes. When described by a single NP, a strong constraint determined in one region, or for one process, is immediately applied to any other region or process, where that constraint might not be valid. The description of

highly constrained systematics is usually performed through multiple NPs, each independently acting on a specific process, or in a specific reconstructed jet p_{T} bin. This process is called systematic *decorrelation*, and it is motivated by the desire to avoid transferring constraints to topologies and regimes where they may not be valid.

The need to decorrelate systematics is tested by comparing fit results obtained with the correlated and decorrelated schemes. To this purpose, two indicators are particularly useful: the variations in POI significance ($|\Delta\mu|/\sigma$) and the variations in pulls and widths. The first indicator is measured in data fits, making sure that the values of the POIs are kept blinded at all times (only looking at variations $|\Delta\mu|$ is allowed). All decorrelation studies made use of *smoothed* systematics, which are obtained following the procedure outlined in Section 8.2.2.

Table 8.1 summarises the systematic uncertainties included within the profile likelihood used in the analysis measurements. For a given uncertainty, the second column lists each process which has independent nuisance parameters within the likelihood. In case multiple processes are listed, the uncertainty is said to be decorrelated across processes. Otherwise, the word "all" refers to a fully correlated systematic across processes. The third column shows whether a systematic is decorrelated across p_{T} bins or not (all). Finally, the fourth column indicates whether the NPs describing a systematic uncertainty can induce a change in normalisation (N), in the shape of the mass distribution (S), or both (N+S). Further details on the normalisation and shape components of systematics are given in Section 8.2.3.

In the next section, the decorrelation studies performed by the author on the single top normalisation uncertainty are described. Details on the decorrelation studies for the dominant systematic uncertainties characterising the analysis, JMR and JMS, are provided in Appendix E.

Single Top Decorrelation Studies

This section describes the decorrelation studies for the flat 50% systematic uncertainty on the single top normalisation. In the default setup, this uncertainty is fully correlated across regions in the fit (i.e. in an inclusive fit it is described by

Table 8.1: Summary of the systematic uncertainties included within the profile likelihood for the H and Z signal strength extraction. For a given uncertainty, the second column lists each process having an independent NP within the likelihood. The third column describes how the systematic uncertainty is correlated across regions: "all" indicates a fully correlated parameter, "p_{T} bins" indicates a decorrelation between the analysis p_{T} bins, and "LS" means it is decorrelated between the SRL and SRS (see Section 8.2.1). For the inclusive and fiducial analysis configurations, "p_{T} bins" does not apply, and should be understood to mean the same as "all". The fourth column describes the change induced by the parameter. "S" means the mass shape will change while "N" denotes parameters which change the normalization and can result in a migration of events between regions. The table does not show modelling uncertainties that were found to be negligible and thus not included in the fit. $(*)$ Two minor components separately apply to $t\bar{t}$ and $V+\mathrm{jets}$ events. $(\bullet)$ For cross-section limits and measurements, this uncertainty covers relative acceptance across regions instead of the absolute cross-section uncertainty.

Description	Processes	Category	Effect
Reconstructed object systematic uncertainties			
JMR	$t\bar{t}$ | $V+\mathrm{jets}$ | H	p_{T} bins	N+S
JMS Modelling	$t\bar{t}$ | $V+\mathrm{jets}$ | H	p_{T} bins	N+S
JMS (other)	$t\bar{t}$ | $V+\mathrm{jets}$, H	all	N+S
JES	all$^{(*)}$	all	N+S
JER	all	all	N+S
b-jet efficiency	all	all	N+S
c-jet rejection	all	all	N+S
light-jet rejection	all	all	N+S
Process modelling systematic uncertainties			
Renormalisation and factorisation scale	$V+\mathrm{jets}$	all	N+S
Parton shower model	$t\bar{t}$	all	N+S
Matrix element calculation	$t\bar{t}$	all	N+S
Initial- and final-state radiation	$t\bar{t}$	all	N+S
Cross-section and acceptance	$W+\mathrm{jets}$	all	N
	$H^{(\bullet)}$	all	N
	single top	all	N
	$W(\ell\nu)+\mathrm{jets}$	all	N
NLO EW corrections	VBF, VH, $t\bar{t}$H	all	N
Spurious signal	H	p_{T}^{H} bins $\times$ LS	N
	$Z+\mathrm{jets}$	p_{T}^{Z} bins $\times$ LS	N

the same NP in the SRL, SRS and CR$_{t\bar{t}}$). A full decorrelation scheme is tested, where the single top normalisation uncertainty is decorrelated across regions (and across p_{T} bins in the differential setup).

No variations in POI significance are observed when comparing the two correlation schemes on differential H data fits. In the SR, this is explained considering that the single top model is built as scaled-down version of the $t\bar{t}$ template. Since the single top and $t\bar{t}$ backgrounds inhabit the same mass range and have the same shape, it is natural for the fit to not have any constraining power on the much smaller single top background. The same argument is valid in the $\mathrm{CR}_{t\bar{t}}$, where the single top template is obtained from ad-hoc MC samples, but its shape is similar to $t\bar{t}$. The single top yield in the $\mathrm{CR}_{t\bar{t}}$ is also a much smaller fraction than in the SR: its yield amounts to around 2% of $t\bar{t}$ in the $\mathrm{CR}_{t\bar{t}}$, while this figure reaches 9% in the SR.

Figure 8.6 shows that systematic uncertainty pulls in the differential Higgs measurement are mostly unaffected by the choice of decorrelation scheme, with a minor effect only visible on the $\mathrm{CR}_{t\bar{t}}$ single top normalisation NPs. All other NPs (not shown in the picture) are also entirely unaffected by the choice of single top decorrelation scheme.

Since studies confirm that all measurements are unaffected by the choice of correlation scheme, the simpler fully-correlated option is chosen.

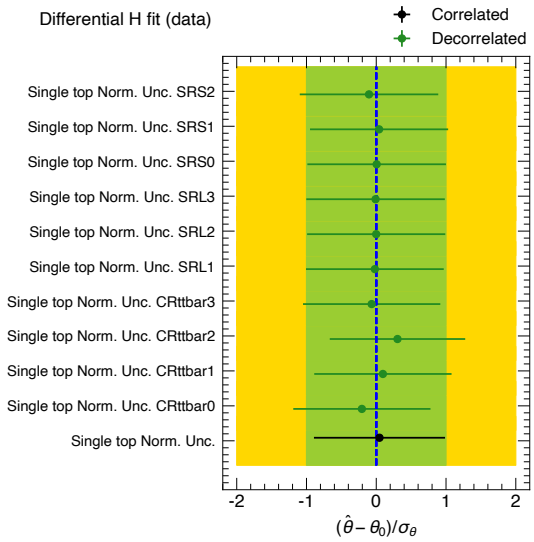

Figure 8.6: Single top normalisation uncertainty pulls and widths in a differential Higgs fit to data. Results are shown both in the fully-correlated scheme (black) and when the single top normalisation uncertainty is decorrelated across regions (green).

8.2.2 Smoothing of Systematics

The analysis presented in this thesis aims at performing measurements over a wide large-R jet p_{T} range, up to and above 1 TeV. In some analysis regions, especially in the differential high-p_{T} ones, the MC samples used for modelling the systematics might have few statistics, leading to large bin-by-bin fluctuations.

This effect needs to be controlled in order to give the fit a stable uncertainty model with minimal statistical noise. Large fluctuations in the systematic uncertainty distributions might be interpreted by the fit as physical features. The fit then can pull and profile uncertainties and parameters describing the nominal processes to accommodate such features, making the measurement untrustworthy. For this reason, a custom systematic *smoothing* algorithm is developed, which is described in this section.

It is natural to develop and study the systematic smoothing procedure in the $\mathrm{CR}_{t\bar{t}}$. This region is, in fact, unblinded from the start, allowing fits to be run both on Asimov and data samples. For a standalone $\mathrm{CR}_{t\bar{t}}3$ ($p_{\mathrm{T}} > 1$ TeV) fit, Figure 8.7 shows the pulls of some of the most important systematics, both in data and Asimov. The presence of strong systematic constraints in data is in part explained by the high purity of the $\mathrm{CR}_{t\bar{t}}$ sample, allowing for a precise $t\bar{t}$ measurement. However, as shall be demonstrated later in this section, such strong constraints can also be an indication of large statistical fluctuations in the systematic samples. The smoothing procedure is used to combat this issue, making the fit more stable and the results trustworthy.

The Procedure

The smoothing procedure was developed internally to the analysis, and it is applied to the ratio of the nominal templates and their systematic uncertainties. The aim is to produce smooth uncertainties that nonetheless retain all physical features that might be present along their mass spectrum.

For any systematic uncertainty, the procedure starts by taking its ratio to the nominal template. In order to reduce fluctuations, the ratio is rebinned into a

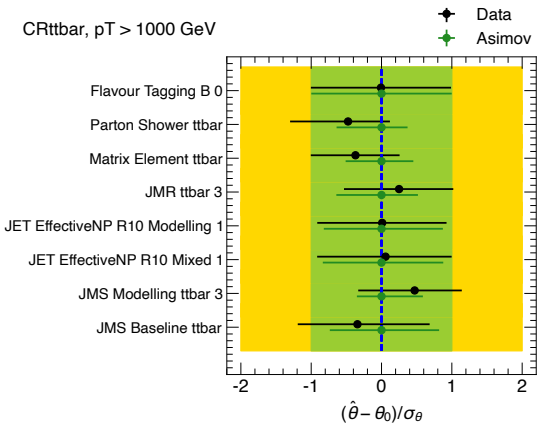

Figure 8.7: Post-fit pulls and width of some of the most important systematic uncertainties from standalone $\mathrm{CR}_{t\bar{t}}3$ ($p_{\mathrm{T}} > 1$ TeV) fits to Asimov and data, without systematic uncertainty smoothing.

histogram with variable size bins. The variable binning proceeds by merging bins low-to-high mass until the relative statistical uncertainty in the bin is lower than a custom threshold t. In order to improve the robustness of the procedure, the threshold is made bin-dependent by multiplying it to the number of bins that are merged (tN_{bins}) in the construction of the given bin. In this way, the statistical uncertainty requirement is loosened on larger bins, making the smoothing less sensitive to small changes in the threshold value.

The rebinned ratio histogram is then fit with a spline[3], which is used for interpolating the central values of the ratio histograms, resulting in a smooth function. Figure 8.8a shows the result of a spline fit to the Top JMR-to-nominal ratio distribution in the $\mathrm{CR}_{t\bar{t}}3$ region. Next, the spline is sampled into a histogram with a uniform 5 GeV binning, resulting in a smoothed version of the original ratio. Finally, the smoothed systematic uncertainty distribution is obtained by multiplying the smoothed ratio histogram to the nominal template.

Figure 8.8b shows the Top JMR-to-nominal ratio distribution in the $\mathrm{CR}_{t\bar{t}}3$, before and after applying the smoothing procedure with a threshold of $t = 0.045$. Across the whole mass range, the smoothed ratio agrees with the original one within the statistical MC uncertainty band. Ensuring a good agreement prevents the smoothing

[3]Splines are piecewise-defined polynomial functions that commonly find application in interpolation and smoothing.

procedure from removing any physical features that might be present along the systematic uncertainty distributions. Nonetheless, the smoothed distribution is observed to provide a much less noisy ratio, which translates in a more trustworthy description of the corresponding systematic uncertainty.

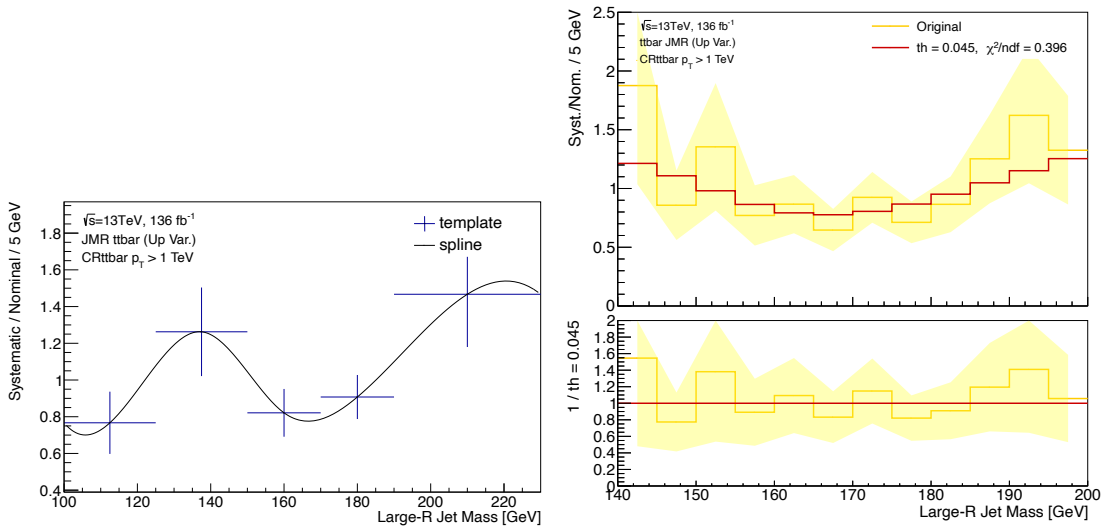

(a) **(b)**

Figure 8.8: Figure (a): result of a spline fit to the Top JMR-to-nominal ratio distribution in the CR$_{t\bar{t}}$3 region. Figure (b): Top JMR-to-nominal ratio distribution in the CR$_{t\bar{t}}$3, before (yellow) and after (red) applying the smoothing procedure with a threshold of $t = 0.045$. The agreement between the two ratios has a χ^2 probability of 0.396.

Threshold optimisation

The smoothing procedure is applied to all systematic uncertainty templates in the SR and CR$_{t\bar{t}}$, both inclusively and in p_{T} bins. For each analysis region, the threshold is optimised by evaluating the performance of the smoothing procedure on all systematic uncertainties, while varying the smoothing threshold by increasingly smaller amounts.

Figure 8.9 shows the distribution of the Top JMR-to-nominal ratio in the CR$_{t\bar{t}}$3, together with smoothed ratios obtained by assuming $t = 0.040$, 0.045 and 0.050. The optimal threshold is defined as the tightest one that does not result in any systematics having significant discrepancies (with regards to the MC statistical uncertainty on the ratio) between the smooth and original ratios. In the CR$_{t\bar{t}}$3

region, the 0.045 threshold is found to be optimal after studying the smoothing performance across the relevant systematic uncertainties.

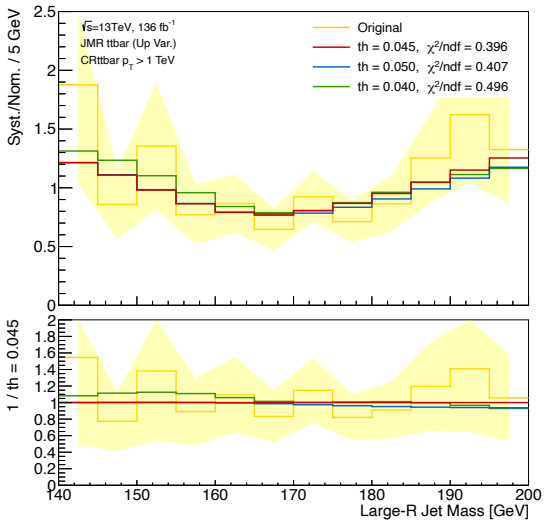

Figure 8.9: Comparison between the original Top JMR-to-nominal ratio distribution in the $\mathrm{CR}_{t\bar{t}}$ region, and those obtained by applying the smoothing procedure with thresholds $t = 0.040$, 0.045 and 0.050.

Summary

The introduction of the systematic uncertainty smoothing procedure strongly mitigates the issues observed in Figure 8.7 and in other analysis regions.

Figure 8.10 shows an extract of the pull plot obtained from a standalone $\mathrm{CR}_{t\bar{t}}3$ ($p_{\mathrm{T}} > 1$ TeV) fit performed with and without systematic smoothing, both to Asimov and data. After the introduction of the smoothing procedure, the strong constraints observed on some high-impact systematics are removed or reduced. This is evidence that the unnatural constraints were caused by the fit interpreting statistical fluctuations as features and using them to falsely constrain the uncertainties. A small constraint on JMR and JMS Modelling is expected due to the high $t\bar{t}$ purity in the $\mathrm{CR}_{t\bar{t}}$. In the fit to data, the smoothing procedure also removes or strongly reduces unnatural pulls on some high-impact uncertainties.

The smoothing procedure outlined in this section is applied to all systematic uncertainties and independently optimised in all analysis regions. Its introduction

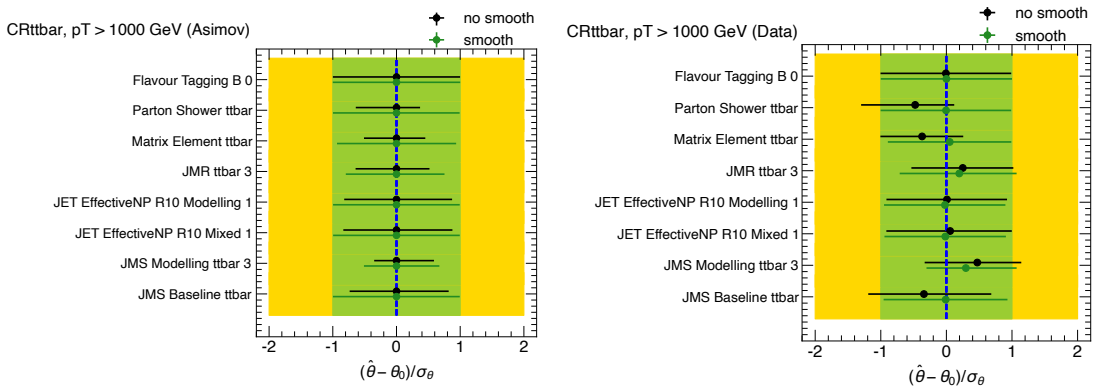

Figure 8.10: Extract of the pull plot obtained from a standalone $CR_{t\bar{t}}3$ ($p_T > 1$ TeV) fit performed with (green) and without (black) systematic smoothing, both in Asimov (left) and data (right).

is proven to be beneficial in the modelling of systematic uncertainties in the high-p_T regions or for processes with low statistical precision. The resulting smooth uncertainties are less affected by large bin-by-bin fluctuations, but they also retain all physical features along their mass spectrum. The use of a full set of smoothed systematics prevents the fit from interpreting statistical fluctuations as features and using them to falsely constrain or pull the uncertainties.

8.2.3 Pruning of Systematics

As previously discussed in Section 6.4.3, the necessary fine sampling of the QCD model during NLL minimisation led to a drastic increase in the fit computation time (CPU time). Since the CPU time is strongly dependent on the number of NPs in the NLL, better performance can be achieved by *pruning* systematics, namely completely or partially removing systematics with negligible impact.

The normalisation and shape components of systematics are pruned independently. Systematics are restricted to be shape-only if their normalisation relative to the nominal template is less than a custom threshold. They are instead completely removed if none of their bins shows a relative variation larger than said threshold.

Care must be taken when removing small systematics from the fit, as through correlations with other systematics they might significantly reduce the total uncertainty on the parameters of interest (POIs). The optimal value of the pruning

threshold reduces the CPU time with a negligible change in the POIs uncertainty. In each analysis region, fits on Asimov data with various thresholds are performed and subsequently compared.

Figure 8.11 shows, both for an inclusive and a differential Asimov fit, the CPU time dependence on the number of retained NPs and pruning thresholds. It is noted that the CPU time strongly depends on the number of NPs. Thus, reducing the complexity of the fit through pruning can be used to keep processing times to a manageable level for studies.

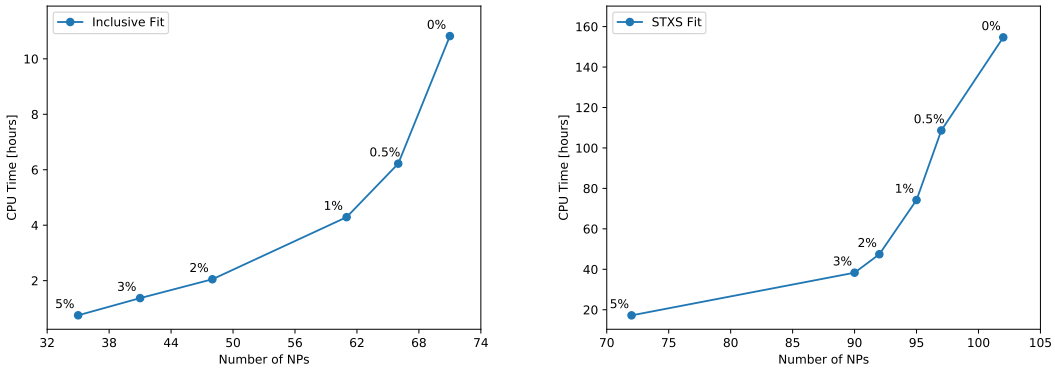

Figure 8.11: CPU time dependence on the number of retained NPs and pruning thresholds both for an inclusive (left) and differential (right) Asimov fit.

Table 8.2 shows the relative change in the POIs total uncertainty induced by setting various pruning thresholds on the inclusive Asimov fit. Uncertainty differences $\Delta\sigma$ are taken with respect to a fit that had no pruning applied. Following this result, a 2% threshold is adopted, as it maintains good fit performance while yielding relative uncertainty changes lower than 3% on all POIs. Also, plots in Figure 8.11 show that moving to higher thresholds gives diminishing returns in terms of CPU time reduction.

In order to make sure the systematic description is not affected by the pruning procedure, pull plots for the various fits are also studied. Figure 8.12 shows a comparison between the pulls of some of the most important systematics characterising the inclusive Asimov fit, obtained assuming different values of the pruning threshold. It is noted that the 2% threshold does not yield any significant change in

Table 8.2: Relative change in total uncertainty of parameters of interest in inclusive Asimov fits for various choices of the pruning threshold. Uncertainty differences $\Delta\sigma$ are taken with respect to a fit where no pruning is applied.

Prun. Th.	$\Delta\sigma_{\mu_H}/\sigma_{\mu_H}$	$\Delta\sigma_{\mu_Z}/\sigma_{\mu_Z}$	$\Delta\sigma_{\mu_{t\bar{t}}}/\sigma_{\mu_{t\bar{t}}}$
0.5%	+0.1%	-0.7%	-0.3%
1%	+0.0%	-0.9%	+0.1%
2%	-0.3%	-2.8%	-1.4%
3%	-0.8%	-4.7%	-9.9%
5%	-2.5%	-6.6%	-30.7%

the pull description. Similar studies show that a 2% pruning threshold is optimal for all analysis measurements.

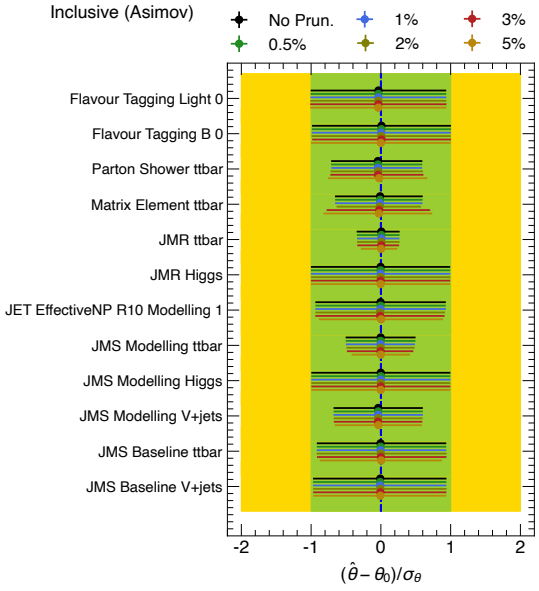

Figure 8.12: Comparison between the pulls of some of the most important systematics characterising the inclusive Asimov fit, obtained assuming various values for the pruning threshold.

The extremely long CPU times observed in Figure 8.11 were later found to be caused by poor optimisation of the fitting framework code. A fix was implemented after the finalisation of the analysis, allowing fits to be performed up to 100 times faster. This large improvement will be beneficial in the next iteration of the analysis, where pruning of systematics will become less crucial in achieving timely results.

8.3 Gamma Parameters

Due to the limited number of events in the MC samples, some of the nominal templates used in the fit might have large bin-by-bin statistical fluctuations. This might lead to biases in the results if the fit interprets such fluctuations as physical features in the template shapes and introduces fake constraints.

Within the fit, the correct way to take into account the MC statistical uncertainties is to use the Beeston-Barlow technique [120]. This consists in adding to the likelihood definition bin-specific nuisance parameters called *gamma parameters*. A gamma parameter is introduced on a template bin if its uncertainty exceeds a certain adjustable threshold. The fit procedure thus gains additional freedom to adjust the template shape within the uncertainty of the MC prediction so that it better adapts to the data. This might be beneficial when the template does not faithfully represent the corresponding process due to a few statistical fluctuations along the mass spectrum.

The impact of gamma parameters on the analysis results is estimated by running multiple Asimov fits, each with a different value for the gamma parameter threshold (in the range 10%-50%). In the inclusive and fiducial fits, regardless of the chosen threshold, variations in total uncertainty lower than 0.2% are observed for all parameters of interest. Such small variations are an indication that the fits are not pulling gamma parameters significantly on any bin in order obtain a better description of the data. For this reason, it is decided not to unnecessarily complicate the inclusive and fiducial fits by introducing gamma parameters.

A larger effect is expected for the differential result, where templates in some of the p_{T} regions offer very low statistical precision. The biggest effect is seen on μ_H^1, with variations in the total uncertainties up to 15%. All other parameters of interest show a much lower impact with variations up to 5%. Similarly to the other measurements, the analysis team decided not to introduce gamma parameters in the differential fit. After all, as will be shown in Chapter 9, the analysis offers very little Higgs sensitivity in the $300 < p_{\mathrm{T}}^H < 450$ GeV range, and a much more precise measurement in a similar phase space is performed by the $VH(\rightarrow b\bar{b})$ analysis [14].

In summary, the introduction of gamma parameters with thresholds in range 10%-50% is expected to have a negligible impact on the analysis results. Thereby, it is decided not to use them in the likelihood description.

8.4 V + jets Mass Resolution External Constraints

When fitting the signal and background models to data, strong interplays might occur between the flexible parametric function used to describe the QCD multijet process and the resonant peaks inhabiting the same mass spectrum. The QCD function parameters can be particularly sensitive to the shape of the resonant peaks, and mismodelling or overestimated systematic uncertainties might lead to unnatural fit solutions.

While the $t\bar{t}$ peak is strongly constrained by the precision measurement performed in the $\mathrm{CR}_{t\bar{t}}$, no such procedure exists for the V + jets resonance, which might thus interfere with QCD during the fit. This effect is measured before unblinding the Higgs and differential Z regions, while performing the Z+jets inclusive measurement used to validate the analysis fit strategy. In this fit, the Higgs boson signal strength is fixed to the SM expectation ($\mu_H = 1$).

Figure 8.13 shows an extract of the correlation matrix of some of the nuisance parameters characterising the inclusive Z measurement. Large correlations are observed between the Z boson signal strength μ_Z, the JMR uncertainty associated with the V + jets process and the QCD function parameters. This corresponds to an unnatural solution where the large V + jets JMR uncertainty is strongly pulled towards high values, thus broadening the Z peak and increasing the fitted μ_Z, while locally downward shifting the QCD function.

This effect is further confirmed by performing similar fits on all of the 58 $\mathrm{VR}_{\mathrm{hyb}}$ data slices (see Section 7.2.2). In a sizable fraction of the fits, the V + jets JMR uncertainty shows large pulls ($> 2\sigma$). This effect hints to a lack of constraint in the model, allowing the fit to converge to an unphysical solution. The issue might be partly caused by the lack of a finalised JMR calibration during the analysis development. The relative flat 20% JMR uncertainty recommended by

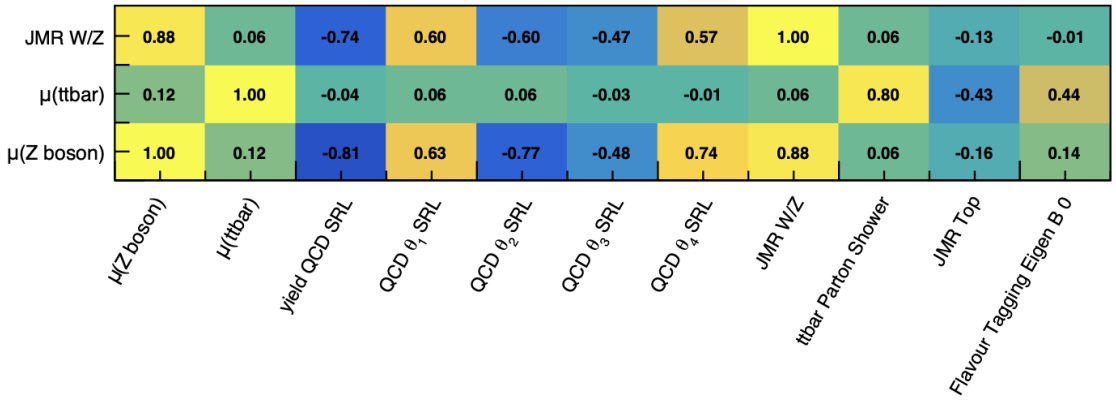

Figure 8.13: Extract of the correlation matrix of an inclusive Z fit in data. Shown are the Z and $t\bar{t}$ signal strengths (μ_Z and $\mu_{t\bar{t}}$), the yield and shape parameters of the QCD function in the SRL (yield QCD SRL, QCD θ_i SRL), the $V+$jets JMR uncertainty (JMR W/Z), and other important systematics.

the ATLAS Collaboration is a very conservative estimate that contributes to a lack of constraint in the model.

In preparation for the unblinding of the Higgs and differential Z regions, the fit response is stabilised by externally constraining the $V+$jets JMR uncertainty. This is done by measuring the width of the $V+$jets mass peak in two data control samples, orthogonal to the SR. These are the VRL and WCR$_{t\bar{t}}$, an additional control region populated by semi-leptonic $t\bar{t}$ events, where a top quark decays hadronically to a resolved Wb pair (see Section 6.3.3). The WCR$_{t\bar{t}}$ provides a high-purity W mass peak measurement, but it is populated by very few events for $p_{\mathrm{T}} > 600$ GeV due to the requirement of a resolved top quark decay. On the other hand, the VRL provides a high sensitivity $V+$jets measurement (10-13σ) across the whole analysis p_{T} range, but it is affected by a larger QCD background. In this region, the $V+$jets process is roughly composed of a 3:1 mixture of W and Z events.

The $W+$jets mass resolution is measured in the WCR$_{t\bar{t}}$ in three W candidate jet p_{T} bins: [200, 275] GeV, [275, 375] GeV and [375, 1500] GeV. This region provides a pure W boson mass peak, with backgrounds (mainly single top) accounting for a few per cent of the total yield. For this reason, it is considered safe to only allow the W boson signal strength μ_W to float in the fit, while fixing the background templates to their SM estimates. Furthermore, only the JMR and the JMS components of

the W + jets process are kept free to float in the fit, as they control the width and position of the mass peak. All other nuisance parameters are fixed to zero to prevent correlations with JMR that could bias the measurement. Each region is independently fitted, and the JMR measurements are obtained as the post-fit values (pulls) and corresponding uncertainties (widths) of the W + jets JMR systematic.

In the VRL, the V + jets mass resolution measurement is performed in two candidate jet p_{T} bins: [450, 650] GeV and [650, 3000] GeV. In contrast to the $\mathrm{WCR}_{t\bar{t}}$, the VRL region is characterised by the presence of large QCD and $t\bar{t}$ backgrounds. The VR data sample is sliced into 5 datasets to maximise the fit precision, while retaining the validity of the QCD polynomial order optimisation (see Section 7.2.1). In an initial phase, fits are performed keeping the V + jets signal strength μ_V free to float, leading to post-fit results compatible with the SM expectations ($\mu_V = 1$). The fits are then rerun setting μ_V to 1, $\mu_{t\bar{t}}$ to the corresponding $\mathrm{CR}_{t\bar{t}}$ estimate, and keeping the QCD parameters free to float. Once again, only the V + jets JMR and JMS systematics are kept free in the fit to avoid correlation with other systematics.

Figure 8.14 shows the results of the JMR measurements performed in the $\mathrm{WCR}_{t\bar{t}}$ and VRL regions. The resolution appears to vary smoothly with large-R jet p_{T}, and its behaviour can be fitted with a $f(x) = a + bx + c/x$ functional form. The figure also shows the result of the fit and the corresponding statistical uncertainty band (68% C.L.).

The constraints derived from the $\mathrm{WCR}_{t\bar{t}}$ and VRL come from W and Z decays into pairs of light quarks. Their end goal, however, is to be applied to the double b-tagged V + jets events in the SR, which are dominated by $Z \to b\bar{b}$. After accounting for the W/Z mass difference, variations in the jet mass width are mainly driven by the properties of the b-hadrons decay. Therefore, the additional systematics that are considered for the transfer of a jet mass resolution constraint from the $W \to q\bar{q}'$ and $Z \to q\bar{q}$ to the $Z \to b\bar{b}$ topology pertain to the modelling of the b-hadron decay. The total systematic uncertainty accounting for the different detector response and quark fragmentation are found to be of the order of 6%. This estimate is inflated to a conservative 10% systematic that is added in quadrature to the JMR uncertainty

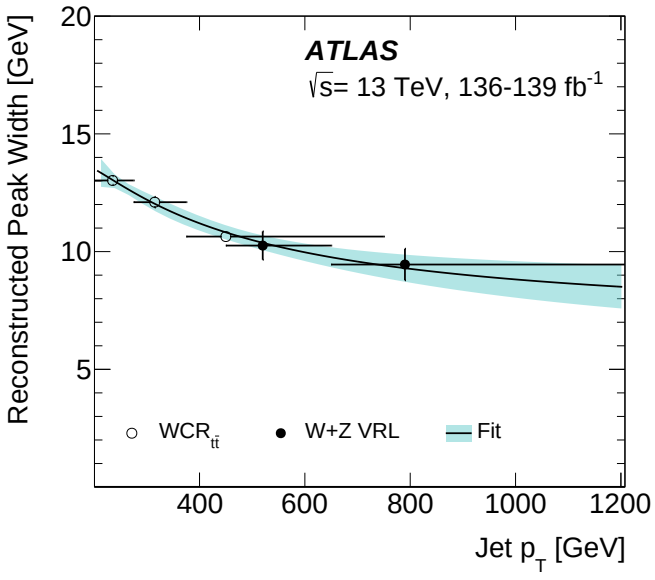

Figure 8.14: Width of the vector boson mass resonance peak as function of large-R jet p_{T}, as measured from fits performed in the WCR$_{t\bar{t}}$ (white circles) and VRL (black circles). The black curve and cyan band represent a fit to the measurements and the corresponding 68% confidence level error band [1].

values obtained from the fits. The measured values of the $V+$jets JMR are found to only differ by 2.5% from the ones obtained from simulations, while they are constrained down to around 14-22% of their previous values.

The values of the JMR constraints to be used in the SR fits are calculated, both inclusively and each differential bin, by averaging - or *folding* - the function value and error over the p_{T} spectrum of the region in question. This is done to correctly account for the increasing statistical uncertainty as a function of large-R jet p_{T}. The folding is performed by sampling the $Z+$jets p_{T} spectrum in the corresponding SR region 250 000 times, noting the function value and error at the sampled p_{T}, and then averaging the values. In the inclusive fit, the constraint is determined by folding over the SRL $Z+$jets p_{T} spectrum. Folding over the SRS spectrum is observed to have a negligible effect ($< 1\%$) on the fitted value of μ_Z.

The JMR measurements described in this section are introduced in the likelihood descriptions as external Gaussian constraints. Thanks to the precision of the measurements, the corresponding constraints effectively reduce the ability of the fit to pull the JMR uncertainty towards high values, thus rejecting the unnatural

alternative fit solution. The method appears to be working well in the inclusive Z fit, reducing the correlation between V + jets JMR and μ_Z from $\sim 90\%$ to $\sim 30\%$.

9 Results

Contents

9.1 Cross-section Calculation 169
9.2 Standalone CR$_{t\bar{t}}$ Measurements 170
9.3 Inclusive Higgs Boson Measurement 172
9.4 Fiducial Higgs Boson Measurement 175
9.5 Differential Measurements 177
9.5.1 Differential V + jets and Z Boson Results 179
9.5.2 Differential Higgs Boson Result 181
9.6 Future Outlook 188
9.6.1 Preliminary Studies 190

In the previous chapters, this thesis defined the experimental setup and strategy of the analysis, it explained how the signal and background processes are modelled and, finally, it presented the systematic uncertainties and their treatment. This information sets the stage for the current chapter, which provides an overview of the Boosted $H(\rightarrow b\bar{b})$ + jet analysis results.

As already introduced in Section 6.4.1, the main deliverables of the analysis are three Higgs boson results: the *inclusive measurement*, the *fiducial measurement* and the *differential measurement*. Additionally, this chapter presents a differential Z boson measurement aimed at validating the differential fit setup in the SR. The results of this measurement are additional analysis deliverables.

Fit results are given in terms of the Higgs, Z boson and $t\bar{t}$ signal strengths. These PoIs are labelled as "observed" when they are obtained from fits to data. The label "expected" is instead used to refer to fit results obtained on Asimov datasets.

The Higgs signal strengths obtained in the fiducial and differential measurements are converted to upper limits on the Higgs boson production cross-section following the procedure outlined in Section 9.1. The results of standalone $\mathrm{CR}_{t\bar{t}}$ fits are presented in Section 9.2. These high-precision measurements of the $t\bar{t}$ process are used for validating the fit procedure before the Higgs unblinding and studying the level of constraint on the $t\bar{t}$ background. The results of the inclusive, fiducial and differential measurements are presented in Sections 9.3, 9.4 and 9.5, respectively. Finally, Section 9.6 describes possible avenues for improving the Higgs sensitivity in the next analysis iteration.

Author's Contributions Some of the most important work done by the author is the production and validation of the main fit results for the published version of the analysis. A list of his most notable contributions within this chapter is given below.

- Production and validation of final fit results on data, after the full unblinding of the analysis[1]. Finalised results produced by the author are listed in Tables 9.1, 9.2, 9.4, 9.6 and 9.7, as well as shown in Figures 9.2, 9.3 and 9.5.

- Production and validation of expected results for the $\mathrm{CR}_{t\bar{t}}$ standalone, inclusive, fiducial and differential fits using Asimov samples.

- A full understanding of the fit results, the interactions of the various regions, uncertainties and their correlations. For example, studies of pulls and correlations for the inclusive, fiducial, differential and $\mathrm{CR}_{t\bar{t}}$ standalone fits (both for data and Asimov - see Figures 9.1 and 9.8).

[1]The conversion of the measured signal strengths from the analysis fit into 95% CL upper limits was performed by other memebers of the analysis team.

- Implementation within the fitting framework of a tool for summarising the impact of groups of uncertainties on all final measurements. Results are shown in Tables 9.3, 9.5 and 9.8.
- Implemention and testing of the fiducial and differential fits in the fitting framework (including addition of entirely new SRL3 and $\mathrm{CR}_{t\bar{t}}3$ regions).
- Studies of Asimov fit stability with respect to signal injection.
- Determination of $\mathrm{CR}_{t\bar{t}}$ contribution to $t\bar{t}$ sensitivity in all combined fits.
- In-depth systematic constraint studies during the migration from a preliminary setup of the analysis using 0.5 GeV jet mass binning to its final version.

After the publication of the analysis, the author personally performed preliminary studies for a future iteration of the analysis using more recent b-taggers (Section 9.6). Such studies entailed producing new samples featuring the DL1r tagger and estimating the Higgs boson sensitivity gain obtainable with a future b-tagger update.

9.1 Cross-section Calculation

The fiducial and differential measurements are performed in specific phase space volumes defined by selections on the Higgs boson trasverse momentum p_{T}^{H} and rapidity y_H. Such "fiducial volumes" are designed to reflect typical experimental kinematic selections, simplifying the comparison of results with other analyses and theoretical predictions.

The Higgs boson signal strengths μ_H extracted in the fiducial volumes can be reinterpreted as measurements of the Higgs boson production cross-section σ_H using

$$\sigma_H = \frac{\mu_H N_{\mathrm{SM}}}{LA\epsilon}, \tag{9.1}$$

where μ_H is the measured Higgs signal strength, N_{SM} is the Higgs boson yield predicted by the SM, L is the integrated luminosity of the dataset, A is the fiducial acceptance and ϵ is the selection efficiency.

Both the values of A and ϵ are obtained using the Higgs MC samples. The fiducial acceptance A is the fraction of generated Higgs events entering the fiducial volume. The selection efficiency ϵ is instead the fraction of Higgs events in the fiducial volume passing all analysis SR selections.

All fiducial volumes in the analysis are defined for $|y_H| < 2$, which is the range where large-R jet calibrations are typically provided. For this selection, the rapidity y is chosen over the pseudo-rapidity η as the latter is defined in the limit $p_{\mathrm{T}} \gg$ mass, which is not necessarily realised for massive bosons. Furthermore, fiducial selections on p_{T}^H are applied. Due to the analysis selections, the $A\epsilon$ distribution in each region is characterised by a turn-on curve at low p_{T}^H that reaches a plateau after a certain threshold. The fiducial volumes of the fiducial and differential measurements are defined in p_{T}^H ranges providing a stable $A\epsilon$ response, respectively $p_{\mathrm{T}}^H > 450$ GeV and $p_{\mathrm{T}}^H > 300$ GeV. The Higgs boson $A\epsilon$ values in the fiducial volumes of the analysis are summarised in Table F.1 of Appendix F.

As the analysis sensitivity does not allow for high-significance Higgs boson cross-section measurements, 95% confidence level (CL) upper limits are set using the CL_s method [121, 122]. Following ATLAS recommendations, limits are calculated using the q_μ statistic (see Section 2.4 in Reference [121]), which is based on the profile likelihood ratio. By using the profile treatment of nuisance parameters, systematic uncertainties are therefore incorporated in the limits.

9.2 Standalone $\mathrm{CR}_{t\bar{t}}$ Measurements

Standalone fits to the $\mathrm{CR}_{t\bar{t}}$, both inclusively and in candidate jet p_{T} ranges, are performed to validate the fit procedure and assess the level of constraint offered by these high-precision measurements of the $t\bar{t}$ process.

$\mathrm{CR}_{t\bar{t}}$ fits are independently performed on the same kinematic ranges used for the SR results. The only free-floating PoI is the $t\bar{t}$ signal strength ($\mu_{t\bar{t}}$), while the yields of the minor single top and $W(\ell\nu)$ + jets backgrounds are constrained to their SM expectations using 50% and 30% Gaussian priors, respectively. All uncertainty descriptions are included for the $t\bar{t}$ process.

Table 9.1 summarises the observed and expected $\mu_{t\bar{t}}$ results from standalone fits to the various $\mathrm{CR}_{t\bar{t}}$ regions. The $t\bar{t}$ sensitivity is very high, reaching 13σ inclusively in p_{T} (14σ expected). The observed results are largely in agreement with a dedicated $t\bar{t}$ cross-section measurement performed by the ATLAS Collaboration targeting a similar phase space (see Figure 54 of Reference [123]).

Table 9.1: Expected and observed $t\bar{t}$ signal strengths from standalone $\mathrm{CR}_{t\bar{t}}$ fits performed within the probe-jet p_{T} ranges listed in the first column. Results are largely in agreement with a dedicated $t\bar{t}$ cross-section measurement performed by the ATLAS Collaboration in a similar phase space [123].

Probe-jet p_{T} [GeV]	$\mu_{t\bar{t}}$	
	Exp.	Obs.
> 250 (inclusive)	1.00 ± 0.07	0.78 ± 0.06
> 450	1.00 ± 0.09	0.73 ± 0.07
250–450	1.00 ± 0.07	0.85 ± 0.06
450–650	1.00 ± 0.09	0.75 ± 0.07
650–1000	1.00 ± 0.11	0.71 ± 0.08
> 1000	1.00 ± 0.30	0.53 ± 0.20

Figure 9.1a compares the expected (Asimov) and observed (Data) pulls and widths of the six systematic uncertainties having the largest impact on the determination of $\mu_{t\bar{t}}$ in the inclusive $\mathrm{CR}_{t\bar{t}}$ fit. No significant pulls are noted and all corresponding observed and expected constraints are of the same order. The JMR uncertainty is strongly constrained by the fit, which is seen to reduce the uncertainty's width by around 55%. This is expected, considering the high level of precision offered by the $\mathrm{CR}_{t\bar{t}}$ in conjunction with the pre-fit JMR uncertainty being a very conservative estimate (see Section 4.1.3). The Parton Shower and Matrix Element systematics are also slightly constrained, by around 10%-20%. All other systematics do not show any significant pulls or constraints.

The interactions between the various parameters in the standalone inclusive $\mathrm{CR}_{t\bar{t}}$ fit can be studied using the correlation matrix shown in Figure 9.1b. In the plot, only parameters with an absolute correlation greater than 30% with at least one other parameter are shown. It is noted that $\mu_{t\bar{t}}$ is strongly correlated with the FTAG Eigen

B0 (61%), Parton Shower (58%), and JMR (-31%) uncertainties. This is reasonable, considering that these are, in this order, the three systematics with the largest impact on the determination of $\mu_{t\bar{t}}$. Large anti-correlations are also observed between JMR and Parton Shower (-64%) and between JMR and JMS Modelling (-69%). Such correlations are expected between dominant systematics with large shape components, and this behaviour is independently confirmed in Asimov $CR_{t\bar{t}}$ fits.

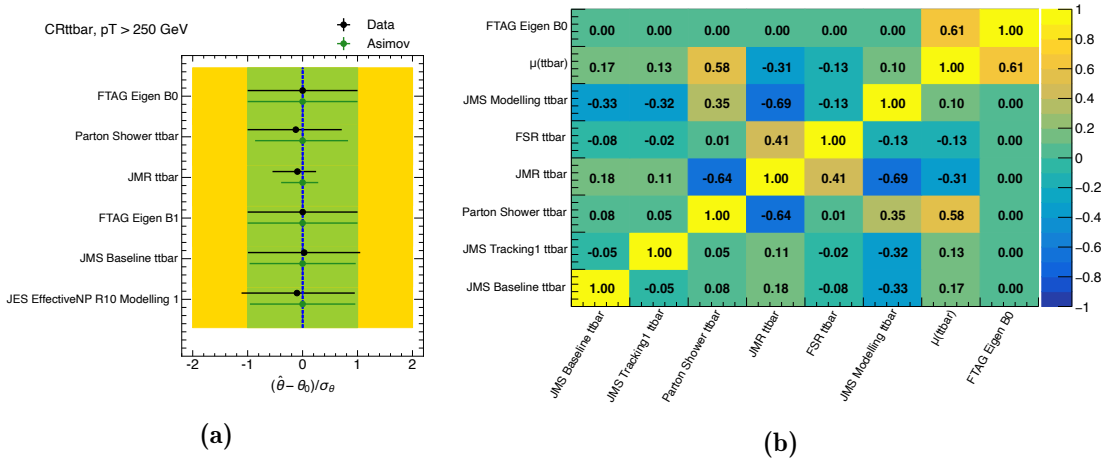

Figure 9.1: Figure (a): pulls and widths of the leading systematic uncertainties in the standalone inclusive $CR_{t\bar{t}}$ fit. The nuisance parameters are ranked, from top to bottom, in descending order of impact on the determination of $\mu_{t\bar{t}}$. Figure (b): correlation matrix of the standalone inclusive $CR_{t\bar{t}}$ fit. Only parameters with an absolute correlation greater than 30% with at least one other parameter are shown.

9.3 Inclusive Higgs Boson Measurement

The inclusive measurement probes the Higgs boson signal strength μ_H over the whole available candidate jet p_{T} range. It is obtained from a simultaneous fit over the SRL, SRS and $CR_{t\bar{t}}$, using the complete signal and background models and all uncertainty descriptions.

In the fit, the H and Z boson signal strengths (μ_H and μ_Z) are free parameters, and they are each described by the same parameter - and thus they are simultaneously determined - in the SRL and SRS. Another free parameter is the $t\bar{t}$ signal strength $\mu_{t\bar{t}}$, which is described by the same parameter in the SRL, SRS and $CR_{t\bar{t}}$. The yield and shape parameters of the QCD models are independently determined

in the SRL and SRS. The yields of the W boson background in the SR and of the minor single top and $W(\ell\nu)+\text{jets}$ processes in the $\text{CR}_{t\bar{t}}$ are constrained to their SM expectations using 10%, 50% and 30% Gaussian priors, respectively.

The Higgs boson signal strength observed in the inclusive measurement is

$$\mu_H = 0.8 \pm 2.5(\text{stat.}) \pm 2.0(\text{syst.}). \tag{9.2}$$

Table 9.2 summarises the expected and observed results for the most important PoIs in the inclusive result. The μ_Z results are corrected to account for NLO EW and NNLO QCD corrections (see Section 7.4.1). The observed Higgs and Z boson signal strengths are in good agreement with the SM predictions. The Higgs boson observed sensitivity is 0.25σ (0.32σ expected). A much more precise measurement is obtained for the $Z+\text{jets}$ process, which is characterised by an observed sensitivity of 5.7σ (5.8σ expected).

The measured $t\bar{t}$ signal strength is compatible with the results obtained from inclusive standalone fits to the $\text{CR}_{t\bar{t}}$, proving that the determination of this process is strongly constrained by the precise measurements achievable in the $\text{CR}_{t\bar{t}}$.

The post-fit yields of all signal and background processes participating in the inclusive fit are given in Table F.2 of Appendix F.

Table 9.2: Expected and observed values of the signal strengths for the H, Z and $t\bar{t}$ components in the inclusive fit.

Result	μ_H	μ_Z	$\mu_{t\bar{t}}$
Expected	1.0 ± 3.2	1.00 ± 0.17	1.00 ± 0.07
Observed	0.8 ± 3.2	1.29 ± 0.22	0.80 ± 0.06

Table 9.3 shows a breakdown of the μ_H uncertainty in terms of individual contributions from various uncertainty groups. The contribution of a group of uncertainties is calculated by repeating the fit fixing all NPs belonging to the group. Then, the contribution is calculated as the difference in quadrature between the total uncertainty and the one obtained from the alternative fit with fixed NPs. From the table, it is noted that the inclusive H measurement is statistically limited.

The extent of the systematic component, however, is comparable to the statistical one, and it is dominated by the large-R jet systematics.

Table 9.3: Breakdown of the μ_H total uncertainty (first row) in terms of contributions from individual uncertainty groups, for the inclusive H measurement. The total uncertainty is subdivided into the statistical and systematic component. The latter is then further broken down into contributions from various systematic uncertainty groups.

Uncertainty Contribution	$\sigma(\mu_H)$
Total	3.2
Statistical	2.5
Systematic	2.0
Large-R Jet Syst.	1.9
Modelling and Theory Syst.	0.5
Flavour Tagging Syst.	0.4

The 10 fit parameters with the highest impact on the determination of μ_H are shown in Figure F.2a of Appendix F. The QCD function parameters, which are characterised, in general, by the largest impacts due to their large correlations with μ_H, are excluded from the figure. As expected from the large correlations between the Z and Higgs boson processes, the μ_Z parameter has the largest impact on the determination of μ_H. Furthermore, the figure confirms that the JMR, JMS Modelling and $t\bar{t}$ modelling systematics are the NPs with the largest impact on μ_H.

Figure 9.2 shows a comparison between the data and the post-fit signal and background candidate jet mass distributions, both in the SRL and SRS. In each plot, the middle panel highlights the mass resonances by subtracting the QCD background both from the data and the model. The bottom panel subtracts all backgrounds instead, leaving only the post-fit Higgs boson template in the model. Good agreement between the data and the post-fit model is observed, yielding reduced χ^2 goodness-of-fit values of 0.19 and 0.67, respectively in the SRL and SRS. For convenience, the $t\bar{t}$ and single top processes are combined into the same distribution called *Top*.

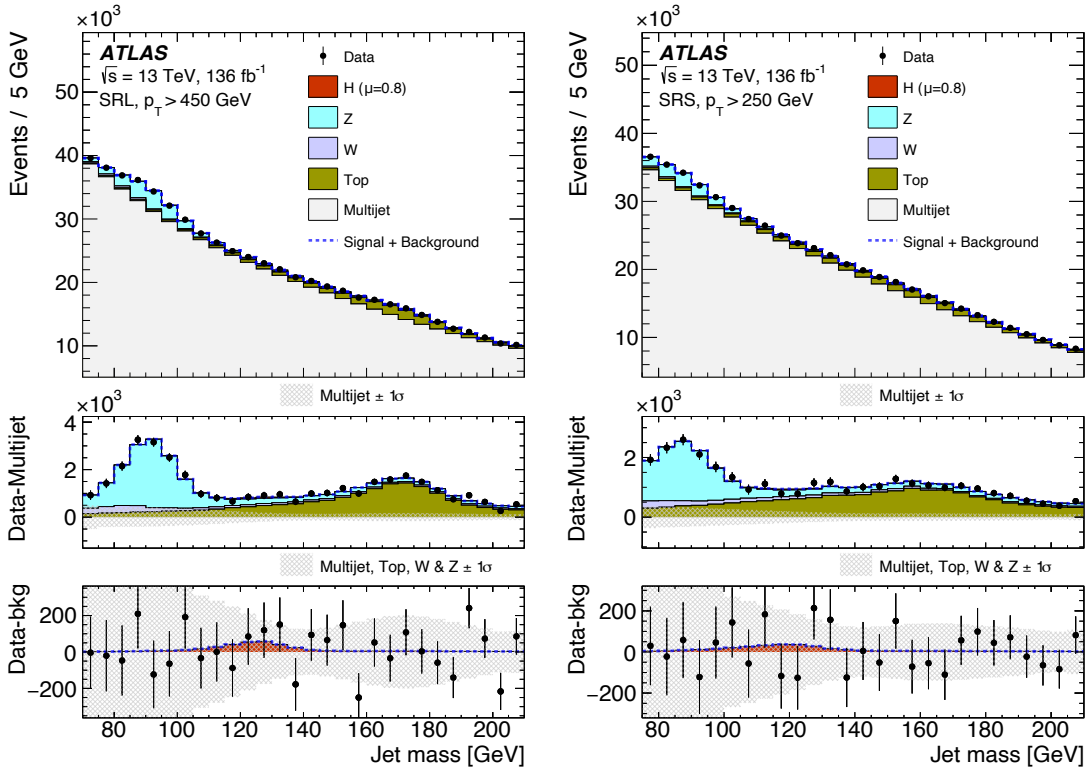

(a) SRL **(b)** SRS

Figure 9.2: Comparison between the data and the signal + background model after the inclusive H fit, both in the (a) SRL ($p_{\mathrm{T}} > 450$ GeV) and (b) SRS ($p_{\mathrm{T}} > 250$ GeV). In each plot, the middle panel subtracts the QCD background distribution both from the data and the model. The bottom panel subtracts all backgrounds instead, leaving only the Higgs boson template in the model. The $t\bar{t}$ and single top processes are combined into the same distribution called *Top*.

9.4 Fiducial Higgs Boson Measurement

The fiducial Higgs boson measurement is performed through a simultaneous fit of the SRL, SRS and $\mathrm{CR}_{t\bar{t}}$ regions, restricting their candidate jet p_{T} range to $p_{\mathrm{T}} > 450$ GeV.

The Higgs boson template is split into two components, one belonging to the fiducial volume defined by $p_{\mathrm{T}}^{H} > 450$ GeV, $|y_H| < 2$, the other being outside of this region ($p_{\mathrm{T}}^{H} < 450$ GeV). The modelling of the two components is presented in Section 7.1.1. Within the fit, the Higgs boson template outside of the fiducial volume is fixed to the SM expectation, and all its uncertainty descriptions are included. On the other hand, the signal strength μ_H associated to the template belonging to the fiducial volume is a free parameter in the fit.

The Higgs boson signal strength observed in the fiducial measurement is

$$\mu_H = -0.1 \pm 2.6(\text{stat.}) \pm 2.3(\text{syst.}), \tag{9.3}$$

The observed (expected) 95% CL upper limit on the Higgs boson cross-section is found to be

$$\sigma_H(p_{\text{T}}^H > 450 \text{ GeV}) < 115 \text{ (128) fb}. \tag{9.4}$$

Table 9.4 summarises the expected and observed results of the main PoIs in the fiducial measurement. The μ_Z results are corrected to account for NLO EW and NNLO QCD corrections. The Higgs and Z boson signal strengths are seen to agree within uncertainties with the SM predictions. The $t\bar{t}$ signal strength and its uncertainty are consistent with the result obtained from a standalone $\text{CR}_{t\bar{t}}$ fit with $p_{\text{T}} > 450$ GeV.

The post-fit yields of all signal and background processes participating in the fiducial fit are given in Table F.3 of Appendix F.

Table 9.4: Expected and observed values of the signal strengths for the H, Z, and $t\bar{t}$ components in the fiducial measurement. The value for μ_H refers to the fiducial volume $|y_H| < 2$ and $p_{\text{T}}^H > 450$ GeV, while those for μ_Z and $\mu_{t\bar{t}}$ pertain to regions of jet p_{T} above 450 GeV.

Result	μ_H	μ_Z	$\mu_{t\bar{t}}$
Expected	1.0 ± 3.4	1.00 ± 0.18	1.00 ± 0.08
Observed	-0.1 ± 3.5	1.30 ± 0.22	0.75 ± 0.06

Table 9.3 shows a breakdown of the μ_H total uncertainty in terms of individual contributions from various uncertainty groups. Because of the similar p_{T} range being probed, the uncertainty breakdown of the fiducial result is very similar to the inclusive one. Likewise, the fiducial measurement is statistically limited, with a systematic component that is comparable to the statistical one. The 10 fit parameters with the highest impact on the determination of μ_H are shown in Figure F.2b of Appendix F.

Table 9.5: Breakdown of the μ_H total uncertainty (first row) in terms of contributions from individual uncertainty groups, for the fiducial H measurement. The total uncertainty is subdivided into the statistical and systematic component. The latter is then further broken down into contributions from various systematic uncertainty groups.

Uncertainty Contribution	$\sigma(\mu_H)$
Total	3.5
Statistical	2.6
Systematic	2.3
Large-R Jet Syst.	2.2
Modelling and Theory Syst.	0.8
Flavour Tagging Syst.	0.2

Figure 9.3 shows a comparison between the data and the post-fit signal and background mass distributions, both in the SRL and SRS. In each plot, the middle panel subtracts the QCD background both from the data and the model, while the bottom panel subtract all backgrounds. The Higgs boson signal is not visible in the plots as the $p_{\mathrm{T}}^{H} < 450$ GeV component (fixed to SM) is very small, and the signal strength of the component within the fiducial region is $\mu_H = -0.1$.

9.5 Differential Measurements

As thoroughly discussed in Section 1.4, some BSM scenarios predict that, in the presence of new physics particles, large Higgs cross-section enhancements might be observable approaching a hypothetical new physics energy scale. It is thus beneficial to study the evolution of the Higgs boson production cross-section as a function of p_{T}^{H} by carrying out a differential H measurement.

In order to set up the differential measurement, the SRL and SRS are split into candidate jet p_{T} bins as discussed in Section 7.1.2, and corresponding regions are also defined for the $\mathrm{CR}_{t\bar{t}}$. In each p_{T} bin of the SR, the Higgs boson mass template is subdivided into five contributions according to values of p_{T}^{H} and y_H (see Section 6.4.1). In the fit, the yields of the Higgs contributions are controlled by the signal strengths μ_H^i ($i = \{0, 1, 2, 3, 4\}$). In line with the strategy defined

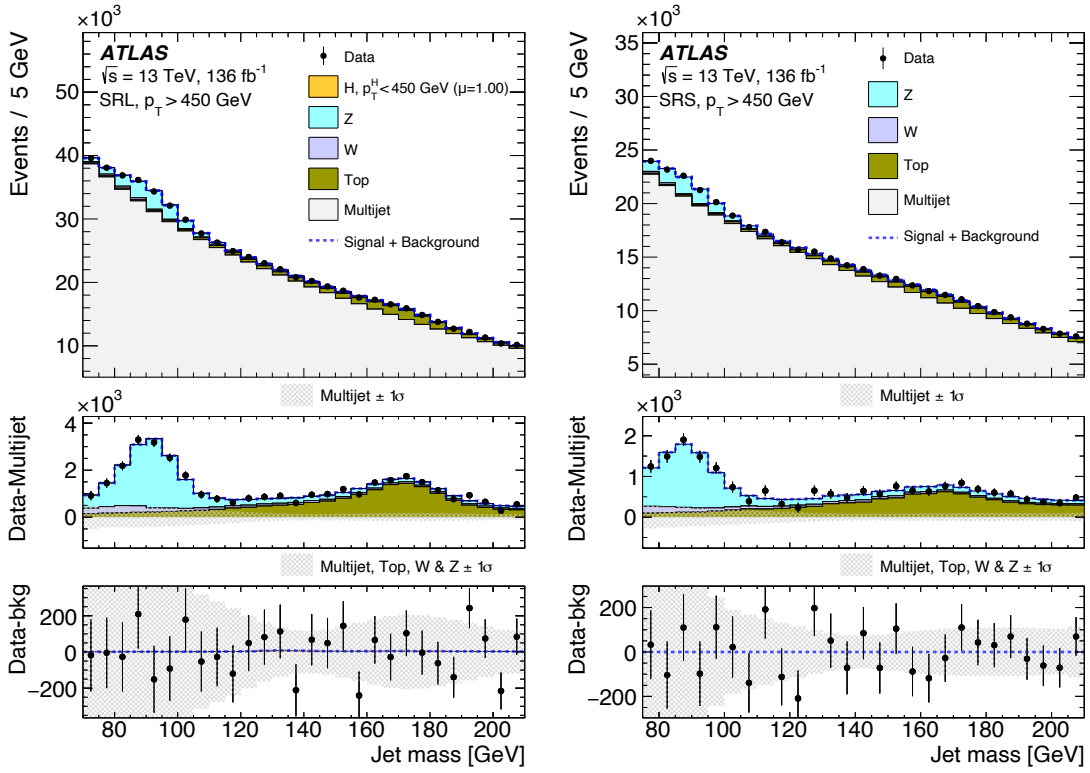

(a) SRL **(b)** SRS

Figure 9.3: Comparison between the data and the signal + background model after the fiducial H fit, both in the (a) SRL ($p_{\mathrm{T}} > 450$ GeV) and (b) SRS ($p_{\mathrm{T}} > 450$ GeV). In the middle panel, the QCD background distribution is subtracted both from the data and the model. The bottom panel also subtracts the remaining backgrounds, leaving only the Higgs template in the model. The Higgs boson signal is not visible in the plots as the $p_{\mathrm{T}}^{H} < 450$ GeV component (fixed to SM) is very small, and the signal strength of the component within the fiducial region is $\mu_H = -0.1$. The $t\bar{t}$ and single top processes are combined into the same distribution called *Top*.

for the fiducial measurement, the Higgs template corresponding to the lowest p_{T}^{H} range is fixed to SM expectation ($\mu_H^0 = 1$), as it falls outside of the fiducial volume of the differential measurement ($p_{\mathrm{T}}^{H} > 300$ GeV and $|y_H| < 2$). All other Higgs signal strengths are treated as free parameters in the fit and they are each described by the same parameter across candidate jet p_{T} bins.

Higgs bosons belonging to a p_{T}^{H} template are predominantly reconstructed in the corresponding candidate jet p_{T} range. Therefore, as previously shown in Figure 7.6, almost every reconstructed p_{T} range contains a dominant Higgs template component covering the corresponding p_{T}^{H} range. Since migration effects are small and strong

constraints are not expected to be coming from non-corresponding regions, the fitting procedure is simplified by neglecting the uncertainty descriptions on non-corresponding Higgs templates in each region. The only exception is the SRS0, where the dominant p_{T1}^{H} and p_{T2}^{H} templates have comparable expected (pre-fit) yields. In this case, the systematic uncertainties of both templates are included in the fit. Asimov fits performed with and without this simplification in the Higgs boson uncertainty description showed negligible variations in the expected results.

Other free parameters in the fit are the μ_Z signal strengths, one for each of the four candidate jet p_{T} ranges, and each described by the same parameter in the SRL and SRS p_{T} bins. Similarly, the $\mu_{t\bar{t}}$ signal strengths are each described by the same parameter in the SRL, SRS and $\mathrm{CR}_{t\bar{t}}$ p_{T} bins. Finally, the yield and shape parameters of the QCD models in every signal region are free to float in the fit.

Before performing the differential H measurement, the complex fit strategy described above is tested on the $V+\mathrm{jets}$ resonance, both in the VR and SR. These tests also allow the study of the interaction between the flexible QCD model and a resonance structure (i.e.the vector bosons) that is topologically similar to the Higgs boson one. In the SR, a remarkable experimental achievement is being able to observe evidence for Z boson production for $650 < p_{\mathrm{T}}^{Z} < 1000$ GeV. In preparation to discussing the differential H results, a brief summary of the $V+\mathrm{jets}$ validation fits is provided in the next section.

9.5.1 Differential $V+\mathrm{jets}$ and Z Boson Results

Before unblinding the Higgs region, the differential fit setup is tested on the $V+\mathrm{jets}$ process. The validation is performed through two independent fits. The first is a differential measurement of the $V+\mathrm{jets}$ process in the VRL, while the second targets the Z boson peak in the signal regions.

In the first fit, the VRL is initially divided into five independent subsets, such that the QCD functional form optimised for the SRL remains a valid description. The fit is set up similarly to the differential H measurement. The $V+\mathrm{jets}$ mass template is divided into five components V^i ($i = \{0, 1, 2, 3, 4\}$) according to p_{T}^{V} ranges that are

numerically equal to the p_{T}^{H} ranges of the differential H setup. Results are given in terms of the four V + jets signal strengths μ_V^i ($i = \{1, 2, 3, 4\}$), which control the normalisations of the corresponding V + jets templates. The signal strength associated to the lowest p_{T}^{V} template is fixed to SM expectation ($\mu_V^0 = 1$) in the fit. Measurements are performed independently on each of the five VRL slices and the results are averaged. A comparison between the data and the post-fit model mass distributions in the VRL1, VRL2 and VRL3 is shown in Figure F.1 of Appendix F.

The second fit constitutes a replica of the differential H setup, where the Z boson process takes the role of the Higgs. Due to the blinding stage of the analysis, the Higgs boson is treated like a background, and it is fixed to SM expectation ($\mu_H = 1$) with no uncertainty descriptions. Table 9.6 summarises the observed and expected results of the differential Z fit. The reported μ_Z values take into account the NLO EW and NNLO QCD corrections (see Section 7.4.1), and they appear to be in good agreement with the SM predictions. In the $450 < p_{\mathrm{T}}^{Z} < 650$ GeV region the Z boson is precisely measured with around 6σ sensitivity. Evidence of Z boson production is also observed for $650 < p_{\mathrm{T}}^{Z} < 1000$ GeV, with a sensitivity of around 3.5σ.

Table 9.6: Expected and observed values of the signal strengths for the Z and $t\bar{t}$ components in the differential Z fit. The value for μ_Z refers to a fiducial volume, while those for $\mu_{t\bar{t}}$ pertain to the corresponding jet p_{T} regions.

p_{T}^{Z} [GeV]	μ_Z		Jet p_{T} [GeV]	$\mu_{t\bar{t}}$	
	Exp.	Obs.		Exp.	Obs.
300–450	1.00 ± 1.06	1.22 ± 1.13	250–450	1.00 ± 0.07	0.85 ± 0.07
450–650	1.00 ± 0.18	1.36 ± 0.22	450–650	1.00 ± 0.07	0.77 ± 0.06
650–1000	1.00 ± 0.32	1.25 ± 0.36	650–1000	1.00 ± 0.09	0.74 ± 0.08
>1000	1.00 ± 1.60	2.08 ± 1.70	>1000	1.00 ± 0.22	0.57 ± 0.17

Figure 9.4 shows the observed μ_V and μ_Z differential results (black points) obtained without applying any higher-order EW or QCD corrections, divided by the nominal prediction from Sherpa 2.2.8 at NLO QCD and LO EW accuracy. They are compared to SM predictions (coloured bands) using higher order EW and QCD

corrections. Both μ_V and μ_Z results show good agreement with SM predictions taking into account both NLO EW and NNLO QCD corrections.

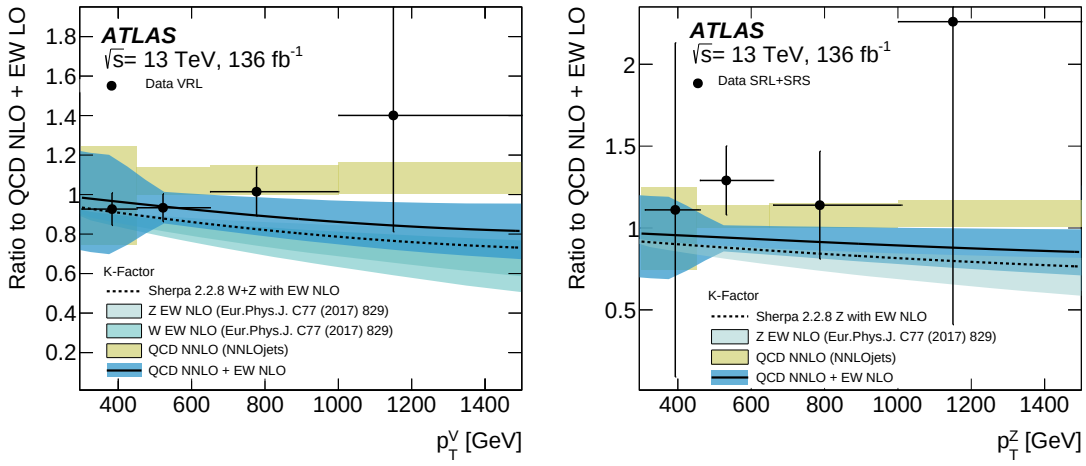

(a) V + jets in VRL **(b)** Z + jets in SR

Figure 9.4: Summary of the differential V + jets (left) and Z (right) results, respectively obtained in the VRL and SR. The results shown (black points) do not take into account NLO EW and NNLO QCD corrections, and they are divided by their expected values from the nominal Sherpa 2.2.8 generator at LO EW and NLO QCD accuracy. They are compared to the NLO EW correction provided by Sherpa 2.2.8, the external NNLO QCD corrections described in Section 7.4.1, and their product. The black points are located at the weighted centre of the bin considering the underlying p_{T}^{V} or p_{T}^{Z} spectrum [1].

The differential V + jets and Z measurements provide robust and trustworthy results that are in agreement with theoretical predictions. This represents a validation of the differential fit setup and paves the way to the unblinding of the Higgs mass window in the SR p_{T} bins. Observing evidence of Z boson production for $650 < p_{\mathrm{T}}^{Z} < 1000$ GeV with around 3.5σ significance constitutes a substantial experimental achievement. For this reason, the Z boson signal strength results listed in Table 9.6 are considered as additional analysis deliverables.

9.5.2 Differential Higgs Boson Result

After the Higgs boson unblinding, the differential H measurement is performed following the prescriptions outlined at the beginning of the section. The Higgs

boson signal strengths observed in the differential measurement are

$$\mu_H^1(300 < p_{\mathrm{T}}^H < 450 \text{ GeV}) = -6 \pm 16(\text{stat.}) \pm 7(\text{syst.}), \tag{9.5}$$

$$\mu_H^2(450 < p_{\mathrm{T}}^H < 650 \text{ GeV}) = -3 \pm 3(\text{stat.}) \pm 4(\text{syst.}), \tag{9.6}$$

$$\mu_H^3(650 < p_{\mathrm{T}}^H < 1000 \text{ GeV}) = 5 \pm 6(\text{stat.}) \pm 3(\text{syst.}), \tag{9.7}$$

$$\mu_H^4(p_{\mathrm{T}}^H > 1000 \text{ GeV}) = 18 \pm 30(\text{stat.}) \pm 10(\text{syst.}). \tag{9.8}$$

The signal strength results are extracted in the fiducial region $p_{\mathrm{T}}^H > 300$ GeV, $|y_H| < 2$ and they are used to set the following observed (expected) 95% CL upper limits on the Higgs boson production cross-section:

$$\sigma_H(300 < p_{\mathrm{T}}^H < 450 \text{ GeV}) < 2.9 \text{ (3.1) pb}, \tag{9.9}$$

$$\sigma_H(450 < p_{\mathrm{T}}^H < 650 \text{ GeV}) < 89 \text{ (102) fb}, \tag{9.10}$$

$$\sigma_H(650 < p_{\mathrm{T}}^H < 1000 \text{ GeV}) < 39 \text{ (34) fb}, \tag{9.11}$$

$$\sigma_H(p_{\mathrm{T}}^H > 1000 \text{ GeV}) < 9.6 \text{ (7.4) fb}. \tag{9.12}$$

Table 9.7 summarises the observed and expected values of the four free-floating Higgs signal strengths, as well as the μ_Z and $\mu_{t\bar{t}}$ results obtained in the four candidate jet p_{T} bins. All reported μ_Z results are corrected to account for NLO EW and NNLO QCD corrections. The μ_H and μ_Z results are in good agreement with the SM prediction, while the $t\bar{t}$ signal strengths are compatible with results from standalone $\mathrm{CR}_{t\bar{t}}$ fits in the same kinematic ranges and dedicated $t\bar{t}$ measurements in similar phase spaces.

The post-fit yields of all signal and background processes participating in the differential H fit are given in Table F.4 of Appendix F.

Figure 9.5 shows a comparison between the data and the post-fit signal and background mass distributions in all signal regions. As for the previous measurements, the middle panels subtract the QCD background both from the data and the model, while the bottom panels subtract all backgrounds. Good agreement is observed between the post-fit model and the data in every region.

The inter-correlations between the differential μ_H measurements in p_{T}^H bins, and correlations between the μ_H measurements and μ_Z measurements in p_{T} bins are

Table 9.7: Expected and observed values of the signal strengths for the H, Z, and $t\bar{t}$ components in the differential fits. The value for μ_H refers to a fiducial volume, while those for μ_Z and $\mu_{t\bar{t}}$ pertain to the corresponding jet p_{T} regions.

p_{T}^H [GeV]	μ_H	
	Exp.	Obs.
300–450	1 ± 18	-6 ± 18
450–650	1.0 ± 3.3	-3 ± 5
650–1000	1 ± 6	5 ± 7
>1000	1 ± 30	18 ± 32

Jet p_{T} [GeV]	μ_Z		$\mu_{t\bar{t}}$	
	Exp.	Obs.	Exp.	Obs.
250–450	1.0 ± 1.1	1.8 ± 1.1	1.00 ± 0.07	0.85 ± 0.06
450–650	1.00 ± 0.17	1.28 ± 0.22	1.00 ± 0.07	0.76 ± 0.06
650–1000	1.00 ± 0.33	1.4 ± 0.4	1.00 ± 0.09	0.74 ± 0.08
>1000	1.0 ± 1.6	2.4 ± 1.7	1.00 ± 0.22	0.57 ± 0.18

shown in Figure 9.6. These represent a good indicator of the sanity of the differential H boson fit setup. The correlation matrix of the Higgs signal strengths shows very small interactions between measurements performed in different p_{T}^H ranges. This is expected, considering the small migration effects between non-corresponding p_{T}^H and p_{T} regions seen in Figure 7.6. Each Higgs boson signal strength is primarily determined in a single p_{T} range, while negligible constraints are obtained in other regions, due to the corresponding p_{T}^H template being very small.

The interactions between μ_H and μ_Z measurements are seen to primarily originate in corresponding p_{T}^H and p_{T} regions. This, again, attests the small migration effects characterising the Higgs boson mass templates. The observed positive correlations between μ_H and μ_Z in corresponding p_{T}^H-p_{T} ranges are expected considering their interaction with the dominant QCD background. In order to increase one of these signal strengths, the fit would primarily reduce the QCD background yield, which, however, extends across the whole mass spectrum. Therefore, this creates a deficit underneath the other resonance, requiring the corresponding signal strength to be increased as well.

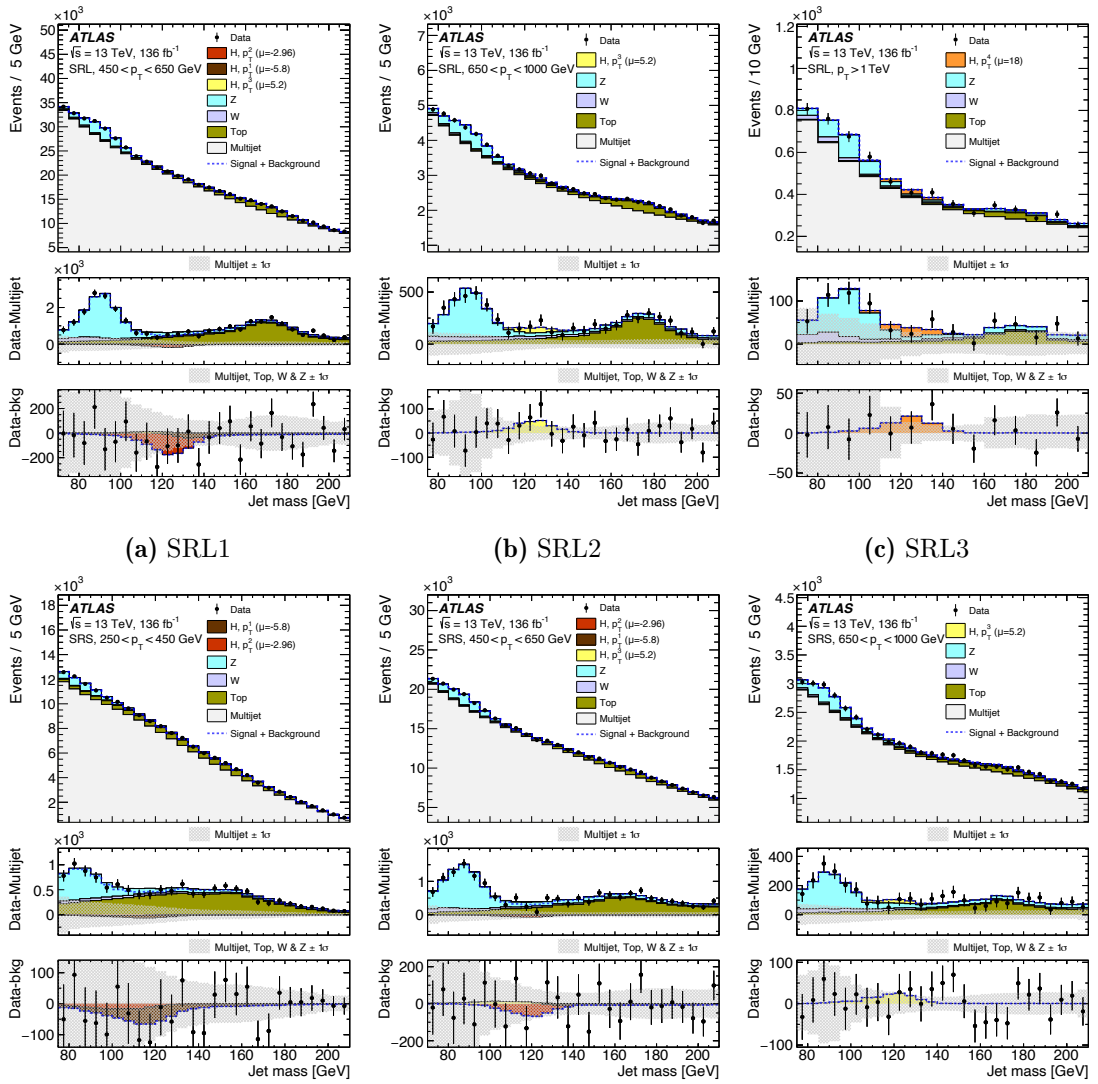

(a) SRL1 **(b)** SRL2 **(c)** SRL3

(d) SRS0 **(e)** SRS1 **(f)** SRS2

Figure 9.5: Comparison between the data and the signal + background model after the differential H fit, in the (a) SRL1 ($450 < p_{\mathrm{T}} < 650$ GeV), (b) SRL2 ($650 < p_{\mathrm{T}} < 1000$ GeV), (c) SRL3 ($p_{\mathrm{T}} > 1$ TeV), (d) SRS0 ($250 < p_{\mathrm{T}} < 450$ GeV), (e) SRS1 ($450 < p_{\mathrm{T}} < 650$ GeV) and (f) SRS2 ($650 < p_{\mathrm{T}} < 1000$ GeV). In each plot, the middle panel subtracts the QCD background both from the data and the model. The bottom panel subtracts all backgrounds, leaving only the Higgs template in the model. The $t\bar{t}$ and single top processes are combined into the same distribution called *Top*.

The Higgs boson signal strength results are converted into cross-section estimates and upper limits, which are summarised in Figure 9.7. The black points represent the differential cross-section results divided by the SM predictions, while the grey bands are the uncertainties on the measurements. Finally, the black lines are the 95% CL upper limits on the H boson production cross-section in each p_{T}^{H}

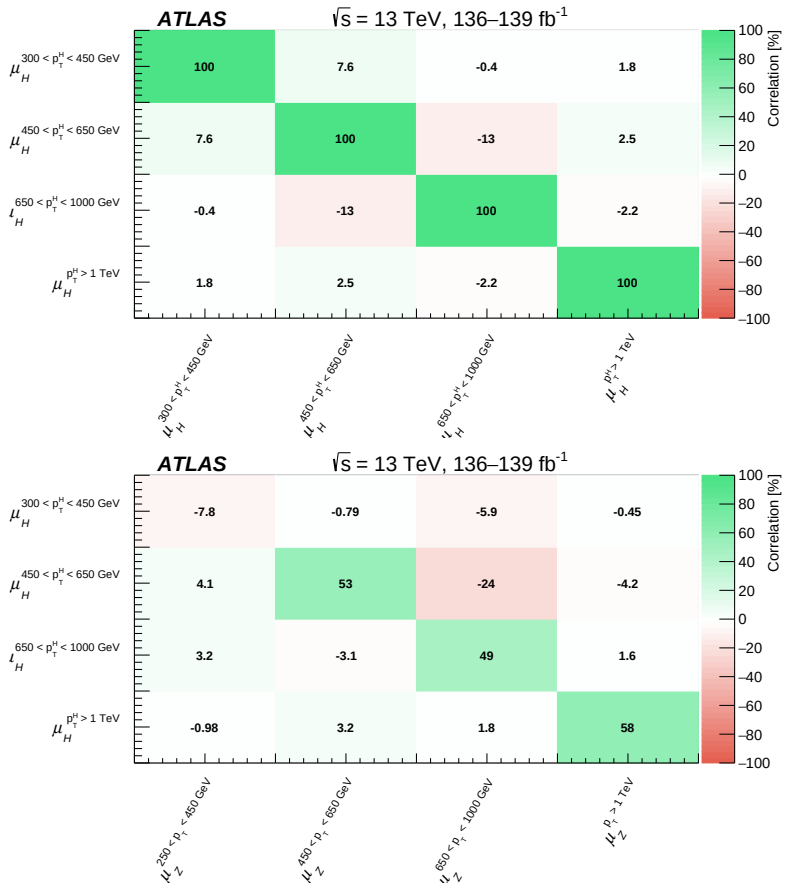

Figure 9.6: Inter-correlations between the differential μ_H measurements in p_{T}^H bins, and correlations between the μ_H measurements and μ_Z measurements in p_{T} bins [1].

bin. The most sensitive Higgs boson measurement is performed in the p_{T}^H range 450–650 GeV. This is expected, considering that μ_H^2 is mainly determined in the SRL1 and SRS1, namely the regions populated by the highest numbers of events. The cross-section measurement in the lowest p_{T}^H bin is instead characterised by comparably poor sensitivity, as this component is mainly determined in the SRS0. The sensitivity for $p_{\mathrm{T}}^H > 650$ GeV progressively deteriorates, as event yields drop and statistical uncertainties increase.

Table 9.8 shows the uncertainty breakdown for the four Higgs boson signal strengths. Every measurement is statistically limited, with the exception of μ_H^2, whose total uncertainty is dominated by the systematic component. This is reasonable, considering that the Higgs measurement in this p_{T}^H range is primarily constrained in the SRL1 and SRS1, the most populated regions in terms of number

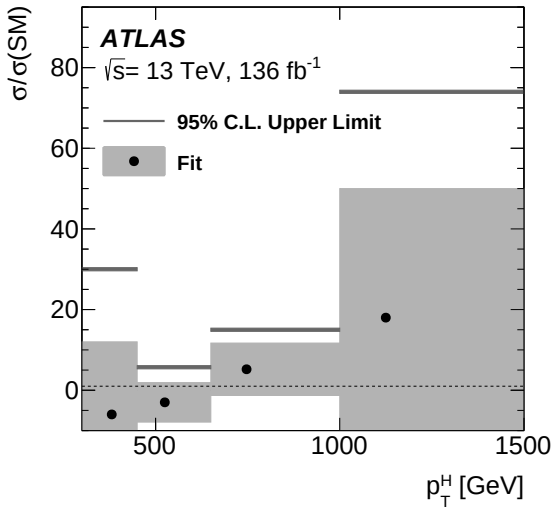

Figure 9.7: Summary of the Higgs differential cross-section results (black points) divided by the SM predictions (σ(SM)). The points are located at the weighted centre of the bin considering the underlying p_{T}^{H} spectrum. The grey bands represent the measurement uncertainties, while the black lines are the 95% CL upper limits on the Higgs cross-section measurements [1].

of events. The large-R jet uncertainties are the largest contribution to the systematic component, driven by JMS effects. The impact of flavour tagging uncertainties is seen to increase above 1 TeV mainly due to the high-p_{T} extrapolation uncertainty on the calibrations. The $t\bar{t}$ modelling systematic uncertainties, driven by the Parton Shower and Matrix Element contributions, are largest in the lowest p_{T} bin, while they are observed to decrease above 450 GeV. This is due to the top quark decay products becoming more collimated at high-p_{T}, thus reducing the contamination around the Higgs boson mass peak. The 10 fit parameters with the highest impact on the determination of the most systematically limited Higgs boson signal strengths μ_H^2 and μ_H^3 are shown, respectively, in Figures F.2c and F.2d of Appendix F.

Figure 9.8 shows that the fit is able to reduce (constrain) the dominant JMS uncertainty component (JMS Modelling) in V + jets events by 30%-40% for $p_{\mathrm{T}} >$ 450 GeV, and by 20%-65% for $t\bar{t}$ events over the full jet p_{T} range. The $t\bar{t}$ JMR uncertainty is constrained by 55%-70% below 1 TeV, but only by 10% above 1 TeV. Thanks to the high purity of the $\mathrm{CR}_{t\bar{t}}$, the fit constrains the $t\bar{t}$ Parton Shower and Matrix element systematic uncertainties by 20%-30%. All other nuisance parameters

Table 9.8: Breakdown of the Higgs signal strengths total uncertainties (first row) in terms of contributions from individual uncertainty groups, for the differential H measurement. The total uncertainty is subdivided into the statistical and systematic component. The systematic uncertainty is also broken down in terms of various groups of systematic sources.

Uncertainty Contribution	$\sigma(\mu_H^1)$	$\sigma(\mu_H^2)$	$\sigma(\mu_H^3)$	$\sigma(\mu_H^4)$
Total	18	5.0	6.5	32
Statistical	16	3.0	5.5	30
Systematic	7	3.9	3.4	10
Large-R Jet Syst. (Tot.)	6	3.8	3.4	9.5
Modelling and Theory Syst.	4	0.7	0.7	2
Flavour Tagging Syst.	0.2	0.4	0.4	2

in the fit do not show significant pulls or constraints.

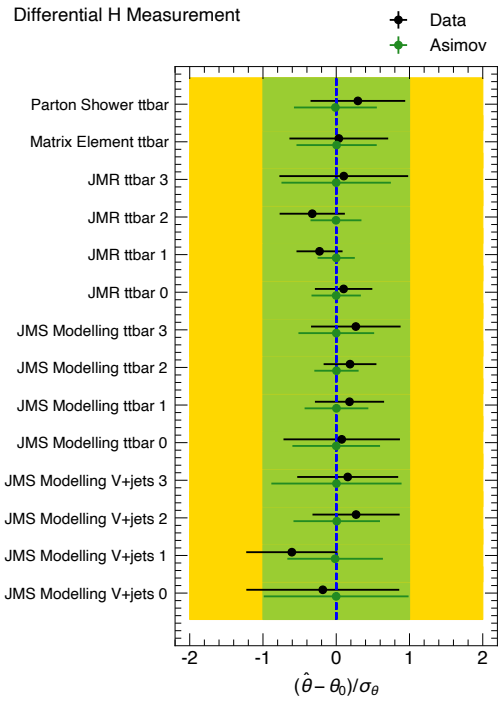

Figure 9.8: Pulls and widths of some of the most impactful systematics characterising the differential H measurement. Not shown are the V + jets JMR uncertainties which are externally constrained following the procedure outlined in Section 8.4. All other uncertainties missing from the plot are not significantly constrained or pull.

9.6 Future Outlook

The results presented this far in the chapter have been published in May 2022 and they can be found in Reference [1]. The analysis sensitivity to the Higgs boson is seen to be strongly limited by the large statistical uncertainties due to the low number of events in the signal regions. Therefore, major sensitivity improvements are expected in future analysis iterations as more pp collision data are collected by the ATLAS detector. At the time of writing, the LHC Run 3 has just started and it is expected to deliver an integrated luminosity of around 400 fb^{-1}. Since almost all results have been found to be statistically limited, a future iteration of the analysis exploiting the combined Run 2 + Run 3 dataset is thus expected to achieve a higher Higgs sensitivity by at least 50%[2].

Currently, the ATLAS Collaboration is working on the next iteration of the Boosted $H(\to b\bar{b})+$jet analysis, which will make use of the full Run 2 dataset, while updating the analysis strategy and event selections to more refined techniques. As previously discussed, recent advancements in the b-tagging algorithms are expected to significantly increase the signal-to-background ratio in the signal regions. In particular, the next iteration of the analysis will likely take advantage of D_{Xbb}, a dedicated tagger for boosted $H \to b\bar{b}$ large-R jets (see Appendix A) whose calibration is currently being finalised.

Another promising avenue for suppressing background events in the signal regions is exploiting the substructure features of large-R jets. The information about the energy correlation between large-R jet constituents can be described using various *jet substructure variables* [124]. These are found to be particularly useful at separating large-R jets compatible with a two-prong substructure (like Higgs or vector boson jets) from those having a three-prong substructure (like top quark jets). Despite some promising initial results, additional care must be taken in order to prevent the substructure variable selections from sculpting the mass spectrum of background events. In the next iteration of the analysis, the information about

[2]The sensitivity of a statistically limited analysis can be calculated as $S/\sqrt{B}$, where S and B are, respectively, the measured yields of the signal and background processes.

the internal structure of jets could be paired with mass decorrelation techniques to suppress the $t\bar{t}$ background contamination in the SR.

Finally, more precise measurements will be possible thanks to advancements in the estimation of the jet mass and energy resolution uncertainties [125] and to innovative large-R jet reconstruction techniques that are currently being developed [126].

A measurement analogous to the one presented in this thesis has recently been performed by the CMS Collaboration [15], achieving significantly better Higgs boson sensitivity. The main reason for the improvement is to be found in the larger signal-to-background ratio that characterises the signal region. The dedicated neural network-based $H \to b\bar{b}$ jet tagger used by the CMS analysis yields, in fact, a QCD multijet background that is approximately smaller by a factor of 2 with respect to that of the analysis presented in this thesis. Additional Higgs sensitivity is also gained by exploiting jet substructure variables. Finally, recent studies within the ATLAS flavour tagging group have suggested that the optimisation of the low-level taggers might not optimal for high-p_{T} jets.

The analysis presented in this thesis probes $H \to b\bar{b}$ events inclusively in production mode. This maximises sensitivity while still allowing access to possible cross-section enhancements in the ggF process. Nevertheless, important insights on the nature of the Higgs boson can be obtained by also measuring the differential Higgs boson cross-section for individual production processes. For instance, an analysis specifically targeting high-p_{T} $H \to b\bar{b}$ events produced through the VH process is being developed by the ATLAS Collaboration. In this analysis, the signal regions are defined by requiring one large-R jet in the event to be tagged by D_{Xbb} (Higgs jet), while another jet must reconstruct a hadronic vector boson decay.

As previously mentioned, the next iteration of the analysis presented in this thesis is still at an early development stage, and finalised results are not yet available. However, preliminary studies have been carried out by the author in order to quantify the effect of introducing recently developed b-tagging algorithms. The results of these studies are summarised in the next section.

9.6.1 Preliminary Studies

As discussed in Section 4.2.2 and Appendix A, the deep neural network-based DL1r and D_{Xbb} b-taggers are characterised by significantly lower mistag rates than MV2c10. Therefore, a simple update of the b-tagging algorithm in the analysis strategy might lead to a sizable background reduction in the SR and a consequent increase in Higgs boson sensitivity.

In preparation to the next analysis iteration, studies are performed to assess the level of improvement expected by switching from the MV2c10 to the DL1r b-tagger. In order to perform a fair comparison, no other changes in the analysis selection are made and the same b-tagging efficiency working point is used (77%). A comparison between MV2c10 and D_{Xbb} is also planned, once the full calibration of this tagger is finalised.

Figure 9.9 compares the simulated Higgs boson mass distributions obtained in the signal regions by using either the MV2c10 or the DL1r tagger. It is interesting to note that using the DL1r tagger leads to a 10% (9%) Higgs boson yield reduction in the SRL (SRS). This is expected, considering that DL1r is characterised by ~10% lower b-tagging efficiency for track jet $p_{\mathrm{T}} > 40$ GeV (see Figure 4.10a). By looking at the ratio panel, however, DL1r appears to be more efficient at rejecting top quark jets from $t\bar{t}$H events contaminating the high-mass tail of the Higgs distribution.

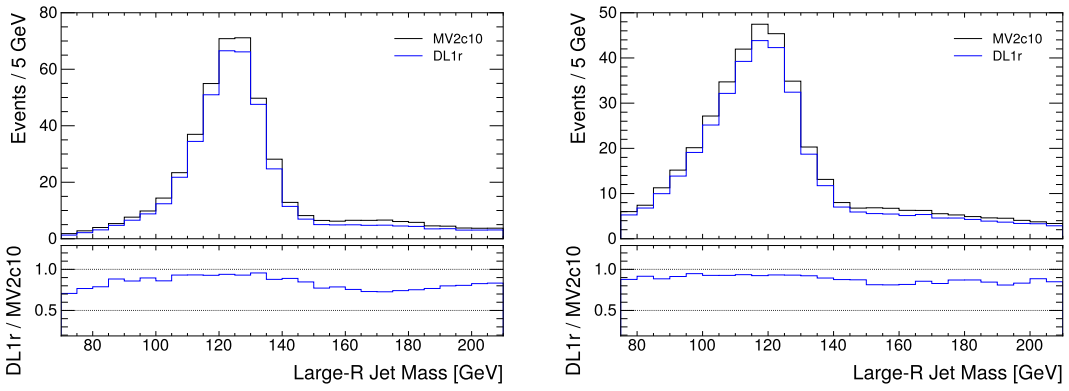

(a) Higgs SRL **(b)** Higgs SRS

Figure 9.9: Simulated Higgs boson mass distributions obtained in the SRL (a) and SRS (b) using either the MV2c10 or the DL1r b-tagging algorithm.

Figure 9.10 compares the simulated $t\bar{t}$ mass distributions obtained in the SRL, SRS and $CR_{t\bar{t}}$ by using either the MV2c10 or the DL1r tagger. In the SRL (SRS), the distribution obtained using the new tagger is characterised by a very similar shape to the MV2c10 one, but it features a 41% (32%) lower yield. This strong reduction is related to the lower mistagging rate of the DL1r tagger. Top quark jets populating the SR are characterised, for the most part, by a true b-subjet coming from the top quark decay and by at least one track jet from the W boson hadronic decay that is mistagged as a b-subjet. Therefore, the lower mistagging rate of the DL1r tagger prevents more top quark jets from being double b-tagged and entering the SR. The same effect does not, of course, characterise the $CR_{t\bar{t}}$, which specifically targets top quark jets by requiring exactly one b-tagged subjet. In this region, the $t\bar{t}$ mass distributions are very similar, differing by only a few per cent in yield.

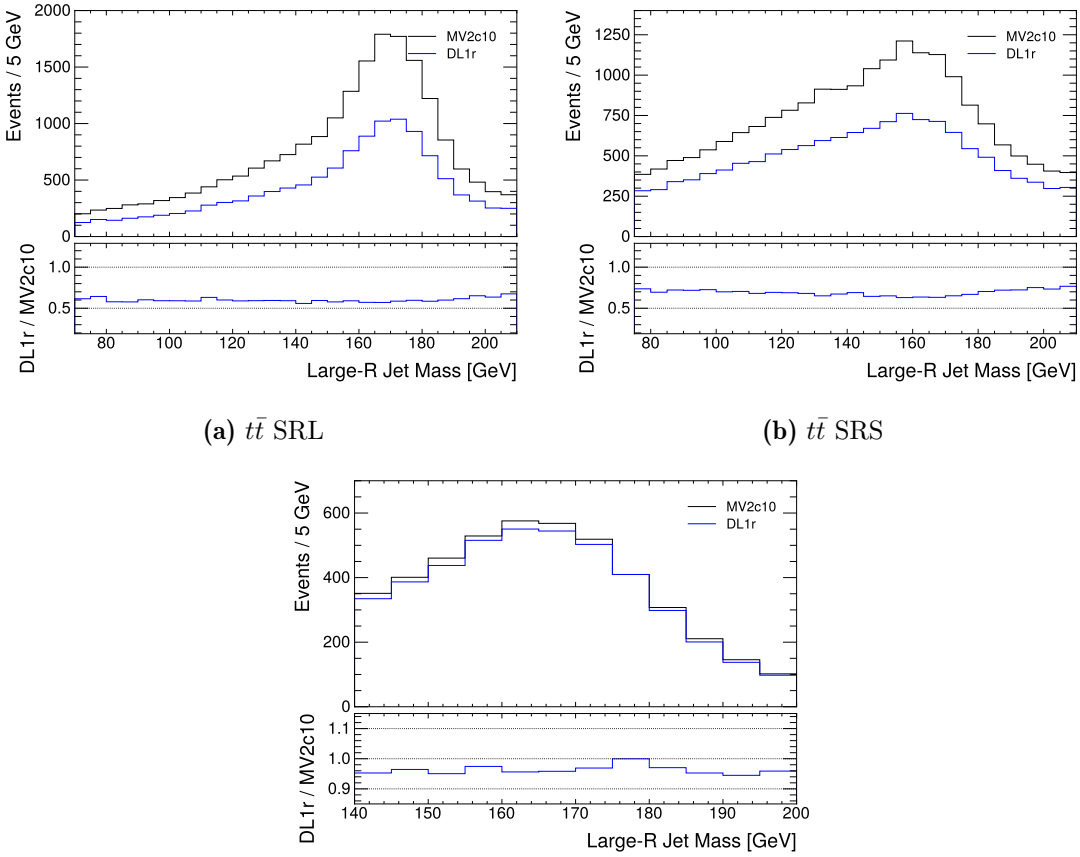

(a) $t\bar{t}$ SRL

(b) $t\bar{t}$ SRS

(c) $t\bar{t}$ $CR_{t\bar{t}}$

Figure 9.10: Simulated $t\bar{t}$ boson mass distributions obtained in the SRL (a), SRS (b) and $CR_{t\bar{t}}$ (c) using either the MV2c10 or the DL1r b-tagging algorithm.

Once properly corrected to match the SR kinematics, the VR data constitute the environment where the QCD multijet function is tested and optimised (see Section 7.2). Figure 9.11 compares the candidate jet mass distributions in data obtained in the VRL and VRS by using either the MV2c10 or the DL1r tagger. The two distributions have very similar shapes, meaning that the currently used QCD model might still be valid in a future iteration of the analysis using DL1r. The slightly lower yield of the MV2c10 distribution is explained by its higher mistag rate, leading to fewer events passing the 0-tag requirements of the validation regions.

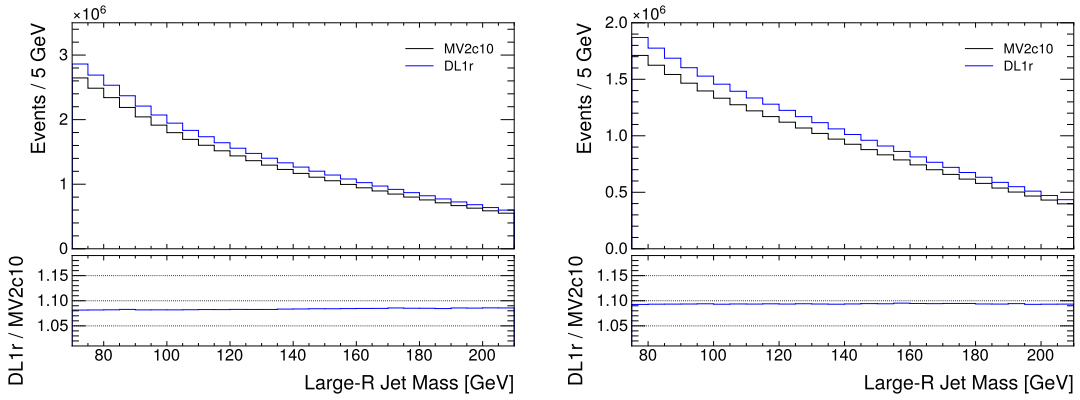

(a) Data VRL **(b)** Data VRS

Figure 9.11: Candidate jet mass distributions in data obtained in the VRL (a) and VRS (b) using either the MV2c10 or the DL1r b-tagging algorithm.

The goal of these preliminary studies is to estimate the improvement in Higgs sensitivity achievable by simply updating the b-tagging algorithm. At the time of writing, the new iteration of the analysis is, however, at an early development stage and the SR data is still blinded. Without ever looking at the jet mass distribution, a rough estimate of the amount of background in the SR can be obtained, however, by simply counting the number of events in the datasets and subtracting the Higgs yield expected from MC. Compared to MV2c10, the SRL and SRS datasets selected using the DL1r tagger are characterised, respectively, by around 34% and 32% lower background yields (B). Considering that, correspondingly, the signal yield (S) is reduced by around 10%, simply updating the b-tagging algorithm to DL1r is expected to increase the Higgs boson sensitivity ($S/\sqrt{B}$) of the analysis by around 10%.

Further improvement is expected when moving to the D_{Xbb} tagger, which shows better background rejection than DL1r, especially for top quark jets (see Appendix A). Furthermore, early studies hinted that using the D_{Xbb} tagger might result in a ~15% increase in SR Higgs yield with respect to MV2c10. Differently from the case of DL1r, however, a new analysis selection needs to be defined when introducing the D_{Xbb} tagger. An analogous signal region definition is achievable by requiring candidate jets to pass the D_{Xbb} Higgs tagging score corresponding to the 60% WP ($2 \times 77\%$ single b-tagging efficiencies). A new selection must, however, be introduced for the VR, as an equivalent to the 0-tag requirement characterising these regions cannot be defined as a simple cut on the D_{Xbb} score. Finally, a new definition of the $\text{CR}_{t\bar{t}}$ would be necessary, which might take advantage of the top quark output probability provided by the D_{Xbb} tagger.

At the time of writing, a finalised analysis strategy able to exploit the full potential of the D_{Xbb} tagger still needs to be developed. The new tagger is promising and it is expected to significantly improve the Higgs boson sensitivity of the next analysis iteration. However, more research is necessary in order to optimise the new analysis strategy and to prevent the event selections from potentially sculpting the jet mass distributions of the background processes.

Future iterations of the analysis using larger datasets, targeting specific production processes and exploiting more sophisticated b-tagging algorithms will be important parts of the Run 3 Higgs programme, complementing the established measurements at lower p_{T}^{H}.

10 Conclusions

This thesis presents Higgs boson cross-section measurements obtained from high-transverse momentum $H \to b\bar{b}$ decays. The results use $\sqrt{s} = 13$ TeV pp collision data collected by the ATLAS experiment during the full Run 2 of the LHC, corresponding to an integrated luminosity of 136 fb^{-1}.

The Higgs boson is reconstructed as a single large-R calorimeter jet associated with two b-tagged VR track jets. At least one additional large-R calorimeter jet is required in the event, representing the recoil target of the high-p_{T} Higgs boson. The $H \to b\bar{b}$ final states are selected inclusively in Higgs boson production mode.

At high p_{T}, the Higgs boson production is sensitive to the virtual fermion loop in the ggF production mode, including possible contributions from Beyond the Standard Model phenomena. In some scenarios, the presence of new physics contributions could induce strong Higgs boson cross-section enhancements in the high-p_{T} phase space studied by the analysis without significant deviations from the increasingly well measured production at lower p_{T} values, giving these results importance for effective field theory interpretations.

Cross-section measurements are performed in a fiducial region where the generator-level Higgs boson transverse momentum (p_{T}^{H}) and rapidity (y_H) satisfy $p_{\mathrm{T}}^{H} > 450$ GeV, $|y_H| < 2$. A differential measurement is also performed in the p_{T}^{H}

ranges 300–450 GeV, 450–650 GeV, 650–1000 GeV and > 1 TeV. In each range, $|y_H| < 2$ is also required.

The observed (expected) 95% confidence level upper limits on the Higgs boson production cross-section in the fiducial and differential regions are

$$\begin{aligned}
\sigma_H(p_{\mathrm{T}}^H > 450 \text{ GeV}) &< 115 \text{ (128) fb;} \\
\sigma_H(300 < p_{\mathrm{T}}^H < 450 \text{ GeV}) &< 2.9 \text{ (3.1) pb;} \\
\sigma_H(450 < p_{\mathrm{T}}^H < 650 \text{ GeV}) &< 89 \text{ (102) fb;} \\
\sigma_H(650 < p_{\mathrm{T}}^H < 1000 \text{ GeV}) &< 39 \text{ (34) fb;} \\
\sigma_H(p_{\mathrm{T}}^H > 1 \text{ TeV}) &< 9.6 \text{ (7.4) fb.}
\end{aligned}$$

All Higgs boson results are consistent with the SM predictions, with no evidence found for cross-section enhancements at high p_{T}. For the first time at ATLAS, the Higgs boson decaying to $b\bar{b}$ is probed at the TeV scale, inclusively in production mode.

At the time of writing, the LHC Run 3 has just started, and it is expected to deliver an integrated luminosity of around 400 fb^{-1}. Since almost all Higgs boson measurements presented in this thesis are statistically limited, sensitivity improvements as large as 50% are expected in future iterations of the analysis exploiting the combined Run 2 + Run 3 dataset. Avenues for increased analysis sensitivity also include the use of jet substructure variables for improving signal purity and a dedicated neural-network-based double b-tagger aiming at boosted resonances decaying to a $b\bar{b}$ pair.

The analysis presented in this thesis constitutes a blueprint for further studies of very high-p_{T} Higgs boson production. Potential future explorations include process-specific selections and dedicated probes of ggF production. Of additional interest is the BSM interpretation of this result, where a search for a dark matter mediator decaying to a $b\bar{b}$ pair could be performed across the probed mass range.

Appendices

A

$g \to b\bar{b}$ Calibration - Recent Developments

The results presented in Chapter 5 capture the calibration of the MV2-based double b-tagger at a rather early development stage. Since then, however, the analysis team has moved on to exploring more advanced algorithms based on neural network methods. This section describes the latest, the *Boosted* $X \to b\bar{b}$ *tagger*, and it summarises the main changes to the calibration procedure.

A.1 The Boosted $X \to b\bar{b}$ Tagger

The Boosted $X \to b\bar{b}$ tagger (D_{Xbb}) [127] is a dedicated double b-tagging algorithm based on a neural network. It is applied at the large-R jet level, and it combines the b-tagging information of up to three subjets along with the large-R jet kinematics (p_{T} and η). Its main purpose is to identify large-R jets originating from massive particles X, like the Higgs, decaying into a boosted pair of b quarks.

The b-tagging information is supplied to the tagger by the high-level b-tagging algorithm DL1r. As already explained in Section 4.2.2, this deep neural network-based algorithm outputs the probabilities for a jet to be a b-, c-, or light-jet. The DL1r tagger benefits from a dedicated optimization for VR track jets.

The Boosted $X \to b\bar{b}$ tagger combines the subjet flavour information and the large-R jet kinematics using a deep neural network. For any assessed large-R

jet, three outputs are provided, representing the probabilities for it to be a Higgs (p_{Higgs}), QCD (p_{QCD}) and top-quark (p_{top}) jet. These values are combined into a single discriminant D_{Xbb}, which is defined as

$$D_{\text{Xbb}} = ln\left(\frac{p_{\text{Higgs}}}{f_{\text{top}} \cdot p_{\text{top}} + (1 - f_{\text{top}}) \cdot p_{\text{QCD}}}\right), \tag{A.1}$$

where f_{top} determines the fraction of the top-quark background.

The tagger's performance for the recommended choice of $f_{\text{top}} = 0.25$ is evaluated on simulated samples in terms of Higgs tagging efficiency versus background rejection [128]. The Higgs tagging efficiency is defined as the fraction of generated $H \to b\bar{b}$ jets that are tagged by D_{Xbb}, while the background rejection factors are defined as the reciprocal values of the mistagging efficiencies for top quark and QCD multijet events.

Figure A.1 shows the QCD multi-jet and top-jet background rejection of the D_{Xbb} tagger as a function of the Higgs tagging efficiency. For comparison, the double b-tagging performance of the MV2 and DL1r algorithms is also shown. The large-R jets used in the comparison are required to satisfy $p_{\text{T}} > 500$ GeV, $|\eta| < 2$ and $76 < m < 146$ GeV.

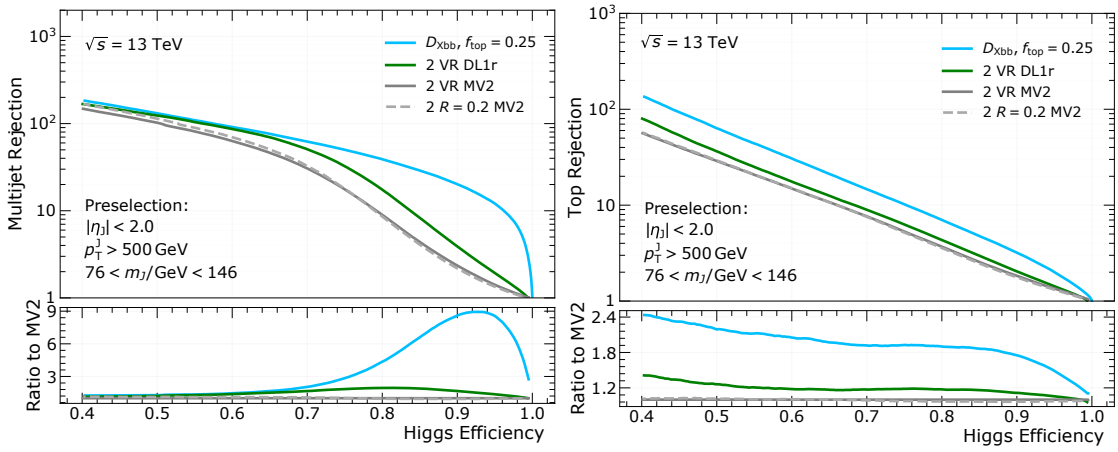

Figure A.1: QCD multi-jet and top-jet rejection factors for the D_{Xbb} tagger (cyan), as a function of the Higgs tagging efficiency. For comparison, the double b-tagging performance of the MV2 (grey) and DL1r (green) algorithms is also shown. For the MV2 tagger, both results obtained by tagging two individual VR track jets (solid grey line) and by tagging two individual fixed radius jets with $R = 0.2$ (dashed grey line) are shown. The large-R jets used in the comparison are required to satisfy $p_{\text{T}} > 500$ GeV, $|\eta| < 2$ and $76 < m < 146$ GeV [128].

Within this kinematic region, the D_{Xbb} algorithm is seen to significantly outperform both single b-tagging algorithms in top rejection and perform generally better in multijet rejection. Performance studies provide recommended working points for the D_{Xbb} tagger corresponding to 50%, 60% and 70% Higgs tagging efficiency.

A.2 Changes to the $g \to b\bar{b}$ Calibration

At the time of writing, preliminary calibrations of the D_{Xbb} tagger using high-p_{T} $Z(\to b\bar{b})\gamma$ and $Z(\to b\bar{b})$ + jets events have been released [127]. A finalised calibration using high-p_{T} $g \to b\bar{b}$ events is still an ongoing effort within the ATLAS Collaboration. The $g \to b\bar{b}$ calibration setup described in Section 5.1 has changed considerably and it is currently dedicated to the calibration of the D_{Xbb} tagger. For the sake of brevity, a list of the most important changes is reported below.

- **Full Run 2 Data:** Differently from the previous iteration, that only used 2017 collision data, the latest tagger calibration takes advantage of the full Run 2 dataset, corresponding to an integrated luminosity of 139 fb^{-1}.

- **Prescaled Triggers:** The previous calibration used an unprescaled trigger, whose high p_{T} threshold effectively limited the large-R jet momentum to $p_{\text{T}} > 500$ GeV. Since the decay products of a Higgs boson start being clusterable into large-R jets at around $p_{\text{T}} = 250$ GeV, this had the undesired effect of excluding a sizeable portion of the phase space region relevant to the tagger. In the latest tagger calibration, this issue has been solved by using prescaled triggers with lower p_{T} thresholds. This has allowed the calibration to reduce the minimum large-R jet p_{T} requirement to 250 GeV.

- **Three Subjet Flavour Definition:** As previously mentioned, the $X \to b\bar{b}$ tagger classifies jets considering up to three highest p_{T} subjets. To reflect this, the large-R jet flavour labelling has been updated to include the flavour of the third jet (if present). On top of the B, C and L labels already used for the muon and non-muon jets, the additional label x can be given to the

third jet, in case it is missing. This new classification determines 36 possible tri-flavour combinations. These are finally combined into the usual di-flavour combinations BB, BL, CC, CL and LL according to a D_{Xbb} similarity criterion.

- **Fit Software and Systematics:** Switching to a new fit software has allowed to seamlessly include systematic uncertainties in the fit, correctly accounting for their correlations. In addition, a complete set of systematic uncertainties is now available, including the dominant parton shower systematic.

- **Calibration Procedure:** In the previous calibration setup, the events used to compute the scale factors were a subset of those used for the flavour correction, which could potentially introduce a bias in the results. In order to solve this issue, in the new calibration events are first divided into *pass* and *fail* regions, depending on whether the $g \to b\bar{b}$ candidate passes or fails the Boosted $X \to b\bar{b}$ tagger. Both regions are further split into large-R jet p_{T} bins and in each of them $\langle s_{d_0} \rangle$ flavour templates for j_{μ}^{trk} and $j_{\mathrm{non}-\mu}^{\mathrm{trk}}$ are extracted. Independently in every large-R jet p_{T} bin, the j_{μ}^{trk} and $j_{\mathrm{non}-\mu}^{\mathrm{trk}}$ $\langle s_{d_0} \rangle$ distributions are simultaneously fit in both *pass* and *fail* regions (i.e. 4 simultaneous fits per p_{T} bin). The scale factors $k_{b\bar{b}}$, defined in the *pass* regions as in Equation 5.6, enter the likelihood definition and are thus obtained directly from the fit. An additional constraint is given by the anti-tag scale factors $k_{\text{anti-}b\bar{b}}$, which are defined in the *fail* regions and are related to $k_{b\bar{b}}$ as

$$k_{\text{anti-}b\bar{b}} = \frac{1 - \epsilon_{b\bar{b}}^{\mathrm{data}}}{1 - \epsilon_{b\bar{b}}^{\mathrm{MC}}} = \frac{1 - k_{b\bar{b}}\epsilon_{b\bar{b}}^{\mathrm{MC}}}{1 - \epsilon_{b\bar{b}}^{\mathrm{MC}}}. \tag{A.2}$$

As a result, in the new iteration, scale factors are given in large-R jet p_{T} bins, and they are thus of more immediate use for analyses that rely heavily on these objects.

B

Muon-in-Jet Correction

A serious challenge that must be faced when attempting to measure the Higgs boson is that other resonant processes inhabit the same mass range. Both the vector bosons and the top-quark can, in fact, be reconstructed within a single large-R jet, thus creating two large resonances that surround the Higgs mass peak. In addition to disentangling the various resonances, the jet mass resolution accuracy is important when considering the interplay between resonances and the dominant QCD multijet background. When fitting signal and background models to the signal regions, the QCD might compensate for an inaccurate mass resolution, biasing the measured yields of the resonances inhabiting the mass range (like the Higgs or Z bosons). The resolution of the jet mass measurement is thus of crucial importance in the extraction of the Higgs signal.

Unfortunately, because of the very nature of the $b\bar{b}$ final state, several effects can degrade the jet mass resolution. The relatively large semi-leptonic BR of b-hadrons decays leads to escaping neutrinos and charged leptons, including identified muons, that are not included in the reconstructed jets. This has the undesired effect of biasing the jets' p_{T}, energy and mass towards lower values. Additionally, the standard jet energy calibrations introduced in Section 4.1.3 do not consider the effects of semi-leptonic decays, leading to a degradation in mass resolution.

These effects can be partially accounted for by applying a *muon-in-jet* correction to the kinematic properties of jets. This means adding to any associated track jet's four-momentum that of the closest ΔR-matched muon with $p_{\mathrm{T}} > 10$ GeV, identified within its cone. The muon calorimetric deposits are then subtracted to ensure that no double counting occurs in the large-R jet mass computation. No attempt to correct for escaping neutrinos has been made in this analysis.

Figure B.1 shows the effect of the muon-in-jet correction on the mass distribution of leading and sub-leading Higgs jets in simulation. The peak of the mass distribution shifts by about 0.5 GeV for the leading and by about 1.5 GeV for the sub-leading jet, while the standard deviation is reduced by about 5% and 12% respectively. The reason why the correction is larger for the sub-leading jet is that the energy loss due to semi-leptonic decays can cause a jet to be demoted to second highest-p_{T} jet in the event. For this reason, sub-leading jets are more likely to contain semi-leptonic b-hadron decays and their mass resolution is worse than that of leading jets.

In the analysis, the muon-in-jet correction is only applied to the large-R jet mass in the signal regions and to the large-R jet p_{T} used in the differential cross-section determination.

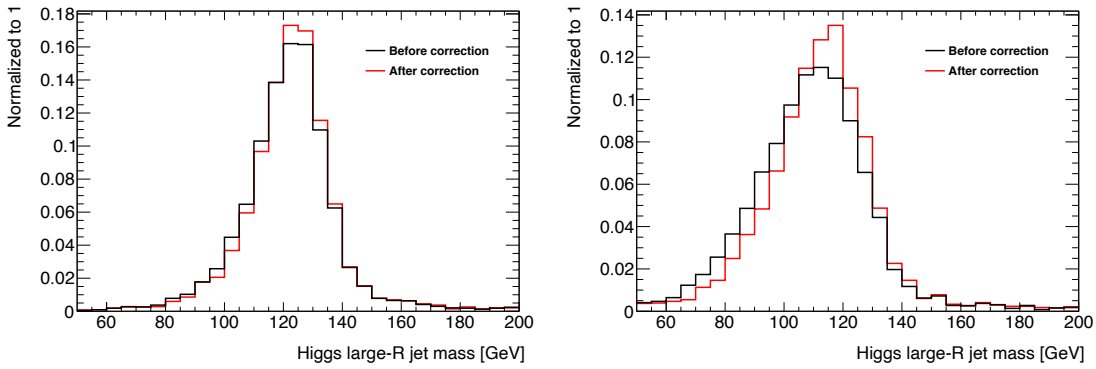

Figure B.1: Mass distribution of leading (left) and sub-leading (right) large-R jets truth-matched to a Higgs boson in simulation, before and after the muon-in-jet correction.

C

QCD Polynomial Order Optimisation

The optimal polynomial order of the QCD function in each analysis region is determined on the ensemble of hybrid VR slices by performing various statistical tests, which are briefly described in this appendix.

LLR Test A log-likelihood ratio (LLR) test is used to find the minimum number of parameters needed to describe the QCD background in the SR, either inclusively or in p_{T} bins. The LLR test statistic is defined as

$$t_N = -2 \ln \frac{L(x|N)}{L(x|N+1)}, \tag{C.1}$$

where x represents the data being fitted, $L(x|N)$ is the likelihood function for a QCD function of order N (null hypothesis), while $L(x|N+1)$ is the likelihood for a function of order $N+1$ (alternative hypothesis). By Wilk's theorem [129], this test statistic follows a χ^2 distribution with one degree of freedom when the null hypothesis accurately describes the data. In this case, p-values are uniformly distributed.

The LLR test is performed on the best available proxy of the QCD background in the SR, namely the ensemble of $\mathrm{VR}_{\mathrm{hyb}}$ slices with subtracted SR resonances. QCD functions of various polynomial orders are fit to every slice and the corresponding likelihood values are obtained. For any given N, the distribution of the LLR test statistic t_N and, correspondingly, the distribution of p-values can be obtained.

The cumulative distribution functions (CDF) of p-values for the inclusive VRL_{hyb} and VRS_{hyb} regions are shown in Figure C.1. Since uniformly distributed p-values would result in a linear cumulative distribution, the minimum polynomial order that describes the QCD in the SRL is found to be $N = 3$, while for SRS is $N = 4$. Similarly, the minimum polynomial order is determined in every other analysis region. It is important to note that this test determines the *minimum* polynomial order that accurately describes the data, meaning that, to the purpose of this test alone, the value of N must be greater than 3 (4) in the SRL (SRS).

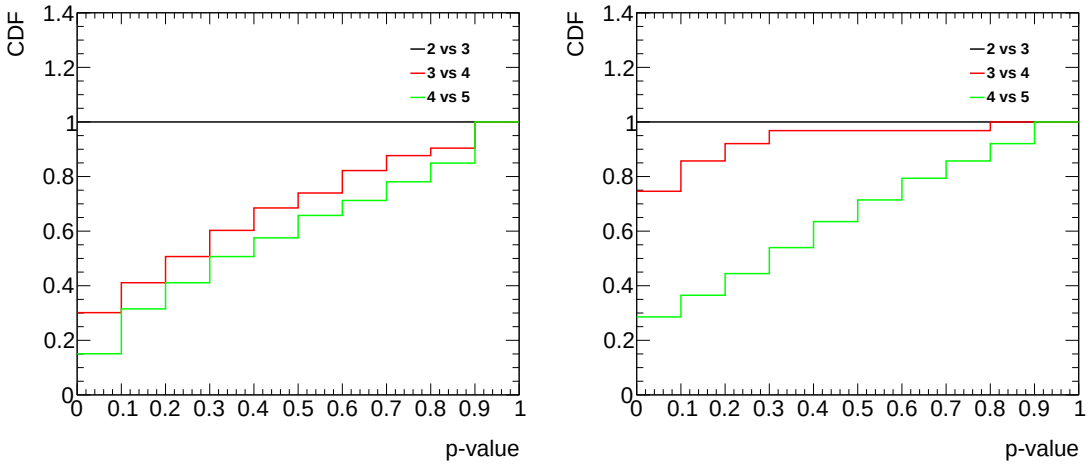

Figure C.1: Cumulative distribution functions (CDF) of p-values for the LLR test performed in the inclusive leading (left) and subleading (right) regions. The test compares a null hypothesis that assumes a QCD polynomial order $N = 2, 3, 4$ to an alternative hypothesis assuming $N + 1$. Of the tested polynomial orders, $N = 3$ and $N = 4$ show the best linearity in the leading and subleading regions, respectively.

Linearity Test While the LLR test ensures a good description of the data over the full mass range, the extraction of the Higgs and Z boson resonances is sensitive to local effects. The QCD model must have the right degree of flexibility for the fit to be able to reliably extract the mass resonances, independently of their actual yield in data.

For the Higgs boson signal, a linearity test compares the injected Higgs signal strength μ_H to its average fitted value across the hybrid VR slices. The signal injection is done by scaling the yield of the Higgs boson resonance in each VR_{hyb}

slice by 0, 1 and 2 times its expected value in the region. For each injection factor, a profile likelihood fit is performed in every $\mathrm{VR_{hyb}}$ slice, keeping μ_H, μ_Z and the QCD function parameters free to float, while $\mu_{t\bar{t}}$ is fixed to the value obtained from a standalone fit in the corresponding $\mathrm{CR}_{t\bar{t}}$ region. The linearity of the fit response to signal injection is studied as a function of the polynomial order N of the QCD function. In a similar fashion, linearity studies are also carried out for the in Z boson resonance.

Figure C.2 shows the fitted versus injected μ_H obtained from hybrid VRL data slices for $N = 0$, 1 and 2. The fitted values shown in the plot are the average of the fit results obtained across $\mathrm{VR_{hyb}}$ slices. Despite all tested polynomial orders showing relatively good linearity, $N = 5$ is chosen as it provides the best reconstruction of the injected Higgs yield. Similarly, the test is carried out both for the Higgs and Z boson resonances in all the inclusive and differential analysis regions.

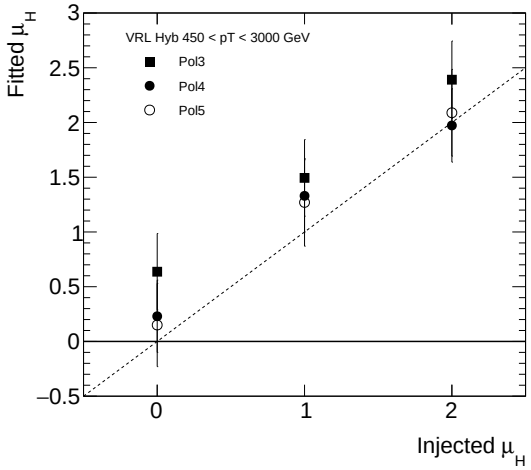

Figure C.2: Fitted versus injected values of μ_H for VRL hybrid data slices for $N = 0$, 1 and 2. The fitted values are the average of the fit results obtained across $\mathrm{VR_{hyb}}$ slices.

Spurious Signal Test A spurious signal test gauges the tendency of a model to fit a signal different than the one injected, or fit a signal where there is none. The sensitivity of the QCD model to these local effects can be assessed using two indicators.

The first indicator is $F_{2\sigma}$, the fraction of fits to $\mathrm{VR_{hyb}}$ slices with resonances injected at nominal rates ($\mu^{\mathrm{inj.}}_{H/Z} = 1$), returning a signal strength beyond twice its statistical error, i.e. $|\mu_{H/Z} - 1| > 2\sigma^{\mathrm{stat.}}_{\mu_{H/Z}}$. In each analysis region, the polynomial order optimised with the previous tests is incremented until $F_{2\sigma}$ is compatible with 0.05, both for the Higgs and Z boson resonances. Figure C.3a shows $F_{2\sigma}$ as a function of the polynomial order N, obtained from fits to inclusive $\mathrm{VR_{hyb}}$ slices built with $\mu^{\mathrm{inj.}}_{H} = 1$. Both in the leading and subleading regions, the choice of $N = 5$ provides a value of $F_{2\sigma}$ that is compatible with 0.05 within uncertainties, while lower polynomial orders do not satisfy the condition. The same result is obtained for the Z boson resonance.

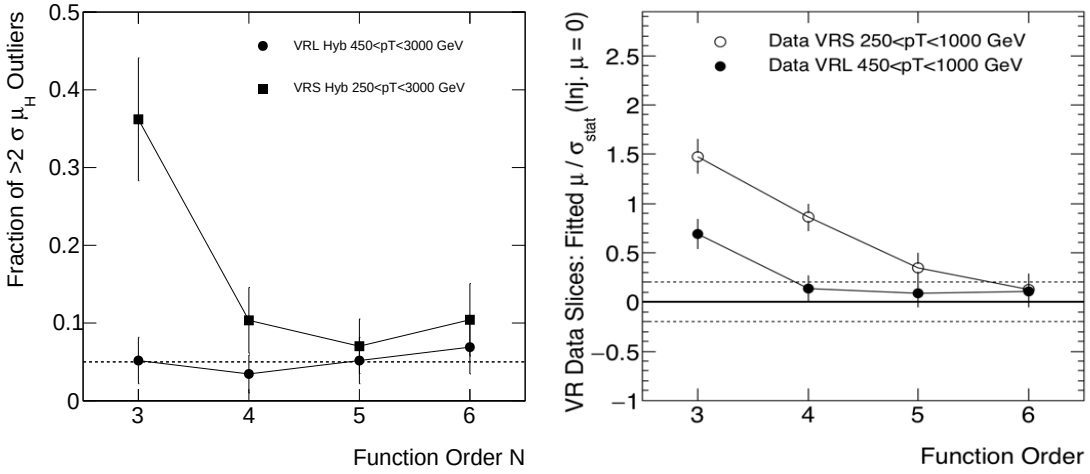

(a) **(b)**

Figure C.3: Spurious signal tests measuring the sensitivity of the QCD model to local effects in proximity of the Higgs and Z boson resonances, during the fit. Figure (a) shows the $F_{2\sigma}$ indicator as a function of the polynomial order N, obtained from fits to inclusive $\mathrm{VR_{hyb}}$ slices built with $\mu^{\mathrm{inj.}}_{H} = 1$. Figure (b) shows the $\langle \mu_H / \sigma^{\mathrm{stat.}}_{H} \rangle$ indicator as a function of the polynomial order N, obtained from fits to inclusive $\mathrm{VR_{hyb}}$ slices built with $\mu^{\mathrm{inj.}}_{H} = 0$. The polynomial order $N = 5$ is chosen as it makes both indicators compatible with the respective thresholds of 0.05 and 0.2, both in the leading and subleading regions.

The second indicator is $\langle \mu_H / \sigma^{\mathrm{stat.}}_{H} \rangle$, the average Higgs signal strength fitted on $\mathrm{VR_{hyb}}$ slices when no Higgs is injected ($\mu^{\mathrm{inj.}}_{H} = 0$), divided by its statistical error. This test measures the tendency of the model to misinterpret statistical fluctuations as signal. In line with recommendations from the ATLAS Collaboration, the polynomial order optimised with the previous tests is incremented until $\langle \mu_H / \sigma^{\mathrm{stat.}}_{H} \rangle < 0.2$ is

satisfied. Figure C.3b shows the average $\langle \mu_H / \sigma_H^{\text{stat.}} \rangle$ as a function of the polynomial order N, obtained from fits to inclusive VR_{hyb} slices built with $\mu_H^{\text{inj.}} = 0$. Both in the leading and subleading regions, results for $N = 5$ are compatible with 0.2 within uncertainties, while lower functional orders do not satisfy the condition.

D

Single Top tW Interference with $t\bar{t}$

The precise simulation of the single top tW process is particularly challenging, given that, at NLO, the Feynman diagrams representing this process interfere with LO $t\bar{t}$ diagrams. Single top tW diagrams at NLO, like those shown in Figure D.1 for the reaction $gg \to t\bar{t}^* \to t\bar{b}W^-$, are said to be *doubly-resonant*, meaning that the intermediate $\bar{t}^*$ propagator can be produced on-mass-shell. This is to distinguish them from the *singly-resonant* diagrams characterising the production of single top tW at LO (see Figure 7.12a). The impact of the doubly-resonant diagrams on the tW cross-section strongly increases when the top propagator starts becoming resonant. In the example, this happens when the invariant mass of the $\bar{b}W^-$ pair is comparable to the top quark mass. In principle, a complete NLO calculation of the

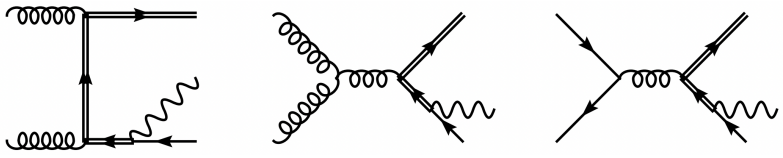

Figure D.1: Doubly-resonant Feynman diagrams for the single top tW process at NLO.

single top tW process must take into account both the singly- and doubly-resonant diagrams. The amplitude of the tW process at NLO can be expressed as

$$|\mathcal{A}_{tW}|^2 = |\mathcal{A}_{1t} + \mathcal{A}_{2t}|^2 = |\mathcal{A}_{1t}|^2 + 2\mathfrak{Re}(\mathcal{A}_{1t}\mathcal{A}_{2t}^*) + |\mathcal{A}_{2t}|^2, \tag{D.1}$$

where $\mathcal{A}_{1t}$ and $\mathcal{A}_{2t}$ are the amplitudes obtained exclusively from singly- and doubly-resonant diagrams, respectively.

The calculation of the interference term, however, is extremely difficult in the perturbative assumption. Therefore, two approximate methods are devised for computing the tW component of the single top process: the *diagram subtraction* (DS) and the *diagram removal* (DR) schemes. In the DR scheme, the doubly-resonant diagrams are removed from the calculation, together with the interference term, i.e. only $|\mathcal{A}_{1t}|^2$ is calculated. On the other hand, the DS scheme implements a subtraction term that cancels the doubly-resonant contribution $|\mathcal{A}_{2t}|^2$, while keeping the interference term. Further details on the implementation of the DR and DS schemes can be found in Reference [130]. It follows that the difference between the single top tW events simulated using the two different schemes is proportional to the interference term.

Since the kinematic regime spanned by the analysis presented in this thesis includes the top quark mass, the contribution of the interference term is expected to be sizable. The yield of the single top tW events simulated using the DS scheme and populating the signal regions is found to be 40-60% lower than that obtained using the DR scheme (see Figure 8.4).

E

Systematic Decorrelation Tests

This appendix provides details on the decorrelation tests carried out for the dominant systematic uncertainties characterising the analysis, i.e. JMR and JMS.

Jet Mass Resolution Decorrelation Studies

Following recommendations provided by the ATLAS Collaboration, the JMR uncertainty is decorrelated between the $t\bar{t}$, V+jets and Higgs processes. Additionally, the JMR is also decorrelated across the four differential p_{T} bins. This gives rise to a total of 3 JMR NPs in the inclusive measurement, and 12 NPs in the differential measurement. Within the fit, these numbers are doubled considering that the normalisation and shape components of any systematic are treated separately.

To motivate the decorrelation across p_{T} bins, some early tests were initially performed using differential Z fits to data. In these fits, the Higgs signal strength in every p_{T} bin was set to the SM expectation. They also did not include the external JMR constraints introduced in Section 8.4, nor a separate Z signal strength for $p_{\mathrm{T}} > 1$ TeV. In the early stages of the analysis, the differential fit was, in fact, performed in three bins, with the last one ($\mu_Z^{p_{\mathrm{T}}2}$) covering the $p_{\mathrm{T}} > 650$ GeV range.

An indication that the full correlation scheme might induce biases in the fit was observed in the variations of POI significance ($|\Delta\mu_Z|/\sigma$) obtained after decorrelating the V + jets JMR uncertainty in a differential Z data fit. A sizable effect was

observed on the Z signal strengths, with shifts as large as 0.55σ, 0.34σ, 1.58σ in $\mu_Z^{p_{\mathrm{T}}0}$, $\mu_Z^{p_{\mathrm{T}}1}$, and $\mu_Z^{p_{\mathrm{T}}2}$, respectively.

To gain a better understanding of the effect, the $V+\text{jets}$ JMR pulls were also studied, and they are shown in Figure E.1a. In the fully-correlated scheme, the $V+\text{jets}$ JMR uncertainty looks strongly constrained and pulled. On the other hand, decorrelating JMR across p_{T} bins shows that both the pull and the constraint are driven by the central momentum bin (b1: 450–650 GeV). In this bin, the fit is able to strongly constrain the $V+\text{jets}$ JMR uncertainty thanks to the higher number of events. The other bins, however, have a much smaller constraining power and show a quite different pull behaviour. Thus, in the fully-correlated scheme, the strong constraint of the $V+\text{jets}$ JMR uncertainty in the central bin is directly transferred to the other bins, where it is not valid. This induces biases, which are attested by the larger significance shifts observed in these regions. The results of these early studies motivated the decorrelation of the $V+\text{jets}$ JMR uncertainty across p_{T} bins. As the Higgs boson and $V+\text{jets}$ processes have similar topologies, it is also decided to decorrelate the Higgs boson JMR uncertainty across p_{T} bins.

During the same tests discussed above, the $t\bar{t}$ signal strengths were determined via a simultaneous fit to the $\mathrm{CR}_{t\bar{t}}$ p_{T} bins, as it is standard in the analysis. Due to the high purity, the $t\bar{t}$ measurements performed in the $\mathrm{CR}_{t\bar{t}}$ have the power to strongly constrain the $t\bar{t}$ JMR uncertainty, meaning that the validity of the full correlation scheme across p_{T} bins needs to be checked. Differently from $V+\text{jets}$, no significant variation in significance is observed for $\mu_{t\bar{t}}^{p_{\mathrm{T}},i}$ $(i=0,1,2)$. However, the JMR pulls in Figure E.1b show significant variations across p_{T} bins, motivating the decision to also decorrelate the $t\bar{t}$ JMR across p_{T} bins.

The studies presented above were repeated after the finalisation of the analysis strategy, leading to the same conclusions.

Jet Mass Scale Decorrelation Studies

The various components of the JMS systematic represent some of the most impactful uncertainties in the analysis. Following ATLAS recommendations, the JMS

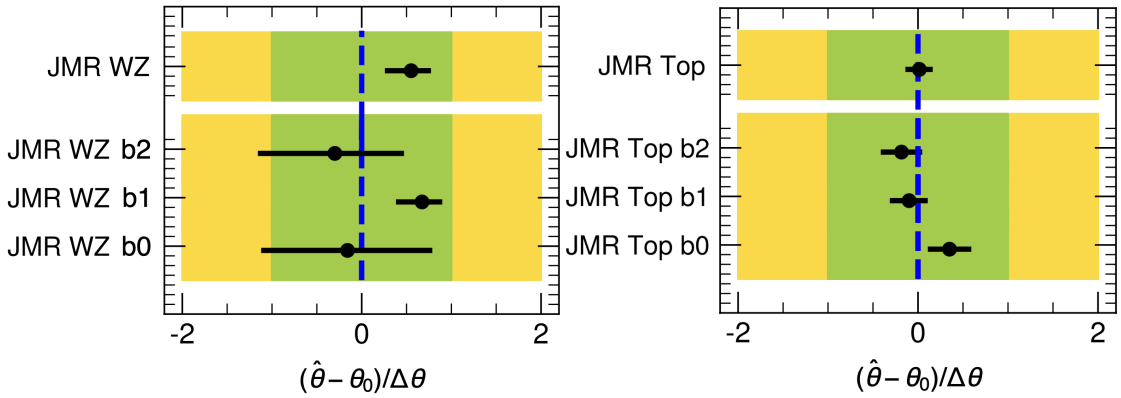

(a) $V+$jets JMR pulls **(b)** $t\bar{t}$ JMR pulls

Figure E.1: Jet mass resolution (JMR) uncertainty pulls and widths for the $V+$jets (a) and $t\bar{t}$ (b) processes, in an early analysis stage. In both figures, the first pull from the top is obtained before decorrelating JMR, while the others are the pulls obtained after decorrelating JMR across the preliminary p_{T} regions b0 ($250 < p_{\mathrm{T}} < 450$ GeV), b1 ($450 < p_{\mathrm{T}} < 650$ GeV) and b2 ($p_{\mathrm{T}} > 450$ GeV).

components are decorrelated into two NPs each: one describing $t\bar{t}$, and the other collectively describing Higgs and $V+$jets. This is to avoid transferring constraints across processes with different topologies.

In the differential measurements, some p_{T} bins might provide strong constraints to the components of such an impactful systematic. Similarly to JMR, decorrelation studies are performed on differential Z fits in data. It is important to note that all decorrelation studies presented in this section are performed after the introduction of the external constraints on $V+$jets JMR presented in Section 8.4. The variations in μ_Z significance are studied both by decorrelating the JMS components one by one and in various groups. In some groups, uncertainties other than the JMS components are added for testing. The results of these studies are summarised in Table E.1. Results on $\mu_Z^{p_{\mathrm{T}}0}$ are not shown since this signal strength is not one of the analysis deliverables, and it is instead fixed to the SM expectation in the differential fits (see Section 6.4.1).

When decorrelating JMS Modelling alone, the studies show shifts of 0.22σ, 0.28σ and 0.42σ in $\mu_Z^{p_{\mathrm{T}}1,2,3}$, respectively. Such variations are small, but non negligible, hinting to the presence of small biases induced by the full correlation of this dominant JMS component. It is also noted that decorrelating more JMS components does not

significantly increase the observed shifts. For this reason, it is decided to decorrelate JMS Modelling across p_{T} bins, but to leave the other components fully correlated. Additionally, it is decided to decorrelate the Higgs JMS Modelling uncertainty away from $V+$jets, as the two processes are produced using different generators (Powheg-Box v2 and Sherpa 2.2.8, respectively) and transferring constraints from the precisely measured Z peak to the Higgs boson might not be valid.

Table E.1: Relative variations of Z signal strength in a differential Z measurement, induced by the decorrelation across p_{T} bins of the uncertainties listed in the first column. The variations are expressed as $\Delta(i) = |\Delta\mu_Z^{p_{\mathrm{T}}i}|/\sigma_Z^{p_{\mathrm{T}}i}$, where $\sigma_Z^{p_{\mathrm{T}}i}$ is the total uncertainty on the $\mu_Z^{p_{\mathrm{T}}i}$ signal strength, as measured using the default correlation scheme.

Decorrelated NP	$\Delta(1)$	$\Delta(2)$	$\Delta(3)$
JMS Modelling	0.22	0.28	0.42
JMS Modelling, JMS Baseline	0.18	0.26	0.42
JMS Modelling, JMS Baseline, JES Topology	0.14	0.26	0.40
JMS Modelling, $\mu_{R,F}$	0.25	0.30	0.40
JMS All	0.22	0.23	0.40
JMS All, $t\bar{t}$ ME/PS, $\mu_{R,F}$	0.24	0.22	0.40

F

Results - Support Material

This appendix provides support material to Chapter 9.

F.1 Higgs Boson Acceptance and Efficiency

Table F.1: Higgs boson signal acceptance times efficiency ($A \times \epsilon$) within the fiducial volumes of the analysis. Values are shown both inclusively ("All") and for each Higgs production mode. Along with the p_{T}^{H} ranges shown, $|y_H| < 2$ is required.

Process	p_{T}^{H} Range [GeV]				
	> 450	300–450	450–650	650–1000	> 1000
All	0.24	1.3×10^{-2}	0.23	0.31	0.23
ggF	0.26	0.7×10^{-2}	0.25	0.35	0.28
VBF	0.22	0.4×10^{-2}	0.21	0.32	0.25
VH	0.27	1.7×10^{-2}	0.26	0.30	0.20
$t\bar{t}$H	0.20	4.7×10^{-2}	0.19	0.24	0.19

F.2 Yield Tables

This section provides information about the post-fit yields of the processes characterising the Higgs boson measurements performed by the analysis. Post-fit yields for

the inclusive, fiducial and differential Higgs boson measurements are summarised, respectively, in Tables F.2, F.3 and F.4.

Table F.2: Event yields and associated uncertainties after the global likelihood fit in the inclusive region. The total background yield can differ from the sum of the individual components due to rounding.

Process	SRL	SRS	$CR_{t\bar{t}}$
Multijet	$590\,700 \pm 4200$	$529\,300 \pm 3500$	–
Z + jets	$16\,100 \pm 2800$	$12\,000 \pm 2100$	–
W + jets	3050 ± 720	2510 ± 500	–
Top	$16\,300 \pm 1900$	$15\,900 \pm 2000$	3737 ± 68
$W(\ell\nu)$ + jets	–	–	53 ± 16
H	400 ± 1500	300 ± 1300	–
Total	$626\,530 \pm 820$	$560\,090 \pm 770$	3790 ± 66
Data	626 532	560 083	3791

Table F.3: Event yields and associated uncertainties after the global likelihood fit in the $p_{\mathrm{T}}^{H} > 450$ GeV fiducial region. The total background yield can differ from the sum of the individual components due to rounding.

Process	SRL	SRS	$CR_{t\bar{t}}$
Multijet	$591\,000 \pm 4100$	$370\,800 \pm 2400$	–
Z + jets	$16\,400 \pm 2800$	9300 ± 1500	–
W + jets	3080 ± 720	1690 ± 340	–
Top	$16\,100 \pm 1700$	8800 ± 1100	2062 ± 50
$W(\ell\nu)$ + jets	–	–	41 ± 12
H $p_{\mathrm{T}}^{H} < 450$ GeV	98.0 ± 8.4	41.6 ± 2.7	–
H $p_{\mathrm{T}}^{H} > 450$ GeV	0 ± 1300	-20 ± 700	–
Total	$626\,530 \pm 810$	$390\,660 \pm 640$	2103 ± 48
Data	626 532	390 665	2104

Table F.4: Event yields and associated uncertainties after the global likelihood fit of the differential regions. The total background yield can differ from the sum of the individual components due to rounding.

	SRL					
Jet p_{T} [GeV]	450–650		650–1000		$>$ 1000	
Multijet	509 400	± 3700	72 300	± 1100	5580	± 360
Z + jets	13 100	± 2200	2600	± 780	390	± 270
W + jets	2300	± 520	630	± 160	98	± 30
Top	13 300	± 1200	2380	± 280	155	± 47
H p_{T0}^{H}	38	± 8	5	± 1	0.3	± 0.1
H p_{T1}^{H}	−290	± 890	−15	± 46	−1	± 3
H p_{T2}^{H}	−900	± 1500	−28	± 47	−0.5	± 0.8
H p_{T3}^{H}	58	± 71	250	± 310	3	± 4
H p_{T4}^{H}	–		14	± 24	60	± 100
Total	537 040	± 750	78 180	± 280	6283	± 79
Data	537 038		78 177		6283	

	SRS					
Jet p_{T} [GeV]	250–450		450–650		650–1000	
Multijet	157 400	± 2900	340 600	± 2100	48 020	± 720
Z + jets	4000	± 2500	8000	± 1300	1630	± 530
W + jets	800	± 160	1370	± 250	364	± 83
Top	7800	± 1000	7370	± 760	1150	± 160
H $p_{\mathrm{T}}^{H}0$	41	± 8	20	± 4	2.0	± 0.4
H $p_{\mathrm{T}}^{H}1$	−400	± 1300	−110	± 330	−5	± 16
H $p_{\mathrm{T}}^{H}2$	−130	± 210	−450	± 750	−8	± 14
H $p_{\mathrm{T}}^{H}3$	–		90	± 110	140	± 170
H $p_{\mathrm{T}}^{H}4$	–		–		25	± 43
Total	169 420	± 420	356 910	± 600	51 320	± 230
Data	169 418		356 910		51 324	

	$\mathrm{CR}_{t\bar{t}}$							
Jet p_{T} [GeV]	250–450		450–650		650–1000		$>$ 1000	
Top	1676	± 43	1605	± 41	426	± 21	27.7	± 6.0
$W(\ell\nu)$ + jets	12.3	± 3.5	22.9	± 6.5	14	± 4	5.9	± 1.7
Total	1688	± 43	1628	± 41	440	± 21	33.6	± 5.8
Data	1687		1628		442		34	

F.3 Differential V + jets Result

Before unblinding the Higgs region, the differential fit setup is tested on the V + jets process in the WCR$_{t\bar{t}}$ and VRL regions. Figure F.1 shows the post-fit candidate jet mass distribution in the VRL1 ($450 < p_{\mathrm{T}} < 650$ GeV), VRL2 ($650 < p_{\mathrm{T}} < 1000$ GeV) and VRL3 ($p_{\mathrm{T}} > 1$ TeV), after subtracting the QCD multijet background. The V + jets contribution is split into five generator "truth" p_{T}^{V} volumes labelled p_{T}^{0}-p_{T}^{4} for $p_{\mathrm{T}}^{V} < 300$ GeV, 300–450 GeV, 450–650 GeV, 650–1000 GeV, and > 1 TeV, respectively. Good agreement between the data and the model is observed in all regions.

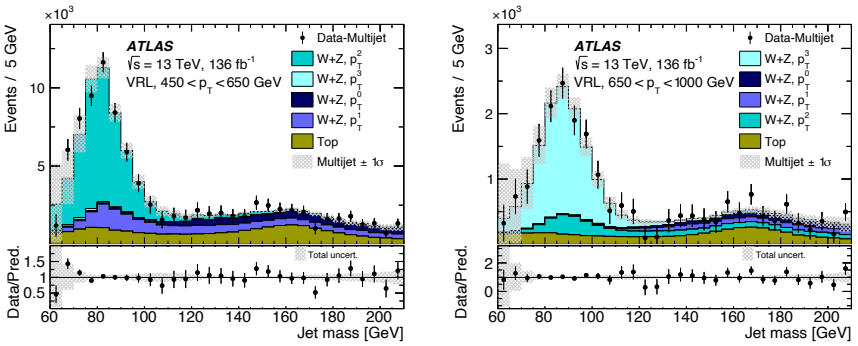

(a) VRL1 **(b)** VRL2

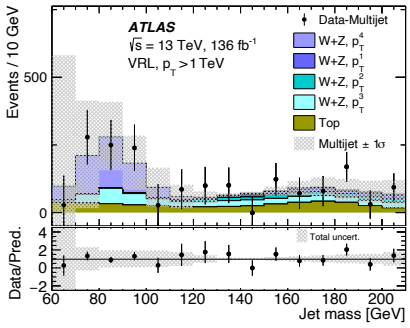

(c) VRL3

Figure F.1: Post-fit leading jet mass distributions after the multijet background is subtracted in the validation region for data (points with error bars) and the V + jets (W + Z) and Top components (histograms) for (a) VRL1, (b) VRL2, and (c) VRL3 (shown in wider 10 GeV jet mass bins). The $t\bar{t}$ normalization and its uncertainty are set to the corresponding values from the CR$_{t\bar{t}}$. The mass range has been extended down to 60 GeV for only this fit to show the level of agreement along the rising edge of the V + jets mass distribution. The ratio of the data to the background prediction is shown in the lower panel. The shaded areas indicate the 68% CL for all background processes [1].

F.4 Impact Rankings

This section provides impact ranking plots for all analysis measurements. For a specific parameter of interest μ, a ranking plot shows the 10 highest-impact fit parameters in the determination μ. The pre-fit and post-fit impact on μ is described by the top axis. It is found by fixing each fit parameter (θ) to $\pm 1\sigma$, extracting the resulting μ value and comparing it to the best-fit value, $\hat{\mu}$, such that $\Delta\mu = \mu - \hat{\mu}$ (see Equation 8.5). Blue (green) colour indicates (anti-)correlation between θ and μ. Also shown are pulls and widths of the nuisance parameters, described by the bottom axis (see Equation 8.4).

All plots presented in this section rank the fit parameters according to their impact on the determination of the Higgs boson signal strength. For the differential measurement, one plot for each of the four Higgs boson signal strengths is shown. Since ranking plots are mainly used in this thesis to quantify the relative importance of systematic uncertainties, the QCD function parameters are excluded from the ranking. It is important to remember, however, that the QCD parameters correlate greatly with the Higgs boson signal strength, and they usually have the highest impacts.

Figure F.2 shows the ranking and pull plot of the 10 parameters (excluding those on the QCD function) with the highest impact on the determination of μ_H in the inclusive fit (Figure F.2a), μ_H in the fiducial fit (Figure F.2b), and the most systematically limited Higgs boson signal strengths μ_H^2 and μ_H^3 in the differential fit (Figures F.2c and F.2d). The parameter with the highest impact on the determination of the Higgs boson signal strength in every region is μ_Z in the corresponding p_{T} range. The figures further confirm that the JMR, JMS Modelling and $t\bar{t}$ modelling systematics are the nuisance parameters with the largest impact on the Higgs boson measurements performed by the analysis.

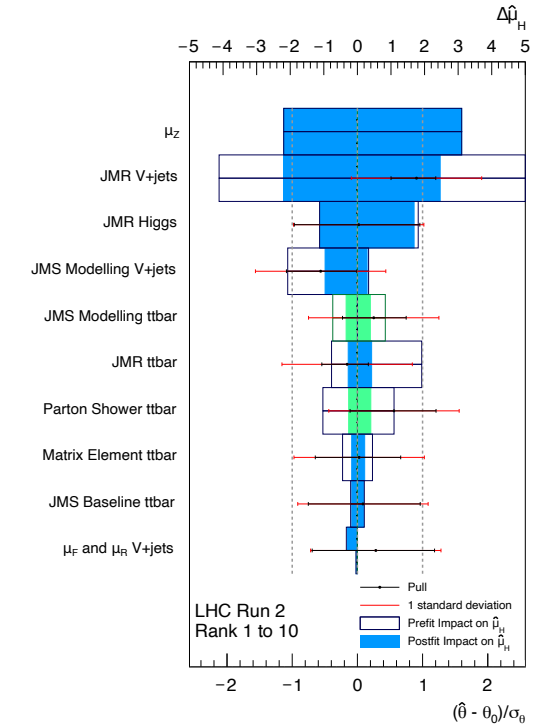

(a) Inclusive μ_H

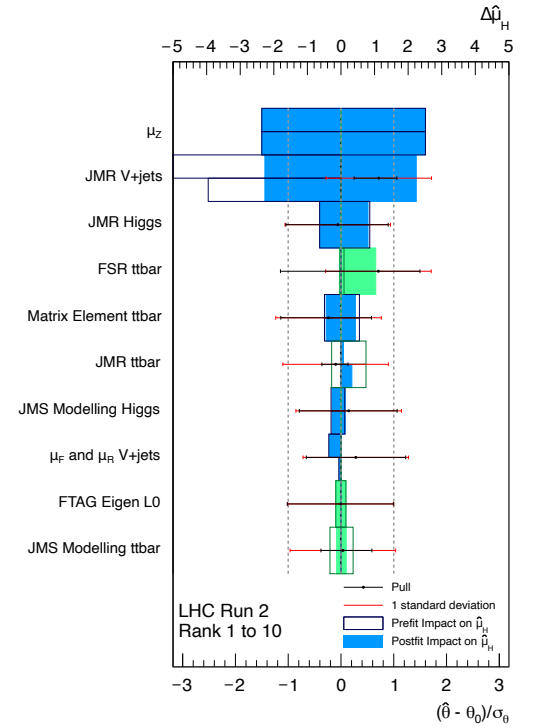

(b) Fiducial μ_H

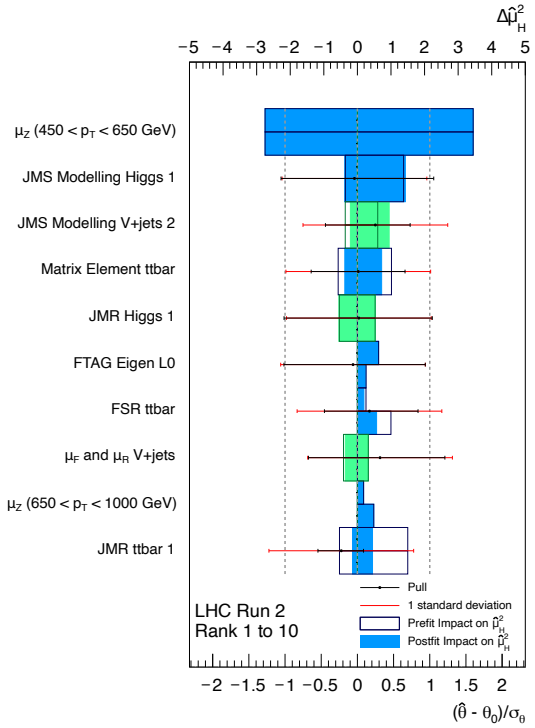

(c) Differential μ^2_H

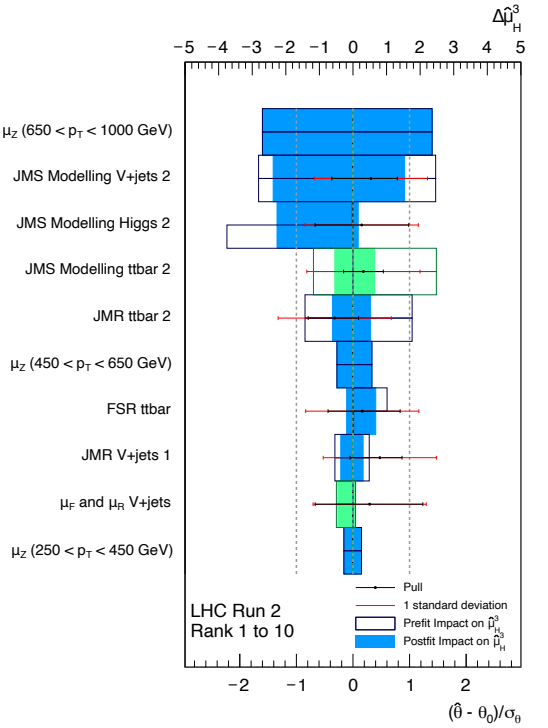

(d) Differential μ^3_H

Figure F.2: Ranking and pull plot of the 10 highest-impact parameters on (a) μ_H in the inclusive fit, (b) μ_H in the fiducial fit, and (c) μ^2_H and (d) μ^3_H in the differential fit.

References

[1] ATLAS Collaboration. "Constraints on Higgs boson production with large transverse momentum using $H \to b\bar{b}$ decays in the ATLAS detector". In: *Physical Review D* 105.9 (May 2022). URL: https://doi.org/10.1103%2Fphysrevd.105.092003.

[2] Migle Stankaityte. *Probing high energy Higgs bosons using $H \to b\bar{b}$ decays in $\sqrt{s} = 13$ TeV proton-proton collisions at the ATLAS experiment*. Presented 03 Dec 2021. URL: http://cds.cern.ch/record/2800522.

[3] ATLAS Collaboration. "Observation of a new particle in the search for the Standard Model Higgs boson with the ATLAS detector at the LHC". In: *Phys. Lett. B* 716 (2012), p. 1. arXiv: 1207.7214 [hep-ex].

[4] CMS Collaboration. "Observation of a new boson at a mass of 125 GeV with the CMS experiment at the LHC". In: *Phys. Lett. B* 716 (2012), p. 30. arXiv: 1207.7235 [hep-ex].

[5] ATLAS Collaboration. "Combined measurements of Higgs boson production and decay using up to 80 fb^{-1} of proton–proton collision data at $\sqrt{s} = 13$ TeV collected with the ATLAS experiment". In: *Phys. Rev. D* 101 (2020), p. 012002. arXiv: 1909.02845 [hep-ex].

[6] CMS Collaboration. "Combined measurements of Higgs boson couplings in proton–proton collisions at $\sqrt{s} = 13$ TeV". In: *Eur. Phys. J. C* 79 (2019), p. 421. arXiv: 1809.10733 [hep-ex].

[7] Matthias Schlaffer et al. "Boosted Higgs shapes". In: *The European Physical Journal C* 74.10 (Oct. 2014). URL: https://doi.org/10.1140%2Fepjc%2Fs10052-014-3120-z.

[8] Massimiliano Grazzini et al. "Modeling BSM effects on the Higgs transverse-momentum spectrum in an EFT approach". In: *Journal of High Energy Physics* 2017.3 (Mar. 2017). URL: https://doi.org/10.1007%2Fjhep03%282017%29115.

[9] ATLAS Collaboration. "Measurement of the Higgs boson mass in the $H \to ZZ^* \to 4\ell$ and $H \to \gamma\gamma$ channels with $\sqrt{s} = 13$ TeV pp collisions using the ATLAS detector". In: *Phys. Lett. B* 784 (2018), p. 345. arXiv: 1806.00242 [hep-ex].

[10] ATLAS Collaboration. "Combined measurement of differential and total cross sections in the $H \to \gamma\gamma$ and the $H \to ZZ^* \to 4\ell$ decay channels at $\sqrt{s} = 13$ TeV with the ATLAS detector". In: *Phys. Lett. B* 786 (2018), p. 114. arXiv: 1805.10197 [hep-ex].

[11] ATLAS Collaboration. "Observation of $H \to b\bar{b}$ decays and VH production with the ATLAS detector". In: *Phys. Lett. B* 786 (2018), p. 59. arXiv: 1808.08238 [hep-ex].

[12] CMS Collaboration. "Observation of Higgs Boson Decay to Bottom Quarks". In: *Phys. Rev. Lett.* 121 (2018), p. 121801. arXiv: 1808.08242 [hep-ex].

[13] ATLAS Collaboration. "Measurements of WH and ZH production in the $H \to b\bar{b}$ decay channel in pp collisions at 13 TeV with the ATLAS detector". In: *Eur. Phys. J. C* 81 (2021), p. 178. arXiv: 2007.02873 [hep-ex].

[14] ATLAS Collaboration. "Measurement of the associated production of a Higgs boson decaying into b-quarks with a vector boson at high transverse momentum in pp collisions at $\sqrt{s} = 13$ TeV with the ATLAS detector". In: *Phys. Lett. B* 816 (2021), p. 136204. arXiv: 2008.02508 [hep-ex].

[15] CMS Collaboration. "Inclusive search for highly boosted Higgs bosons decaying to bottom quark-antiquark pairs in proton–proton collisions at $\sqrt{s} = 13$ TeV". In: *JHEP* 12 (2020), p. 085. arXiv: 2006.13251 [hep-ex].

[16] ATLAS Collaboration. *Search for boosted resonances decaying to two b-quarks and produced in association with a jet at $\sqrt{s} = 13$ TeV with the ATLAS detector*. ATLAS-CONF-2018-052. 2018. URL: https://cds.cern.ch/record/2649081.

[17] C. Burgard. *TikZ Example: Standard Model of Physics*. 2016. URL: https://texample.net/tikz/examples/model-physics.

[18] Luigi Di Lella and Carlo Rubbia. "The Discovery of the W and Z Particles". In: *Adv. Ser. Direct. High Energy Phys.* 23 (2015), pp. 137–163.

[19] F. Englert and R. Brout. "Broken Symmetry and the Mass of Gauge Vector Mesons". In: *Phys. Rev. Lett.* 13 (9 Aug. 1964), pp. 321–323. URL: https://link.aps.org/doi/10.1103/PhysRevLett.13.321.

[20] Peter W. Higgs. "Broken Symmetries and the Masses of Gauge Bosons". In: *Phys. Rev. Lett.* 13 (16 Oct. 1964), pp. 508–509. URL: https://link.aps.org/doi/10.1103/PhysRevLett.13.508.

[21] John Ellis, Mary K. Gaillard, and Dimitri V. Nanopoulos. "A Historical Profile of the Higgs Boson. An Updated Historical Profile of the Higgs Boson". In: (2016). 22 pages, 5 figures, update of arXiv:1201.6045, to be published in the volume "The Standard Theory of Particle Physics", edited by Luciano Maiani and Gigi Rolandi, pp.255-274, 255–274. 20 p. arXiv: 1504.07217. URL: https://cds.cern.ch/record/2012465.

[22] R.L. Workman et al. (Particle Data Group). "Review of Particle Physics". In: *Progress of Theoretical and Experimental Physics* 2022.8 (Aug. 2022). 083C01. URL: https://doi.org/10.1093/ptep/ptac097.

[23] ATLAS Collaboration. *A combination of measurements of Higgs boson production and decay using up to 139 fb^{-1} of proton–proton collision data at $\sqrt{s} = 13$ TeV collected with the ATLAS experiment*. ATLAS-CONF-2020-027. 2020. URL: https://cds.cern.ch/record/2725733.

[24] K. Becker et al. *Precise predictions for boosted Higgs production*. 2020. URL: https://arxiv.org/abs/2005.07762.

[25] ATLAS Collaboration. "The ATLAS Experiment at the CERN Large Hadron Collider". In: *JINST* 3 (2008), S08003.

[26] "LHC Machine". In: *JINST* 3 (2008). Ed. by Lyndon Evans and Philip Bryant, S08001.

[27] Oliver Sim Brüning et al. *LHC Design Report*. CERN Yellow Reports: Monographs. Geneva: CERN, 2004. URL: https://cds.cern.ch/record/782076.

[28] Esma Mobs. "The CERN accelerator complex in 2019". In: (2019). General Photo. URL: https://cds.cern.ch/record/2684277.

[29] ATLAS Collaboration. *Luminosity determination in pp collisions at $\sqrt{s} = 13$ TeV using the ATLAS detector at the LHC*. ATLAS-CONF-2019-021. 2019. URL: https://cds.cern.ch/record/2677054.

[30] ATLAS Collaboration. "ATLAS data quality operations and performance for 2015–2018 data-taking". In: *JINST* 15 (2020), P04003. arXiv: 1911.04632 [physics.ins-det].

[31] ATLAS Collaboration. *ATLAS Insertable B-Layer Technical Design Report*. ATLAS-TDR-19; CERN-LHCC-2010-013. 2010. URL: https://cds.cern.ch/record/1291633. Addendum: ATLAS-TDR-19-ADD-1; CERN-LHCC-2012-009. 2012. URL: https://cds.cern.ch/record/1451888.

[32] ATLAS Collaboration. *Track Reconstruction Performance of the ATLAS Inner Detector at $\sqrt{s} = 13$ TeV*. ATL-PHYS-PUB-2015-018. 2015. URL: https://cds.cern.ch/record/2037683.

[33] Particle Data Group. *Atomic and Nuclear Properties of Materials*. Last Revised: Oct. 2021. URL: https://pdg.lbl.gov/2021/AtomicNuclearProperties (visited on 09/15/2022).

[34] Christian W. Fabjan and Fabiola Gianotti. "Calorimetry for particle physics". In: *Rev. Mod. Phys.* 75 (4 Oct. 2003), pp. 1243–1286. URL: https://link.aps.org/doi/10.1103/RevModPhys.75.1243.

[35] Francesca Cavallari. "Performance of calorimeters at the LHC". In: *J. Phys. Conf. Ser.* 293 (2011). Ed. by Yifang Wang, p. 012001.

[36] ATLAS Collaboration. "Operation of the ATLAS trigger system in Run 2". In: *JINST* 15 (2020), P10004. arXiv: 2007.12539 [hep-ex].

[37] Yasuyuki Okumura. "Triggering in ATLAS in Run 2 and Run 3". In: *PoS* EPS-HEP2021 (2022), p. 788.

[38] E. Perez. "Determination of Parton Distribution Functions, Impact of HERA Data and Consequences for the LHC". In: *Acta Physica Polonica B* 39.9 (Sept. 2008), p. 2095.

[39] T Sjöstrand. "Monte Carlo Generators". In: (2007), 23 p. URL: http://cds.cern.ch/record/999717.

[40] Peter Skands. "Introduction to QCD". In: *Theoretical Advanced Study Institute in Elementary Particle Physics: Searching for New Physics at Small and Large Scales*. 2013, pp. 341–420. arXiv: 1207.2389 [hep-ph].

[41] Matteo Cacciari, Gavin P Salam, and Gregory Soyez. "The anti-k_t jet clustering algorithm". In: *Journal of High Energy Physics* 2008.04 (Apr. 2008), pp. 063–063. URL: https://doi.org/10.1088%2F1126-6708%2F2008%2F04%2F063.

[42] Jonathan M. Butterworth et al. "Jet Substructure as a New Higgs-Search Channel at the Large Hadron Collider". In: *Physical Review Letters* 100.24 (June 2008). URL: https://doi.org/10.1103%2Fphysrevlett.100.242001.

[43] A. Altheimer et al. "Boosted objects and jet substructure at the LHC. Report of BOOST2012, held at IFIC Valencia, 23rd–27th of July 2012". In: *The European Physical Journal C* 74.3 (Mar. 2014). URL: https://doi.org/10.1140%2Fepjc%2Fs10052-014-2792-8.

[44] ATLAS Collaboration. "Topological cell clustering in the ATLAS calorimeters and its performance in LHC Run 1". In: *Eur. Phys. J. C* 77 (2017), p. 490. arXiv: 1603.02934 [hep-ex].

[45] David Krohn, Jesse Thaler, and Lian-Tao Wang. "Jet trimming". In: *Journal of High Energy Physics* 2010.2 (Feb. 2010). URL: https://doi.org/10.1007%2Fjhep02%282010%29084.

[46] Stephen D. Ellis and Davison E. Soper. "Successive combination jet algorithm for hadron collisions". In: *Physical Review D* 48.7 (Oct. 1993), pp. 3160–3166. URL: https://doi.org/10.1103%2Fphysrevd.48.3160.

[47] ATLAS Collaboration. "Identification of boosted, hadronically decaying W bosons and comparisons with ATLAS data taken at $\sqrt{s} = 8\,\text{TeV}$". In: *Eur. Phys. J. C* 76 (2016), p. 154. arXiv: 1510.05821 [hep-ex].

[48] ATLAS Collaboration. *Jet mass reconstruction with the ATLAS Detector in early Run 2 data*. ATLAS-CONF-2016-035. 2016. URL: https://cds.cern.ch/record/2200211.

[49] ATLAS Collaboration. "Jet energy scale measurements and their systematic uncertainties in proton–proton collisions at $\sqrt{s} = 13\,\text{TeV}$ with the ATLAS detector". In: *Phys. Rev. D* 96 (2017), p. 072002. arXiv: 1703.09665 [hep-ex].

[50] ATLAS Collaboration. "In situ calibration of large-radius jet energy and mass in 13 TeV proton–proton collisions with the ATLAS detector". In: *Eur. Phys. J. C* 79 (2019), p. 135. arXiv: 1807.09477 [hep-ex].

[51] ATLAS Collaboration. *Monte Carlo Calibration and Combination of In-situ Measurements of Jet Energy Scale, Jet Energy Resolution and Jet Mass in ATLAS*. ATLAS-CONF-2015-037. 2015. URL: https://cds.cern.ch/record/2044941.

[52] ATLAS Collaboration. "Jet mass and substructure of inclusive jets in $\sqrt{s} = 7\,\text{TeV}$ pp collisions with the ATLAS experiment". In: *JHEP* 05 (2012), p. 128. arXiv: 1203.4606 [hep-ex].

[53] David Krohn, Jesse Thaler, and Lian-Tao Wang. "Jets with variable R". In: *Journal of High Energy Physics* 2009.06 (June 2009), pp. 059–059. URL: https://doi.org/10.1088%2F1126-6708%2F2009%2F06%2F059.

[54] ATLAS Collaboration. *Variable Radius, Exclusive-k_T, and Center-of-Mass Subjet Reconstruction for Higgs($\to b\bar{b}$) Tagging in ATLAS*. ATL-PHYS-PUB-2017-010. 2017. URL: https://cds.cern.ch/record/2268678.

[55] Matteo Cacciari, Gavin P Salam, and Gregory Soyez. "The catchment area of jets". In: *Journal of High Energy Physics* 2008.04 (Apr. 2008), pp. 005–005. URL: https://doi.org/10.1088%2F1126-6708%2F2008%2F04%2F005.

[56] Matteo Cacciari and Gavin P. Salam. "Pileup subtraction using jet areas". In: *Physics Letters B* 659.1-2 (Jan. 2008), pp. 119–126. URL: https://doi.org/10.1016%2Fj.physletb.2007.09.077.

[57] ATLAS Collaboration. "Performance of jet substructure techniques for large-R jets in proton–proton collisions at $\sqrt{s} = 7\,\text{TeV}$ using the ATLAS detector". In: *JHEP* 09 (2013), p. 076. arXiv: 1306.4945 [hep-ex].

[58] ATLAS Collaboration. *Optimisation and performance studies of the ATLAS b-tagging algorithms for the 2017-18 LHC run*. ATL-PHYS-PUB-2017-013. 2017. URL: https://cds.cern.ch/record/2273281.

[59] ATLAS Collaboration. *Secondary vertex finding for jet flavour identification with the ATLAS detector*. ATL-PHYS-PUB-2017-011. 2017. URL: https://cds.cern.ch/record/2270366.

[60] ATLAS Collaboration. *Topological b-hadron decay reconstruction and identification of b-jets with the JetFitter package in the ATLAS experiment at the LHC*. ATL-PHYS-PUB-2018-025. 2018. URL: https://cds.cern.ch/record/2645405.

[61] ATLAS Collaboration. *Expected performance of the ATLAS b-tagging algorithms in Run-2*. ATL-PHYS-PUB-2015-022. 2015. URL: https://cds.cern.ch/record/2037697.

[62] ATLAS Collaboration. *Optimisation of the ATLAS b-tagging performance for the 2016 LHC Run*. ATL-PHYS-PUB-2016-012. 2016. URL: https://cds.cern.ch/record/2160731.

[63] A. Hoecker et al. *TMVA - Toolkit for Multivariate Data Analysis*. 2007. URL: https://arxiv.org/abs/physics/0703039.

[64] ATLAS Collaboration. "ATLAS b-jet identification performance and efficiency measurement with $t\bar{t}$ events in pp collisions at $\sqrt{s} = 13\,\text{TeV}$". In: *Eur. Phys. J. C* 79 (2019), p. 970. arXiv: 1907.05120 [hep-ex].

[65] ATLAS Collaboration. *Measurement of b-tagging efficiency of c-jets in $t\bar{t}$ events using a likelihood approach with the ATLAS detector*. ATLAS-CONF-2018-001. 2018. URL: https://cds.cern.ch/record/2306649.

[66] ATLAS Collaboration. *Calibration of light-flavour b-jet mistagging rates using ATLAS proton–proton collision data at $\sqrt{s} = 13$ TeV*. ATLAS-CONF-2018-006. 2018. URL: https://cds.cern.ch/record/2314418.

[67] ATLAS Collaboration. *ATLAS Flavor-Tagging Calibration Results with 80.5 fb^{-1}*. 2019. URL: https://atlas.web.cern.ch/Atlas/GROUPS/PHYSICS/PLOTS/FTAG-2019-003/.

[68] François Chollet et al. *Keras*. https://keras.io. 2015.

[69] ATLAS Collaboration. *Identification of Jets Containing b-Hadrons with Recurrent Neural Networks at the ATLAS Experiment*. ATL-PHYS-PUB-2017-003. 2017. URL: https://cds.cern.ch/record/2255226.

[70] ATLAS Collaboration. *Performance of 2019 recommendations of ATLAS Flavor Tagging algorithms with Variable Radius track jets*. 2019. URL: http://atlas.web.cern.ch/Atlas/GROUPS/PHYSICS/PLOTS/FTAG-2019-006/.

[71] ATLAS Collaboration. "Muon reconstruction and identification efficiency in ATLAS using the full Run 2 *pp* collision data set at $\sqrt{s} = 13\,\text{TeV}$". In: *Eur. Phys. J. C* 81 (2020), p. 578. arXiv: 2012.00578 [hep-ex].

[72] ATLAS Collaboration. "Muon reconstruction performance of the ATLAS detector in proton–proton collision data at $\sqrt{s} = 13\,\text{TeV}$". In: *Eur. Phys. J. C* 76 (2016), p. 292. arXiv: 1603.05598 [hep-ex].

[73] ATLAS Collaboration. "Identification of boosted Higgs bosons decaying into *b*-quark pairs with the ATLAS detector at 13 TeV". In: *Eur. Phys. J. C* 79 (2019), p. 836. arXiv: 1906.11005 [hep-ex].

[74] ATLAS Collaboration. *Vertex Reconstruction Performance of the ATLAS Detector at $\sqrt{s} = 13$ TeV*. ATL-PHYS-PUB-2015-026. 2015. URL: https://cds.cern.ch/record/2037717.

[75] Torbjörn Sjöstrand et al. "An introduction to PYTHIA 8.2". In: *Computer Physics Communications* 191 (June 2015), pp. 159–177. URL: http://dx.doi.org/10.1016/j.cpc.2015.01.024.

[76] *ATLAS Athena Guide: Athena Releases, ATLAS Software Documentation Website*. https://atlassoftwaredocs.web.cern.ch/athena/athena-releases/.

[77] S. Agostinelli et al. "GEANT4–a simulation toolkikt. GEANT4. A Simulation toolkit". In: *Nucl. Instrum. Methods Phys. Res., A* 506 (July 2002), 250–303. 54 p. URL: https://cds.cern.ch/record/602040.

[78] C. Peterson et al. "Scaling violations in inclusive e^+e^- annihilation spectra". In: *Phys. Rev. D* 27 (1 Jan. 1983), pp. 105–111. URL: https://link.aps.org/doi/10.1103/PhysRevD.27.105.

[79] Fred James and Matthias Winkler. "MINUIT User's Guide". In: (June 2004).

[80] ATLAS Collaboration. *Tracking Studies for b-tagging with 7 TeV Collision Data with the ATLAS Detector*. ATLAS-CONF-2010-070. 2010. URL: https://cds.cern.ch/record/1281352.

[81] Manuel Bähr et al. "Herwig++ physics and manual". In: *The European Physical Journal C* 58.4 (Nov. 2008), pp. 639–707. URL: https://doi.org/10.1140%2Fepjc%2Fs10052-008-0798-9.

[82] ATLAS Collaboration. "Search for resonances in the mass distribution of jet pairs with one or two jets identified as *b*-jets in proton–proton collisions at $\sqrt{s} = 13\,\text{TeV}$ with the ATLAS detector". In: *Phys. Rev. D* 98 (2018), p. 032016. arXiv: 1805.09299 [hep-ex].

[83] ATLAS Collaboration. "Performance of pile-up mitigation techniques for jets in *pp* collisions at $\sqrt{s} = 8\,\text{TeV}$ using the ATLAS detector". In: *Eur. Phys. J. C* 76 (2016), p. 581. arXiv: 1510.03823 [hep-ex].

[84] Simone Alioli et al. "A general framework for implementing NLO calculations in shower Monte Carlo programs: the POWHEG BOX". In: *Journal of High Energy Physics* 2010.6 (June 2010). URL: http://dx.doi.org/10.1007/JHEP06(2010)043.

[85] Paolo Nason. "A New Method for Combining NLO QCD with Shower Monte Carlo Algorithms". In: *Journal of High Energy Physics* 2004.11 (Nov. 2004), pp. 040–040. URL: http://dx.doi.org/10.1088/1126-6708/2004/11/040.

[86] Stefano Frixione, Paolo Nason, and Carlo Oleari. "Matching NLO QCD computations with parton shower simulations: the POWHEG method". In: *Journal of High Energy Physics* 2007.11 (Nov. 2007), pp. 070–070. URL: http://dx.doi.org/10.1088/1126-6708/2007/11/070.

[87] Keith Hamilton, Paolo Nason, and Giulia Zanderighi. "MINLO: multi-scale improved NLO". In: *Journal of High Energy Physics* 2012.10 (Oct. 2012). URL: http://dx.doi.org/10.1007/JHEP10(2012)155.

[88] John M. Campbell et al. "NLO Higgs boson production plus one and two jets using the POWHEG BOX, MadGraph4 and MCFM". In: *Journal of High Energy Physics* 2012.7 (July 2012). URL: http://dx.doi.org/10.1007/JHEP07(2012)092.

[89] Keith Hamilton et al. "Merging H/W/Z + 0 and 1 jet at NLO with no merging scale: a path to parton shower + NNLO matching". In: *Journal of High Energy Physics* 2013.5 (May 2013). URL: http://dx.doi.org/10.1007/JHEP05(2013)082.

[90] Paolo Nason and Carlo Oleari. "NLO Higgs boson production via vector-boson fusion matched with shower in POWHEG". In: *Journal of High Energy Physics* 2010.2 (Feb. 2010). URL: http://dx.doi.org/10.1007/JHEP02(2010)037.

[91] H. B. Hartanto et al. "Higgs boson production in association with top quarks in the POWHEG BOX". In: *Physical Review D* 91.9 (May 2015). URL: http://dx.doi.org/10.1103/PhysRevD.91.094003.

[92] Gionata Luisoni et al. "$HW/HZ + 0$ and 1 jet at NLO with the POWHEG BOX interfaced to GoSam and their merging within MiNLO". In: *Journal of High Energy Physics* 2013.10 (Oct. 2013). URL: http://dx.doi.org/10.1007/JHEP10(2013)083.

[93] Gavin Cullen et al. "Automated one-loop calculations with GoSam". In: *The European Physical Journal C* 72.3 (Mar. 2012). URL: http://dx.doi.org/10.1140/epjc/s10052-012-1889-1.

[94] Richard D. Ball et al. "Parton distributions for the LHC run II". In: *Journal of High Energy Physics* 2015.4 (Apr. 2015). URL: http://dx.doi.org/10.1007/JHEP04(2015)040.

[95] K. Becker et al. *Precise predictions for boosted Higgs production*. 2021. arXiv: 2005.07762 [hep-ph].

[96] ATLAS Collaboration. "Measurement of the Z/γ^* boson transverse momentum distribution in pp collisions at $\sqrt{s} = 7\,\text{TeV}$ with the ATLAS detector". In: *JHEP* 09 (2014), p. 145. arXiv: 1406.3660 [hep-ex].

[97] Enrico Bothmann et al. "Event generation with Sherpa 2.2". In: *SciPost Physics* 7.3 (Sept. 2019). URL: http://dx.doi.org/10.21468/SciPostPhys.7.3.034.

[98] Stefano Frixione et al. "Single-top hadroproduction in association with a W boson". In: *Journal of High Energy Physics* 2008.07 (July 2008), pp. 029–029. URL: https://doi.org/10.1088%2F1126-6708%2F2008%2F07%2F029.

[99] ATLAS Collaboration. *ATLAS Pythia 8 tunes to 7 TeV data*. ATL-PHYS-PUB-2014-021. 2014. URL: https://cds.cern.ch/record/1966419.

[100] Richard D. Ball et al. "Parton distributions with LHC data". In: *Nuclear Physics B* 867.2 (Feb. 2013), pp. 244–289. URL: http://dx.doi.org/10.1016/j.nuclphysb.2012.10.003.

[101] ATLAS Collaboration. "The ATLAS Simulation Infrastructure". In: *Eur. Phys. J. C* 70 (2010), p. 823. arXiv: 1005.4568 [physics.ins-det].

[102] ATLAS Collaboration. *The Pythia 8 A3 tune description of ATLAS minimum bias and inelastic measurements incorporating the Donnachie–Landshoff diffractive model*. ATL-PHYS-PUB-2016-017. 2016. URL: https://cds.cern.ch/record/2206965.

[103] ATLAS Collaboration. *Simulation of top-quark production for the ATLAS experiment at $\sqrt{s} = 13$ TeV*. ATL-PHYS-PUB-2016-004. 2016. URL: https://cds.cern.ch/record/2120417.

[104] ATLAS Collaboration. *Study of top-quark pair modelling and uncertainties using ATLAS measurements at $\sqrt{s} = 13$ TeV*. ATL-PHYS-PUB-2020-023. 2020. URL: https://cds.cern.ch/record/2730443.

[105] Wouter Verkerke and David Kirkby. *The RooFit toolkit for data modeling*. 2003. URL: https://arxiv.org/abs/physics/0306116.

[106] Boosted VH(bb) Analysis Group. *Single top Wt modelling in VH(bb) analysis*. URL: https://indico.cern.ch/event/1032853/contributions/4343385/attachments/2236074/3790004/210429_stopWt_VHbb_boosted.pdf.

[107] Ulla Blumenschein et al. *Pushing the precision frontier at the LHC with V+jets*. 2018. URL: https://arxiv.org/abs/1802.02100.

[108] A. Gehrmann-De Ridder et al. "Precise QCD predictions for the production of a Z boson in association with a hadronic jet". In: *Physical Review Letters* 117.2 (July 2016). URL: https://doi.org/10.1103%2Fphysrevlett.117.022001.

[109] A. Gehrmann-De Ridder et al. "The NNLO QCD corrections to Z boson production at large transverse momentum". In: (2016). URL: https://arxiv.org/abs/1605.04295.

[110] ATLAS Collaboration. "Optimisation of large-radius jet reconstruction for the ATLAS detector in 13 TeV proton–proton collisions". In: *Eur. Phys. J. C* 81 (2020), p. 334. arXiv: 2009.04986 [hep-ex].

[111] ATLAS Collaboration. "Measurements of b-jet tagging efficiency with the ATLAS detector using $t\bar{t}$ events at $\sqrt{s} = 13$ TeV". In: *JHEP* 08 (2018), p. 089. arXiv: 1805.01845 [hep-ex].

[112] K. Becker et al. *Precise predictions for boosted Higgs production*. 2020. URL: https://arxiv.org/abs/2005.07762.

[113] Jon Butterworth et al. "PDF4LHC recommendations for LHC Run II". In: *Journal of Physics G: Nuclear and Particle Physics* 43.2 (Jan. 2016), p. 023001. URL: https://doi.org/10.1088%2F0954-3899%2F43%2F2%2F023001.

[114] Johannes Bellm et al. "Herwig 7.0/Herwig++ 3.0 release note". In: *The European Physical Journal C* 76.4 (Apr. 2016). URL: https://doi.org/10.1140%2Fepjc%2Fs10052-016-4018-8.

[115] CERN. *CERN Yellow Reports: Monographs, Vol 2 (2017): Handbook of LHC Higgs cross sections: 4. Deciphering the nature of the Higgs sector*. en. 2017. URL: https://e-publishing.cern.ch/index.php/CYRM/issue/view/32.

[116] Johan Alwall et al. "MadGraph 5: going beyond". In: *Journal of High Energy Physics* 2011.6 (June 2011). URL: https://doi.org/10.1007%2Fjhep06%282011%29128.

[117] J. M. Lindert et al. "Precise predictions for V + jets jets dark matter backgrounds". In: *The European Physical Journal C* 77.12 (Dec. 2017). URL: https://doi.org/10.1140%2Fepjc%2Fs10052-017-5389-1.

[118] L. A. Harland-Lang et al. "Parton distributions in the LHC era: MMHT 2014 PDFs". In: *The European Physical Journal C* 75.5 (May 2015). URL: https://doi.org/10.1140%2Fepjc%2Fs10052-015-3397-6.

[119] Torbjörn Sjöstrand. "Jet fragmentation of multiparton configurations in a string framework". In: *Nuclear Physics B* 248.2 (1984), pp. 469–502. URL: https://www.sciencedirect.com/science/article/pii/0550321384906072.

[120] Roger Barlow and Christine Beeston. "Fitting using finite Monte Carlo samples". In: *Computer Physics Communications* 77.2 (1993), pp. 219–228. URL: https://www.sciencedirect.com/science/article/pii/001046559390005W.

[121] Glen Cowan et al. "Asymptotic formulae for likelihood-based tests of new physics (vol 71, pg 1554, 2011)". In: *European Physical Journal C* 73 (July 2013).

[122] Alexander L. Read. "Presentation of search results: The CL(s) technique". In: *J. Phys. G* 28 (2002). Ed. by M. R. Whalley and L. Lyons, pp. 2693–2704.

[123] ATLAS Collaboration. "Measurements of top-quark pair differential and double-differential cross-sections in the ℓ+jets channel with pp collisions at $\sqrt{s} = 13\,\text{TeV}$ using the ATLAS detector". In: *Eur. Phys. J. C* 79 (2019), p. 1028. arXiv: 1908.07305 [hep-ex]. Erratum: in: *Eur. Phys. J. C* 80 (2020), p. 1092.

[124] Andrew J. Larkoski, Gavin P. Salam, and Jesse Thaler. "Energy correlation functions for jet substructure". In: *Journal of High Energy Physics* 2013.6 (June 2013). URL: https://doi.org/10.1007%2Fjhep06%282013%29108.

[125] ATLAS Collaboration. *Measurement of the ATLAS Detector Jet Mass Response using Forward Folding with* $80\,fb^{-1}$ *of* $\sqrt{s} = 13$ *TeV pp data*. ATLAS-CONF-2020-022. 2020. URL: https://cds.cern.ch/record/2724442.

[126] ATLAS Collaboration. *Optimisation of large-radius jet reconstruction for the ATLAS detector in* 13 *TeV proton–proton collisions*. ATLAS-CONF-2020-021. 2020. URL: https://cds.cern.ch/record/2723736.

[127] ATLAS Collaboration. *Efficiency corrections for a tagger for boosted* $H \to b\bar{b}$ *decays in pp collisions at* $\sqrt{s} = 13$ *TeV with the ATLAS detector*. ATL-PHYS-PUB-2021-035. 2021. URL: https://cds.cern.ch/record/2777811.

[128] ATLAS Collaboration. *Identification of Boosted Higgs Bosons Decaying Into* $b\bar{b}$ *With Neural Networks and Variable Radius Subjets in ATLAS*. ATL-PHYS-PUB-2020-019. 2020. URL: https://cds.cern.ch/record/2724739.

[129] S. S. Wilks. "The Large-Sample Distribution of the Likelihood Ratio for Testing Composite Hypotheses". In: *Annals Math. Statist.* 9.1 (1938), pp. 60–62.

[130] Stefano Frixione et al. “Single-top hadroproduction in association with a W boson”. In: *Journal of High Energy Physics* 2008.07 (July 2008), pp. 029–029. URL: https://doi.org/10.1088%2F1126-6708%2F2008%2F07%2F029.